UNIVERSITÀ
DEGLI STUDI
FIRENZE

DOTTORATO DI RICERCA IN
Area del Farmaco e Trattamenti Innovativi

CICLO XXXIV

COORDINATORE Prof. Carla Ghelardini

Role of neuroinflammation in the symptoms associated to neuropathic pain: targeting microglia with innovative treatments

Settore Scientifico Disciplinare BIO/14

Dottorando
Dott. Borgonetti Vittoria

Tutore
Prof. Galeotti Nicoletta
Nicoletta Galeotti

Coordinatore
Prof. Ghelardini Carla

Anni 2018/2021

Ciao Gino

Alla fine siamo tutti un po' pazzi

Abstract

The immune system in mammals contains a wide array of cells which serves to maintain normal physiologic conditions and promote the repairing processes of damaged tissues. Many of these activities are mediated by soluble factors, such as chemokines and cytokines, which are released from immune cells and bind to specific receptors or interact with other cellular targets, resulting in the activation of selected genes. This cross talk between different cell types maintains the homoeostatic balance of the immune system. Microglia cells, located in the brain and spinal cord, represent the immune cells of the central nervous system (CNS) and, along with astrocytes, constitute the first line of defense in the CNS. Several studies developed over the years show that a lesion of peripheral nerves can lead to the variation of plasticity in central synapses at structural and functional level. Specifically, these alterations lead to an imbalance between excitatory and inhibitory synapses in the dorsal horns of the spinal cord where we find the pain pathways, which could be the cause of the phenomenon of hypersensitivity at the base of the pathophysiological process. The origin of this imbalance is still not fully clarified, but with increasing certainty it has emerged how the activation of microglia cells present at the spinal level could play a fundamental role. Neuropathic pain (NP) is the most difficult to treat type of pain; the patient hardly achieves a complete analgesic effect, but only obtains a reduction in symptoms. Therefore, therapy is often unsatisfactory due to both the poor efficacy and side effects of the drugs used. The purpose of this thesis is precisely to find innovative therapies that target factors involved in microglial activation and its shift into pro-inflammatory microglia.

In NP, microglia represent a key modulator of the various processes that characterize this chronic and disabling disease, which can be summarized as: neuroinflammation, neurodegeneration, and demyelination. The multiple mechanisms of the innovative treatments studied in this work for reducing microglial activation produced two main effects: reduction of neuroinflammation by promoting the phenotypic shift of microglia, and counteraction of demyelination. Our findings highlight the key role of microglia in the neuronal maintenance and open a broader vision of NP therapy through an approach that can resolve the causes rather than being a simple symptomatic intervention. The targets on which we have mainly focused our attention are modulators of genetic transcription: HDAC1 and HuR, and their silencing with different therapeutical approaches, induced a slow-down of pathology. Innovation is also brought by the type of administration used, the intranasal delivery, which have an effect at the level of the CNS in a non-invasive way compared to more complex and disabling routes such as intrathecal. In fact, the use of non-invasive routes favors an increase in compliance with the patient, which also ensures a higher effectiveness of therapies and increases quality of life.

Neuropathies are chronic diseases whose main symptoms are associated with pain, but which involve, given their difficulty in resolving, the onset of long-term comorbidities such as anxiety, depression, insomnia, and loss of cognitive ability. Using a marker of cellular senescence, we evaluated the possible development of microglial aging at the level of the spinal cord (central site of pain) and of the hippocampus (important site of the development of anxiety and depression). Indeed, preventing microglial senescence means reducing the possibility of having an alteration in the homeostasis of the CNS, that leads to aging and deterioration of the cognitive abilities of the person.

Another aspect that has emerged rather recently is the possible connection between microglia and all kind of addictive conditions, including those produced by alcohol. Indeed, about 50% of individuals who exhibit alcohol dependence develops the so called “alcoholic neuropathy”. In the spinal cords of alcohol-dependent animals that develop neuropathy, we observed an increase in the expression of microglial markers, thus opening a new avenue in the possible involvement of microglia also in these forms of neuropathy.

In conclusion, a stressful correlation between neuroinflammation, demyelination, and degeneration in central and peripheral neuropathies was observed in this thesis (Figure). Given that microglia activation is an important crossroads in the onset and regulation of these processes, this work suggest that its role should be more deeply investigated and considered as an important drug target. Indeed, restoring normal physiological conditions in the nervous environment through the modulation of specific microglial targets is an innovative approach to move towards more effective, safe, and personalized therapies.

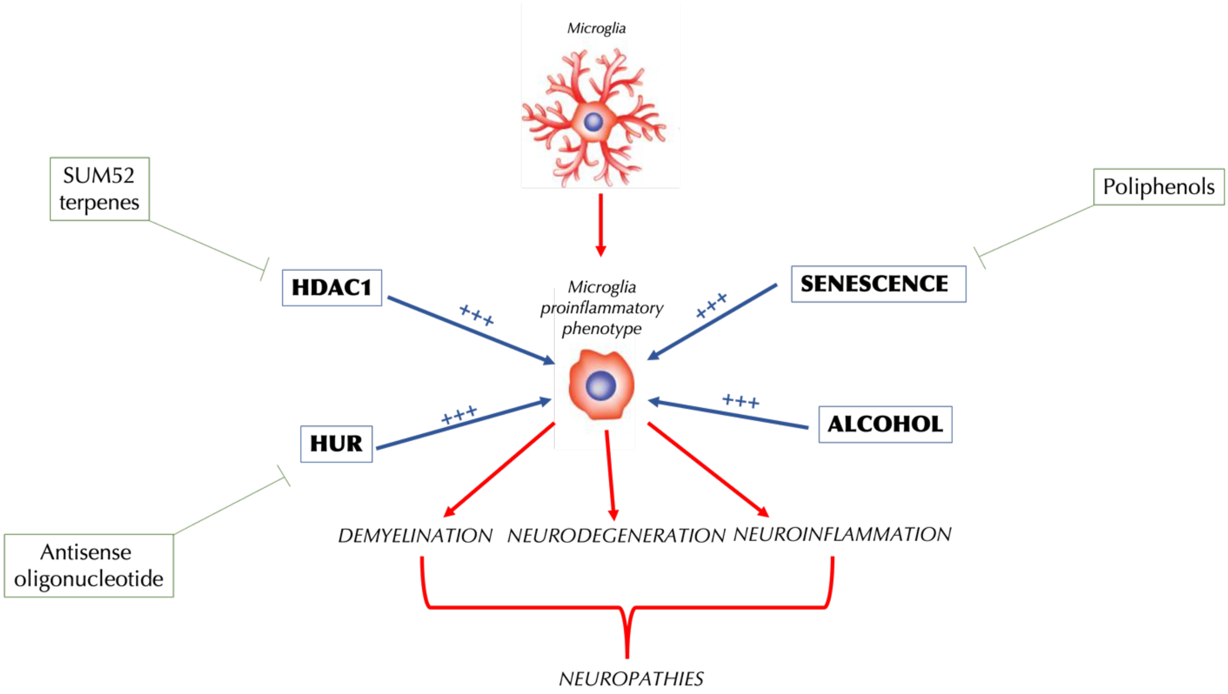

TABLE OF CONTENTS

Chapter 1

Introduction

The immune system in mammals contains a wide array of cells which serves to maintain normal physiologic conditions and promote the repairing processes of damaged tissues. Many of these activities are mediated by soluble factors, such as chemokines and cytokines, which are released from immune cells and bind to specific receptors or interact with other cellular targets, resulting in the activation of selected genes. This cross talk between different cell types maintains the homoeostatic balance of the immune system[1]. Microglia cells, located in the brain and spinal cord, represent the immune cells of the central nervous system (CNS) and, along with astrocytes, constitute the first line of defense in the CNS[2]. These central immune cells have several functions in the CNS, such as synaptic plasticity, immune surveillance, neuroinflammation, inflammatory suppression, and neuroprotection[3]. In healthy condition, microglia are inactive (resting-microglia), have a branched morphology, and a small soma with cellular processes[4]. Upon stimulation these cells rapidly become "activated" and undergo morphological and molecular changes in response to signals from the damaged tissue[5]. Activated microglia is commonly divided into two cell populations: pro-inflammatory phenotype (M1) and the anti-inflammatory phenotype (M2). In the classical activation state, M1, microglia assume an amoeboid morphology, migrate toward the stimulus, and promote inflammation by releasing inflammatory cytokines, such as TNF-α, IL-6, and IL-1β, and by attracting immune cells, such as neutrophils and monocytes[4]. This effect leads to the activation of additional glial cells, facilitating their mobility to the injured area. The result is an amplification of the inflammatory response, a loss of myelin, disruption of the blood-brain barrier (BBB), and increased cell death with loss of neurons, thus increasing the extent of the initial injury[6]. Regarding the M2 phenotype (alternative activation), this state promotes anti-inflammatory effects, such as tissue repair and reconstruction of the extracellular matrix, alleviates acute inflammation and is favored by the release of anti-inflammatory cytokines, such as IL-10 and TGF-β[7]. Thus, M1 microglia exacerbate existing neuronal damage, whereas M2 microglia appear to have neuroprotective activity. This first classification of M1/M2 microglia fail to capture the complexity of microglial activity which changes rapidly in response to local conditions as well as tissue type. Chronic activation of microglia plays a major role in disorders characterized by nervous tissue inflammation, thus, in this PhD thesis, we focused on the role of microglia in neuropathic pain (NP) and investigated possible therapeutic strategies targeting microglial functions in this chronic condition. Several studies developed over the years show how the lesion of peripheral nerves leads to the variation of plasticity in central synapses at structural and functional level. Specifically, these alterations lead to an imbalance between excitatory and inhibitory synapses in the dorsal horns of the spinal cord where we find the pain pathways, which could be the cause of the phenomenon of hypersensitivity at the base of the pathophysiological process. The origin of this imbalance is still not fully clarified, but with increasing certainty it has emerged how the activation of microglia cells present at the spinal level could play a fundamental role[8]. In the early stages of inflammation following nerve injury, microglia seem to have almost a protective role against neuronal damage, but then this neuroprotective activity is lost, as they begin to produce inflammatory cytokines and chemokines and to recall immune cells along with additional glial cells. Indeed, it has been hypothesized that the early stages of NP are characterized by strong neuroinflammation that is not controlled. Around the site of injury there is the release of inflammation factors such as histamine, prostaglandins, and cytokines (IL-6, IL-1β, and TNF-α), which generates a state of hyperexcitability[9]. This persistent inflammatory state induces damage at the neuronal level that can result in myelin loss and thus demyelination 6. Microglia also play important roles in remyelination[10] and the ability of microglia/macrophages to phagocyte myelin debris is critical for promoting OPC recruitment and differentiation into myelinating cells[11]. Many cytokines, growth factors, and soluble factors are known to be secreted by microglia/macrophages and they can induce regenerative effect on neurons[12]. New emerging evidence have revealed that peripheral NP also activated microglia in brain regions including the thalamus, amygdala, venous tegmental area, nucleus accumbens (NAc), ACC, stria terminalis nucleus, hippocampus, and periaqueductal gray. However, it is still unknown how microglia are activated in these brain regions, which are at considerable distance from the sites of injury in peripheral nerves[13]. This role in different areas of the CNS suggests that microglia are not only related to the symptomatology of pain and its causes but may also play a role in the onset of comorbidities that are often associated with the patient suffering from neuropathy (both peripheral and central). Moreover, microglia are strongly implicated in several central pathological conditions, including major depressive disorder (MDD), anxiety disorders, and post-traumatic stress disorder (PTSD), such that we can speak of microgliopathies[14].

The microgliosis that occurs following peripheral nerve injury, such as in NP conditions, does not occur in case of acute inflammatory process. Microgliosis takes days to manifest after nerve injury and the adaptation mechanisms induced by microglia function occurs mainly in chronic pain and not in acute inflammatory pain[15]. Thus, NP is a non-nociceptive pain due to an injury, disease, or dysfunction of the central or peripheral nervous system. It is a somewhat different situation from the nociceptive of inflammatory pain "messages" that travel along healthy nerves to damaged tissue (as in a fall or cut, or arthritic knee). NP is usually subdivided according to the cause of nerve injury.

Some common causes of peripheral NP include diabetes (painful diabetic neuropathy (PDN), NP after surgery or trauma, spinal cord injury, trigeminal neuralgia, and human immunodeficiency virus (HIV), or central NP which includes multiple sclerosis (MS) and neuromyelitis optica (NMO)[9]. NP is the most difficult to treat type of pain; the patient hardly achieves a complete analgesic effect, but only obtains a reduction in symptoms. Increasingly, multidisciplinary approaches are being used, with pharmacological interventions combined with physical or cognitive interventions, or both. For example, medications that are sometimes used to treat depression (TCAs, SNRIs) or epilepsy (gabapentin o pregabalin) can be very effective in some people with NP[16]. Whereas if we look at commonly used painkillers such as ibuprofen (a non-steroidal anti-inflammatory drug) they are usually not considered effective in that type of pain. Therefore, therapy is often unsatisfactory due to both the poor efficacy and side effects of the drugs used, as available drugs only treat the symptomatology associated with pain and does not take in consideration the actual cause of the onset of the condition. Failure to modulate and regulate the triggers of NP leads to progression and chronicity of the disease with worsening of the patient's condition and quality of life[17]. Since microglia is crucial both in the early stages of the disease, with the increase of neuroinflammation and at the same time in the later stages by modulating the processes of demyelination and senescence, the purpose of this thesis is to find therapeutic strategies that can intervene in the modulation of microglia activity not only to block the symptoms associated with pain but also to treat the causes that generate pain.

This thesis is divided into four sections aimed at investigating etiopathogenetic mechanisms of NP and related comorbidities to identify specific targets for innovative therapeutic approaches:

1) Epigenetics of NP: focus on histone deacetylase enzymes. In this section it is investigated the selective modulation of HDAC1 by synthetic substances but also by bioactive compounds extracted from medicinal plants, for the treatment of NP.
2) Post-transcriptional regulation of gene expression. In this section it is investigated the targeting of the RNA-Binding Protein HuR as a novel therapeutic approach for central and peripheral neuropathies through the reduction of neuroinflammation and promoting myelinization.
3) Comorbidities of NP. In this section the onset and progression of main comorbidities are investigated with a focus on the role of senescent microglia.
4) Alcoholic neuropathy: in this section it is investigated how chronic ethanol exposure induces NP in mice by promoting neuroinflammation and microglia activation.

The purpose that connects these sections is to find innovative treatments that would overcome the main drawbacks of available therapy, such as low efficacy and high incidence of side effects, that largely reduce the patient's quality of life. In addition, we will focus on the investigation of innovative delivery routes of administration that can increase patient's compliance (mostly oral and intranasal).

Chapter 2
Materials and methods

2.1. Animals

2.1.1. Ce.S.A.L. (Centro Stabulazione Animali da Laboratorio, University of Florence)

Experiments for SNI were performed on male CD1 mice (24-26 g, 4- week-old) from Envigo, female SJL mice (18-20 g, 10-12- week-old) at immunization were used to induce PLP$_{139–151}$EAE and MOG$_{35–55}$ EAE model were performed on C57 female mice (20-25 g, 10-week-old) from Envigo (Varese, Italy). Charles River Laboratories Animals were housed in the Ce.S.A.L. (Centro Stabulazione Animali da Laboratorio, University of Florence) vivarium and used one day after their arrival. Mice were housed in standard cages, kept at 23 ± 1 °C with a 12-h light/dark cycle, light on at 7 a.m., and fed with standard laboratory diet and tap water ad libitum. The cages were placed in the experimental room 24 h before behavioural testing for acclimatization. Experiments were conducted in accordance with international laws and policies (Directive 2010/63/EU of the European parliament and of the council of 22 September 2010 on the protection of animals used for scientific purposes; Guide for the Care and Use of Laboratory Animals, U.S. National Research Council, 2011). Protocols were approved by the Animal Care and Research Ethics Committee of the University of Florence, Italy, under license from the Italian Department of Health (410/ 2017-PR). All studies involving animals are reported in accordance with the ARRIVE guidelines for experiments involving animals39. Protocols were designed to minimize the number of animals used and their suffering. The number of animals per experiment was based on a power analysis9 and calculated by G power software.

2.1.2. The Scripps Research Institute (San Diego, USA)

Male and female C57BL/6J mice were obtained from the Jackson Laboratory (ME) and group-housed in a temperature and humidity-controlled vivarium on a 12 h reversed light/dark cycle (lights turn off at 8AM) with food and water available ad libitum.

All procedures were approved by The Scripps Research Institute Institutional Animal Care and Use Committee and conform to the National Institutes of Health Guide for the Care and Use of Laboratory Animals.

2.2. In vivo models

2.2.1. Neuropathies models

2.2.1.1. Peripheral neuropathy

2.2.1.1.1 Spared Nerve Injury

Mononeuropathy was induced by SNI, and this model of pain in mice has been in use for several years[18]. Mice were anesthetized with a mixture of 4% isoflurane in O_2/N_2O (30:70 v/v) and placed in a prone position. The right hind limb was slightly elevated, and a skin incision was made on the lateral surface of the thigh. The sciatic nerve was exposed at mid-thigh level distal to the trifurcation and freed of connective tissue; the three peripheral branches (sural, common peroneal and tibial nerves) of the sciatic nerve were exposed without hurting nerve structures. Both tibial and common peroneal nerves were ligated with a microsurgical forceps (5.0 silk, Ethicon; Johnson & Johnson Intl, Brussels, Belgium) and transacted together. The sural nerve was carefully preserved by avoiding any nerve stretch or contact with surgical tools. Muscle and skin were closed in two distinct layers with silk 5.0 sutures. Intense, reproducible, and long-lasting thermal and mechanical allodynia-like behaviors are measurable in the non-injured sural nerve skin extensions. The sham procedure consisted of the same surgery without ligation and transection of the nerves.

2.2.1.1.2. Chronic-intermittent ethanol two-bottle choice paradigm

Male and female C57BL/6J mice were exposed to a limited-access ethanol (15% w/v) two-bottle choice (2BC) paradigm, followed by either CIE exposure in vapor chambers (La Jolla Alcohol Research, La Jolla, CA), to induce alcohol dependence, or air exposure in identical chambers[19]. To establish baseline drinking, 2BC testing was performed 5 days per week for 3 consecutive weeks. Mice were singly housed 30 min before the lights were turned off and given 2 h-access to two drinking tubes containing either 15% ethanol or water. Following this 3-week baseline phase, mice were divided into two balanced groups with equal ethanol and water consumption. The Dep and Non-Dep groups were exposed to CIE vapor and air, respectively. Mice in the Dep group were injected i.p. with 1.75 g/kg ethanol + 68.1 mg/kg pyrazole (alcohol dehydrogenase inhibitor) and placed in vapor chambers for 4 days (16 h vapor on, 8 h off). Naïve and Non-Dep mice were injected with 68.1 mg/kg pyrazole in saline. After pyrazole injection, Naïve mice were placed back in their home cages, while Non-Dep mice were transferred into air chambers for the same intermittent period as the Dep group. The vapor/air exposure was followed by 72 h of abstinence and 5 days of 2BC testing. This regimen was repeated three additional times for a total of five full rounds. Before euthanasia, Dep mice were exposed to a single ethanol vapor exposure (16 h), and tail blood was collected to determine terminal BELs. All protocols involving the use of experimental animals in this study were approved by The Scripps Research Institute (TSRI) Institutional Animal Care and Use Committee and were consistent with the National Institutes of Health Guide for the Care and Use of Laboratory Animals.

2.2.1.2. Central neuropathy

2.2.1.2.1. Experimental Autoimmune Encephalomyelitis (EAE) model

Mice were immunized subcutaneously (s.c.) in the flanks and at the base of the tail with a total of 200 μg of two different peptide (synthesized by EspiKem Srl., University of Florence, Italy)[20]:

$PLP_{139–151}$: Relapsing-remitting multiple sclerosis

$MOG_{35–55}$: Chronic progressive multiple sclerosis

Peptides were emulsified in complete Freund adjuvant (CFA; Sigma, Milan, Italy) supplemented with 4 mg/ml of Mycobacterium tuberculosis (strain H37Ra; Difco Laboratories, Detroit, MI). Control mice received CFA without PLP139–151. Immediately thereafter, and again 48 h later, all mice received an intraperitoneal (i.p.) injection of 500 ng Pertussis Toxin (Sigma) in 100 μl phosphate buffer saline (PBS). General health and body weights of all mice were assessed prior to immunization and once daily thereafter in a blinded manner until the completion of the study. Locomotor coordination and nociceptive threshold were analyzed before onset and regularly while the disease[21].

2.2.2. Behavioral tests

2.2.2.1. Clinical Disease Score

Clinical disease scoring of EAE and sham mice (control group) was undertaken once daily in a blinded manner to evaluate the severity and extent of motor function deficits using a 5-point scale with half-point gradations[21]. EAE scores were daily assessed: score 0, no obvious changes in motor functions; score 0.5, distal paralysis of the tail; score 1, complete tail paralysis; score 1.5, mild paresis of 1 or both hind legs; score 2, severe paresis of hind legs; score 2.5, complete paralysis of 1 hind leg; score 3, complete paralysis of both hind legs; and score 3.5, complete paralysis of hind legs and paresis of 1 front leg. EAE clinical disease was classified as present by clinical scores ≥ 1, whereas clinical scores ≤ 0.5 were regarded as disease remission or absence. Mice reaching a score of 3.5 were excluded from the study.

2.2.2.2. Locomotor activity

2.2.2.2.1 Rotarod

The apparatus consisted of a base platform and a rotating rod with a diameter of 3 cm and a non-slippery surface. The rod was placed at a height of 15 cm from the base. The rod, 30 cm in length, was divided into 5 equal sections by 6 disks. Thus, up to 5 mice were tested simultaneously on the apparatus, with a rod-rotating speed of 16 rpm. The integrity of motor coordination was assessed based on the number of falls from the rod in 30 s, as described[21].

2.2.2.2.2. Hole Board Test

The spontaneous locomotor activity was evaluated by using the hole-board test. The apparatus consisted of an elevated arena (40 cm × 40 cm; 1 m above the floor) with 16 evenly spaced holes (3 cm diameter; four lines of four holes each). Mice were placed individually on the center of the board and allowed to explore the plane freely for a period of 5 min each. Movements of the animal on the plane (spontaneous mobility) were automatically recorded by two photobeams, crossing the plane from midpoint to midpoint of opposite sides, thus dividing the plane into four equal quadrants. Miniature photoelectric cells, in each of the 16 holes, recorded the head-dips in the holes by the mice. This head-dipping behavior represents the exploratory activity of mice[21].

2.2.2.3. Nociceptive Behavior

2.2.2.3.1. Mechanical Threshold (von Frey's Test filaments)

The Von Frey test is used to evaluate mechanical allodynia[22]. The tests were carried out both before the operations, using the data obtained as a reference, and afterwards for comparison. Mechanical nociception was measured by Von Frey monofilaments. Mice were placed in single plexiglass chambers [8.5 x 3.4 x 3.4 (h) cm]. After a settling period of 1 h inside the chambers, the mechanical threshold was measured through a stimulus using Von Frey monofilaments with increasing degree of strength (0.04, 0.07, 0.16, 0.4, 0.6, 1.0, 1.4, 2.0 g) on both legs, ipsilateral and contralateral. The response was defined by the withdrawal of the paw three times out of five stimuli performed. In the event of a negative response, the next higher-grade strand was applied, and the averages of the responses were finally calculated.

2.2.2.3.2. Hot Plate Test

The hot plate test involves measuring the animal's response time to hot stimulus using an electrically heated circular metal surface (24 cm diameter). In the evaluation of thermal hyperalgesia to heat, the temperature is maintained at approximately 52.5°C. Mice were placed on the hot plate, surrounded by a transparent acrylic cage. The latency of the response, consisting of licking or shaking of the paw, or jumping, was measured in seconds. The mice were immediately withdrawn as soon as one of these symptoms occurred. Animals were tested one at a time and were not accustomed to the experimental system prior to testing. Tests were carried out both before operations, obtaining a baseline, and after operations had taken place, and finally response averages were calculated[23].

2.2.2.3.3. Hargreaves' plantar test

Thermal nociceptive threshold was measured using Hargreaves' device, as described. Paw withdrawal latency in response to radiant heat (infrared) was assessed using the plantar test apparatus (Ugo Basile, Comerio, Italy). Each mouse was placed under a transparent Plexiglas box (7.0 × 12.5 cm^2, 17.0 cm high) on a 0.6-cm-thick glass plate and allowed to acclimatize for 1–2 h before recording. The radiant heat source consisted of an infrared bulb (Osram halogen-bellaphot bulb; 8 V, 50 W) that was positioned 0.5 cm under the glass plate directly beneath the hind paw. The time elapsed between switching on the infrared radiant heat stimulus and manifestation of the paw withdrawal response was measured automatically. The intensity of the infrared light beam was chosen to give baseline latencies of 10 s in control mice. A cut-off of 20 s was used to prevent tissue damage. Each hindpaw was tested 2–3 times, alternating between paws with an interval of at least 1 min between tests. The interval between two trials on the same paw was of at least 5 min. Nociceptive response for thermal sensitivity was expressed as thermal paw withdrawal latency in seconds. All determinations were averaged for each animal[22].

2.2.2.4. Antidepressant-like activity

2.2.2.4.1. Tail Suspension Test

Mice were suspended from a plastic rod mounted 50 cm above the floor by adhesive tape placed to the upper middle of the tail. The time during which mice remained immobile was measured with a stopwatch during a test period of 6 min. Mice were considered immobile when they hung passively and completely motionless, except movements caused by respiration. Immobility was considered as depression- like behavior (behavioral despair) and was measured in the first 2 min of the test, when animals react to the unavoidable stress, and in the last 4 min, when the behavioral despair is established[24].

2.2.2.4.2. Sucrose splash test

The test is aimed at assessing the level of depression of the mouse. A 10% sucrose solution in H2O is prepared and a small amount of this is placed on the animal's back. The mouse is placed inside a box and the time it has spent cleaning is measured compared to the total duration of the test 5 minutes. The purpose is to obtain information about the state of depression of the mouse, in fact the more this will be marked, the more difficult the animal will tend to clean itself[25].

2.2.2.5. Anxiolytic-Like Activity

2.2.2.5.1. Light-Dark Box

The light-dark box apparatus (length 50 cm, width 20.5 cm, and height 19 cm) consisted of two equal acrylic compartments, one dark (black) and one illuminated by a 60-W bulb lamp (white). A dark insert (with black walls and lid, nontransparent for visible light) was used to divide the arena into two equal parts. The two compartments communicated by a small door (10 cm × 3.2 cm) at floor level in the wall of the insert that allowed animals to move freely from one compartment to another. Each mouse was released in the center of the light compartment with its head facing away from the door and allowed to explore the arena for 5 min. Behavioral parameters recorded were the latency to the first step into the dark compartment, the time spent in the light chamber and the number of full-body transitions between chambers since previously described as a reflection of anxiety in this apparatus. After testing, animals were removed from the light-dark box and returned to their home cage in colony room. After each test, the apparatus was cleaned with 70% ethanol to remove the olfactory cues and allowed to dry before the next subject was tested. This test exploited the conflict between the animal’s tendency to explore a new environment and its fear of bright light[24].

2.2.2.5.2. Open field test

This is a test used to assess the animal's anxiety levels. A rectangular box (78 x 60 x 39 cm) is used, on which an internal perimeter is traced such as to deviate about 3 cm from the walls. The mouse is positioned in the center of the room and then the time it remains in the internal portion is measured, compared to a total duration of five minutes[26].

2.2.2.6. Evaluation of Mnemonic Functions

2.2.2.6.1. Novel Object Recognition Test

Memory-related responses were measured using the novel object recognition test (NORT), which is based on natural exploratory activity of mice. NORT evaluates the rodent's ability to recognize a novel object in the environment and measures a form of recognition memory. To perform the NORT, an open field device (cylinder diameter: 78 cm, height walls: 60 cm) was used. Mice were allowed to explore the open field. No object was placed in the box during the habituation session. Then, in the first session (training phase), animals were placed in the middle of the arena and presented with two identical objects (A1 and A2), placed 16 cm from the wall and 37 cm apart, for 5 min. Object exploration was measured manually using a stopwatch by an experienced observer blind to drug treatment. Exploration was defined as sniffing or touching the object with the nose or mouth. To measure short-term memory or long-term memory, the animals were placed back in the open field after 3-h or 24-h delay in the home cage, respectively, and presented with two objects, the familiar A1 (the same as the training phase) and a novel object B for 5 min (test phase). The objects were always placed in the same location. To secure the objects in place, Velcro into the base of the objects was used. Objects A1 and B had different shapes, colors, and sizes that had no significance for animals. The objects and the apparatus were cleaned with ethanol solution between trials to remove the olfactory cues. The test phase reflects the preference for the novel object. Recognition index for the novel object was calculated (TB-TA1/TB + TA1) × 100 (TA = time spent exploring familiar object; TB = time spent exploring the novel object). Discrimination index was calculated (TA1+TB)/TA1 x100. During the training session, both objects are novel (TA1-2) and the time spent on both objects should be similar[27].

2.2.3. Routes of administration

2.2.3.1. Intrathecal administration (i.t.)

The animals were placed in a transparent plastic box and anaesthetized with a mixture of 4% isoflurane in O2/N2O (30:70 v/v). The lower half of the animal's back was shaved and scrubbed with povidoneiodine. The animals were then placed in a prone position on a Styrofoam board (25 cm × 13 cm × 6 cm), with the mask opening fixed 12 cm from the end of the board. Then the isoflurane concentration was lowered to 1.5–2% for the remainder of the procedure. The mice's forelimbs were extended towards the front and fixed to the board with tape, taking care not to force the neck. The hind limbs were left to hang off the board, lying on the table. In that way, the animal's vertebral column was flexed around the L3–L5 level, widening these intervertebral spaces. The lumbar puncture needle was introduced perpendicular to the surface through the widest intervertebral space and lowered until it met the vertebral body. Occasionally, a short flicking of the tail or of a limb was observed. Animals then recovered in their home cage before testing[21].

2.2.3.2. Intranasal administration (i.n.)

The mice were placed in the supine position and 10 μL of substance were slowly dropped alternately into each nostril of the animal with a micropipette[28].

2.2.3.3. Oral administration (p.o.)

Gavage administration involves intubating the mouse with an intubation needle attached to a graduated syringe. The dose is administered into the esophagus. Intubation needles for mice are typically constructed of stainless-steel tubing with a stainless-steel ball tip to reduce the likelihood of esophageal perforation and dose aspiration. Acceptable tube sizes fall in the 22- to 18-gauge range, with the largest bore reserved for older mice (e.g., ≥25 g). Tube length can range from 1 to 3 inches. The ball tip is 1.25 to 2.25 mm in diameter. Commercially available intubation needles can be straight or curved. The choice of shape is a matter of personal preference on the part of the dosing technician. Prior to administration, the test substance should be prepared in liquid form at an appropriate concentration. Solid substances will require dissolution or suspension in a harmless vehicle. The preferred vehicle is water. If the substance is insoluble in water, various agents may be added to improve wetting and reduce settling. For the actual process of dose administration, the mouse must be weighed and the appropriate dose to be administered must be calculated. The appropriate dose volume should be aspirated into the dosing syringe by removing air; at this point the animal is then taken from the skin of the back and neck and head, tilted back to form a straight line from the nose through the back of the throat and to the stomach. The intubation needle is inserted into the back of the mouth, then tilted back slightly, if necessary, to enter the esophagus. The mouse usually facilitates entry into the esophagus by swallowing the ball of the needle. When properly positioned, the tube can be easily inserted deep into the esophagus, but it is not necessary to reach the stomach. When in place, the dose should be administered slowly to avoid suffocation of the animal, but promptly enough to reduce the likelihood that the mouse will fight and may injure itself[22].

2.2.3.4. Subcutaneous administration (s.c.)

Subcutaneous administration injections are performed by gently pulling upward on the skin of the animal's back, for example at the level of the flanks. The appropriately sized needle is then inserted into the animal's dermis. If more than one injection is to be made, the injection site should be varied to reduce the likelihood of local reactions. If the injection is successful, a small area of swelling at the injection site can usually be noted. The concentrations of the drugs have been prepared to administer a volume of liquid not exceeding 10 ml per kg of body weight[22].

2.2.3.5. Intraperitoneal administration (i.p.)

The injection is performed by grasping the animal to keep the skin of the abdomen well stretched. The syringe needle is inserted into the lower abdominal quadrant of the animal to form an angle of about 45° with the plane formed by the abdomen itself, indifferently to the right or left of the midline of the abdomen. The intraperitoneal route is a route of administration used only in the animals and is characterized by a large absorbent surface and a very rapid absorption[29].

2.3. Cell culture

A murine microglial line BV-2 (mouse, C57BL / 6) was used for this study. The cells, kindly provided to us by Prof. Biagi of the University of Siena, were thawed and placed in a 75 cm2 flask (Sarstedt, Milan) in a medium containing RPMI with the addition of 10% of heat-inactivated (56 °C, 30 min) fetal bovine serum (FBS, Gibco®, Milan) and 1% glutamine. Cells were grown at 37 °C and 5% CO2 with daily medium change[30].

A human neuroblastoma cell line SH-SY5Y was kindly donated by Prof. Lorenzo Corsi (University of Modena and Reggio Emilia, Italy), was cultured in DMEM and F12 Ham's nutrients mixture (Sigma-Aldrich), containing 10% heat-inactivated FBS (Sigma-Aldrich), 1% L-glutamine (Sigma-Aldrich), and 1% penicillin-streptomycin solution (Sigma-Aldrich) until confluence (70–80%). The cells were grown in a humidified atmosphere with 5% CO2 at 37 °C. EDTA-trypsin solution (Sigma-Aldrich) was used for detaching the cells from flasks, and cell counting was performed using a hemocytometer by Trypan blue staining as previously reported[31].

2.3.1. Cell viability

2.3.1.1. CCK-8 (cell counting kit) assay

Cell viability was performed using a Cell Counting Kit (CCK-8, Sigma-Aldrich) according to the manufacturer's instructions. A total of 5×10^5 cells/well were seeded into 96-wells plates and grown to confluence. The absorbance was measured at 450 nm using a MP96 microplate reader spectrophotometer (Safas, Monte Carlo, Principality of Monaco). The treatments were performed in six replicates in three independent experiments, and cell viability was calculated by normalizing the values to the control's mean[30].

2.3.1.2. SRB (sulforhodamine B) assay

Cell viability was assessed by SRB assay. Cells are seeded in 96-well plates, each corresponding to a different treatment (2x104 cells in 200 µl). RPMI 1640 serum-free medium is added to the wells in an amount of 100 µl followed by 25µl of 50% TCA trichloroacetic acid. The plate is then left to incubate at 4°C for one hour. This is followed by 5 washes of the wells with double distilled water (100µl per well). The plate is left overnight to dry at room temperature. The next day, a solution of SRB 4 mg/ml in 1% acetic acid is added at 30µl per well for 30 minutes at room temperature. This is followed by 4 washes with 1% acetic acid (200µl per well). Then add the wells with 200µl of TRIS HCl solution at pH 10 for five minutes. Finally, the absorbance is read on the spectrophotometer at a wavelength of 570 nm. The treatments were performed in six replicates in three independent experiments, and cell viability was calculated by normalizing the values to the control's mean[32].

2.3.2. Preparation of tissue and cell lysate

To examine protein expression, mice were sacrificed tissues were removed after surgery. Samples were homogenized in a lysis buffer containing 25 mM Tris-HCl ph (7.5), 25 mM NaCl, 5 mM EGTA, 2.5 mM EDTA, 2 mM NaPP, 4 mM PNFF, 1 mM di Na3VO4, 1 mM PMSF, 20 µg/ml leupeptin, 50 µg/ml aprotinin, 0.1% SDS (Sigma-Aldrich, Milan, Italy). The homogenate was centrifuged at 12000 × g for 30 min at 4 °C and the pellet was discarded. Proteins from cells were extracted by RIPA buffer (50 mM Tris-HCl pH 7.4, 150 mM NaCl 1% sodium deoxycolate, 1% Tryton X-100, 2 mM PMSF) (Sigma-Aldrich) and the insoluble pellet was separated by centrifugation (12000 × g for 30 min, 4 °C). The total protein concentration in the supernatant was measured using Bradford colorimetric method (Sigma-Aldrich)[22].

2.4. Western Blotting

Protein samples (40 µg of protein/sample) were separated by 10% SDS- PAGE. Proteins were then blotted onto nitrocellulose membranes (120 min at 100 V) using standard procedures. Membranes were blocked in PBST containing 5% non-fat dry milk for 120 min and incubated overnight at 4°C with primary antibodies. The blots were rinsed three times with PBST and incubated for 2 h at room temperature with HRP-conjugated secondary antibody and then detected by chemiluminescence detection system (Pierce, Milan, Italy). Signal intensity (pixels/mm^2) was quantified using ImageJ (NIH)[23].

2.5. Cytokines dosage with ELISA assay

2.5.1. Plasma

Blood samples were taken from the ventricle with a standard cardiac puncture method, centrifuged at 3000 × g for 10 min at 4 °C, and the plasma was collected. TNF-α, IL-1β, and IL-17 protein levels were evaluated by using noncompetitive sandwich ELISA (Biolegend e-Bioscience DX Diagnostic, Monza, Italy), following the supplier instructions. The absorbance was measured at 450 nm using a MP96 microplate reader spectrophotometer (Safas, Monaco), and cytokine levels were expressed as picograms per milliliter according to a standard calibration curve[21].

2.5.2. Tissue

The levels of proinflammatory cytokines TNF-α, IL-1β, and IL-17 were measured on aliquots (100 μl) of spinal cord ho- mogenate supernatants by using the Murine TNF-α, IL-1β, and IL-17A Mini ABTS ELISA Development Kits (#900- M54, #900-M47, and #900-M392, Peprotech, London, UK), following the protocol provided by the manufacturer. Briefly, frozen spinal cord samples were homogenized in 200 μl of lysis buffer (#9803 Cell Signaling Technologies, Danvers, MA) containing Protease Inhibitors Cocktail (#S8830, Sigma-Aldrich, St. Louis, MO) and 1 mM PMSF (Sigma-Aldrich) with UltraTurrax T25 (IKA Labortechnik, Staufen, Germany), followed by a 30-min centrifugation step at 10,000′ g and 4 °C. The supernatant was transferred in a clean vial and used for further determinations. Each sample was repeated in duplicate (220 μg of total protein for each sample). Values are expressed as picograms per microgram of total proteins determined over an albumin standard curve[21].

2.5.3. BV2

After the incubation time, samples were frozen (at -80 °C) and thawed for 3 times and the supernatants were collected for analysis. Non-competitive sandwich ELISA kit (Biolegend e-Bioscience DX Diagnostic, Italy) were used for the dosages of TNF-α, IL-6, IL-8, IL-10, following the procedure reported in the datasheet. Absorbance was recorded at 450 nm using a SAFAS MP96 spectrophotometer[23].

2.6. Immunofluorescence

2.6.1. BV2

Briefly, $3x10^5$ cells were seeded into Superfrost® Plus Microscope slides (#041300, Menzel-Glaser, Germany) and cultured for 24h. Cells were fixed with 4% paraformaldehyde for 15 min at room temperature. Following incubation with blocking buffer (PBS, containing 1% bovine serum albumin) for 1h at RT, a primary antibody 1:200 in PBS 5 was added for 2h at RT. Primary antibody was removed and fixed cells were incubated in secondary antibodies labelled for 1 h at room temperature (RT). Sections were coverlipped using UltraCruz® Aqueous Mounting Medium with DAPI (Santa Cruz Biotechnology) to identify the nucleus. Images were acquired with a Leica DM6000B fluorescence microscope. The immunofluorescence intensity was calculated by Image J (NIH)[23].

2.6.2. Senescence-Associated Heterochromatic Foci Analysis (SAHF)

Cells are initially seeded in 24-well plates, where previously sterilized slides are placed at the bottom of the wells (1x104 cells in 500µl of minimal medium with 3% serum per well). After appropriate treatments, the medium is aspirated, PFA 4% is added and incubated for 30 minutes at room temperature. This is followed by an initial wash of the wells with 1x PBS, then an amount of 0.1% PBS-Triton solution for 5 min. After 3 successive washes with PBS 1x the slide is sealed with a drop of a 1 µg/mL DAPI solution in mounting medium (90% glycerol + PBS 1X). Let dry in the dark at room temperature overnight, then store the slides covered at -20°C. After about a week they are ready to be observed with an OLYMPUS BX63F fluorescence microscope connected to a PC with an image acquisition card[33].

2.6.3. Tissue

For immunofluorescence analysis biological samples have been fixed in formalin at 4% for 24 h, dehydrated in alcohol, included in paraffin, and finally cut into 20 µm sections (spinal cords) and 10 µm (sciatic nerve, dorsal root ganglia). Primary antibodies used were added and diluted in 1% BSA in PBS overnight at 4° C. After rinsing in PBS containing 0.01% Triton-X-100, sections were incubated in secondary antibodies at room temperature for 2 hours. Sections were coverslipped using Vectorshield mounting medium (Vector Laboratories, Burlingame, CA). A Leica DM6000B fluorescence microscope equipped with a DFC350FX digital camera with appropriate excitation and emission filters for each fluorophore was used to acquire representative images. Images were acquired with 35 to 340 objectives using a digital camera. The immunofluorescence intensity was calculated using Image J[34].

2.6.4. Colocalization analysis

Colocalization of 2 different labels was measured using EzColocalization plugin (ImageJ). The extent of colocalization was determined by calculating the Mander overlap coefficient and the Pearson correlation coefficient (PCC). Mander overlap coefficient measures the percentage of overlap of 2 signals computationally standardizing size and intensity and is characterized by a range of values between 0 (complete anticolocalization) and 1 (complete colocalization). Pearson correlation coefficient quantifies the correlation between individual fluorophores considering their intensities. Pearson correlation coefficient is characterized by determined value range: 21, which indicate anticolocalization; 11, which indicates colocalization; and 0, which indicates there is no colocalization[35].

2.7. Hematoxylin and Eosin Staining

Mice were perfused with 4% neutral buffered formalin. Longitudinal, 8-µm sections were cut and mounted on charged glass slides. The slides were stained with 5% hematoxylin and 1% eosin (H&E), and inflammation scores were averaged from both sections. The slides were incubated in hematoxylin (5 min). Water was run over the slides for 5 min before 30-s incubation in eosin. After a tap water rinse, the slides were dehydrated by serial incubation in increasing ethanol and then xylene before being coverslipped with Permount mounting medium (Thermo Fisher Scientific, Waltham, MA). The slides were viewed on a Nikon (Tokyo, Japan) Eclipse E200 and imaged with a Nikon DS-Fi1 camera with NIS Elements software, and 10X images were merged in Adobe Photoshop 8.0 (San Jose, CA). Spinal cord pictures were graded for inflammation by a blinded investigator ac- cording to the following scale: 0 = absent or minimal infiltrates, 1 = moderate infiltrates throughout, 2 = moderate infiltrates with severe areas, and 3 = severe infiltrates throughout[21].

2.8. Luxol fast blue (LFB) myelin staining

Luxol fast blue (LFB) is a commonly used method to visualize myelin through an optical microscope, it is used to detect demyelination in the CNS. Like immunofluorescence, biological samples have been fixed in formalin at 4% for 24 h, dehydrated in alcohol, included in paraffin, and finally cut into 20 µm sections. Then, slides have been washes 2 times in PBSB-Tryton 0.3% and left complete drying. After that colorant LFB has been added on the slides and put at 60 ° C for 4 hours. Subsequently, slides have been washed in EtOH 96% and in H_2O. The decolorization step has been made with lithium carbonate (0.1% in H20) for 15 seconds and EtOH 70% for 30 seconds. The decolorization step has been made until there was a contrast between the blue of the white and the gray matter. Afterwards, final washings have been made with: EtOH 96% for 3 minutes, EtOH 100% for 3 minutes, Xylene for 5 minutes. Finally, we mounted the slides with a mounting medium and stored at room temperature. The slides were viewed on a OLYMPUS BX63F[21].

2.9. Evaluation of BBB disruption

The level of BBB disruption was detected by quantitative measurement for Evans blue content, as previously described at day 30 after immunization. Briefly, mice were intra- peritoneally injected with 2% Evans blue solution at a dose of 5.0 ml/kg per mouse. The dye was allowed to circulate for

4 h, and the mice were subsequently anesthetized and perfused transcardially with saline to remove the Evans blue dye in the vascular system. The brain and lumbar spinal cord were immediately removed, and images were captured. Tissues were homogenized with 2.5 ml PBS and mixed with 2.5 ml 50% trichloroacetic acid to precipitate protein overnight at 4 °C. The samples were centrifuged for 30 min at 10,000 × g, and the supernatants were measured at 610 nm for the absorbance of Evans blue by using a MP96 spectrophotometer (Safas, Monaco). The Evans blue content was expressed as micrograms per gram of brain and lumbar spinal cord[21].

2.10. *Statistical analysis*

The data and statistical analysis in this study comply with the recommendation on experimental design and analysis in pharmacology[36]. *Behavioural test***:** results are given as mean ± s.e.m.; 8-10 mice per group were used One-way and two-way analysis of variance, followed by Tukey and Bonferroni *post hoc* test, respectively, were used for statistical analysis. *Western blotting and ELISA:* results are given as the mean ± s.e.m. of band intensities. Five mice per treatment group were used and each run was in triplicate. The differences between groups were determined by one-way ANOVA followed by Tukey *post hoc* test. *Immunofluorescence*: immunoreactive areas are mean values (± s.e.m) of five separate experiments. Individual experiments consisted of five tissue sections of each of the six animals per group. Differences among mean immunoreactive areas or mean relative areas were statistically analysed by one-way ANOVA, followed by Tukey *post hoc* test or Student's *t* test. For each test, a *P* value less than 0.05 was considered significant. After ANOVA, the post hoc tests were run only if F achieved the necessary level of statistical significance.

Cell Line: data are expressed as the mean ± SEM of five experiments and assessed by One-way ANOVA followed by Tukey post hoc test. For each test a value of $p < 0.05$ was considered significant. The computer program GraphPad Prism version 9.1.2 (GraphPad Software Inc., San Diego, CA, USA) was used in all statistical analyses.

2.11. List of treatments

Pregabalin (PREG) (30 mg kg^{-1} i.p) (Sigma Aldrich) used as a reference drug, was dissolved in saline, and administered intraperitoneally 3 h before testing.

U0126: a well-known mitogen-activated protein kinase (MEK) inhibitor, (20 µg per mouse) was dissolved in 20% dimethyl sulfoxide (DMSO) and it was administered i.t. 60 min before testing. (Sigma-Aldrich, Italy).

(±)-baclofen (BACL) (4 mg kg^{-1} s.c) (Sigma Aldrich) used as a reference drug was dissolved in saline and administered with subcutaneous injection 45 min before testing

D-amphetamine hydrochloride (AMPH) (2 mg kg^{-1} i.p) (Sigma-Aldrich) used as a reference drug was dissolved in saline and administered intreaperitoneally 15 min before testing.

SAHA (suberoylanilide hydroxamic acid) (Sigma-Aldrich, Italy) dissolved in 5% DMSO and administered (intrathecal or intranasal) 15 min before the tests. Drug concentrations were prepared in such a way that the necessary dose could be administered in a volume of 5 µl per mouse by intrathecal (i.t.), 10 µL per mouse by intranasal (i.n.) or 10 mg kg^{-1} by i.p. administration. For cell culture SAHA (5µM) was dissolved in ethanol 96% V/V.

i-BET762 (4S)-6-(4-Chlorophenyl)-N-ethyl-8-methoxy-1-methyl-4H[1,2,4]triazolo[4,3,a][1,4]-benzodiazepine-4-acetamide (Sigma-Aldrich, Italy), dissolved in 5% DMSO and administered (intrathecal or intranasal) 15 min before the tests. Drug concentrations were prepared in such a way that the necessary dose could be administered in a volume of 5 µL per mouse by intrathecal (i.t.), 10 µL per mouse by intranasal (i.n.) or 10 mg kg^{-1} by i.p. administration.

SUM52 a selective HDAC1 and BRD4 dual inhibitor, was synthesized in the laboratory of Prof. Maria Novella Romanelli (University of Florence, Italy) dissolved in 5% DMSO and administered (intrathecal or intranasal) 15 min before the tests.

Zingiber officinale **Roscoe (ZOE)** obtained by CO2 supercritical extraction and standardized to contain 24.73% total gingerols and 3.03% total shogaols, was kindly provided by INDENA S.p.A. (Milan, Italy) dissolved in 1% sodium carboxymethyl cellulose (CMC) for *in vivo* studies. For cell culture ZOE (10 µg mL^{-1}) was dissolved in ethanol 96% V/V.

6-gingerol (GIN) was purchased from Sigma-Aldrich (Milan, Italy) was dissolved in ethanol 96% V/V at the concentration of 1 µg mL^{-1}.

6-shogaol (SHO) was purchased from Extrasynthese (Genay, France). was dissolved in ethanol 96% V/V at the concentration of 0.17 µg mL^{-1}.

Terpenoid-enriched fraction (ZTE) ZTE was dissolved in 1% sodium carboxymethyl cellulose (CMC) and administered by gavage before testing at the doses of 10 mg kg^{-1}, at the concentration of presents in ZOE. For cell culture ZTE 3 μg mL^{-1} was dissolved in ethanol 96% V/V.

Zingiberene (ZNG) was purchased from Sigma-Aldrich (Milan, Italy) and was dissolved in ethanol 96% V/V for *in vitro* test used at the concentration of 5μm. For *in vivo* test we used it at the concentration of 1 mg kg^{-1} orally administered and previously dissolved in CMC 1%.

LG325 a selective histone deacetylase 1 (HDAC1) inhibitor, was synthesized in the laboratory of Prof. Maria Novella Romanelli (University of Florence, Italy)

***Cannabis sativa* L. extract (var Kompolti) free of terpenes components and titled at 0.4730% in CBD (K1)** in extra virgin olive oil. K1 was tested at the dose of 10, 25 and 50 mg kg^{-1} to determine the dose-response curve trough oral administration using gavage and administered after 10 days from surgery. The vehicle that has been used is the 1% sodium carboxymethyl cellulose (CMC).

***Cannabis sativa* L. extract (var Kompolti) containing terpenes components and titled at 0.4244% in CBD (K2)** in extra virgin olive oil. K2 was tested at the dose of 10, 25 and 50 mg kg^{-1} to determine the dose-response curve trough oral administration using gavage and administered after 10 days from surgery. The vehicle that has been used is the 1% sodium carboxymethyl cellulose (CMC). Cannabis essential oil (CEO), obtained by steam distillation of K2 and administered at the dose of 0.45 mg kg^{-1} after oral administration.

AM630 inverse agonist of the cannabinoid CB2 receptor previously solubilized in DMSO / Tween80 / physiological (1: 1:10) and administered intraperitoneally 30 minutes before the test.

AM251 reverse agonist of cannabinoid CB1 receptor previously solubilized in DMSO / Tween80 / physiological (1: 1:10) and administered intraperitoneally 30 minutes before the test.

Cannabidiol (CBD) (Sigma-Aldrich) was purchased from Sigma-Aldrich (Milan, Italy) and was dissolved in ethanol 96% V/V

Beta caryophyllene (CAR) (Sigma-Aldrich) was purchased from Sigma-Aldrich (Milan, Italy) and was dissolved in ethanol 96% V/V

Antisense oligonucleotide administration

Phosphorothioate oligonucleotides (ODNs) (resistant to exonuclease-mediated degradation) were used (Tib Molbiol, Genoa, Italy). The antisense ODN (ASO) against:

HuR 5’- A*T*AACCATTAGACATT*G*T-3

HuD 5′-G*T*TCTGGAGCCTCATC*T*T-3′

where the asterisks indicate the phosphorothioate phosphate groups. An 18 mer fully degenerate ODN (dODN), where each base was randomly G, or C, or A, or T, was used as control ODN treatment. To enhance both uptake and stability, ODNs were preincubated at 37℃ for 30 minutes with 13 μM DOTAP (Sigma, Milan, Italy), an artificial cationic lipid. The experimental protocol to test the effect of ASO on behavioural and *in vitro* tests included 3 control groups: dODN (as control ODN), vehicle (DOTAP 13 μM), and saline.

Intrathecal administration of antisense oligonucleotide administration

In SNI model mice received a single intrathecal injection of DOPAT, dODN, or ASO every 3 days, starting from day 3 from surgery, for a total of 4 injections. The spinal cords, sciatic nerve and dorsal root ganglia for in vitro tests were removed on day 10. Drug concentrations were prepared in such a way that the necessary dose of dODN (1 nmol/mouse) or ASO (1 nmol/mouse) could be administered in a volume of 5 mL per mouse.

Intranasal administration of antisense oligonucleotide administration

A 5-mL aliquot of DOTAP, dODN, or ASO was slowly dropped alternatively to each nostril with a micropipette tip. A total of 10 mL of solution containing 1 nmol of ODNs was delivered every 2 days starting from day 3 in SNI model and the spinal cords for *in vitro* tests were removed on day 10. Using the EAE model, treatments performed before immunization neutralize the effect of an artificial disease induction and do not always address the therapeutic potential of drugs for patients at risk. HuR and HuD silencing were, thus, produced starting from day 14 from immunization, corresponding to the first disease peak. To achieve the protein knockdown, mice received a single intranasal injection every 2 days. The spinal cords were removed on day 30 postimmunization.

Extract of *Melissa officinalis* L. (MDE), provided by the company DemBiotech titolated in 5.17% P/P total polyphenols equivalent in rosmarinic acid (4.02%) and dissolved in distillated water and used at the dose of 150 mg kg^{-1} *in vivo* (po administration) and 10 μg mL^{-1} for cell culture.

Rosmarinic acid (AR) (Sigma, Aldrich) was dissolved in distillated water and used at the dose of 6 mg kg^{-1} *in vivo* (po administration) and used for *in vitro* cell culture at the concentration of 0.4 μg mL^{-1}.

2.12. List of antibodies:

2.12.1. Western Blotting

Primary antibodies

1. Brd4 (1:1000; Santa Cruz Biotechnology)
2. acetyl Histone H3 (Lys9) acH3K9 (1:1000 Santa Cruz Biotechnology)
3. IL-6 (1:1000; Santa Cruz Biotechnology)
4. STAT1 phosphorylated on Tyr701 pSTAT1, (1:500 Santa Cruz Biotechnology)
5. p38 phosphorylated on Thr180/Tyr182 (p-p38), (1:500; Cell Signaling Technology)
6. IBA1 1:1000 Santa Cruz Biotechnology
7. IL-1ß (1:1000 Bioss antibodies)
8. pERK 1/2, phosphorylated on Thr202/Tyr204 (1:500 Cell Signaling Technology)
9. p38 phosphorylated on Thr180/Tyr182 (p-p38), (1:500; Cell Signaling Technology)
10. pJNK1, phosphorylated on Thr183/Tyr185 (1:750, Santa Cruz Biotechnology)
11. p-NFκB p65, phosphorylated on Ser536 (1:500 Santa Cruz Biotechnology)
12. IKBα (1:1000, Santa Cruz Biotechnology)
13. IL-1β (1:1000, Bioss Antibodies)
14. GAPDH (1:5000, Santa Cruz Biotechnology).
15. HDAC-1(1:1000, Santa Cruz Biotechnology),
16. HDAC-2 (1:1000, Santa Cruz Biotechnology),),
17. HDCA-3 (1:1000, Santa Cruz Biotechnology),),
18. HDAC-4 (1:1000, Santa Cruz Biotechnology),),
19. HDAC-5 (1:1000, Santa Cruz Biotechnology),),
20. HDAC-6 (1:1000, Santa Cruz Biotechnology),),
21. HDAC -8 (1:1000, Santa Cruz Biotechnology),),
22. HDAC-11 (1:1000, Santa Cruz Biotechnology)
23. SIRT-1 (1:1000, Santa Cruz Biotechnology)
24. CB2 (1:500, Santa Cruz Biotechnology),
25. iNOS (NOS2) (1:500, Santa Cruz Biotechnology)
26. IBA1 (1:500; Santa Cruz Biotechnology),
27. HuD (1: 1000; Santa Cruz Biotechnology);
28. HuC (1:1000; Santa Cruz Biotechnology)

29. HuR (1:1000, Santa Cruz Biotechnology)
30. HuB (1: 1000; Invitrogen, Milan, Italy)
31. HuR (1:1000, Santa Cruz Biotechnology)
32. CD4 (1:750, Santa Cruz Biotechnology)
33. CD206 (1:500; Abcam, Cambridge, UK).
34. MBP (1:1000 Santa Cruz Biotechnology)
35. S100 α/ß (1:500 Santa Cruz Biotechnology)
36. GAP43 (1:500 Santa Cruz Biotechnology)
37. Neurofilament H (1:1000 Bioss antibodies)
38. β-Galactosidase (1:1000 Santa Cruz Biotechnology)
39. CSF-1 (1:1000; Abcam)
40. IBA-1 (1:500; Abcam)
41. GAPDH (1:2000 Santa Cruz Biotechnology)
42. β-Actin (1:3000 Santa Cruz Biotechnology)

Secondary antibodies

HRP-conjugated mouse anti-rabbit (1:3000, Santa Cruz Biotechnology)
HRP-goat anti-mouse (1:5000, Bioss Antibodies)
Peroxidase-AffiniPure Goat Anti-Rabbit IgG (H+L)
Peroxidase-AffiniPure Goat Anti-Mouse IgG (H+L)

2.12.2. Immunofluorescence

1. GFAP (1:200 Santa Cruz Biotechnology)
2. CD11b (1:100 Bioss antibodies)
3. p-p38 (1:100 Cell Signaling Technology).
4. anti-pp65 (1:200 Santa Cruz Biotechnology)
5. CB2 (1:100 Santa Cruz Biotechnology)
6. CD11b (1:100 Bioss antibodies)
7. TMEM119 (1:100; Abcam)
8. p-p38 (1:100; Cell Signaling)
9. pERK (1:100; Santa Cruz Biotechnology)
10. HuR (1:100; Santa Cruz Biotechnology)
11. IBA1 (1:100; Santa Cruz Biotechnology

12. IκBα (1:100; Santa Cruz Biotechnology)
13. CD11b (1:100; Bioss antibodies)
14. TMEM119 (1:100; Abcam)
15. CD206 (1:100; Abcam)
16. Neurofilament H (1:100 Bioss antibodies)
17. HuD (1: 100; Santa Cruz Biotechnology)
18. HuR (1:100, Santa Cruz Biotechnology)
19. MBP (1:100, Santa Cruz Biotechnology)
20. S100 α/ß (1:100, Santa Cruz Biotechnology)
21. GAP43 (1:500 Santa Cruz Biotechnology)

Secondary antibodies

1. Goat anti-rabbit Invitrogen Alexa Fluor 488 (490-525, 1:400; Thermo Fisher Scientific)
2. Goat anti-mouse Invitrogen Alexa Fluor 568 (578-603, 1:400; Thermo Fisher Scientific),
3. Mouse anti-goat Cruz Fluor 594 (592-614, 1:400; Santa Cruz Biotechnology)

Chapter 3

Selective modulation of HDAC1 by synthetic substances and bioactive compounds, extracted from medicinal plants, for the treatment of neuropathic pain

3.1. Introduction

Genotype and environmental factors represent a major contributor to the onset of NP[37]. Indeed, epigenetic processes are key mechanisms underlying gene-environment interactions and have been linked to numerous human disorders, including chronic pain[38]. Hence, epigenetic modifications are reversible mechanisms that can increase or suppress gene expression without alterations in the underlying DNA sequence. Genetic information stored in DNA is encompassed within the chromatin structure in which the nucleosome represents the basic unit. The nucleosome is composed of two copies of each central histone, H2A, H2B, H3, and H4, around which the DNA is wrapped. This structure is organized into two different levels: the euchromatin that contains most of the genes and is transcriptionally active, and the heterochromatin that comprises the nuclear material and is mostly silent[39]. Epigenetic alterations change the state of chromatin between euchromatin or heterochromatin. The most characterized epigenetic processes include DNA methylation, histone modification (e.g., acetylation, methylation, phosphorylation), and gene silencing associated with noncoding RNAs (ncRNAs), and these mechanisms are highly interconnected. Of the several epigenetic changes, growing evidence suggests that histone acetylation processing plays a key role in the development and maintenance of chronic pain[40,41]. Histones have an accessible lysine-rich aminoterminal, and the major types of epigenetic modifications of histones include lysine acetylation. Acetylation and deacetylation of histone proteins are catalyzed by acetyltransferases (HATs) and deacetylases (HDACs), respectively. HACs are members of the "writers" of the epigenetic code, enzymes that catalyze the addition of post-translational modifications on histones, resulting in a more relaxed chromatin structure (euchromatin) that favors active transcription. In contrast, HDACs act as "erasers," enzymes that catalyze the removal of markings, which condense chromatin (heterochromatin) by repressing transcription[39].

Control of histone acetylation processes involves numerous enzymes with specific activities: histone acetylation writers (e.g., HATs) erasers (e.g., HDACs) and readers (e.g., BRD4) Eighteen HDAC isoforms have been identified in humans and classified into four groups based on sequence similarities: Class I includes HDAC 1, 2, 3, and 8; class IIa includes HDAC 4, 5, 7, and 9; class IIb includes HDAC 6 and 10; class III includes sirtuins 1-7; class IV includes HDAC 11[41].

The analgesic effect of HDAC inhibitors (HDACi) in chronic pain conditions has been described in clinical and preclinical studies[37]. Several studies have also indicated that nerve injury up-regulates histone deacetylase enzymes, and treatment with histone deacetylase inhibitors relieves NP. Even though there is consensus on the observation of a trend toward increased expression of HDACs in spinal cord of neuropathic animals, different pattern of expression of selective isoforms has been reported depending on the animal model used and diversity on time point of investigation. Concerning class I, HDAC1 expression has been reported to be increased from post-surgical day 1–7 in the ipsilateral lumbar spinal dorsal horn in a rat model of spinal nerve ligation (SNL)[42] and in a mouse model of partial sciatic nerve ligation (pSNL)[43]. In the spared nerve injury (SNI) model in mice HDAC1 was significantly increased in the ipsilateral side from day 7 to 21 after surgery[23,44]. Similarly, in a rat chronic constriction injury (CCI) model, nerve injury upregulated the expression of HDAC1 protein and mRNA in the dorsal root ganglia with a peak on day 7[45]. In rats that underwent a CCI procedure, increased expression of the spinal HDAC2 mRNA and protein was observed on day 7, 14, and 21 after surgery[46].

In addition to physio- pathological diversity among experimental models of NP, differences in the expression of individual isoforms can also be related to the different cellular distribution of HDAC s. HDAC1 has been reported to be expressed in neurons[47] and to be abundantly overexpressed after injury in microglia. HDAC2 has a neuronal localization and an overexpression in astrocyte was detected during neuropathy[48]. These findings indicate that epigenetic regulation of transcriptional programs in the dorsal horn after injury is cell specific and individual HDAC isoforms might result differently expressed depending on their role and pattern of activation in neuronal and glial cells during neuropathy. Several studies have also indicated that nerve injury up-regulates histone deacetylase enzymes, and treatment with HDACi relieves NP[49–51]. Aberrant histone deacetylation was found to be associated with several pathological conditions and HDACi have emerged as therapeutic interventions, prominently as potent anticancer agents[52]. In the last two decades US Food and Drug Administration (FDA) approved the use of some HDACi for cancer therapy. Suberoylanilide hydroxamic acid (SAHA), commercially known as Vorinostat, was approved in 2006 for the treatment of cutaneous T-cell lymphoma[52]. Panobinostat, an orally active molecule, was approved in 2015 for the treatment of multiple myeloma[53]. Valproic acid, an antiepileptic drug, was found to preferentially inhibit class I HDACs in the millimolar-micromolar range[54] and it has been evaluated in clinical trials for hematological and solid tumor malignancies[55]. Even though HDACi have been largely studied as anticancer therapy[56], increasing evidence shows that they could be a potential therapeutic option for neurological and neurodegenerative disorders[57] and several clinical studies on the use of HDACi for the treatment of neurodegenerative diseases are ongoing.

The analgesic effect of HDACi in chronic pain conditions has been recently described in clinical and preclinical studies. Administration of the pan-inhibitor SAHA ameliorated SNL-induced mechanical allodynia and thermal hyperalgesia[42], bone cancer pain[58], alcohol withdrawal-induced hyperalgesia[59] in rats, SNI-induced hyperalgesia in mice[23], and orofacial NP[60]. A comparable pain-relieving activity was showed by more selective inhibitors in several experimental models. Classes I and IIa HDACi valproic acid mitigated NP in SNL[61,62] and spinal cord injury (SCI) in rats[63], and in diabetic neuropathy in mice[64]. Similarly, sodium butyrate, a class I and IIa HDACi[65,66], attenuated thermal and mechanical hyperalgesia in the CCI model. HDAC pan inhibitors can, thus, modulate numerous neuronal functions other than pain perception. These compounds might also have other bioactivities (i.e., valproic acid) for which are clinically used that may influence the pain sensitivity. The lack of specificity and selectivity of HDACi employed in these studies represents a major concern on identifying their role on NP. Moreover, the nonselective activity of some HDAC pan-inhibitors raises concerns about drug toxicity and some serious side effects have been reported for SAHA, TSA, and romidepsin[67,68].

The aim of this work is to evaluate which HDAC isoform is more involved in the processes of NP, and to find new selective synthetic modulators or bioactive molecules, extracted from medicinal plants.

3.2. Results

3.2.1. HDAC class I and IV are overexpressed in LPS-stimulated BV2 and in ipsilateral side of SNI mice spinal cord

3.2.1.1 Expression of HDACs in SNI spinal cord mice and -BV2 stimulated with LPS

It has recently been highlighted how epigenetics can influence the modulation of microglial activity and how some HDACi have been shown to have protective activity towards the neuroinflammation process[69]. A recent study conducted by Lee and collaborators[70] demonstrated how the inhibition of HDAC1 leads to a significant reduction in the activation of NF-κBp65, a well-known marker of microglial activation. The stimulation with LPS for 24 h has been demonstrated to cause morphological and phenotype changes in BV2. In this condition we observed that HDAC1, 2, 3, and 8 (i.e., class I HDACs) and HDAC11 (class IV) were up regulated, while no effects were produced in HDAC4, 5, 6 (class II), and SIRT (class III). A significant reduction in HDAC6 levels was observed in microglial cells following inflammatory stimulation (Figure 3.1A). In the SNI model, animals with neuropathy showed an increase in HDAC1 and HDAC2 expression in the spinal cord, compared to control, while no effect was observed regarding the expression of HDAC3, 8, and 11 (Figure 3.1B).

Figure 3.1C shows the colocalization of HDAC1 with CD11b, a marker of pro-inflammatory phenotype microglia, thus, suggesting the activation of HDAC1 and HDAC2 as a target in microglial activation in the spinal cord of animals with neuropathy**.** These results are in line with the findings of a study conducted by Kannan and collaborators[71], where the maximum gene expression of HDAC4, 5, and SIRT-1 was observed with short inflammatory stimuli (4-8 h) while it decreased with time. On the other hand, the increase in the expression of HDAC1, 2, and 3 following stimulations with LPS in microglial cells and their correlation with neuroinflammatory processes is much better documented[72]. The anti-inflammatory activities of HDAC8 and HDAC11 at the microglial level also appear to be interesting. A recent study showed that inhibition of HDAC8 reduced neuroinflammation by modulating microglial activation[73].

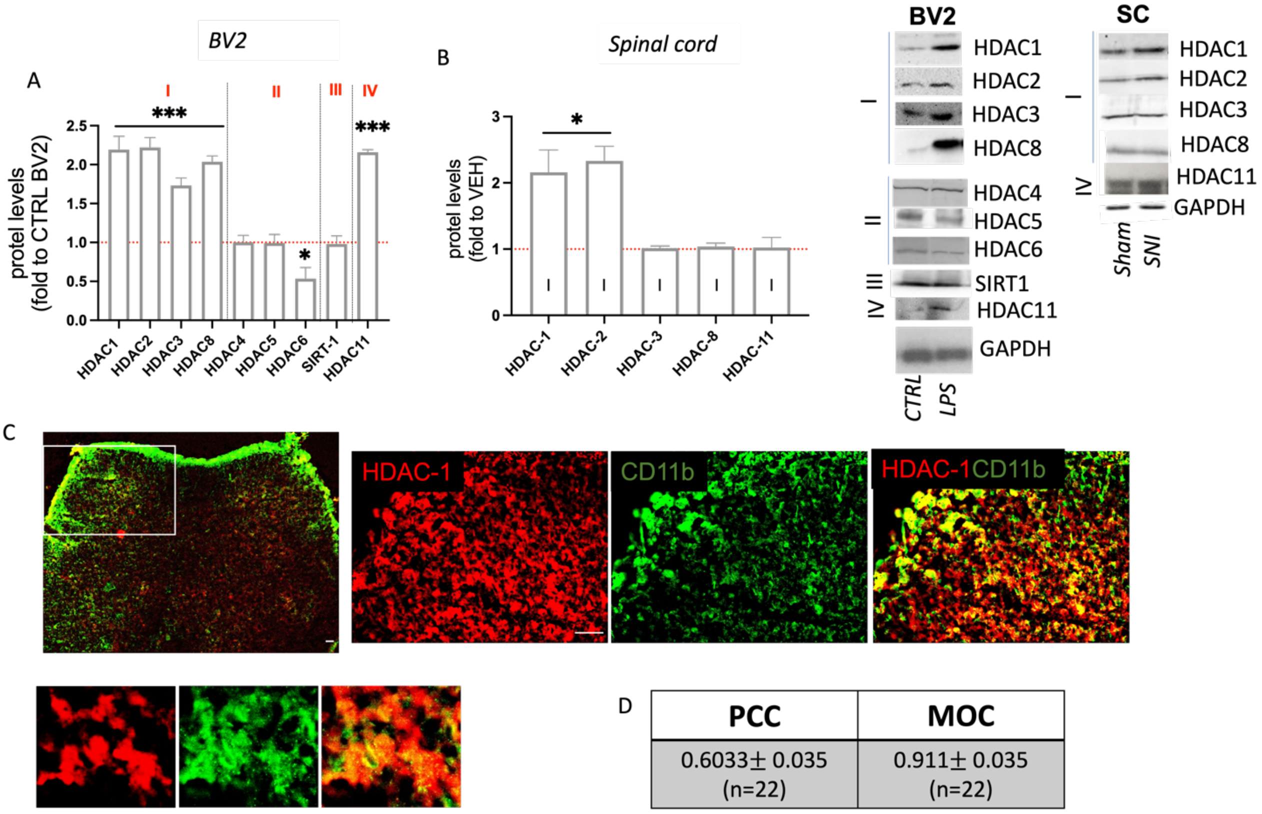

PCC	MOC
0.6033± 0.035 (n=22)	0.911± 0.035 (n=22)

Figure 3.1 A) HDACs isoforms expression in LPS-stimulated BV2 (250 ng mL^{-1}) for 24h, compared to untreated microglia cells (red dashed line; One-way ANOVA ***p<0.001 *p<0.5). B) Expression of HDAC1, 2, 3, 8, and 11 in spinal cord tissue of animal with neuropathy compared the sham group (red dashed line; One-way ANOVA *p<0.05). C) A representative colocalization images of HDAC1 (red) and CD11b (green) in the spinal cord tissue of SNI mice with different magnification: 5x and 20x (scale bar 50µm). D) Quantification of Pearson's coefficient (PCC) and Mander's coefficient (MOC). Representative blots are also showed.

3.2.1.2. HDAC1 inhibitors attenuates nociceptive behaviour in SNI mice

SNI procedure induced a persistent mechanical and thermal allodynia in the ipsilateral side of injured mice starting from 3 days after surgery[34] and the experiments were conducted on day 10 after surgery when mechanical (Figure 3.2A) and thermal (Figure 3.2D) pain hypersensitivity was well established. The HDAC pan-inhibitor SAHA was investigated for a mechanical (Figure 3.2A) and thermal (Figure 3.2D) antiallodynic activity by performing dose-response curves in SNI mice after i.n. administration. The dose of 3 µg attenuated the SNI-induced pain hypersensitivity that was reversed at 10 µg with an intensity comparable to pregabalin. The dose of 1 µg was devoid of any activity. The antiallodynic effect was of an intensity comparable to that showed by SAHA 10 µg i.t. and by pregabalin, used as reference drug (Figure 3.2A, D). Time-course studies were performed at the minimal dose that increased the pain threshold (3 µg; Figure 3.2B, E) and at the maximum effective dose (10 µg; Figure 3.2C, F). SAHA produced a long-lasting effect that peaked at 60 min after administration, persisted at 90 min and then disappeared at 120 min. Similar time-course profiles were observed for curves obtained at the minimum or maximum effective dose.

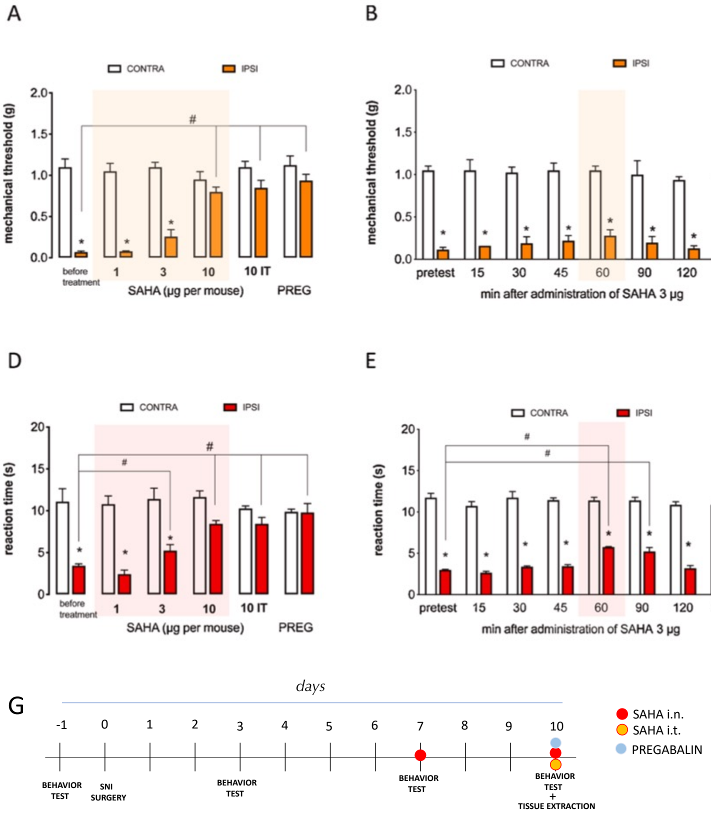

Figure 3.2 SAHA prevented pain hypersensitivity in SNI neuropathic mice. (A) Dose-response curve of SAHA (1-10 µg per mouse i.t.) in the von Frey test showed antiallodynic activity in the ipsilateral side (ipsi) of SNI mice in the absence of any effect in the contralateral (contra) side. Pregabalin (30 mg/kg i.p.; PREG) was used as reference drug. $^*P < 0.05$ vs contra; $^\#P < 0.05$ vs ipsi before treatment. Time-course curves of SAHA administered at 3 µg (B) or 10 µg (C) per mouse i.t. for mechanical antiallodynic activity. $^*P < 0.05$ vs contra; $^\#P < 0.05$ vs ipsi before treatment. (D) Dose-dependent reversal of thermal allodynia by SAHA (1-10 µg per mouse i.t.) with efficacy comparable to pregabalin. $^*P < 0.05$ vs contra; $^\#P < 0.05$ vs ipsi before treatment. Time-course curves of SAHA at 3 µg (E) or 10 µg (F) per mouse i.t.

against thermal allodynia. (G) Representative figure of experimental protocol. Experiments were performed on post-surgery day 7 and 10: SNI (n=8), SAHA i.n. (n=8), SAHA i.n. (n=8) PREG (n=6). *P < 0.05 vs contra; #P < 0.05 vs ipsi before treatment.

3.2.2. SUM52, a novel dual inhibitor of HDAC1 and BRD4, reduces NP symptoms through inhibition of microglia proinflammatory activation

3.2.2.1. Brd4 inhibitors attenuated nociceptive behaviour in SNI mice

The histone code is coded by "reader" domains. Readers show affinity for a specific mark, and recruitment of readers leads to increased transcriptional activity. Bromodomain and extra-terminal domain (BET) proteins belong to the "reader" family and is composed of four proteins: Brd2, Brd3, Brd4, and the testis-specific protein bromodomain (BRDT). These proteins contain two N-terminal bromodomains that specifically identify and bind lysine acetylated residues on histone tails to promote transcription[39]. Combination therapy, a dual drug approach that can simultaneously target multiple disease-related targets, has attracted attention in recent years[74]. One of the most prominent areas of synergistic approaches involves the combination of multiple direct epigenetic therapies, and it can be hypothesized that simultaneous modulation of multiple pain-related epigenetic targets could represent a promising prospect for NP therapy. Thus, the aim of the present study was to investigate the effects produced by the combination of HDAC and BET inhibitors in a mouse model of trauma-induced neuropathy and to investigate whether the mechanism of action may be related to a microglial modulation. I.n. dose-response curve for the Brd4 inhibitor iBET762 showed that the doses of 3 μg per mouse was devoid of any effect. Increasing doses induced a progressive attenuation of the mechanical nociceptive behaviour reaching the maximum antiallodynic activity at the dose of 50 μg per mouse (Figure 3.3A). i-BET762 also reversed thermal allodynia in a dose-dependent manner. The dose of 3 μg was ineffective, at 10 μg there was a partial reversal of allodynia that was completely abolished at 25 and 50 μg with reaction time values comparable to contralateral side values (Figure 3.3D). The antiallodynic effect was of an intensity comparable to that of i.t. iBET762 (50 μg) and pregabalin (Figure 3.3A, D). Results from time-course studies, performed at the minimum (10 μg; Figure 3.3B, E) and maximum effective dose (50 μg; Figure 3.3C, F), showed that i-BET762 was endowed with a prolonged activity the peaked 90 min after administration and persisted up to 120 min. The antiallodynic effect of the investigated epigenetic modulators was produced in the ipsilateral side of SNI mice. At effective doses no significant variation of the pain threshold was detected in the contralateral side, indicating that SAHA, i-BET762 as well as their combination were devoid of any activity in the absence of pre-established NP.

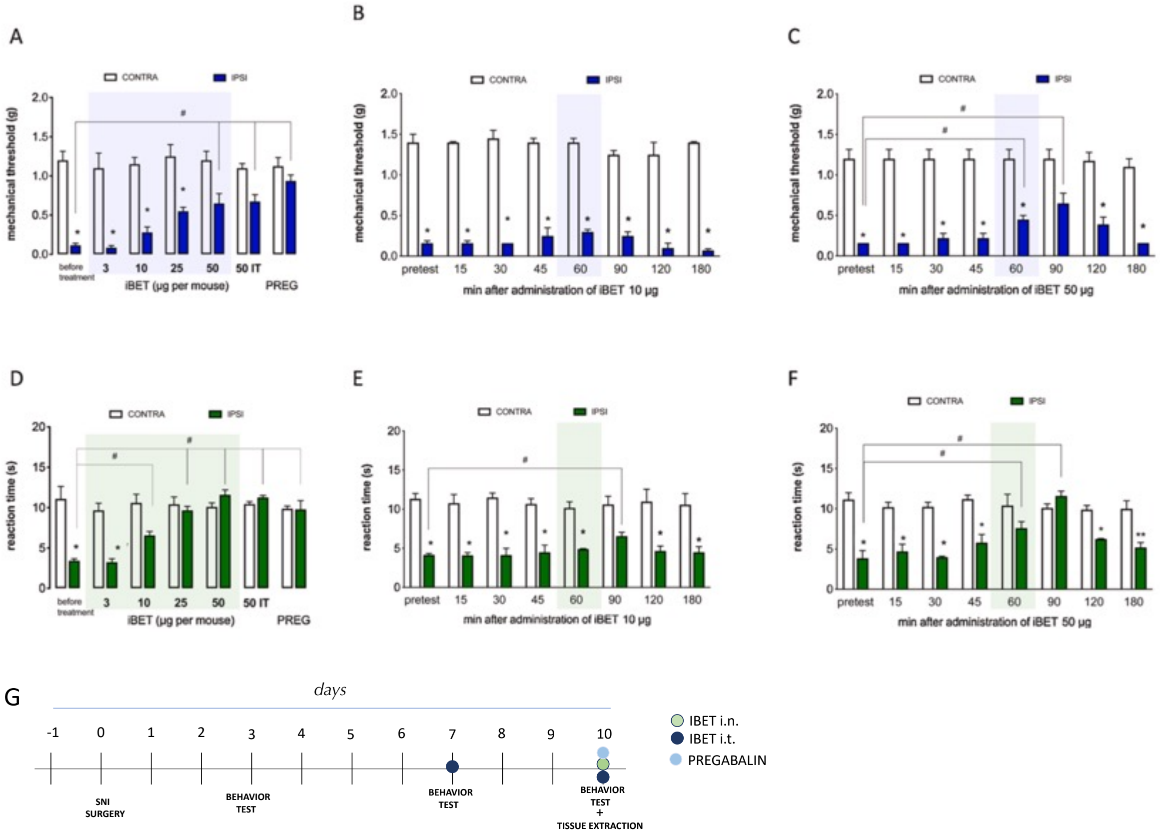

Figure 3.3 Antiallodynic activity of i-BET762 in SNI neuropathic mice. (A) i-BET762 (3-50 µg per mouse i.t.) dose-dependently attenuated mechanical allodynia in the ipsilateral side (ipsi) of SNI mice. No effect was detected on the contralateral side (contra). Pregabalin (30 mg/kg i.p.; PREG) was used as reference drug. $^*P < 0.05$ vs contra; $\#P < 0.05$ vs ipsi before treatment. Time-course curves of i-BET762 administered at (B) 10 µg or (C) 50 µg per mouse i.t. in the von Frey test (mechanical allodynia). $^*P < 0.05$ vs contra; $\#P < 0.05$ vs ipsi before treatment. (D) Dose-response curve of i-BET762 (3-50 µg per mouse i.t.) in the Hargreaves' plantar test (thermal allodynia) showing an efficacy comparable to pregabalin. $^*p < 0.05$ vs contra; $\#P < 0.05$ vs ipsi before treatment. Time-course curves of i-BET762 at (E) 10 µg or (F) 50 µg per mouse i.t. against thermal allodynia. (G) Experimental design. Experiments were performed on post-surgery day 7 and 10: SNI (n=8), IBET i.n. (n=8), IBET i.n. (n=8) PREG (n=6). $^*p< 0.05$ vs contra; $\#p < 0.05$ vs ipsi before treatment.

3.2.2.2. Lack of locomotor impairment by combination of i-BET762 and SAHA

To complete the evaluation of the phenotypical effects produced by the combination of Brd4 and HDAC inhibitors, we tested the combination of ineffective doses, partially effective doses, and full effective doses of i-BET762 and SAHA on locomotor behaviour. No animal showed apparent sedation or motor dysfunction by a single administration of any dose of single compounds or their combinations. In addition, all three investigated combinations did not alter the spontaneous mobility (Figure 3.4A) and the exploratory activity (Figure 3.4B), nor modified the motor coordination, evaluated by the rotarod test (Figure 3.4C). Finally, no alteration of body weight was detected following co-administration of the drugs in comparison with drugs administered alone or control untreated group. (Figure 3.4D).

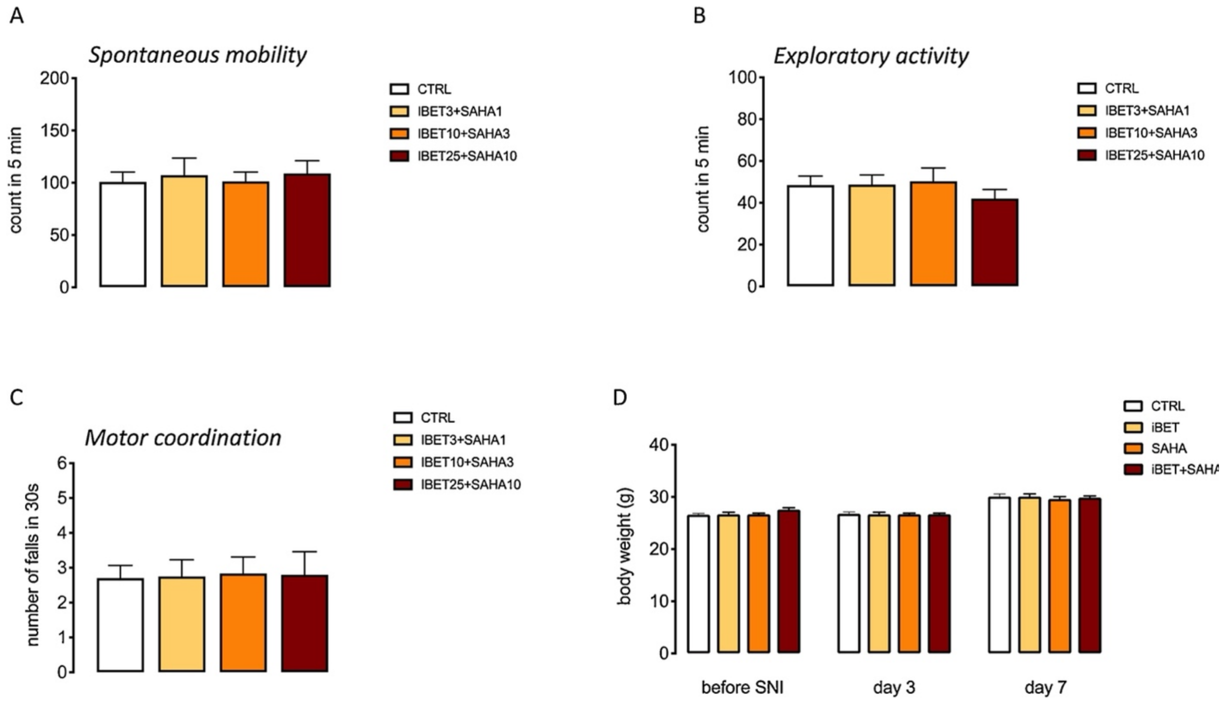

Figure 3.4 Evaluation of biological parameters following co-administration of SAHA and i-BET762 in SNI mice. Combination of SAHA and i-BET762 at each tested doses did not produce any alteration in the (A) spontaneous motility, (B) exploratory activity, and (C) motor coordination in comparison with CTRL SNI mice on day 7 post-surgery. (D) Co-administration of SAHA (3 μg) and i-BET762 (10 μg) on day 7 post-surgery did not alter body weight. Body weights were recorded before surgery, 3 days, and 7 days post-injury. CTRL: untreated SNI mice. Doses are reported in each panel.

3.2.2.3. Effect of epigenetic inhibitor combination on spinal HDAC1 and Brd4 protein expression

Previous findings from our laboratory showed a prominent role of HDAC1-mediated effects on pain hypersensitivity in SNI[39,47] mice and we, thus, decided to focus on HDAC1. Among the BET isoforms, BRD4 is mainly involved in peripheral and central inflammation with a significant role in the pathology of inflammatory diseases[75]. The expression of HDAC1 and Brd4 proteins was detected in lumbar spinal cord samples 7 days after surgery and modulation of protein expression was detected following administration of partially effective doses of i-BET762 (10 μg), SAHA (3 μg), and their co-administration. In the ipsilateral side of SNI mice, an increased expression of HDAC1 protein was detected in comparison with contralateral side. The HDAC1 increase was partially reduced by SAHA and left unaltered by i-BET762. The co-administration of both inhibitors produced a further decrease of HDAC1 expression that returned to basal values (Figure 3.5A). Even though acH3K9 level is increased in peripheral NP conditions, consistent with our previous results[39], SNI mice showed no variation of spinal acH3K9 protein and treatment with i-BET762, SAHA or combination did not produce any significant effect (Figure 3.5B). SNI mice also showed a robust increase in the expression of Brd4 in the ipsilateral side that was slightly reduced by i-BET762 and SAHA. Combination of both drugs drastically reduced Brd4 levels up to control basal values (Figure 3.5C).

To establish a correlation between restoration of HDAC1 and Brd4 protein level and attenuation of pain hypersensitivity by combination of the investigated epigenetic modulators, we behaviourally tested the effects produced by the co-administration of partially effective doses of i-BET762 and LG325, an HDAC1 selective inhibitor with antiallodynic properties[39]. Dose-response curve for i.n. LG325 showed a maximum activity at 5 µg with an efficacy comparable to i.t. administration. The behavioural effects of LG325 are related to a reduction of spinal HDAC1 over-expression. SAHA (i.n. and i.t.) produced similar effects. Combination of the above-mentioned compounds significantly increased the antiallodynic activity of the HDAC1 inhibitor against both mechanical (Figure 3.5D) and thermal (Figure 3.5E) stimuli.

Double staining immunofluorescence experiments showed a homogeneous distribution of HDAC1 and Brd4 within spinal cord sections with a prominent immunostaining in the ipsilateral side dorsal horn of SNI mice (Figure 3.5F; quantification in Figure 3.5G). Co-localization images showed the expression of Brd4 in HDAC1 expressing cells (Figure 3.5F). Quantification analysis confirmed the co-localization showed by immunofluorescence merged images and similar coefficients were detected in the contralateral and ipsilateral sides (Figure 3.5E).

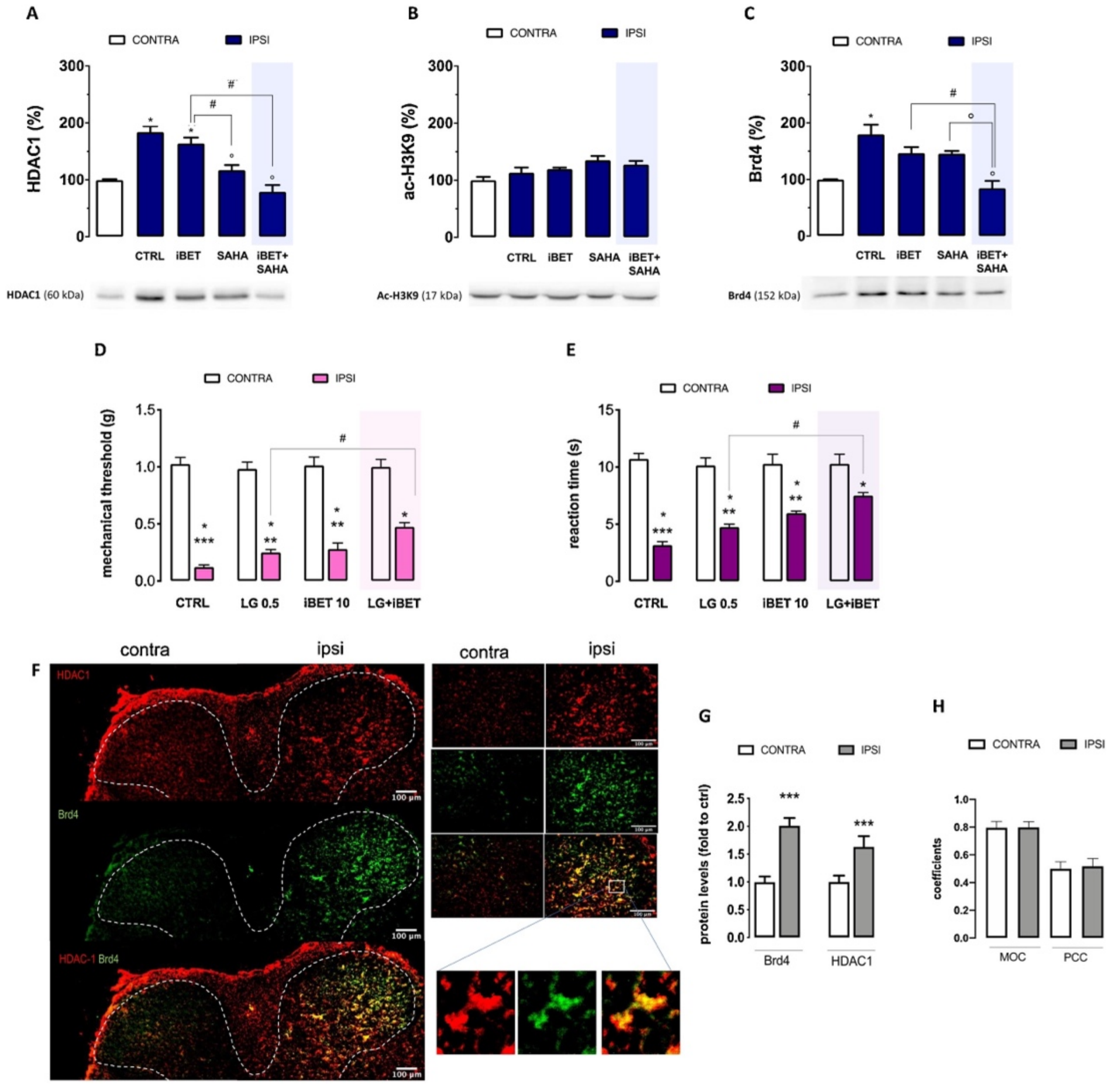

Figure 3.5 Effect of SAHA and i-BET762 combination on HDAC1 and Brd4 expression. (A) Spinal cord samples from SNI mice showed an increased expression of HDAC1 protein in the ipsilateral side that was partially reduced by SAHA (3 µg) whereas it returned to basal values after co-administration of SAHA and i-BET762 (10 µg). $^*P < 0.05$ vs contra; °P < 0.05 vs CTRL ipsi; #P < 0.05 vs i-BET762. (B) Lack of effect on acH3K9 expression by SNI and treatments. (C) SNI procedure increased the expression of spinal Brd4 in the ipsilateral side that was slightly reduced by i-BET762 (10 µg) and SAHA (3 µg). Brd4 returned to basal values after co-administration of both inhibitors. $^*P < 0.05$ vs contra; °P < 0.05 vs SAHA ipsi; #P < 0.05 vs i-BET762 ipsi. Potentiation of antiallodynic activity following co-administration of partially active doses of i-BET762 (10 µg) and LG325 (0.5 µg) against mechanical (D) and thermal (E) allodynia. $^*P < 0.05$ vs contra; #P < 0.05 vs LG325 ipsi. (F) Immunofluorescence microscopy images (low and high magnification) showed the increased expression of HDAC1 and Brd4 in the ipsilateral side and their co-localization in spinal cord sections. Scale bar =50 µm. (G) Quantification analysis of Brd4 and HADC1 expression in the ipsilateral vs contralateral side. $^{***}P < 0.001$ vs contra (Student's t test). (H) Co-localization coefficients showed a high degree of Brd4 in HDAC1 expressing cells co-localization with similar values in the ipsilateral and contralateral sides.

3.2.2.4. Cellular localization of HDAC1

To determine the cellular localization of HDAC1 in spinal cord sections from SNI mice, double labelling immunostaining with classical markers of subpopulations was carried out. Merged images showed a modest co-localization with the neuronal marker NeuN (Figure 3.6A), confirmed by quantification analysis (Figure 3.6B). Similar results were observed following double immunostaining with the astrocyte marker GFAP (Figure 3.6C, D). A more extended co-localization was observed in merged images with glial cell markers IBA1 (Figure 3.6E) and CD11b (Figure 3.6G) that was confirmed by high co-localization coefficient values from quantification analysis (figure 3.6F, H).

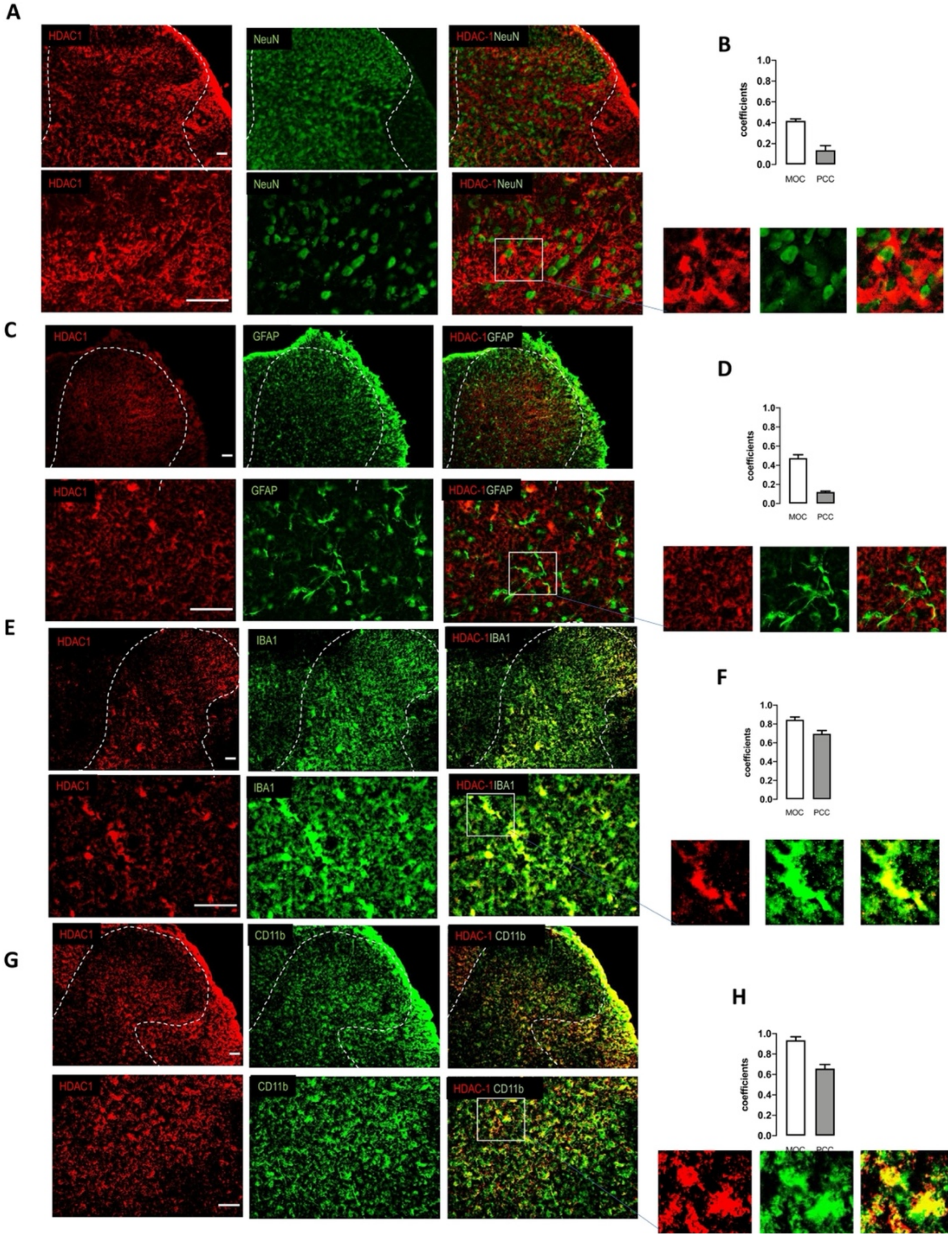

Figure 3.6. Cellular localization of HDAC1 in the spinal cord of SNI mice. Spinal cord sections were harvested 7 days after SNI and double-immunostained for HDAC1 and specific markers to determine co-localization (merged images). (A) Immunostaining for the neuronal marker NeuN (low and high magnification) showed the presence of HDAC1 immunostaining in some neuronal cells. (B) Quantification analysis of HDAC1/NeuN co-localization. (C) Immunofluorescence microscopy images N (low and high magnification) showed a partial expression of HDAC1 in GFAP positive cells. (D) Quantification of HDAC1/GFAP co-localization. Representative images (low and high

magnification) of the immunostaining for IBA1 (E) and CD11b (G) illustrate the high degree of HDAC1 expression on microglial cells. Quantification of the HDAC1/IBA1 (F) and HDAC1/CD11b (H) colocalization. Scale bars =50 μm.

3.2.2.5. Effect of HDAC and Brd4 inhibitors combination on neuroinflammation

A characteristic feature of neuroinflammation is the activation of glial cells in the spinal cord and brain, leading to the release of proinflammatory mediators. Nerve injury results in remarkable microgliosis in the spinal cord and numerous studies have demonstrated the contribution of microglia in the development of NP[76]. Our findings showing an upregulation of microglia markers that was reversed by HDAC and Brd4 inhibitors administration encouraged us to further investigate the role of this epigenetic events on SNI-induced microglia activation.

Our results showed that, compared with control mice, SNI mice exhibited markedly increased expression of IBA1 (Figure 3.7A) and iNOS, a marker of proinflammatory microglia (Figure 3.7B) in the ipsilateral side in comparison with the contralateral side. The IBA1 level returned to control values following treatment with SAHA (3 μg) or with i-BET762 (10 μg) and iNOS overexpression was partially reduced. The co-administration of both inhibitors did not produce any further reduction of iNOS content (Figure 3.7A, B). Evaluation of the effects produced on proinflammatory transcription factors, such as NF-kB and STAT1, we observed that phosphorylation of the p65 subunit of NF-kB (Figure 3.7C) and of STAT1 (Figure 3.7D) were largely increased by SNI surgery. i-BET762, SAHA as well as their combination robustly reduced the p-p65 increase with a similar efficacy. Levels of proinflammatory cytokines IL-1β (Figure 3.7E) and IL-6 (Figure 3.7F) were determined. A robust increase of IL-1β was detected in the ipsilateral side. i-BET762 treatment did not alter IL-1β overexpression whereas SAHA largely reduced the cytokine content up to control values. Combination of i-BET762 and SAHA did not further potentate the effect of SAHA. A significant increase of spinal IL-6 was also detected that remained unchanged after i-BET762 or SAHA administration. Conversely, co-administration of both inhibitors completely abolished the cytokine overexpression. Finally, the effects of epigenetic modulation on MAPK p38 phosphorylation were investigated. Spinal cord samples from ipsilateral side of SNI mice showed a robust over-phosphorylation of p38 that was left unaltered by i-BET762, SAHA and their combination (Figure 3.7G).

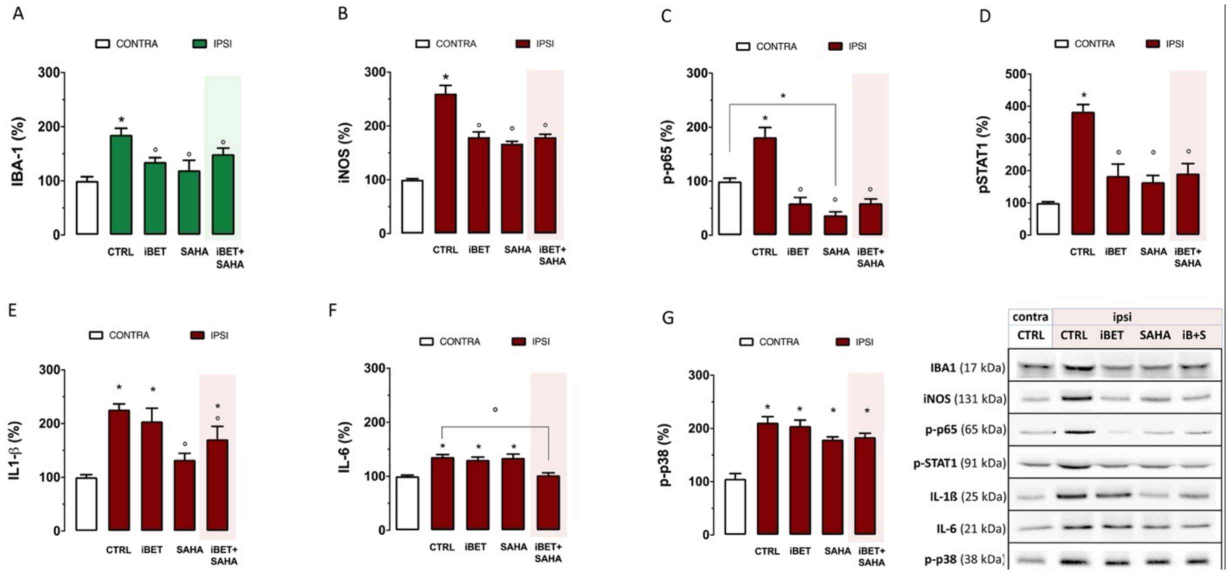

Figure 3.7. Effect of HDAC and Brd4 inhibitors combination on SNI-induced microglia activation. (A) Spinal cord samples from SNI mice showed an increase of the microglial marker IBA1 in the ipsilateral side that was abolished by i-BET762 (10 µg), SAHA (3 µg) and their combination. (B) Increase of the proinflammatory microglia marker iNOS in the ipsilateral side that was partially prevented by i-BET762, SAHA and their combination. SNI mice showed an increased phosphorylation of the proinflammatory transcription factors (C) p65 and (D) STAT1 in the ipsilateral side in comparison with the contralateral side that were reduced by i-BET762, SAHA and their combination with comparable efficacy. SNI increased the levels of proinflammatory cytokines (E) IL-1β and (F) IL-6 in the ipsilateral side. Il-1β content was reduced by SAHA and combination with similar efficacy. IL-6 was selectively reduced by i-BET762 and SAHA combination. (G) Mice exposed to SNI showed an increased phosphorylation of p38 MAPK in the ipsilateral side that remained unmodified after treatments. Experiments were conducted on day 10p< post-SNI. *$p < 0.05$ vs SNI contralateral side. °$p < 0.05$ vs SNI ipsilateral side.

3.2.2.6. SUM52, a novel dual inhibitor of HDAC1/BRD4 reduced pain symptoms through the inhibition of microglia proinflammatory activation

Aside of using two inhibitors simultaneously, we also evaluated the effect of SUM52, a synthetic compound with dual activity towards the two different targets, synthetized by Prof Romanelli of the University of Florence. SUM52 was tested following intranasal administration at increasing concentrations of 10, 50, 75, and 100 µM in animals with peripheral neuropathy. Figure 3.8A shows that SUM52 can reduce thermal allodynia following intranasal administration 60 minutes after administration at 50 and 75µM. SUM52 50µM also reduces mechanical allodynia, with a peak activity at 60 min (Figure 3.8B). The effect and peak activity (60 min) are consistent with that reported for SAHA (Figure 3.9A) and IBET (Figure 3.9B). No differences were observed between SUM52 50 µM, SAHA 10 µg, iBET 50 µg, and SAHA+iBET after intranasal administration on mechanical allodynia (Figure 3.9A-D) and thermal hyperalgesia (Figure 3.9E-H). SUM52 is auto fluorescent and emits at a wavelength of 488 nm, so it was possible to visually confirm that the molecule was able to reach the spinal cord following intranasal administration (Figure 3.10A) and at the same time it was also possible to quantify the presence of this molecule in the spinal cord (Figure 3.10B).

As shown in the figure, SUM52 can reduce the expression of HDAC1 (Figure 3.10C) and BRD4 (Figure 3.10D). By means of autofluorescence, it was also possible to identify the cellular localization of SUM52. In fact, double labelling with IBA1 confirmed a localization of the molecule in the microglial cells of the spinal cord (Mander's coefficient 0.876, Figure 3.10E). In addition, a reduction in the expression of IBA1 was observed in SNI animals compared to non-operated animals (dashed black line) (Figure 3.10F).

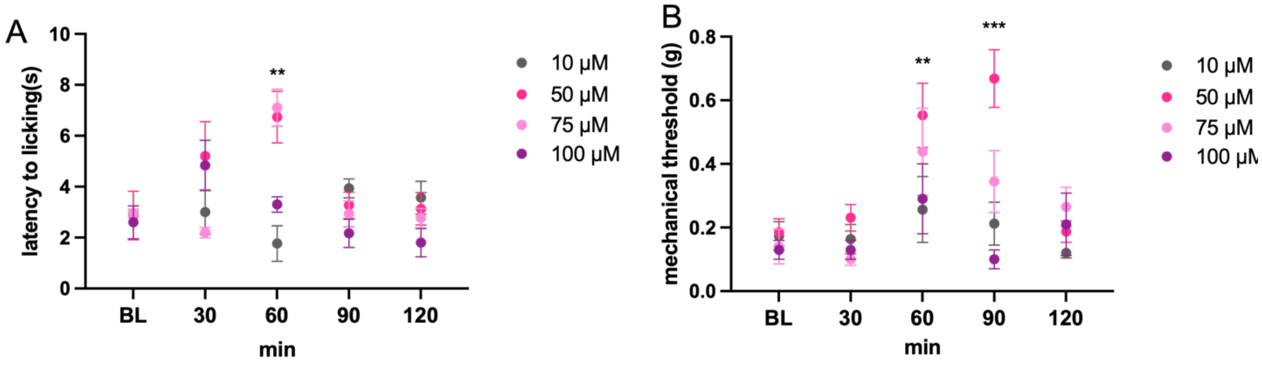

Figure 3.8 Antinociceptive effect of SUM52 in SNI mice model. Time course and dose response curve of SUM52 in (A) thermal allodynia and (B) mechanical allodynia at 10, 50, 75, and 100 μM. (***p<0.001 **p<0.01 vs BL).

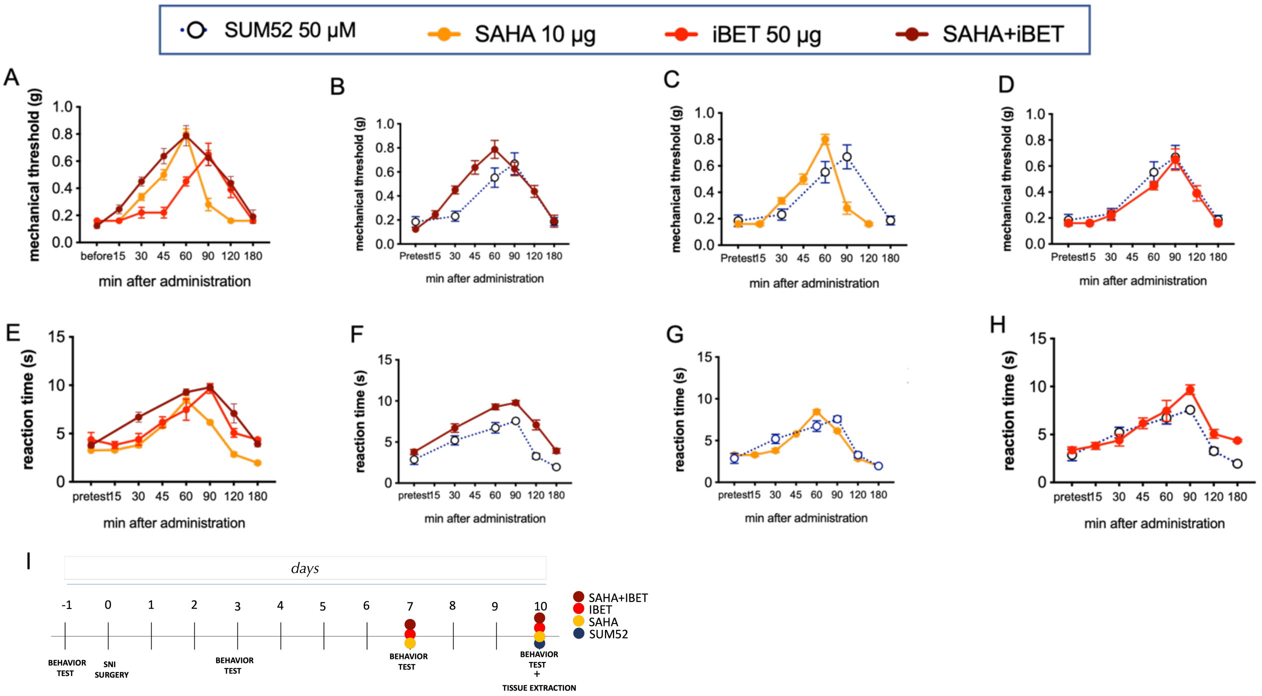

Figure 3.9 Comparison of the effect on (A-D) mechanical allodynia and (E-H) thermal hyperalgesia of SUM52 50μM, SAHA 10μg, iBET 50μg and SAHA+iBET after intranasal administration. (I) Experimental design. Experiments were performed on post-surgery day 7 and 10: SNI (n=8), SAHA+ IBET i.n. (n=8), SAHA (n=8), IBET i.n. (n=8), SUM52 (n=8).

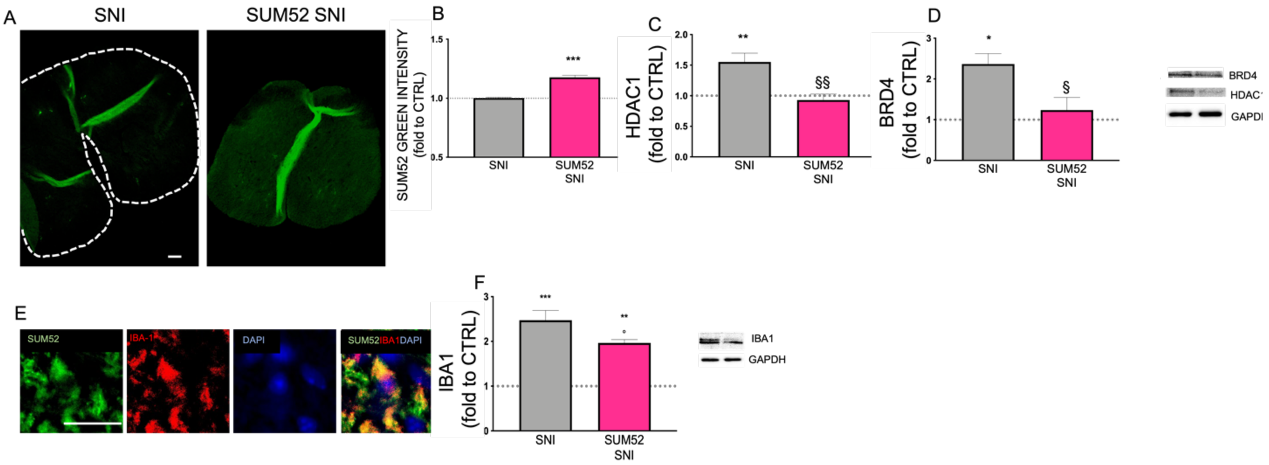

Figure 3.10 (A) Representative image of SUM52 (green) in spinal cord tissue of SNI animals after intranasal administration and (B) quantitative analysis. ***$p<0.001$ vs SNI. SUM52 50 µM reduced (C) HDAC1 and (D) BRD4 protein expression in spinal cord of SNI mice compared the SNI control group. ***$p<0.001$ vs CTRL (dashed black line) §§$p<0.01$ §$p<0.05$ vs SNI group. (E) Representative immunofluorescence images to identify SUM52 (green) colocalization with IBA1(red). (F) IBA1 expression was reduced in SUM52 SNI group compared the SNI group (***$p<0.001$ **$p<0.01$ vs CTRL, °$p<0.05$ vs SNI group).

3.2.3. Zingiberene, a sesquiterpene isolated from Zingiber officinale Roscoe rhizome extract, alleviates NP in mice by reducing neuroinflammation through the inhibition of class I HDAC isoforms

3.2.3.1. Evaluation of anti-hyperalgesic effect of *Zingiber officinale* Roscoe rhizome extract in a mice model of peripheral neuropathy (SNI)

According to the World Health Organization (WHO), an increasing number of patients support the use of herbal treatments because they are generally considered safer than conventional medicine[77]. Recently, an important biological role has been attributed to curcumin, a phenolic compound derived from *Curcuma longa* L. (*Zingiberaceae*) rhizome (turmeric), in the management of pain[78]. However, even though different strategies have been studied to improve the absorption of curcumin (i.e., nanocrystals, emulsions, liposomes, nanogels), its low bioavailability limits its application as a therapeutic agent. Moreover, the lack of information about the safety profile of the novel curcumin formulation, together with their expensive costs, raised the need to search for other herbal species with similar activity, but with a more favourable bioavailability profile[79]. *Zingiber officinale* Roscoe (Zingiberaceae), commonly known as ginger, is an Asian-native species belonging to the same family of turmeric and it is widely used as a spice. Ginger is enlisted in many official pharmacopoeias of different countries, including European Pharmacopoeia 9th ed. The dried rhizome, the part of the plant with biological activities, contains a complex mixture of bioactive compounds with the essential oil and oleoresin representing the most abundant substances of the phytocomplex. The non-volatile components, to which the characteristic pungent taste is attributed, include gingerols, shogaols, paradols and zingerone[80]. Several studies have proved that *Z. officinale* rhizome possesses a broad range of pharmacological actions and it can be efficiently used for treating nausea and vomiting, gastrointestinal problems, hyperglycaemia, dysmenorrhea, inflammatory disorders, and pain. Despite the similarity between ginger and turmeric chemical composition, ginger and its main constituents have been shown to possess an optimal pharmacokinetic profile, thus, overcoming one of the main limitations for the therapeutic use of turmeric. Indeed, it has been recently observed that ginger administered p.o. is neuroprotective in different *in vivo* models of neurological disorders[81,82], supporting its capability to reach the CNS. Importantly, according to the European Medicines Agency (EMA), safety data for ginger are generally positive and only few minor adverse effects have been observed [83]. Thus, the first aim of this study was to investigate the possible analgesic effect of a standardized *Z. officinale* rhizomes extract (ZOE) obtained by CO2 supercritical extraction, in a mice model of peripheral mononeuropathy, i.e., the spared nerve injury (SNI), to further elucidate exploring the mechanism of action of ZOE and its main constituents in an *in vitro* model of neuroinflammation.

The chemical characterization of ZOE is shown in the Tables 3.1 and 3.2. ZOE contains 24.73% total gingerols and 3.03% total shogaols, and the amount of GIN and SHO resulted to be 10.07% and 1.68%, respectively. Regarding the volatile fraction, ZTE was found to be 30.10 %, with zingiberene (ZNG) being the most abundant volatile constituent (28.2%).

Table 3.1 HPLC-DAD quantification of 6-gingerol (GIN), 6-shogaol (SHO) and terpenoid-enriched fraction (ZTE) in the standardized extract from *Zingiber officinale* Roscoe rhizomes (ZOE). Data are expressed as % ± standard deviation

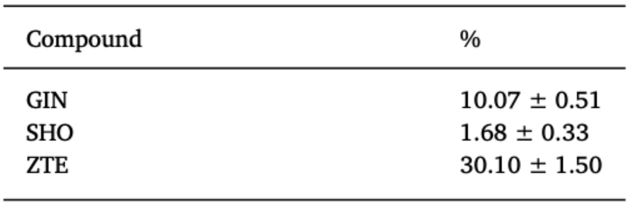

Compound	%
GIN	10.07 ± 0.51
SHO	1.68 ± 0.33
ZTE	30.10 ± 1.50

Table 3.2 Chemical composition of the volatile compounds in the standardized extract from *Zingiber officinale* Roscoe rhizomes (ZOE). Data are expressed as % relative peak area ± standard deviation.

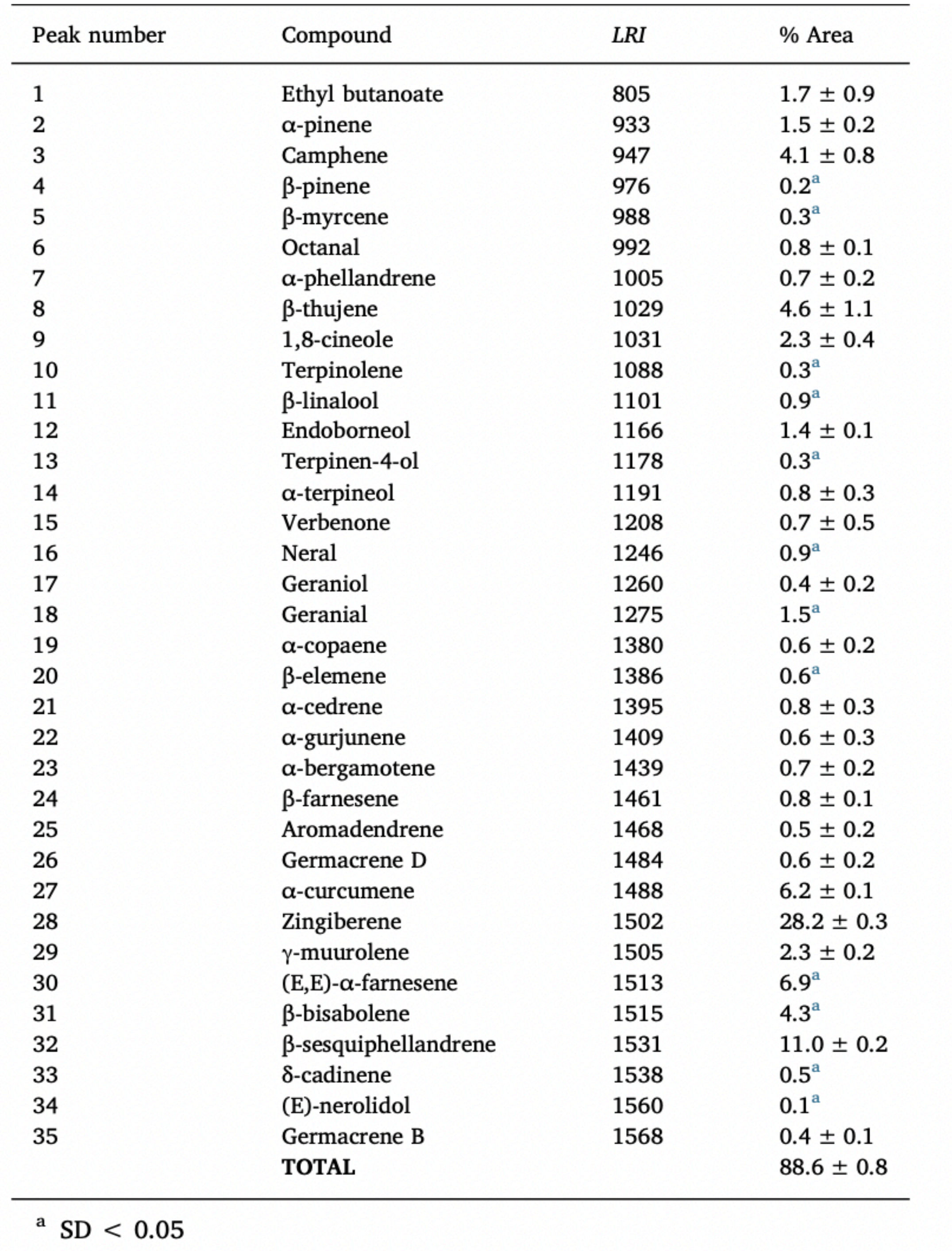

Peak number	Compound	*LRI*	% Area
1	Ethyl butanoate	805	1.7 ± 0.9
2	α-pinene	933	1.5 ± 0.2
3	Camphene	947	4.1 ± 0.8
4	β-pinene	976	0.2[a]
5	β-myrcene	988	0.3[a]
6	Octanal	992	0.8 ± 0.1
7	α-phellandrene	1005	0.7 ± 0.2
8	β-thujene	1029	4.6 ± 1.1
9	1,8-cineole	1031	2.3 ± 0.4
10	Terpinolene	1088	0.3[a]
11	β-linalool	1101	0.9[a]
12	Endoborneol	1166	1.4 ± 0.1
13	Terpinen-4-ol	1178	0.3[a]
14	α-terpineol	1191	0.8 ± 0.3
15	Verbenone	1208	0.7 ± 0.5
16	Neral	1246	0.9[a]
17	Geraniol	1260	0.4 ± 0.2
18	Geranial	1275	1.5[a]
19	α-copaene	1380	0.6 ± 0.2
20	β-elemene	1386	0.6[a]
21	α-cedrene	1395	0.8 ± 0.3
22	α-gurjunene	1409	0.6 ± 0.3
23	α-bergamotene	1439	0.7 ± 0.2
24	β-farnesene	1461	0.8 ± 0.1
25	Aromadendrene	1468	0.5 ± 0.2
26	Germacrene D	1484	0.6 ± 0.2
27	α-curcumene	1488	6.2 ± 0.1
28	Zingiberene	1502	28.2 ± 0.3
29	γ-muurolene	1505	2.3 ± 0.2
30	(E,E)-α-farnesene	1513	6.9[a]
31	β-bisabolene	1515	4.3[a]
32	β-sesquiphellandrene	1531	11.0 ± 0.2
33	δ-cadinene	1538	0.5[a]
34	(E)-nerolidol	1560	0.1[a]
35	Germacrene B	1568	0.4 ± 0.1
	TOTAL		88.6 ± 0.8

[a] SD < 0.05

ZOE contains 24.73% total gingerols and 3.03% total shogaols, and the amount of GIN and SHO resulted to be 10.07% and 1.68%, respectively. Regarding the volatile fraction, ZTE was found to be 30.10 %, with zingiberene (ZNG) being the most abundant volatile constituent (28.2%).

Effect of ZOE on anti-nociceptive activity SNI induced mechanical (Figure 3.11A) and thermal allodynia (Figure 3.11D) in the ipsilateral side, starting from 3 days after surgery up to day 21. No hypersensitivity was observed in the contralateral side (Figure 3.11A, D). The dose-response study performed seven days after surgery showed that oral administration of ZOE completely prevented mechanical (Figure 3.11B) and thermal allodynia (Figure 3.11E) at the dose of 200 mg kg^{-1} and no further increase of activity was observed at higher doses. The dose of 100 mg kg^{-1} was ineffective. Time-course experiments showed that, 30min after the administration, ZOE 200 mg kg^{-1} tends to reduce nociceptive symptoms, which became statistically significant after 60 min and peaked at 120 min (Figure 3.11B, E). Although it did not reach significant, ZOE still maintains a tendency to reduce allodynia three h after administration. Notably, the intensity of the anti-hyperalgesic effect of ZOE 200 mg kg^{-1} was like that induced by pregabalin (30 mg kg^{-1}), used as positive control, without any effect on contralateral side (Figure 3.11E, F). Oral repeated administration of ZOE 200 mg kg^{-1} reverted mechanical allodynia in the ipsilateral side 7- and 10 days post-surgery (Figure 3.11G). The administration of ZOE on SNI exposed to repeated administration of the extract showed a time course like the acute administration, with a maximum effect between 60 and 120 min (Figure 3.11H). Repeated exposure to ZOE induced a significant increase of the basal mechanical threshold compared to untreated SNI mice. ZOE administration in mice exposed to repeated treatment induced a peak effect more consistent than acute administration. Repeated administration showed a trend (that did not reach significance) towards an increase in the contralateral side thermal and mechanical threshold (Figure 3.11I). Effect of ZOE p.o. administration on locomotor activity. Mice treated with the highest effective dose of ZOE (200 mg kg^{-1}) were evaluated for motor coordination, by means of the rotarod test, and for spontaneous mobility and exploratory activity, by means of the hole board test. Overall, ZOE-exposed SNI mice did not show any gross behaviour alterations (Figure 3.12A). Oral administration of ZOE did not alter motor exploratory activity (Figure 3.12B) or spontaneous mobility (Figure 3.12C), compared to the control group.

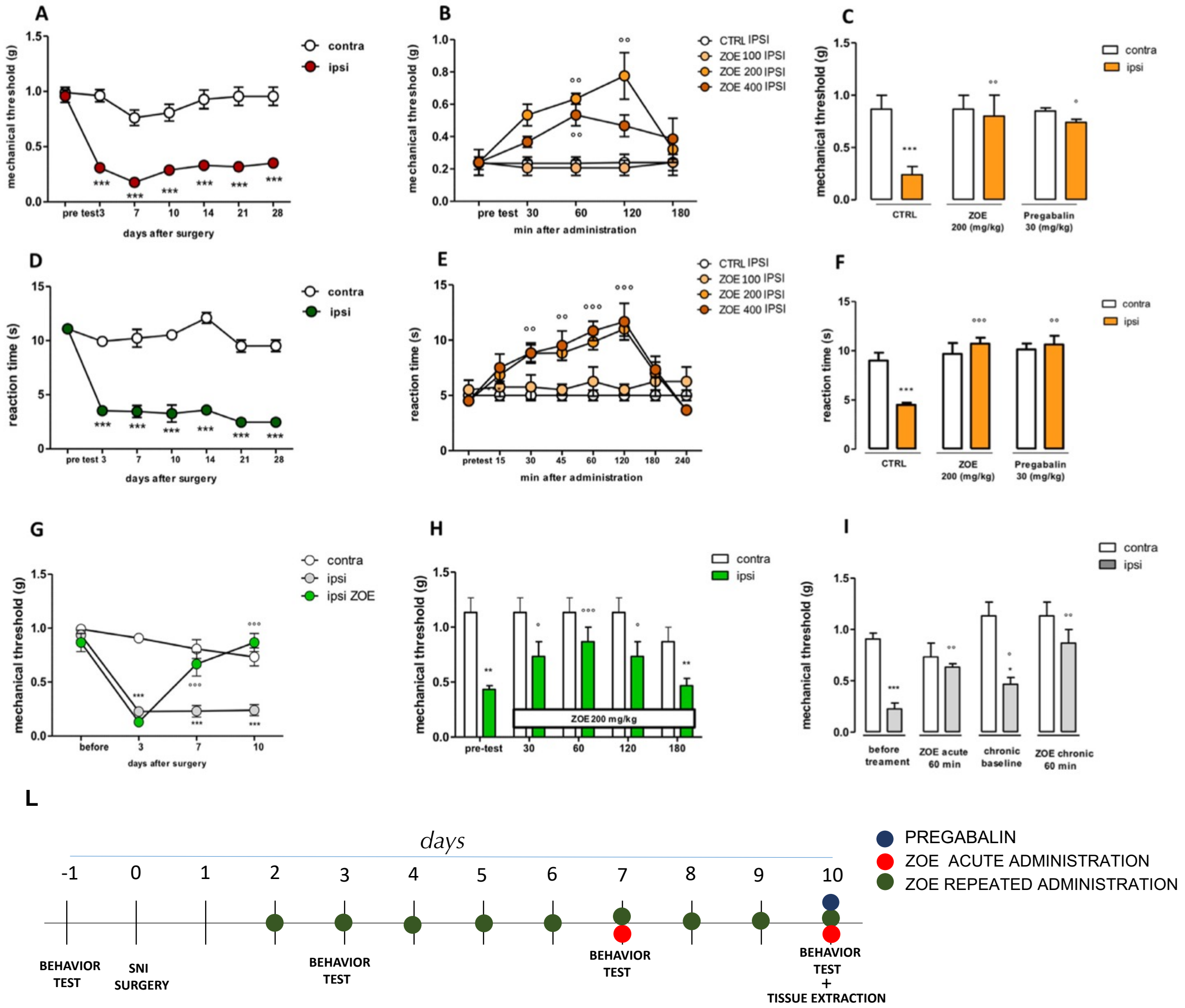
A
mechanical threshold (g)
contra
ipsi
pre test
3
7
10
14
21
28
days after surgery
B
mechanical threshold (g)
CTRL IPSI
ZOE 100 IPSI
ZOE 200 IPSI
ZOE 400 IPSI
pre test
30
60
120
180
min after administration
C
mechanical threshold (g)
contra
ipsi
CTRL
ZOE 200 (mg/kg)
Pregabalin 30 (mg/kg)
D
reaction time (s)
contra
ipsi
pre test 3
7
10
14
21
28
days after surgery
E
reaction time (s)
CTRL IPSI
ZOE 100 IPSI
ZOE 200 IPSI
ZOE 400 IPSI
pretest 15
30
45
60
120
180
240
min after administration
F
reaction time (s)
contra
ipsi
CTRL
ZOE 200 (mg/kg)
Pregabalin 30 (mg/kg)
G
mechanical threshold (g)
contra
ipsi
ipsi ZOE
before
3
7
10
days after surgery
H
mechanical threshold (g)
contra
ipsi
pre-test
30
60
120
180
ZOE 200 mg/kg
I
mechanical threshold (g)
contra
ipsi
before treament
ZOE acute 60 min
chronic baseline
ZOE chronic 60 min
L
days
-1
0
1
2
3
4
5
6
7
8
9
10
PREGABALIN
ZOE ACUTE ADMINISTRATION
ZOE REPEATED ADMINISTRATION
BEHAVIOR TEST
SNI SURGERY
BEHAVIOR TEST
BEHAVIOR TEST
BEHAVIOR TEST + TISSUE EXTRACTION

Figure 3.11. Anti-nociceptive effects of the standardized extract from *Zingiber officinale* Roscoe rhizomes (ZOE) in SNI mice. (A) The long-lasting mechanical allodynia produced by SNI up to 21 days after surgery. (B) The dose-response and the time course curve showed the effect of ZOE 100, 200 and 400 mg kg^{-1} against mechanical allodynia. (C) Comparison of the effect of ZOE (p.o. 200 mg kg^{-1}) on mechanical allodynia to that produced by pregabalin (i.p 30 mg kg^{-1}). (D) The long-lasting thermal hyperalgesia produced by SNI model in mice. (E) The effect of acute oral administration of ZOE 100, 200 and 400 mg kg^{-1} on thermal allodynia after SNI surgery. (F) Comparison of the effect of ZOE 200 mg kg-1 on thermal hyperalgesia to that produced by pregabalin (i.p 30 mg kg^{-1}). (G) The effect of ZOE 200 mg/kg on mechanical allodynia at 3, 7 and 10 days after surgery. (H) Time course of oral repeated administration of ZOE 200 mg kg^{-1}. (I) Comparison of the effect on mechanical allodynia between acute and repeated administration of ZOE 200 mg kg^{-1}. (L) Experimental design. Experiments were performed on post-surgery day 7 and 10: SNI (n=8), ZOE ACUTE ADMINISTRATION. (n=8), ZOE REPEATED ADMINISTRATION (n=8), PREGABALIN (n=8) Data points represent the mean ± SEM. *** $p < 0.001$; ** $p < 0.01$; * $p < 0.05$ vs. contralateral side; °°° $p < 0.001$; °° $p < 0.01$; ° $p < 0.05$ vs. ipsilateral side before the treatment.

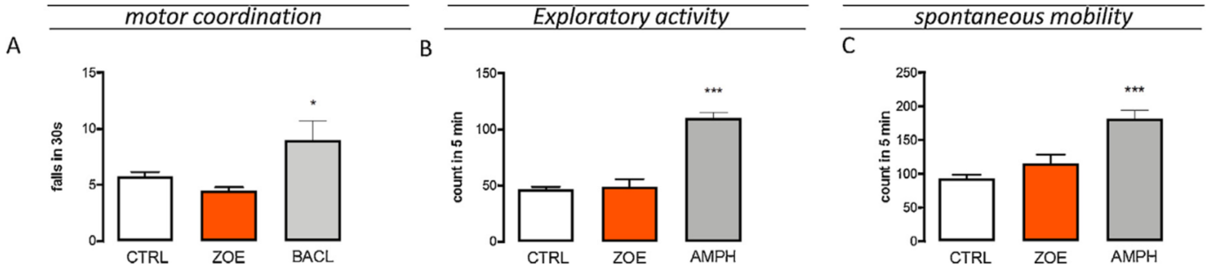

Figure 3.12. Lack of effect of the standardized extract from *Zingiber officinale* Roscoe rhizomes (ZOE) on locomotor behaviour. Lack of impairment of (A) motor coordination compared to BACL (* $p < 0.05$ vs. CTRL), (B) exploratory activity and (C) spontaneous mobility compared to AMPH (*** $p < 0.001$ vs. CTRL) in mice treated with ZOE 200 mg kg^{-1}. Data were recorded at the peak of antinociceptive activity.

3.2.3.2. Effect of ZOE on ERK 1/2 activation *in vivo* and *in vitro*

Mitogen-activated protein kinases (MAPKs) play an important role in the spinal mechanism of NP and neuroinflammation[84]. The role of these kinases in the cellular mechanism of action of ZOE was, thus, investigated in SNI animals and in BV2 cells. Consistently with other published work[85], the peak of extracellular signal-regulated kinase (ERK) and p38 mitogen-activated protein kinases (p38) MAPKs phosphorylation in BV2 cells was observed at 30 min of LPS stimulation. The reliability of the *in vitro* model was confirmed by using U0126 10 µM, a well-known MEK inhibitor, as a positive control. ZOE was used at the concentration of 10 µg mL^{-1} according to previously performed cell viability assay and it was able to reduce ERK1/2 activation (Figure 3.13A, B), while no effect was observed on p38 phosphorylation (Figure 3.13C). To confirm that the effect observed in ZOE-treated BV2 cell concurs with the *in vivo* mechanism of action, we evaluated its effects on MAPKs activation in SNI spinal cord mice samples. An increase of phosphorylated ERK (pERK)1 (Figure 3.13D, H) and pERK2 (Figure 3.13E, I) was observed in the ipsilateral side of SNI mice. ZOE completely prevented ERK1 (Figure 3.13D) and ERK2 (Figure 3.13E) activation after acute administration, similarly to U0126 used as positive control. pERK2 levels were also reduced after repeated treatment (Figure 3.13I), whereas no effect on ERK1 phosphorylation was observed (Figure 3.13H). An increase of phosphorylated p-38 (pp38) levels was observed in the spinal cord of SNI mice. Consistently with the results obtained in BV2 cells, ZOE did not reduce p38 phosphorylation, neither after acute (Figure 3.13F) nor repeated administration (Figure 3.13J). In agreement with the literature[86], SNI surgery group showed an isoform-selective activation for c-Jun n-terminal kinase (JNK), with phosphorylated JNK1 (pJNK1) being altered in the injured spinal cord. Acute and repeated treatment with ZOE showed a tendency to reduce pJNK1 activation (Figure 3.13G, K), compared to pERK1.

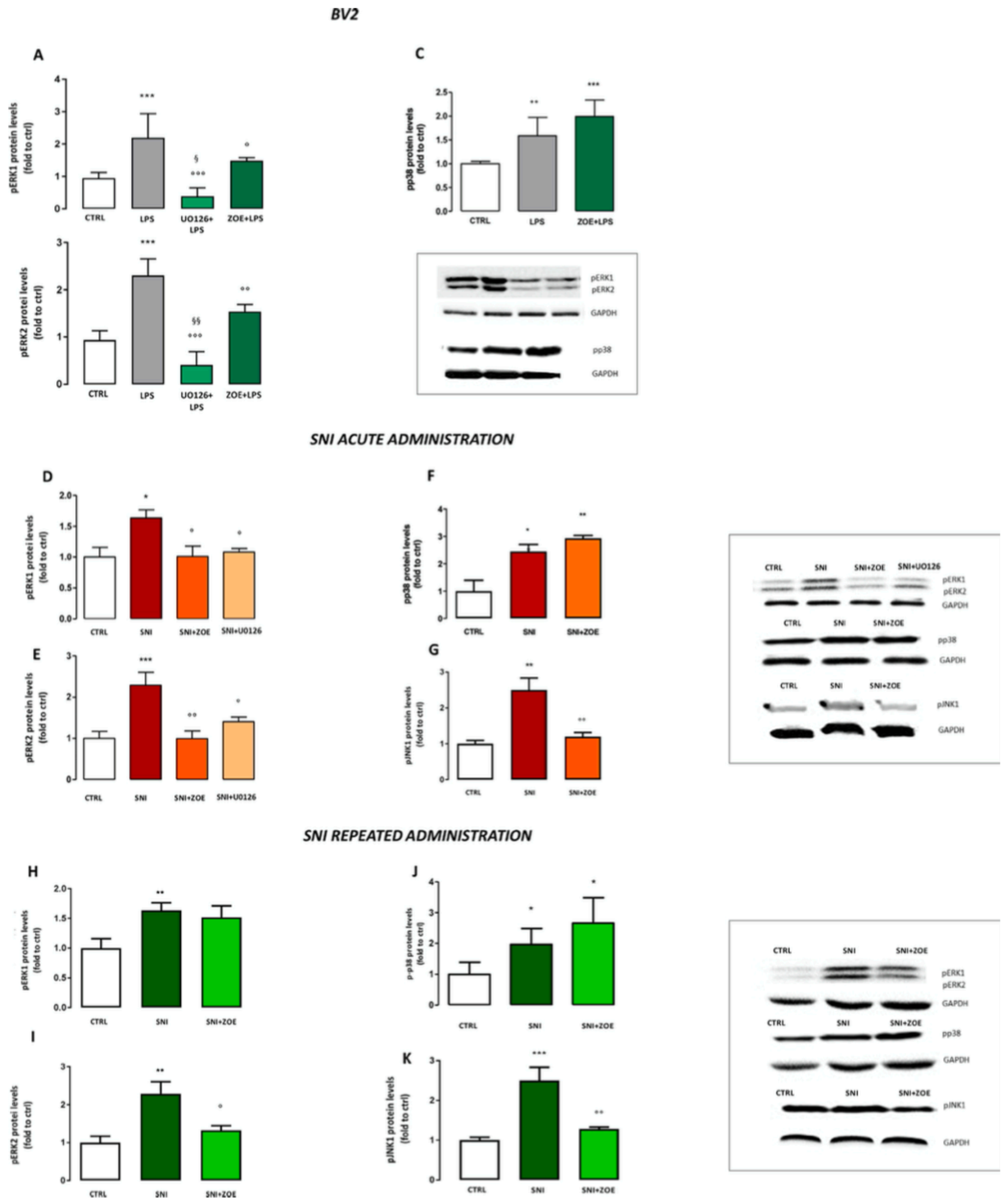

Figure 3.13. Effect of the standardized extract from *Zingiber officinale* Roscoe rhizomes (ZOE) on MAPKs phosphorylation in BV2 cells and in the spinal cord of SNI mice. Effect of ZOE 10 $\mu g\ mL^{-1}$ on (A, B) pERK1/2 and (C) pp38 protein levels in BV2 cell after 30 min of LPS *** $p < 0.001$ vs. untreated BV2; °°° $p < 0.001$; °° $p < 0.01$; °$p < 0.05$ vs. LPS-stimulated BV2; §§ $p < 0.01$ vs. ZOE + LPS; § $p < 0.05$ vs. ZOE + LPS; Effect of ZOE mg kg−1 acute oral administration on the activation of (D, E) pERK1/2, (F) pp38 and (G) pJNK1 activation induced by SNI model in spinal cord samples. Effect of repeated oral administration of ZOE 200 mg kg^{-1} on (H, I) pERK1/2, (J) pp38 and (K) pJNK1 in spinal cord of injured mice. Representative blots are reported. *** $p < 0.001$; ** $p < 0.01$; * $p < 0.05$ vs. controlateral side; °° $p < 0.01$; ° $p < 0.05$ vs. SNI mice.

3.2.3.3. Effect of ZOE on HDAC1 protein expression in the spinal cord

As shown in Figure 3.14A, LPS induced the up regulation of HDAC1 protein expression in BV2 cells. This effect was completely prevented by ZOE pre-treatment, with a similar trend of LG325 a selective HDAC1 inhibitor. Consistently with our previous study, SNI mice showed an increased expression of HDAC1 protein in the ipsilateral side compared to contralateral side. The increase of HDAC1 was significantly prevented by acute (Figure 3.14B) and repeated (Figure 3.14C) ZOE administration, with the efficacy being comparable to LG325.

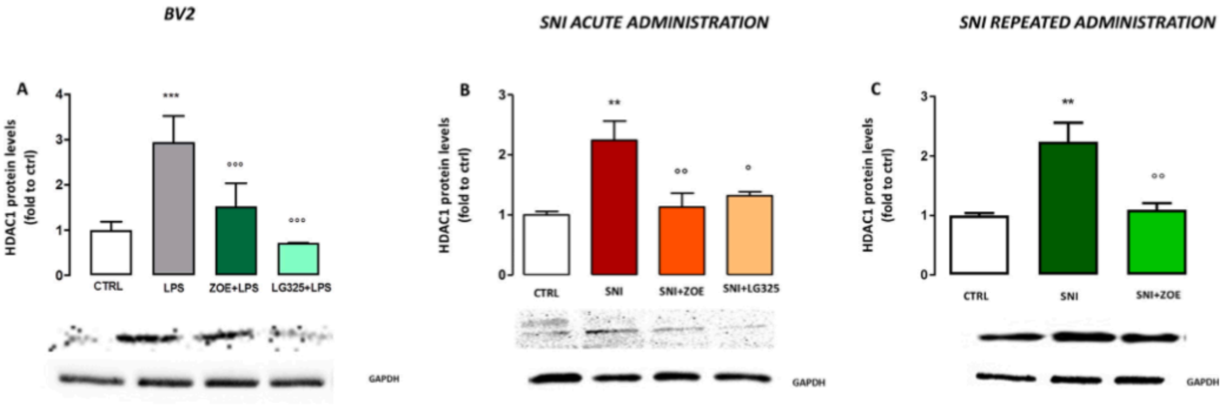

Figure 3.14. Effect of the standardized extract from *Zingiber officinale* Roscoe rhizomes (ZOE) on HDAC1 protein expression. (A) Effect of ZOE ($10\ \mu g\ mL^{-1}$) on the HDAC1 expression in BV2 after 24 h of LPS stimulation. *** $p < 0.001$ vs. untreated BV2; °°° $p < 0.001$ vs. LPS-stimulated BV2. Effect of (B) acute and (C) repeated oral administration of ZOE 200 mg kg^{-1} on HDAC1 protein expression in SNI mice. Representative blots are reported. ** $p < 0.01$; * $p < 0.05$ vs. contralateral side; °° $p < 0.01$; ° $p < 0.05$ vs. SNI mice.

3.2.3.4. Effect of ZOE on NF-κBp65 nuclear translocation in SNI mice and in BV2 cells

Nuclear factor kappa-light-chain enhancer of activated B cells subunit p65 (NF-κBp65) is one of the most important pathways involved in inflammatory processes[87]. Thus, here we investigated its role in ZOE mechanism of action. Time-course studies showed that LPS stimulation induced a phosphorylated-p65 (pp65) nuclear translocation that peaked 1 h after treatment. To evaluate the effect of ZOE on pp65 nuclear translocation, immunofluorescence experiments were carried out. We found pp65 subunit primarily present in the cytoplasm in unstimulated cells (Figure 3.15A), whereas pp65 level in the nucleus were increased after 1 h of LPS stimulation (Figure 3.15B). The treatment with ZOE 10 µg mL^{-1} blocked the nuclear translocation in LPS-stimulated cells (Figure 3.15C). Analysis by fluorescent staining intensity confirmed these results. In fact, the intensity of nuclear fluorescence of pp65 in LPS stimulated cells resulted significantly higher than in the control group and ZOE pre-treatment prevented pp65 nuclear translocation (Figure 3.15D). To confirm that ZOE counteracted the activity of NFκBp65 we showed that 24 h after LPS stimulation the total levels of nuclear factor of kappa light polypeptide gene enhancer in B-cells inhibitor alpha (IKBα) increased and ZOE treatment completely reverted this event (Figure 3.15E). In the spinal cord of SNI mice, we observed an increase of pp65 protein levels, which was completely reverted by ZOE acute treatment (Figure 3.15F). A similar trend was observed for repeated administration, where the expression levels of pp65 were reduced compared to untreated mice (Figure 3.15G).

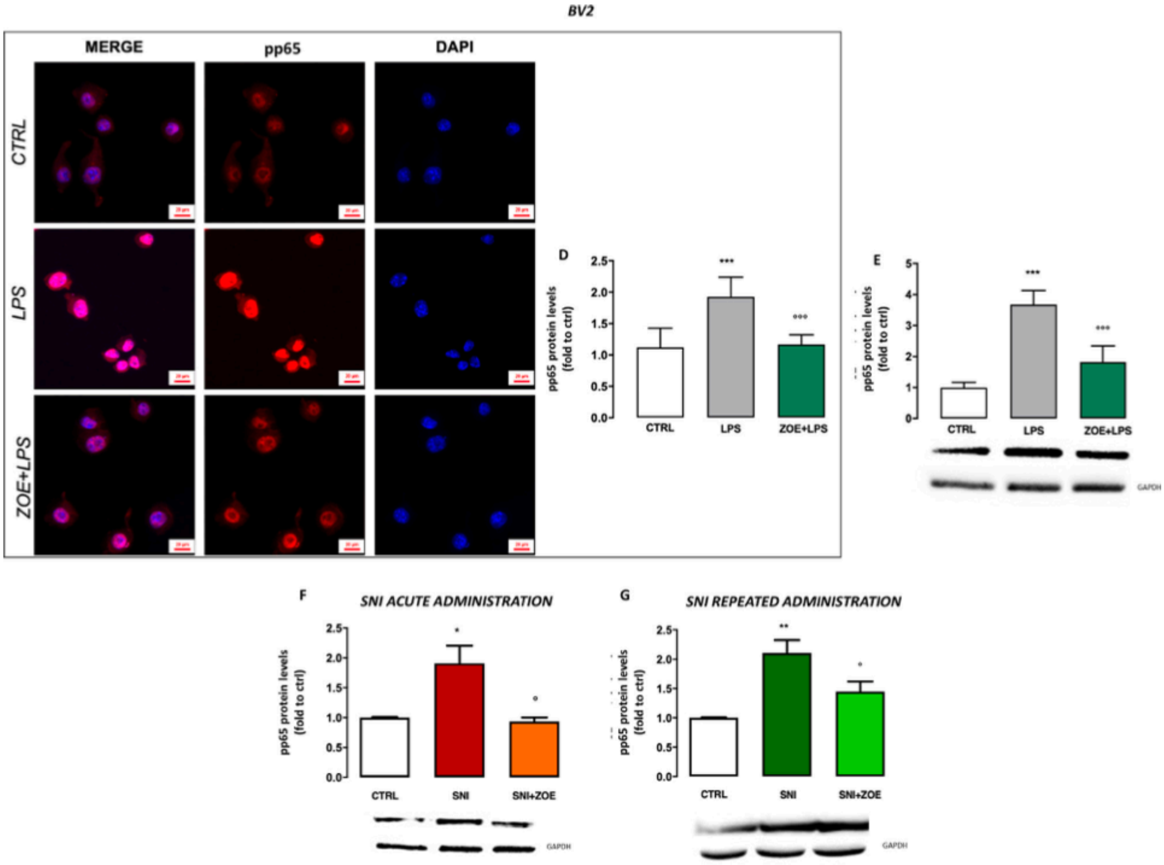

Figure 3.15. Effect of the standardized extract from *Zingiber officinale* Roscoe rhizomes (ZOE) on NF-κB p65 activation. Representative micrograph showing pp65 nuclear translocation in (A) untreated and (B) LPS-stimulated BV2, and (C) the effect of ZOE ($10\ \mu g\ mL^{-1}$) pre-treatment. Scale bar = 20 μm. (D Immunofluorescence quantification). (E) Effect of ZOE ($10\ \mu g\ mL^{-1}$) on pp65 protein expression after 24 h of LPS stimulation in BV2. *** $p < 0.001$ vs. untreated BV2; °°° $p < 0.001$ vs. LPS-stimulated BV2. Effect of ZOE 200 mg kg^{-1} on pp65 nuclear translocation after (F) acute and (G) repeated administration in SNI mice. ** $p < 0.01$; * $p < 0.05$ vs. controlateral side ° $p < 0.05$ vs. SNI mice).

LPS stimulation led to a significant release of the pro-inflammatory cytokines' tumor necrosis factor-α (TNF-α) (Figure 3..16A), interleukin-6 (IL6) (Figure 3.16B), and interleukin-1β (IL-1β) (Figure 3.16C) in BV2 culture medium, which was strongly prevented by ZOE treatment. This effect is confirmed in ipsilateral side of SNI mice, where ZOE significantly reduced IL-1β expression levels after both acute (Figure 3.16D) and repeated administration (Figure 3.16E).

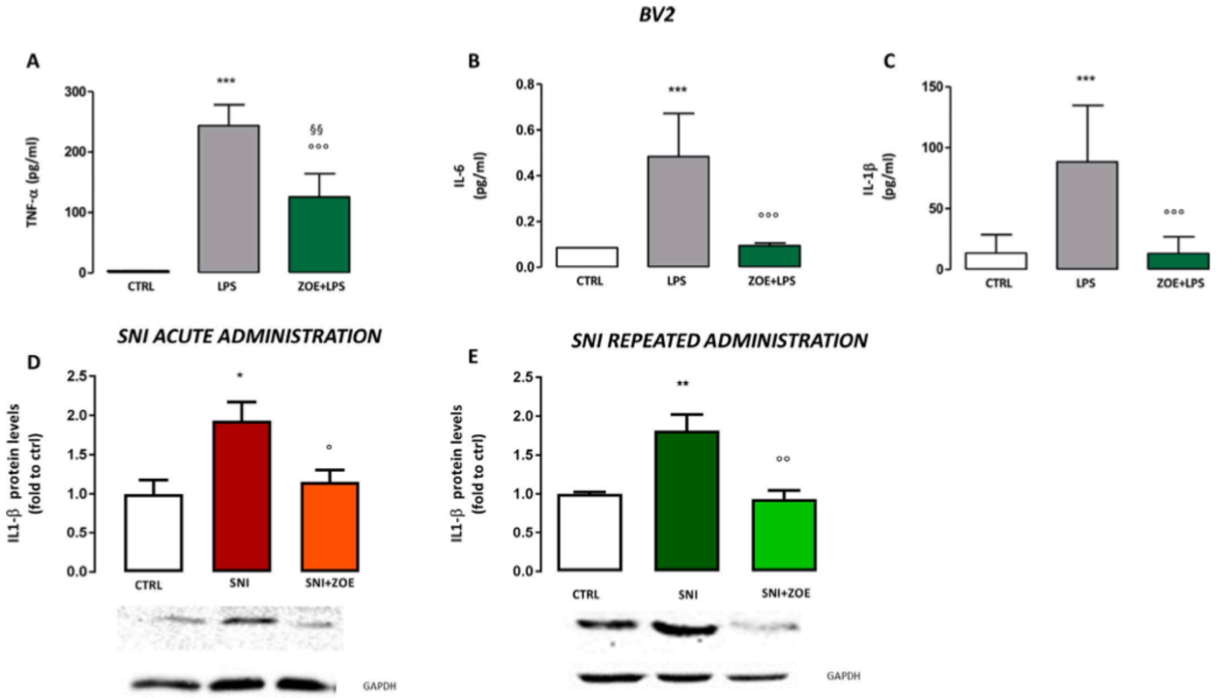

Figure 3.16. Effects of the standardized extract from *Zingiber officinale* Roscoe rhizomes (ZOE) on inflammatory cytokines levels. Quantification of (A) TNF-α, (B) IL-6 and (C) IL-1β released by LPS-stimulated BV2. *** $p < 0.001$ vs. untreated BV2; °°° $p < 0.001$ vs. LPS-stimulated BV2; §§ $p < 0.01$ vs. ctrl. IL-1β expression in SNI mice after both (D) acute and (E) repeated ZOE 200 mg kg^{-1} oral treatment. Representative blots are reported. *** $p < 0.001$; ** $p < 0.01$; * $p < 0.05$ vs. contralateral side; °° $p < 0.01$; ° $p < 0.05$ vs. SNI mice.

3.2.3.5. Effects of ZOE main components in its biological activity

To identify which constituent of ZOE was responsible for its biological effects, we tested the activity of GIN, SHO and ZTE, at the concentration present in the active dose of ZOE, on pERK activation, HDAC1 protein levels and NF-κBp65 pathway activation. Similarly, to ZOE, the pre-treatment of BV2 cells with GIN (1 μg mL^{-1}) and SHO (0.17 μg mL^{-1}) decreased LPS-induced ERK1/2 phosphorylation (Figure 3.17A, B). In contrast, no effect was observed with ZTE (3 μg mL^{-1}) treatment. To dissect the role of MEK1 and the possible binding mode of ZOE constituents in its active site, we performed molecular docking simulations, using U0126 as a positive control. The docking software was able to accurately predict the binding mode of U0126, with a root-mean square deviation (RMSD) of 0.103, compared to the original coordinates in the crystal structure. Gingerols and shogaols were able to bind the active site of MEK1 with binding energies ranging from -7 kcal/mol to -7.7 kcal/mol, which are very similar to that obtained with the known inhibitors, suggesting a similar affinity for the active site of MEK1. In contrast, the volatile compounds gave significantly higher binding energies, except for ZNG, α-copaene, α-curcumene, β-bisabolene and β-sesquiphellandrene. However, the visual inspection of the binding poses revealed that these volatile compounds were not able to replicate the key interactions needed for the inhibitor binding (Figure

3.17C, D, E). Indeed, U0126 makes multiple hydrogen bonds involving the carbonyl group of ASP208, PHE209, and the amino group of LYS97, VAL211 and SER212. Similarly, the carbonyl moiety on the side chain of GIN and SHO can make hydrogen bonds with the amino group of VAL211 and SER212. Moreover, the hydroxyl substituent present on the side chain of GIN makes a hydrogen bond with the carbonyl group of PHE209. Both GIN and SHO completely occupy the cavity space, which accommodates U0126. In the contrast, the ZNG hydrocarbon structure cannot make hydrogen bonds with the active site residues, suggesting a lower affinity for the MEK1 binding site. Regarding HDAC1, ZTE showed an activity similar to ZOE leading to a strong reduction of protein expression. Conversely, GIN and SHO did not modulate this target (Figure 3.17F). Consistently, the increase of IKBα levels, observed after 24 h of LPS stimulation, was completely reverted by ZTE pre-treatment, with GIN and SHO showing no effect (Figure 3.17G).

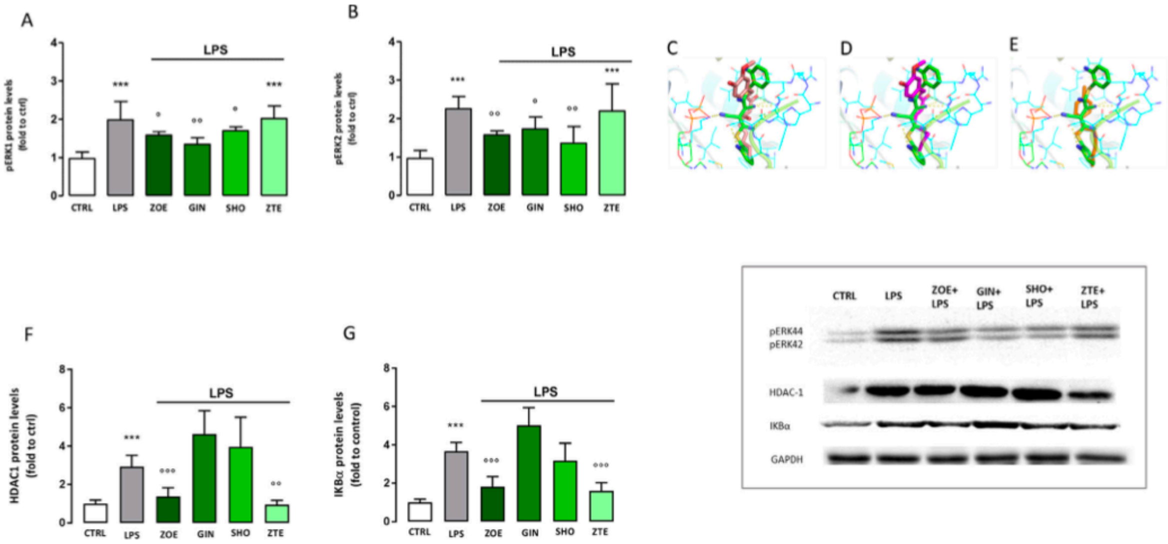

Figure 3.17. Effects of the standardized extract from *Zingiber officinale* Roscoe rhizomes (ZOE) main constituents on the modulation of pERK1/2, HDAC1, and IKBα protein expression. Effect of ZOE (10 μg mL^{-1}), GIN (1 μg mL^{-1}), SHO (0.17 μg mL^{-1}), and ZTE (3 μg mL^{-1}) in the modulation of (A) pERK 1 and (B) pERK2 level induced by LPS (30 min) in BV2 cells. Docking poses of (C) GIN (pink), (D) SHO (magenta), and (E) ZNG (orange), superimposed with U0126 (green). Polar interactions are depicted as yellow dashed lines for U0126 and as green dashed lines for ZOE constituents. Modulation by ZOE (10 μg mL^{-1}), GIN (1 μg mL^{-1}), SHO (0.17 μg mL^{-1}), and ZTE (3 μg mL^{-1}) of (F) HDAC1 and (G) IKBα protein levels in LPS-stimulated BV2 cells. Representative blots are reported. *** $p < 0.001$ vs. untreated BV2; °°° $p < 0.001$; °° $p < 0.01$; ° $p < 0.05$ vs. LPS-stimulated BV2.

Inflammatory factors are known to induce neurotoxicity both *in vivo* and *in vitro*. Similarly, to ZOE, ZTE pre-treatment significantly reduced the LPS-induced release of the pro-inflammatory cytokines TNF-α (Figure 3.18A), IL-1β (Figure 3.18B), and IL-6 (Figure 3.18C) by BV2 cells. In contrast, GIN and SHO did not show any significant effect.

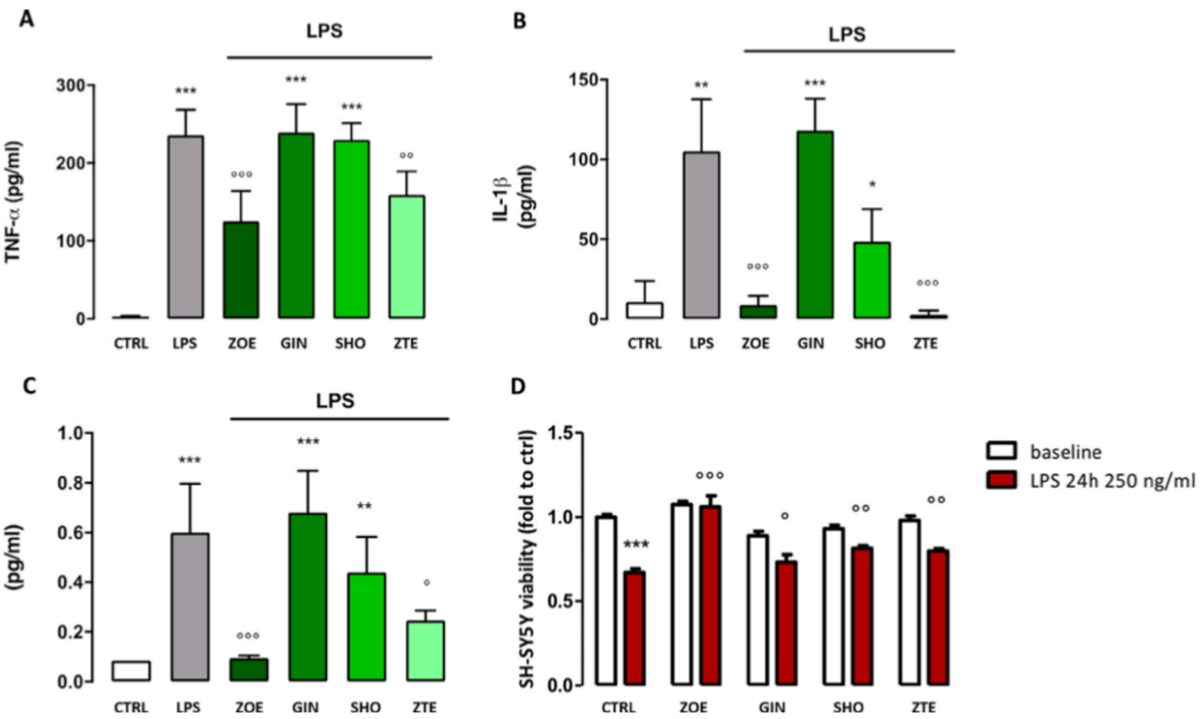

Figure 3.18. Neuroprotective effect of the standardized extract from *Zingiber officinale* Roscoe rhizomes (ZOE) and its main components. Effect of ZOE (10 μg mL^{-1}), GIN (1 μg mL^{-1}), SHO (0.17 μg mL^{-1}), and ZTE (3 μg mL^{-1}) on the release of (A) TNF-α, (B) IL-1β, and (C) IL-6 by LPS-stimulated BV2 cells. *** $p < 0.001$; ** $p < 0.01$; * $p < 0.05$ vs. unconditioned BV2 medium; °°° $p < 0.001$; °° $p < 0.01$ vs. LPS-conditioned BV2 medium. (D) Protective effect of ZOE (10 μg mL^{-1}), GIN (1 μg mL^{-1}), SHO (0,17 μg mL^{-1}), and ZTE (3 μg mL^{-1}) on the neurotoxic effect induced by LPS-conditioned BV2 medium. *** $p < 0.001$ vs. baseline; °°° $p < 0.001$; °° $p < 0.01$; ° $p < 0.05$ vs. LPS-conditioned BV2 medium.

3.2.3.6. Effect of ZOE on inflammation-induced neurotoxicity in SH-SY5Y cells

As shown in Figure 3.18D, LPS-conditioned BV2 medium reduced SHSY5Y cell viability compared to the untreated control, suggesting that the pro-inflammatory cytokines secreted by LPS-activated microglia were able to induce neurotoxicity. LPS-conditioned medium obtained from ZOE-treated BV2 cells completely prevented this cytotoxic effect, returning to basal level. LPS-conditioned medium obtained from GIN-, SHO-, and ZTE-treated BV2 cells was also able to significantly protect SH-SY5Y from the neurotoxic effect of BV2 conditioned medium.

3.2.3.7. ZTE fraction selectively reduced the HDAC1, HDAC2, HDAC3, HDAC8, and HDAC11 activity and protein expression in LPS-stimulated BV2.

As already stated in the first part of this chapter, the terpene component (ZTE) is certainly the main responsible for the activity on HDAC1. To identify the selectivity of action of ZOE, we performed an enzymatic assay. The percentage of inhibition of ZOE, ZTE, and positive control on HDAC1-9, 11, SIRT1-3, and SIRT5-6 are reported in table 3.3. ZTE demonstrated a higher percentage of inhibition on HDAC1, 2, 3, and 8. No effect was observed on the modulation of sirtuins. ZTE, was found to be more potent than ZOE on HDAC1, 2, and 6 isoforms, while ZOE was more active on HDAC6. Very low activity was observed on sirtuins.

Table 3.3 Inhibitory activity of ZOE, ZTE, and reference compounds on HDAC and SIRT isoforms activity.

Enzyme	% inhibition ± SD		
	ZOE (5 μg mL^{-1})	ZTE (1.6 μg mL^{-1})	Reference compound (0.01 μM)
HDAC1	4.5 ± 0.5	9.0 ± 2.0	19.5 ± 0.5*
HDAC2	2.5 ± 0.5	8.5 ± 2.5	14 ± 0.5*
HDAC3	9.5 ± 0.5	9.5 ± 0.5	21 ± 0.5*
HDAC4	2.5 ± 0.5	2.0 ± 0.5	15 ± 0.5°
HDAC5	1.5 ± 1.5	0.5 ± 0.5	29.5 ± 0.5°
HDAC6	0.5 ± 0.5	3.5 ± 0.5	6.0 ± 0.5*
HDAC7	5.0 ± 0.5	4.0 ± 0.5	9.5 ± 0.5°
HDAC8	7.5 ± 0.5	3.0 ± 1.0	11.0 ± 1.0°
HDAC9	2.0 ± 0.5	0.5 ± 0.5	29.5 ± 0.5°
HDAC11	1.0 ± 0.5	0.5 ± 0.5	10.0 ± 0.5°
SIRT1	2.0 ± 0.5	1.0 ± 0.5	11.01 ± 1.0$^{\#}$
SIRT2	0.5 ± 0.5	1.5 ± 0.5	10.0 ± 2.0$^{\wedge}$
SIRT3	1.5 ± 0.5	3.5 ± 0.5	11.0 ± 0.5$^{\wedge}$
SIRT5	1.5 ± 0.5	0.5 ± 0.5	17.5 ± 0.5$^{\wedge}$
SIRT6	2.5 ± 0.5	3.0 ± 0.5	18.5 ± 1.5$^{\wedge}$

* Vorinostat (SAHA) 0.01 μM; ° trichostatin A 0.01 μM; $^{\#}$ suramin 0.01 μM; $^{\wedge}$ nicotinamide 0.01 μM.

As reported in Figure 3.1A, HDAC isoforms 1, 2, 3, 8, and 11 appear to be increased in LPS-stimulated BV2 cells. ZOE reduces the expression of HDAC1, 2, 8, and 11, with an efficacy comparable to that of SAHA, a known HDAC pan inhibitor, used as positive control. No effect was observed on the expression of HDAC3. ZTE, tested at the concentration present in the active dose of ZOE, showed an efficacy comparable to ZOE on the expression of HDAC1 and HDAC11. A reduction of the protein levels of HDAC2 and HDAC8, compared to LPS-stimulated BV2 was also observed, even if with a lower efficacy, compared to ZOE.

3.2.3.8. *In silico* and *in vitro* HDAC1 inhibitory activity of ZNG

Given the selectivity of action of ZOE and ZTE on HDAC1 and 2, we performed molecular docking simulations to identify which ZTE constituent could be responsible for HDAC1 inhibition. As the crystal structure of HDAC1 in complex with an inhibitor is not currently available, we used the crystal structure of HDAC2, in complex with vorinostat (SAHA) as a target. Among the 35 volatile constituents identified in ZOE by GC-MS, ZNG, the most abundant compound, was found to have a better binding affinity compared to other constituents, with a Vina binding energy of -7.1 kcal/mol. Moreover, its lipophilic nature matches the hydrophobic nature of HDAC2 binding site, allowing the establishment of van del Waals contacts with Hys33, Pro34, Asp104, Gly154, Phe155, Hys183, Phe210, Leu276, and Tyr308 (Figure 3.19A). Except from Tyr308, all these interactions are also established by vorinostat, used as a reference compound (Figure 3.19C). Differently from vorinostat, which possess a zinc-binding group, ZNG cannot coordinate the zinc ion present in the binding site oh HDAC1. However, non-zinc binding HDAC inhibitors has already been reported[88]. Indeed, the docking pose of ZNG is very similar to the binding mode of the ethyl ketone-based HDAC1, 2, and 3 selective inhibitor observed in the crystal structure (Figure 3.19D). To confirm the docking results, we evaluated the inhibitory activity of ZNG on HDAC1 *in vitro*, using an enzymatic assay. ZNG showed an IC_{50} of 2.3 μM (Figure 3.19B).

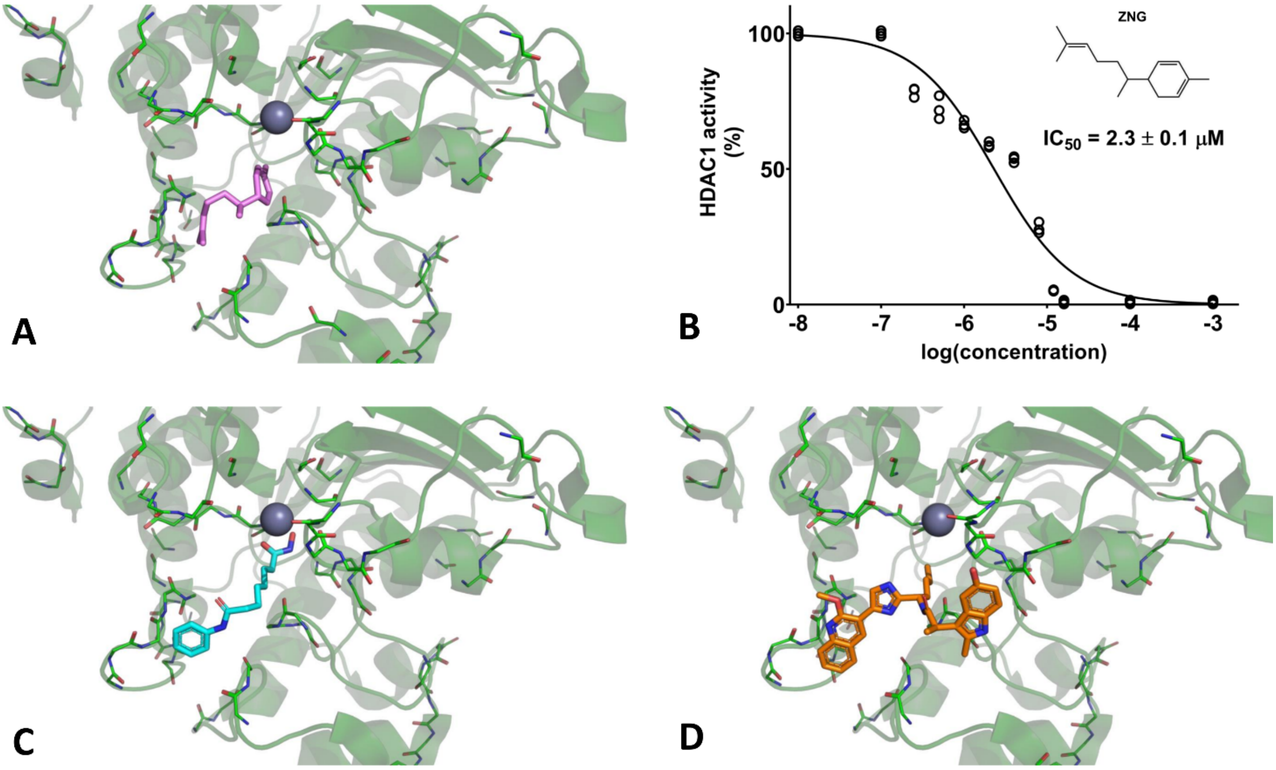

Figure 3.19 Docking pose of zingiberene (ZNG, violet) in the binding site of HDAC2 (A). In vitro HDAC1 inhibitory activity of ZNG (B). For comparison to the experimental binding mode of vorinostat (cyan), PDBID: 4LXZ (C), and the ethyl ketone-based non-zinc binding HDAC1, 2, and 3 inhibitor (orange), PDBID:6WBZ (D) are showed.

3.2.3.9. ZNG reduces HDAC1 protein expression in spinal cord of SNI mice and reduced NP symptoms

HDAC1 inhibitors have shown activity in reducing symptoms associated with NP[54]. To investigate whether the inhibitory activity of ZNG on HDAC1 activity observed *in vitro* may have an effect in reducing symptoms associated with NP, we treated SNI animals with 1mg kg^{-1} ZNG. The oral administration of ZNG reduced thermal hyperalgesia (Figure 3.20A) and mechanical allodynia (Figure 3.20B) in animals with neuropathy after 60 min from administration. We also compared the effect of ZNG on mechanical allodynia with that produced by LG325 and pregabalin (PREG), used as reference drug in NP. ZNG produced a similar effect, compared to the positive controls (Figure 3.20C). In the spinal cords of neuropathic animals, we observed an increase in the expression of HDAC1, which was completely reverted by ZNG, similarly to animals treated with SAHA (Figure 3.20D). HDAC1 can increase the expression of factors related to inflammation and microglial activation. For this reason, we evaluated the effect of ZNG and SAHA on the expression of NF-κBp65. In SNI animals we observed an increase in the expression of this transcription factor, which was completely counteracted by ZNG and SAHA (Figure 3.20E). The activation of NF-κBp65 induces an increase in the expression of pro-inflammatory cytokines. IL-1β is one of the major pro-inflammatory cytokines produced by microglia and is up-regulated in the spinal cord of animals with neuropathy. Consistently, SNI mice showed an increase in the expression of this protein, with ZNG and SAHA reducing this effect to values like the unoperated control (dashed line) (Figure 3.20F).

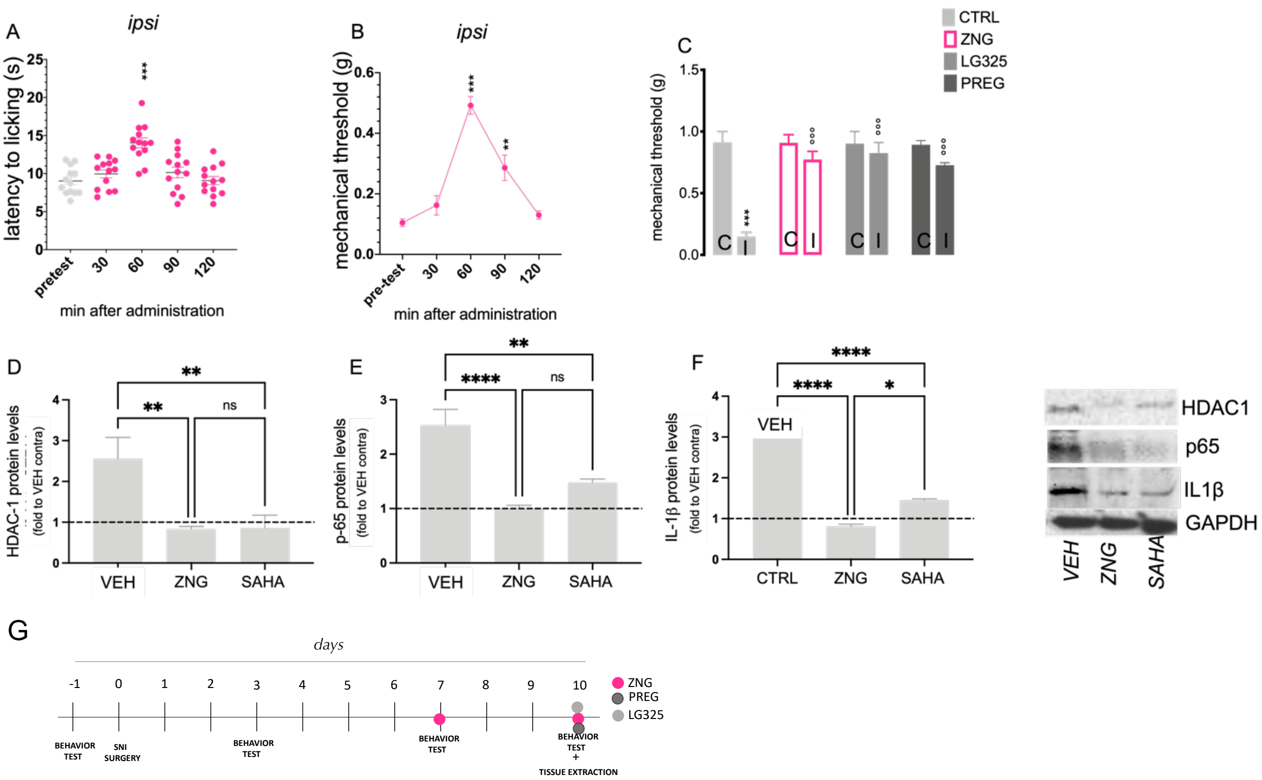

Figure 3.20 Effects of zingiberene (ZNG) on thermal hyperalgesia measured with (A) hot plate test and (B) mechanical allodynia measured with Von Frey filaments after 30, 60, 90, and 120 minutes from oral administration in SNI mice. (Two-way ANOVA ***p<0.001 **p<0.01). (C) Comparison of the effect obtained with ZNG, LG325, and pregabalin (PREG) on mechanical allodynia produced by the SNI model (Two-way ANOVA ***p<0.001 vs CTRL contra, °°°p<0.001 vs CTRL ipsi). (D) HDAC1, (E) p-65, and (F) IL1β protein expression on ipsilateral side of SNI mice spinal cord compared the contralateral side (black dashed line). (G) Experimental design. Experimental design. Experiments were performed on post-surgery day 7 and 10: SNI (n=8), ZNG (n=8), LG325 (n=8) PREGABALIN (n=8) (One-way ANOVA ****P<0.0001, **p<0.01, *p<0.05). Representative blots are also showed.

3.2.4. Cannabis essential oil (CEO) from non-psychotropic Cannabis sativa L. extract reduced symptoms associated to NP through microglial CB2 modulation and HDAC1 inhibition

3.2.4.1. Antinociceptive activity of K2 in an acute model of pain

The interest in *Cannabis sativa* L. phytocomplex as a medicinal tool is a recently emerging topic. Inflammatory diseases represent a promising field of application for cannabis and its preparations, as most of this pathologic condition relies on an inflammatory etiology[89].

Cannabis sativa L. is one of the medicinal plants most widely investigated in the scientific literature for its effect in numerous pharmacological applications and it has been shown to have numerous physiological activities: anti-inflammatory properties, psychoactive properties, antioxidant properties and metabolic effects; it is also used to treat chronic pain[90]. According to recent literature, it is now well-known that activation of the endocannabinoid system is crucial in the modulation of the inflammatory process: indeed, the stimulation of cannabinoid receptors (CBr) leads to the mobilization of several intracellular pathways that counteract the inflammatory cascade[91]. *Cannabis sativa* L. produces over 421 chemical compounds, including cannabinoids, terpenes, and phenolic compound. Research on hemp phytochemicals, as well as the widespread therapeutic use of its products, has been limited due to various reasons including the illegality of cultivation, its psychoactive activities and because of the variability of active components quality and quantity. Δ^9-tetrahydrocannabinol (THC), a partial agonist on CB1 receptor expressed on presynaptic neuronal cells, is the main psychoactive compound of *Cannabis sativa* L. It induces an imbalance between GABA and glutamate transmission. The pharmacodynamics of cannabidiol (CBD), a major investigated non-psychotropic constituent of cannabis, involved the endocannabinoid system and in particular the interaction with CBr, that are expressed mostly in central and peripheral immune system[92]. The role of cannabidiol as an inverse agonist at CBr have been extensively demonstrated. CBD possesses antioxidant, anti-inflammatory and neuroprotective properties, and can act through direct or indirect activation of a plethora of metabotropic and nuclear receptors and ion channels[91]. CBD reduced the activation of cyclooxygenase (COX), iNOS, and TNF-α[93]. CBD modulates the activity of orphan G protein-coupled receptors (GPCRs), indeed antagonizing GPR55[94]. In the same way, other components of Cannabis phytocomplex could modulate the immune response, even if few knowledge is available. β-caryophillene, the most important component of the terpenes fraction in cannabis, is a full agonist at CBr, and its biological activity on inflammation process is still unknown[95]. Caryophyllene, at micromolar concentrations, attenuated the activation of the NF-kB pathway *in vitro*, leading to a reduction of IL-1β, TNF-α, and IL-6 as well as to the inhibition of ROS production in murine microglial cells, following hypoxic exposure[96]. These results have been also confirmed *in vivo* by administering caryophyllene (50 mg kg^{-1}) in a rotenone-induced model of Parkinson's disease in rats. Caryophyllene reduced IL-1β, IL-6, TNF-α, and iNOS expression in the midbrain tissue[97].

These reasons led us to deeply investigate the role of an innovative extract of non-psychotropic *Cannabis sativa* L. on inflammatory process, to evaluate the synergism between the constituents of the extract. For this reason, there is now an attempt to optimize cannabis-derived extracts by reducing the psychoactive component as much as possible. In this work, we decided to investigate the possible analgesic effect of a standardized non-psychotropic extract of *Cannabis sativa* L. enriched in terpenes (K2). Our aim is to outline the pharmacological profile of a standardized non-psychotropic extract lacking Δ^9-THC. To do this, we will compare the activity of K2 with an extract containing only cannabinoids (K1) and the isolated terpene component (CEO). To assess the analgesic effect of K2 extract in an acute model of pain, the hot plate test was used: this evaluates the animal's response time (licking latency) to a hot thermal stimulus (52 ºC). Figure 3.21A shows the dose-response curve of the oral administration of K2. The starting dose of 10 mg kg^{-1} did not induce any analgesic activity. Indeed, the latency time was comparable to that of the sham group (SH). A non-significant trend was observed at 20 mg kg^{-1}. The dose of 25 mg kg^{-1} showed the best efficacy, with animals remaining for longer time on the hot plate. A bell-shaped curve was obtained, indeed at doses of 50 mg kg^{-1} and 100 mg kg^{-1}, the latency time is comparable to that of the sham group. The time course (Figure 3.21B) of K2 25 mg kg^{-1} measured 30, 45, 60, 90, and 120 min after oral administration was also performed. The peak of the effect was registered at 60 min and rapidly decreased 90 min after the administration. The analgesic effect of K2 was compared with that of an extract without the terpenes component (K1), at the active dose of 25 mg kg^{-1} 60 min after oral administration. K2 showed a greater analgesic activity, compared to K1, which did not possess a significant effect compared to the untreated group (Figure 3.21C).

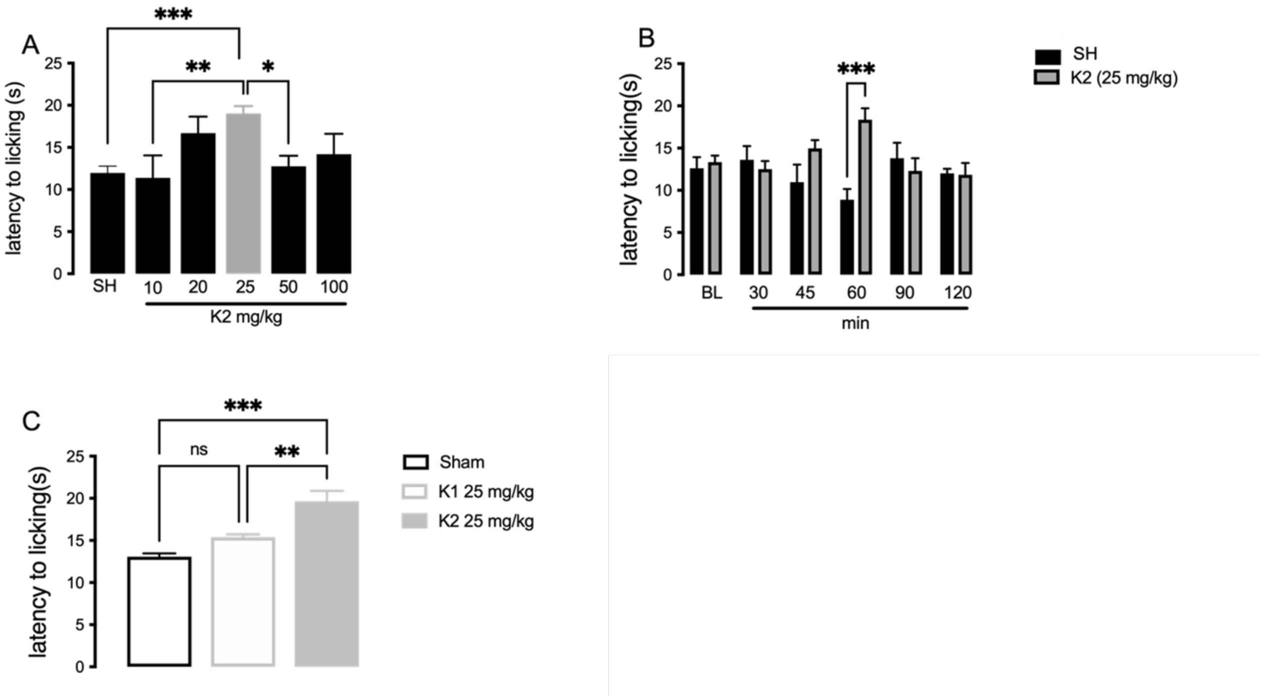

Figure 3.21 Antinociceptive profile of K2 against an acute thermal stimulus (hot plate test). (A) Dose response curve (10-100 mg kg^{-1}) of K2 showed that 25 mg kg^{-1} increased the pain threshold 60 min after the oral administration. (B) Time-course of the active dose at 30, 45, 60, 90, and 120 min (Two-way ANOVA, ***p<0.001). (C) Comparison between K2 (25 mg kg^{-1}) and K1 (25 mg kg^{-1}) after an acute thermal stimulus. (One-way ANOVA, ***p<0.001, **p<0.01).

3.2.4.2. Evaluation of the analgesic effect of K1 and K2 in an animal model of peripheral NP (SNI)

The activity of K1 and K2 was investigated in a NP model, the SNI, using the Von Frey test filaments and hot plate test 10 days after surgery. This model reproduces the most important symptoms (mechanical and thermal allodynia on the paw with the nerve ligation) associated to NP starting from 3 days after surgery.

The time course of the analgesic action of K1, shown in figure 3.22A, indicates that the dose of 10 mg kg^{-1} did not have any effect, while the dose of 25 mg kg^{-1} slightly reduced the mechanical allodynia and this effect disappeared with 50 mg kg^{-1}. The peak of the effect was reached 75 min after administration, decreased at 90 min, and disappeared at 120 min (Figure 3.22B). Similarly, the dose-response curve of the analgesic action of K2, reported in Figure 3.22C, indicated that the dose of 25 mg kg^{-1} totally prevented mechanical allodynia, while 10 and 50 mg kg^{-1} did not show relevant effects. The analgesic effect appears as early as 60 min after administration with a peak at 75 min, similarly to K1 (Figure 3.22D).

Figure 3.22E shows the comparison of the effect of K1 and K2 at their active dose (25 mg kg^{-1}) on thermal hyperalgesia, compared to the sham group. The latency to licking was reduced in VEH SNI group, compared the sham group, and both K1 and K2 reverted this hyperalgesia reporting value similar to that of the sham group. The essential oil (CEO) was extracted from K2. To better understand if the CEO could contribute to the final effect of K2 extract, we tested it at the dose of 0.45 mg kg^{-1}, which correspond to the concentration present in the active dose of K2, in animals with neuropathy. The effect of CEO became significant 60 min after oral administration with a peak of activity at 75 min, that disappeared after 120 min (Figure 3.22F).

The comparison between the three treatments demonstrated that the activity of CEO is comparable to that of K1, while K2 was more potent, with an effect similar to that produced by pregabalin (PREG), used as reference drug (Figure 3.22G). These data suggests that the analgesic activity of the terpenes is similarly crucial to that of cannabinoids for the final activity of the K2 highlighting a strong synergism between the two fractions of the extract.

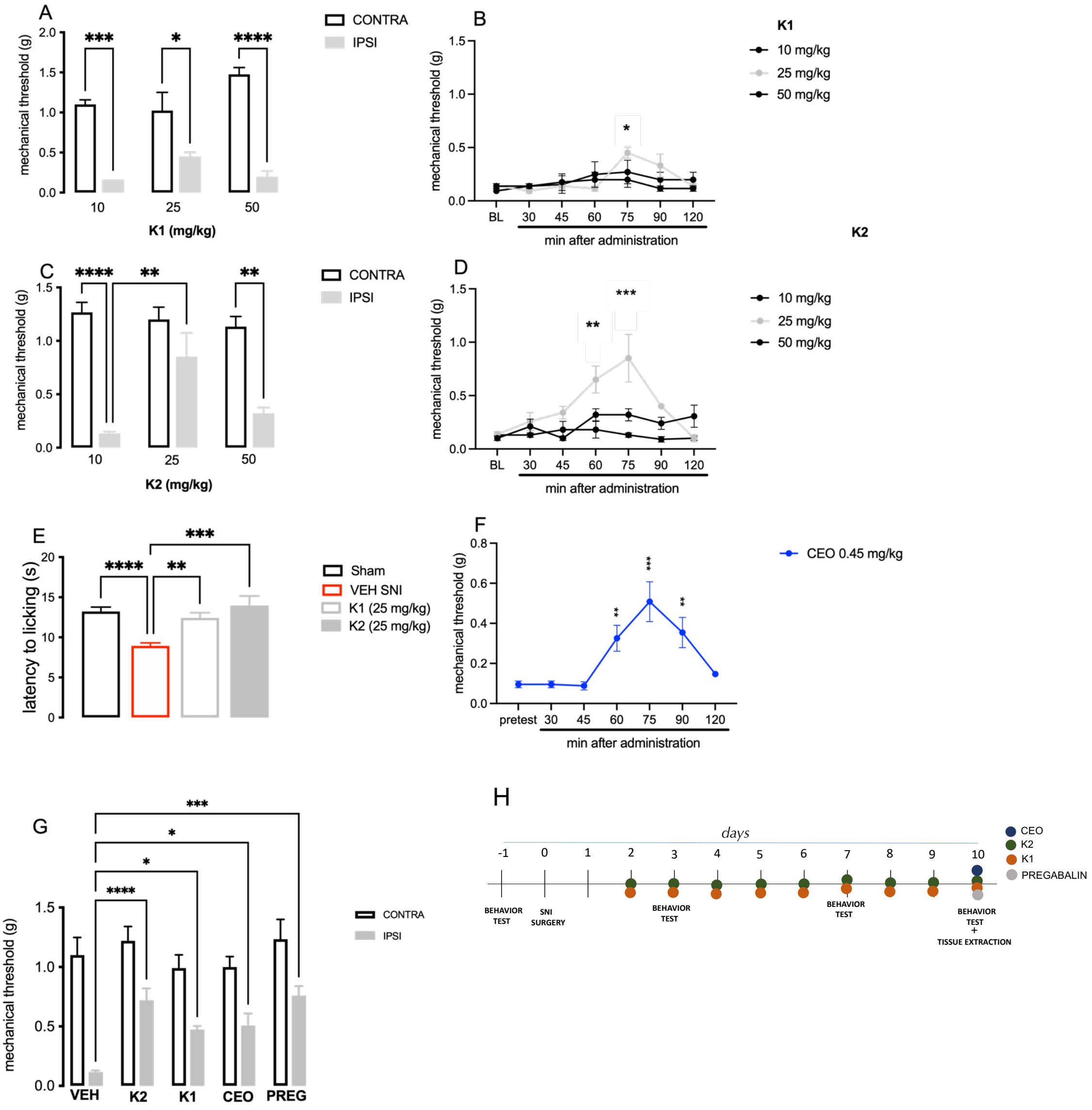

Figure 3.22 The anti-nociceptive activity of Cannabis sativa L. extract without essential oil (K1), Cannabis sativa L. extract with essential oil (K2) and cannabis essential oil (CEO) were investigated in the presence of a condition of persistent pain, by using a model of NP (SNI model) in mice. SNI mice showed a marked mechanical allodynia measured with Von Frey filaments. Dose-response curve shows that (A) K1 and (C) K2 at the dose of 25 mg kg^{-1} showed the maximum effect. Time course shows that the peak of the effect was at 75 min after oral administration for (B) K1 and (D) K2. (E) Hot plate test was used for detecting effect on thermal hyperalgesia induced by K1 and K2 at the dose of 25 mg kg^{-1}. (F) Time course of CEO 0.45 mg kg^{-1} with Von Frey filaments. (G) Comparison of the effect of K1, K2, CEO, and pregabalin (PREG, reference drug) on mechanical allodynia with Von Frey filaments. (I) Experimental procedure. Experiments were performed on post-surgery day 7 and 10: SNI (n=8), K2 (n=8), K1 (n=8), PREGABALIN (n=8). (Two-way ANOVA, post-hoc Tukey ***p<0.001 **p<0.01 *p<0.05).

3.2.4.3. Effects of K2 on mechanical allodynia are prevented by CB2 antagonist

To investigate the possible involvement of cannabinoid receptors in the final analgesic effect of K1, K2, and CEO, we compared the effect on mechanical allodynia in the absence or presence of AM251, a CB1 antagonist and AM630, a CB2 inverse agonist. Figure 3A shows that AM630 antagonized the effect of K2, reducing its analgesic effect by approximately 3-fold, reaching the base line (BL) level of neuropathic controls (dashed line in the graph); the CB1 antagonist AM251 did not modify the efficacy of K2 (Figure 3.23A). Contrarily to K2, the effect of K1 was not reduced by the presence of the two antagonists (Figure 3.23B). Similarly, to K2, instead, AM630 antagonized the effect of CEO, reducing its analgesic effect by approximately 4-fold, whereas AM251 had no effect on the efficacy of CEO (Fig 3.23C). Taken together, these results suggest that K1 had a mechanism of action that is totally independent from CB receptor activation, while K2 and CEO act through the modulation of CB2 receptor but not of CB1.

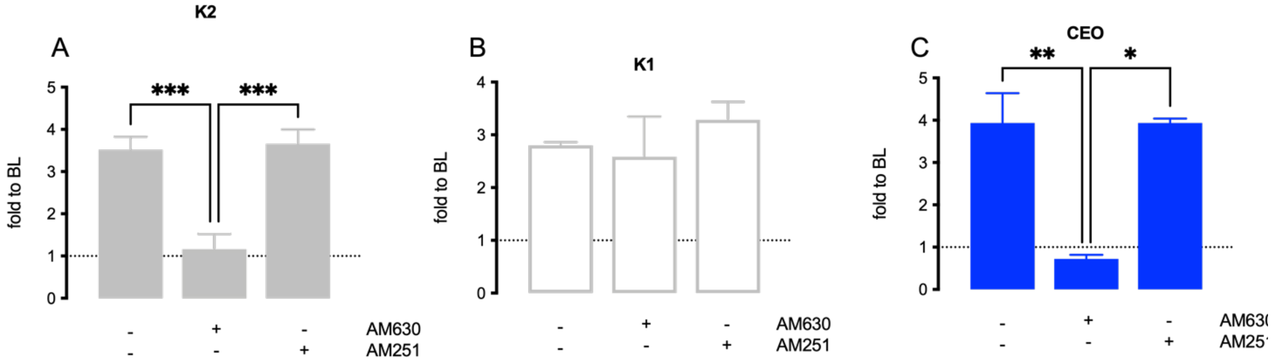

Figure 3.23 Involvement of cannabinoid receptors in final effect of the treatments. The co-administration of AM630 (CB2 inverse agonist) counteracted the effect on allodynia of (A) K2 and (C) CEO in SNI mice but did not reduce the efficacy of (B) K1. AM251 (CB1 antagonist) did not affect the efficacy of any treatment. (One-way ANOVA, Tukey's multiple comparison Test ***p<0.001, **p<0.01 *p<0.05)

3.2.4.4. K2 did not alter locomotor activity and cognitive function

The rotarod test allows to assess coordination and motor function in mice, which is useful to evaluate possible side effects of K2. These conditions can be identified based on the ability of the treated animals to remain balanced on a rotating rod, on which, under normal conditions, they would be able to move. The number of times that the K2-treated animals fell off the rotating rod in 5 min was the same of the sham group (Figure 3.24A). Therefore, it is possible to exclude any impairment of motor coordination and motor function in mice treated with the extract.

With the hole board it was possible to exclude possible locomotor changes induced by the extract or the induction of a sedative effect. Spontaneous mobility was measured by the number of movements made by the animal (Figure 3.24B), while sedation was verified by counting the number of holes in which the animal inserted its head (Figure 3.24C). Animals treated with K2 showed no alterations compared to SH in either of these parameters. In the open field test, animals treated with K2 showed a higher tendency to stay in the center of the box (Figure 3.24D), thus also suggesting an anxiolytic effect of the extract itself.

From these tests it is possible to define that the most active dose of K2 did not compromise the motor and exploratory capacities of the treated animals, but on the contrary reduces the stress levels.

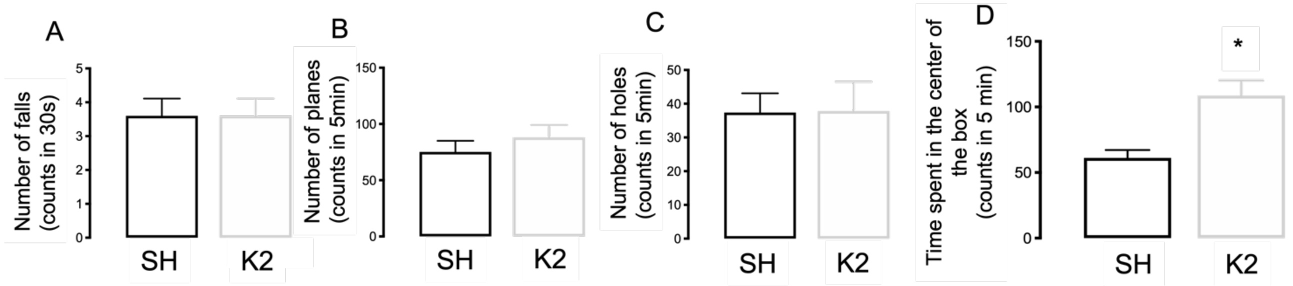

Figure 3.24 Lack of impairment of (A) motor coordination (rotarod test), (B) spontaneous mobility (Hole Board Test), and (C) exploratory activity (Hole Board Test) of K2 at the peak of the effect. (D) K2 did not induce variation on cognitive activity.

3.2.4.5. CB2 expression is increased in the spinal cord of SNI mice and colocalized with microglia marker

As K2 activity was found to be closely linked to CB2 activity, we investigated CB2 expression and localization in animals with neuropathy.

An increase in the expression of CB2 receptors was observed by western blotting in the ipsilateral side of the spinal cord, compared to the contralateral side (Figure 3.25A). These results were then confirmed by immunofluorescence, where an increase in the fluorescence intensity related to CB2 (red,) was observed in the ipsilateral side of SNI mice, together with an increase of the expression of CD11b (a marker of microglial activation; green) (Figure 3.25B, C). The colocalization analysis with Mander's Coefficient (MOC) reported an index of 0.98 ± 0.05 between CD11b and CB2 marker, which correspond to a maximum colocalization between the two targets (Figure 3.25D).

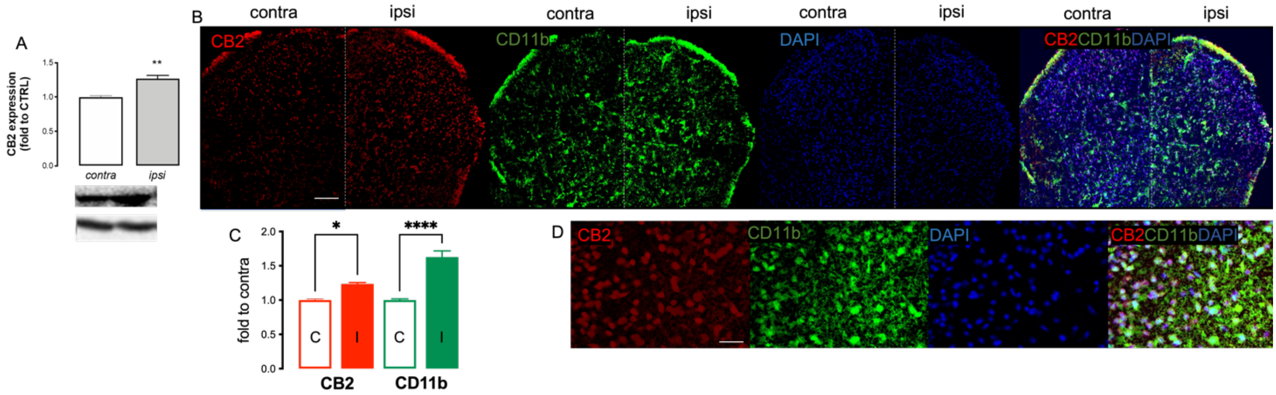

Figure 3.25 CB2 expression and localization in spinal cord of SNI mice. (A) CB2 expression in the contralateral and ipsilateral side of the spinal cord of SNI mice (One-way ANOVA **p<0.01 vs contra). (B) Representative images of the immunofluorescence assay on the spinal cord of SNI mice (CB2: red, CD11b: green, and DAPI: blue) (scale bar 100µm). (C) Quantitative analysis of immunofluorescence images. (D) Higher magnification (40X) of ipsilateral side of the spinal cord of SNI mice (Scale bar 20 µm).

3.2.4.6. Effect of K2 on MAPKs phosphorylation and on markers of microglia activation

A significant increase in the expression of p-ERK44/42 (Figure 3.26A), p-P38 (Figure 3.26B) and p-JNK1 (Figure 3.26C) was observed in the spinal cords of control mice with neuropathy (VEH) 10 days after surgery, compared to the control group (red dashed line).

K2 reduced p-ERK (Figure 3.26A) to lower levels than in control animals (VEH), reaching a level similar to that of control animals without neuropathy, and the presence of the CB2 antagonist totally counteracts this effect. A similar activity was observed on the levels of p-p38 (Figure 3.26B). K2 is also able to reduce the activation of p-JNK1 in neuropathic mice, but in contrast to other MAPKs, AM630 was not able to block this effect (Figure 3.26C).

Neuroinflammation is an important target of NP, in particular microglial activation is one of the main mechanisms involved in pain. We therefore investigated the possible effect of K2 on the main markers of microglial activation: HDAC1 (Figure 3.26D), p-65(Figure 3.26E) and NOS2 (Figure 3.26F), which are significantly increased in the spinal cords of animals with neuropathy.

K2 administration strongly reduced the expression of the enzyme HDAC1 (Figure 3.26D), p-p65 (Figure 3.26E), and NOS2 (Figure 3.26F) in animals with chronic SNI pain, compared to neuropathic animals (VEH). Treatment with the CB2 antagonist AM630 completely blocked the activity of K2 and significantly increased the expression of these neuroinflammatory markers.

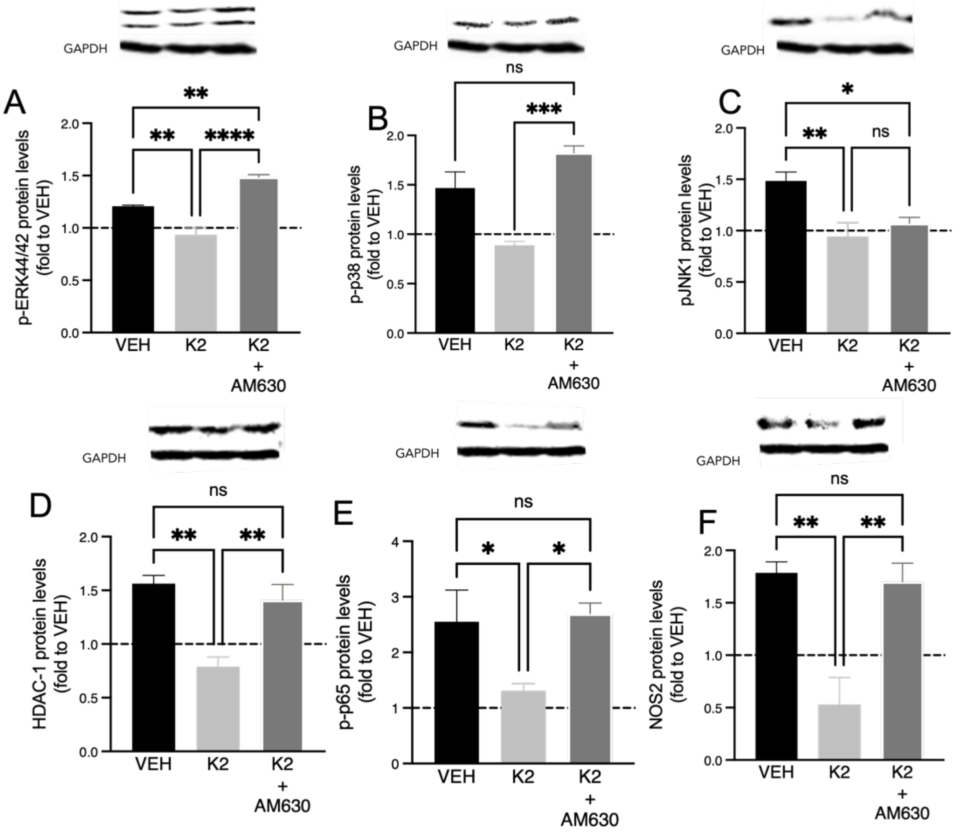

Figure 3.26 Effect of K2 and K2+AM630 on MAPKs phosphorylation in the spinal cord of SNI mice: (A) pERK44/42, (B) pp38, and (C) pJNK1, compared to the untreated SNI control (VEH) group. Effect of K2 and K2+AM630 on (D)

HDAC1, (E) p-p65, and (F) NOS2 in the spinal cord tissue of SNI mice (One-way ANOVA ***p<0.001, **p<0.01, *p<0.05). Representative blots are also showed.

3.2.4.7. Anti-inflammatory effects of K1, K2, CEO, CAR, and CBD in a microglia model of neuroinflammation

LPS reduced IKBα (Figure 3.27A) and up-regulated HDAC1 (Figure 3.27B) protein expression in BV2 cells, after 24 h of stimulation. Similarly, to cannabidiol (CBD), K1 reverted the effect induced by LPS on IKBα in BV2 but had no effect on HDAC1. Differently, K2 was able to counteract the effect of LPS on IKBα and HDAC1, likewise CEO and β-caryophyllene (CAR). All the treatments increased the levels of IL-10, which represents an important anti-inflammatory marker (Figure 3.27C).

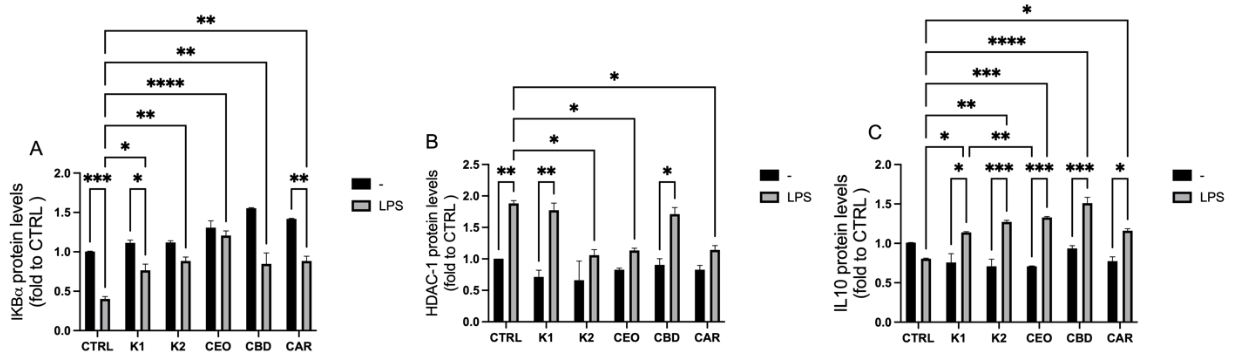

Figure 3.27 Effects of *Cannabis sativa* L. extract without essential oil (K1), *Cannabis sativa* L. extract with essential oil (K2), cannabis essential oil (CEO), cannabidiol (CBD) and ß-caryophyllene (CAR) on (A) IKBα and (B) HDAC1 in unstimulated and LPS-stimulated BV2. (C) Dosage of anti-inflammatory microglia marker IL-10in LPS-stimulated BV2 treated with K1, K2, CEO, CBD, and CAR. (Two-way ANOVA ***p<0.001, **p<0.01 and *p<0.05) Representative blot are also showed.

3.3. Discussion

HDACs control the expression of a plethora of genes involved in pain perception and they are an emerging target for the control of algesia. Recently, we investigated the role of histone deacetylation in a model of NP showing an increase of HDAC1 protein expression in the ipsilateral side of the spinal cord in animal models of mononeuropathy. It has been reported that HDACs could regulate the inflammatory response of glial cells and an anti-inflammatory activity of HDACi via the suppression of microglia-mediated neuroinflammation has been described[98]. Consistently with previous research, we observed that spinal cord sections of SNI mice expressed HDAC1 in neurons, astrocytes, and microglia, with a prominent expression in microglial cells. Increased expression of activated microglia markers was detected in the ipsilateral side of spinal cord sections and SAHA treatment abolished the SNI-induced microglia activation.

Class I HDACi have been reported to cause a reduction of neuroinflammation by modulation of pro-inflammatory cytokine expression in LPS-stimulated BV2 cells[23]. An important cellular event involved in the pro-inflammatory response is the activation of NF-κBp65 and the subsequent transcription of a program of pro-inflammatory genes[87]. Several findings indicate that the inactivation of NF-κBp65 pathways is linked to the repression of HDAC1 levels[70]. In addition, the activation of NF-κBp65 pathway contributes to the onset of neuropathic symptoms. Indeed, the silencing of this pathway is a possible target to control NP in several animal models[99].

We evaluated the efficacy of epigenetic inhibitors following intranasal delivery and we compared the effects with those obtained after intrathecal administration. Comparable efficacy in improving the nociceptive phenotype and in modulating the expression of target proteins was observed. I.n. administration has aroused wide interest in the past few years. I.n. drug delivery is simple and non-invasive, allowing self-medication in patients, and it may be particularly beneficial for CNS-acting drugs since it facilitates a rapid achievement of therapeutic drug concentrations in the brain and cerebrospinal fluid. The i.n. route can transport drugs directly to the brain, but it also allows delivery to the spinal cord of macromolecules[100]. I.n. delivery has been previously used for delivery of small molecules with poor blood brain barrier permeability, peptides or proteins, with minor clinical side effects[101] and there are currently more than 600 clinical trials under way in the USA alone, in which i.n. administration in used. Our results indicate that i.n. administration of SAHA or i-BET762 attenuates pain hypersensitivity caused by peripheral nerve trauma. The combination therapy of partially active doses of SAHA and i-BET762 was more successful in pain relief and in the control of spinal neuroinflammation, compared to monotherapy. This was also observed using the experimental dual-acting molecule SUM52, which confirmed the effects observed by co-administration of the two inhibitors SAHA and i-BET762. Its mechanism of action needs more investigation, so further studies will be required to confirm its activity at the microglial level. Although its colocalization at the microglial level appears to be promising for a mechanism of action mediated primarily by this cell type. Present findings also identify a non-invasive delivery system for epigenetic inhibitors to increase the potential translation to clinics of this multi-pharmacological approach. Taking into consideration that SAHA and i-BET762 are under clinical trials for cancer therapy or already approved, it seems that the use of HDAC and BET inhibitors in combination might represent a proper and safe strategy for the control of NP.

At the same time, we have considered bioactive molecules isolated from medicinal plants from which it is possible to extract molecules with inhibitory activity on HDACs with a certain degree of specificity. The common feature we noticed between the *Zingiber officinale* Roscoe extract and the non-psychotropic *Cannabis sativa* L extract is that only the terpenes component can reduce the expression and activity of HDAC1 at a confirmed microglial level *in vivo* and *in vitro*.

This terpenoid fraction largely decreased HDAC1 expression, NF-κB activation and proinflammatory cytokines release. Terpenes, also known as isoprenoids, are the largest and most diverse group of naturally occurring compounds that are mostly found in plants but larger classes of terpenes such as sterols and squalene can be found in animals. They are responsible for the fragrance, taste, and pigment of plants and they could be classified in monoterpenes, sesquiterpenes, diterpenes and triterpenes[102]. They possessed several pharmacological activities, but this is the first time that this terpenoids showed a selective activity on HDAC1 and a specify pharmacological perspectives.

3.4. Conclusion

In conclusion, targeting HDAC1 could represent an interesting pharmacological approach in NP patients. Indeed, the reduction of HDAC-1 expression, through the inhibition of NF-κB activation and cytokines release, promotes the attenuation of microglia pro-inflammatory phenotype activation. The final aim of this work is to find new therapeutic candidates with specific epigenetic mechanisms for different pathologies, fundamental for the realization of increasingly specific and personalized pharmacological therapies.

Chapter 4

Targeting the RNA-Binding Protein HuR as a novel therapeutic approach for central and peripheral neuropathies trough the reduction of neuroinflammation and promoting myelinization.

4.1. Introduction

NP caused demyelination, which is the loss or damage of the myelin sheath that lines the nerve fibers, causing impaired nerve transmission. Frequently at the basis of demyelination there is an inflammatory and/or immune process[103]. Post-transcriptional processing of gene expression and RNA stabilization of inflammatory proteins play a fundamental role in the regulation of these processes. RNA is the link between DNA and proteins and contains all the information recovered from DNA to regulate cellular functions and promote cell survival. The importance of precise co- and post-transcriptional processing of RNA in the regulation of gene expression has increasingly emerged. These are complex and controlled processes that lead to mRNA maturation, which require the intervention and interaction of various components, including RNA Binding Proteins (RBPs)[104]. RPBs are a class of proteins that bind single or double chain RNA, with different affinities and selectivity, thus regulating the various functions of RNA and the fate of the cells themselves[105]. RBPs accompany and protect RNA from transcription in pre-mRNA in the nucleus to nuclear export up to translation into the cytoplasm)[106]. RBPs interact with RNA by binding to sequences or structural motifs through a restricted and structurally well-defined series of RNA binding domains (RBD)[107]. Through various *in vitro* and *in vivo* studies, more than 1000 RBPs with different biological functions have been identified in humans and mice[108]. They are involved in the coordination and stabilization of complexes with proteins, in the processing and maturation of mRNA, in alternative splicing and splicing, in polyadenylation, in transport and localization within the cell, stabilization, silencing of mRNA mature, and in its degradation[109,110]. Therefore, given the numerous processes in which RBPs are involved, a mutation or alteration of their functions can lead to the development of diseases[39], such as neuro-degenerative pathologies[111], cardiovascular disease[112], tumors[113], and immune system dysregulation[114]. In the nervous system an important family of RBPs that played an important role in the fate of new transcribed mRNA are the ELAV/Hu protein family[115], which consist of four members. Three of them are HuB (erlB), HuC (erlC) and HuD (erlD), are specifically expressed in the neurons[116]. The fourth member HuR/HuA (elrA) is expressed ubiquitously in the organism but predominantly localize in the nucleus[117]. The biological function of ELAV RBPs has been identified in their ability to post-transcriptionally control gene expression by cytoplasmic stabilization and/or enhancement of translation of their mRNA targets. ELAV proteins bind ARE-containing transcripts, which are usually present on the mRNA of proteins such as cytokines, growth factors, and other proteins involved in neuronal differentiation and maintenance[118]. Given their nature of RBPs, ELAVs influence the fate of many mRNAs, modulating simultaneously many different physiological functions: nELAVs (HuD, HuB, HuC) accelerate neuronal differentiation and axonal outgrowth, and modulate neuronal integrity[119], while HuR promotes inflammation and proper functioning of the immune system[120]. HuR, in fact, represents an important regulator of inflammatory and immune processes, above all it is involved in the expression of pro-inflammatory proteins and in the action of cells involved in neuroinflammatory processes, such as microglia. Therefore, a regulation of HuR expression could modulate inflammation and the immune response[120]. Matsye and co-authors (2017) demonstrated the involvement of HuR in the molecular and cellular phenotype of activated microglia[121]. Thus, the knockdown of HuR in microglial cells led to an attenuation of the expression of factors in inflammation, chemotaxis, and cell migration, which is not so much related to a decrease in mRNA stability. On the contrary, this has been linked to the suppression of the promoter activity of NF-κB transcription. It has also been shown that the involvement of HuR in the translation processes, in some cases, may be independent of the stabilizing effect on mRNA.

Because of the complex pathophysiology, even today there is no completely effective treatment for NP; there is no single therapy. In fact, therapy is often unsatisfactory due to poor efficacy and side effects. Furthermore, as has already been mentioned, treatments against NP do not focus on resolving the cause of the pain, but rather on the symptomatology. So, understanding the causal processes of NP (in this case demyelination) and a modulation of them could be an effective therapeutic strategy, allow greater symptom control and improved quality of life[17]. In those diseases characterized by chronic demyelination, where resolution of the cause may also induce a slowing of the disease, such as multiple sclerosis. Inflammation plays a central role in MS; indeed, pro-inflammatory microglia are associated with the demyelization process through the release of cytokines and other mediators of inflammation [10]. MS progresses in different stages, beginning with a cascade of inflammation. The pivotal spark to initiate this cascade seems to be the migration of Th17 into the CNS across the blood–brain barrier (BBB) through the disrupted tight junctions. Consequently, glial cells are activated in the spinal cord leading to excessive release of pro-inflammatory cytokines[122]. So, targeting microglia could represent an interesting target for the development of novel therapeutical approach. Consequently, glial cells are activated in the spinal cord leading to excessive release of pro-inflammatory cytokines. Experimental evidence indicates that microglia are key players in MS pathology[123]. Activated microglia abolishment represses the development of experimental autoimmune encephalomyelitis (EAE), an animal model of MS, by inhibiting the infiltration of inflammatory immune cells[123]. Additionally, *in vivo* imaging revealed that perivascular microglia mediate axonal damage in the spinal cord of EAE mice[124] and activated microglia are abundantly observed in the inflammatory lesions of MS patients[125]. Among the RBP family, HuR is involved in the maintenance of inflammation and in the proper functioning of the immune system by positively regulating the stability of many target mRNAs, such as proinflammatory cytokines[126], and recent findings described the role of HuR in defining the phenotype of activated microglia in amyotrophic lateral sclerosis[127]. In the EAE model the repeated intrathecal administration of anti-HuR antisense oligonucleotide (ASO) reduced the main symptoms reproduced by the model, which reproduce the main clinical signs in MS patients[21]. Based on this evidence, HuR might represent a key regulator also in MS.

The main aim of this work was to target the RNA binding protein HuR to reduce symptoms and to promote myelination associated to NP, in the attempt to find a therapy that not only control the symptoms but also slow down the progression of the disease.

To evaluate this hypothesis, we structured this work into three distinct steps:

1) The role of HuR in NP was investigated in a mouse model of peripheral mononeuropathy, the spared nerve injury (SNI). To this aim, an antisense oligonucleotide (ASO) knockdown of HuR gene expression was used. However, ASOs poorly cross the BBB and require invasive delivery routes. Intranasal (i.n.) delivery is a practical, safe, and effective delivery of therapeutic agents targeting towards the CNS106. To achieve CNS penetration of anti-HuR ASO through a noninvasive delivery method, i.n. administration was used, and the effects produced were compared to those obtained by intrathecal (i.t.) administration.

2) We investigated the effect produced by HuR silencing in a mouse model of relapsing–remitting EAE related (PLP) to progression and severity of EAE-related symptoms. Many reports suggest that microglia play detrimental roles in MS pathology. However, in addition to the proinflammatory phenotype, to dampen neuroinflammation, microglia can adopt an anti-inflammatory phenotype associated with resolving inflammation and tissue repair[128]. Increasing evidence illustrated a pro-remyelination activity of microglia[103]. Regulating transition from the proinflammatory to the anti-inflammatory microglia phenotype might restore homeostasis and improve functional outcomes in MS patients. The role of HuR to influence microglia polarization towards the anti-inflammatory phenotype was also investigated.

3) We investigated the modulation of the symptoms associated with NP and, at the same time, the promotion of neuron regeneration and myelin repair, by HuR silencing. We studied these effects in the SNI model and in the MOG-EAE model of chronic progressive multiple sclerosis (MS) causing a persistent and chronical demyelination. To determine a correlation between HuD and HuR, we directly compared the effect observed in these two models after i.n. administration of antisense oligonucleotide against these ELAVs. Indeed HuD, the most studied member of the nELAVs, showed a role in promoting neuroprotection through the regulation of BDNF and GAP43 was reported[29]. HuD target mRNAs are associated with several neurological disorders, including neurodegenerative disorders such as Alzheimer's, Huntington's, and Parkinson's diseases, mood disorders, epilepsy, schizophrenia, and mental retardation conditions, such as Rett syndrome[115].

4.2. Results

4.2.1 *Intranasal delivery of an antisense oligonucleotide to the RNA-binding protein HuR relieves nerve injury-induced NP, reducing neuroinflammation.*

4.2.1.1 Intranasal antisense oligonucleotide effect on spinal HuR protein expression

In this first step investigated posttranscriptional mechanisms in an animal model of trauma-induced NP, the SNI model, to find novel potential targets for NP treatment.

To investigate into the role of the HuR in injury-induced neuropathy, a knockdown of the HuR protein was obtained by means of an antisense strategy. The utility of ODN-based silencing strategies is compromised by the difficulty to deliver ODNs to the CNS because of their poor capability to cross biological barriers. To avoid invasive delivery routes of ASO administration, we tested the efficacy of ASO i.n. delivery in comparison with i.t. delivery. The efficacy of the antisense treatment schedule was confirmed in the spinal cord cell lysate of naive mice. A drastic reduction of HuR levels was detected after i.t. or i.n. anti-HuR ASO administration, showing a sequence-specific knockdown of the HuR protein produced by the antisense administration. The HuR protein knockdown produced by i.n. ASO was of magnitude comparable to that observed after i.t. ASO (Figure 4.1A). The expression of HuB, HuC, and HuD protein in spinal cord samples from animals previously treated with anti-HuR ASO has been quantified, and no variation of the neuronal ELAV content has been produced by anti-HuR ASO (Figure 4.1B).

4.2.1.2. Increased expression of HuR in spared nerve injury mice

The expression of HuR protein level within the spinal cord was detected 7 days after surgery (Figure 1A) in coincidence with established pain hypersensitivity. Immunofluorescence photo- micrographs of spinal cord sections of SNI mice (Figure 4.1C) and quantification analysis (Figure 4.1D) showed an increase of HuR immunostaining in the ipsilateral side in comparison with the contralateral side, further confirmed by quantification analysis of Western blotting experiments (Figure 4.1E). Anti-HuR ASO reduced the HuR expression in the contralateral side of spinal cord samples from SNI mice and counteracted the HuR increase in the ipsilateral side. Effects of similar intensity were detected after both i.t. and i.n. administration (Figure 4.1E), and the correction of HuR levels represented a biomarker of i.n. ASO activity within the spinal cord. A degenerate oligonucleotide (dODN) of the same length and chemical structure was used as control ODN. The effects of dODN were compared to those produced by the vehicle (DOTAP 13 μM) and saline. No difference was observed among control groups.

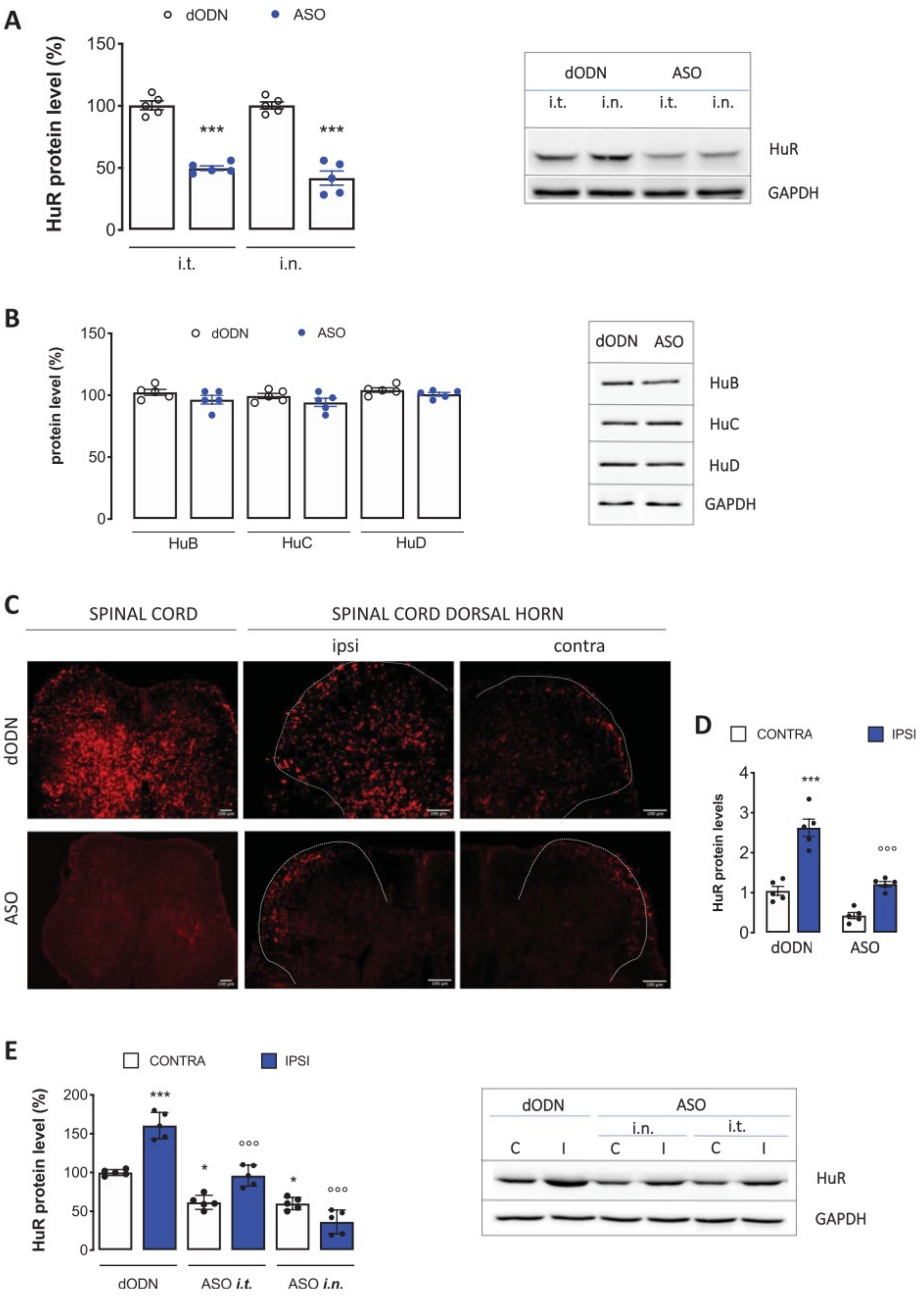

Figure 4.1. Pattern of HuR protein expression in the spinal cord of SNI mice. (A) Anti-HuR ASO drastically decreased the HuR protein content in spinal cord lysates of naive mice after intrathecal (i.t.) or intranasal (i.n.) administration. *P <0.05 vs dODN treated group. (B) No variation in the expression of the neuronal ELAV (HuB, HuC, and HuD) in spinal cord samples from anti-HuR ASO-treated mice. (C) Fluorescence microscopy images showed the increased expression of HuR within the ipsilateral side of spinal cord dorsal horn in SNI mice and the decrease of HuR expression after anti-HuR ASO treatment. Higher magnification of the ipsilateral (ipsi) and contralateral (contra) sides are reported. Scale bars 5 100 mm. (D) Quantification analysis. (E) HuR silencing prevented the HuR upregulation induced by SNI surgery after i.t or i.n. injection. A dODN was used as control ODN treatment. *p< 0.05 vs dODN treated group contra; °p <0.05 vs dODN treated group ipsi. ASO, antisense oligonucleotide; ELAV, embryonic lethal abnormal vision; SNI, spared nerve injury.

4.2.1.3. HuR silencing attenuated nociceptive behaviour in spared nerve injury mice

Spared nerve injury mice developed mechanical allodynia in the ipsilateral side starting from 3 days after surgery that persisted up to day 21. No mechanical hypersensitivity was observed in the contralateral side (Figure 4.2A). To evaluate the involvement of HuR protein overexpression in the SNI-induced NP, the effect produced by anti-HuR administration on nociceptive behaviour was evaluated in the mouse von Frey test (Figure 4.2B). I.n. repeated treatment with anti-HuR ASO significantly reduced mechanical allodynia in the ipsilateral side without any change in the contralateral side with respect to values before treatment.

This effect was detected 7 and 14 days after surgery (Figure 4.2B). The antiallodynic effect of anti-HuR was also detected after i.t. administration, with an effect of similar magnitude to that produced by i.n. treatment. Consistent with i.n. results, i.t. anti- HuR produced no effect on the contralateral side (Figure 4.2C).

The efficacy of anti-HuR treatment in modulating NP was also detected against thermal allodynia. Spared nerve injury mice showed a significant decrease of the thermal pain threshold 3 days after surgery and this pain hypersensitivity remained unmodified up to day 21 (Figure 4.2D). I.n. repeated administration of anti-HuR reverted thermal allodynia in the ipsilateral side at both 7 and 14 days after surgery (Figure 4.2E). Thermal antinociception was also produced by i.t. anti-HuR treatment and the effect was comparable to that induced by i.n. administration (Figure 4.2F). No effect was produced on the contralateral side thermal threshold by i.n. or i.t. anti-HuR ASO (Figure 4.2E, F). The effects of dODN, used as control ODN, were compared to those produced by the vehicle (DOTAP 13 μM) and saline. No difference was observed among control groups.

Spared nerve injury mice did not show any visible sign of altered gross behaviour or poor health, and the body weight was comparable to that of control mice. In addition, specific tests were performed to unmask alterations of locomotor behaviour that were not visible to the operator. Mice were evaluated for spontaneous mobility and exploratory activity by use of the hole board test. Spared nerve injury mice did not show any impairment in the spontaneous mobility and exploratory activity in comparision with the control group. The effect of HuR silencing on body weight and locomotor behaviour was evaluated. Experiments performed on day 7 post surgery showed that i.n. or i.t. repeated administration of anti-HuR ASO did not modify the body weight, spontaneous mobility, and exploratory activity in comparison with the control group.

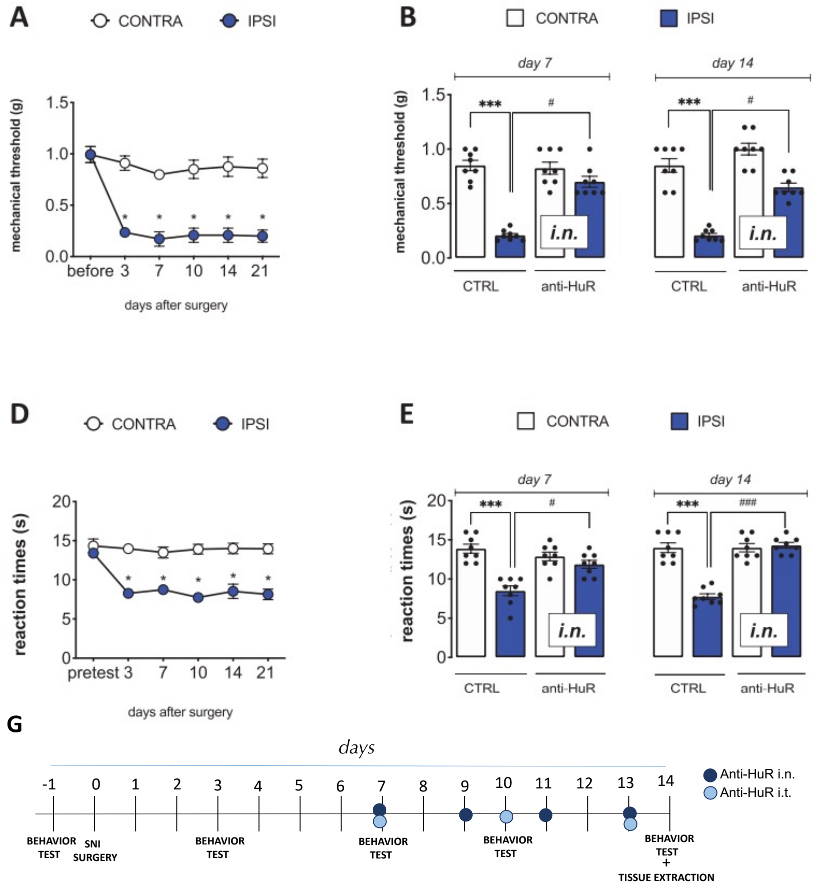

Figure 4.2. Anti-HuR ASO prevented pain hypersensitivity in SNI neuropathic mice. (A) Starting from 3 days after SNI surgery, a significant and long-lasting mechanical allodynia was produced in the ipsilateral (ipsi) side, whereas no alteration in the pain threshold was detected on the contralateral (contra) side. *p < 0.05 vs contra. (B) Intranasal (i.n.) administration of an anti-HuR ASO reversed mechanical allodynia on day 7 and day 14 after surgery. *p < 0.05 vs contra; #p < 0.05 vs ipsi. (C) The SNI-induced mechanical allodynia was prevented by intrathecal (i.t.) anti-HuR ASO with similar efficacy. Results were recorded on day 7 after surgery. *p < 0.05 vs contra; #p < 0.05 vs ipsi. (D) SNI-exposed mice showed a persistent thermal allodynia from day 3 after surgery *p <0.05 vs contra. (E) I.n. anti-HuR ASO completely reversed thermal allodynia on postsurgery day 7 and 14. *p < 0.05 vs contra; #p < 0.05 vs ipsi. (F) I.t. administration ameliorated hyperalgesia with a magnitude comparable to i.n. delivery. (G) Representative figure of experimental protocol. Results were recorded on day 7, 10, and 14 after surgery. Experimental groups are: SNI dODN (n=8), anti HuR i.n (n=8), anti HuR i.t (n=8). *p <0.05 vs contra; #p < 0.05 vs ipsi. CTRL: dODN- treated mice. ASO, antisense oligonucleotide; SNI, spared nerve injury.

4.2.1.4. Tissue and cellular localization of spinal HuR

To investigate the role of HuR in spinal cord mechanisms related to neuropathies, we first determined its expression pattern to identify the glial cell type that express HuR and its cellular localization. Double labelling immunostaining with classic markers of subpopulations was conducted in the mouse spinal cord. Double immunostaining of HuR with CD11b, a marker of microglia, showed the expression of HuR on activated microglial cells (Figure 4.3A, spinal cord; Figure 4.3B, spinal dorsal horn), further demonstrated by colocalization analysis (Figure 4.3C, D). The microglial expression of HuR was also confirmed by colocalization with TMEM119, a selective marker of microglial cells that does not detect infiltrated macrophages (Figure 4.3E–H). Conversely, experiments using GFAP as marker of astrocytes showed a lack of co-expression of HuR with GFAP.

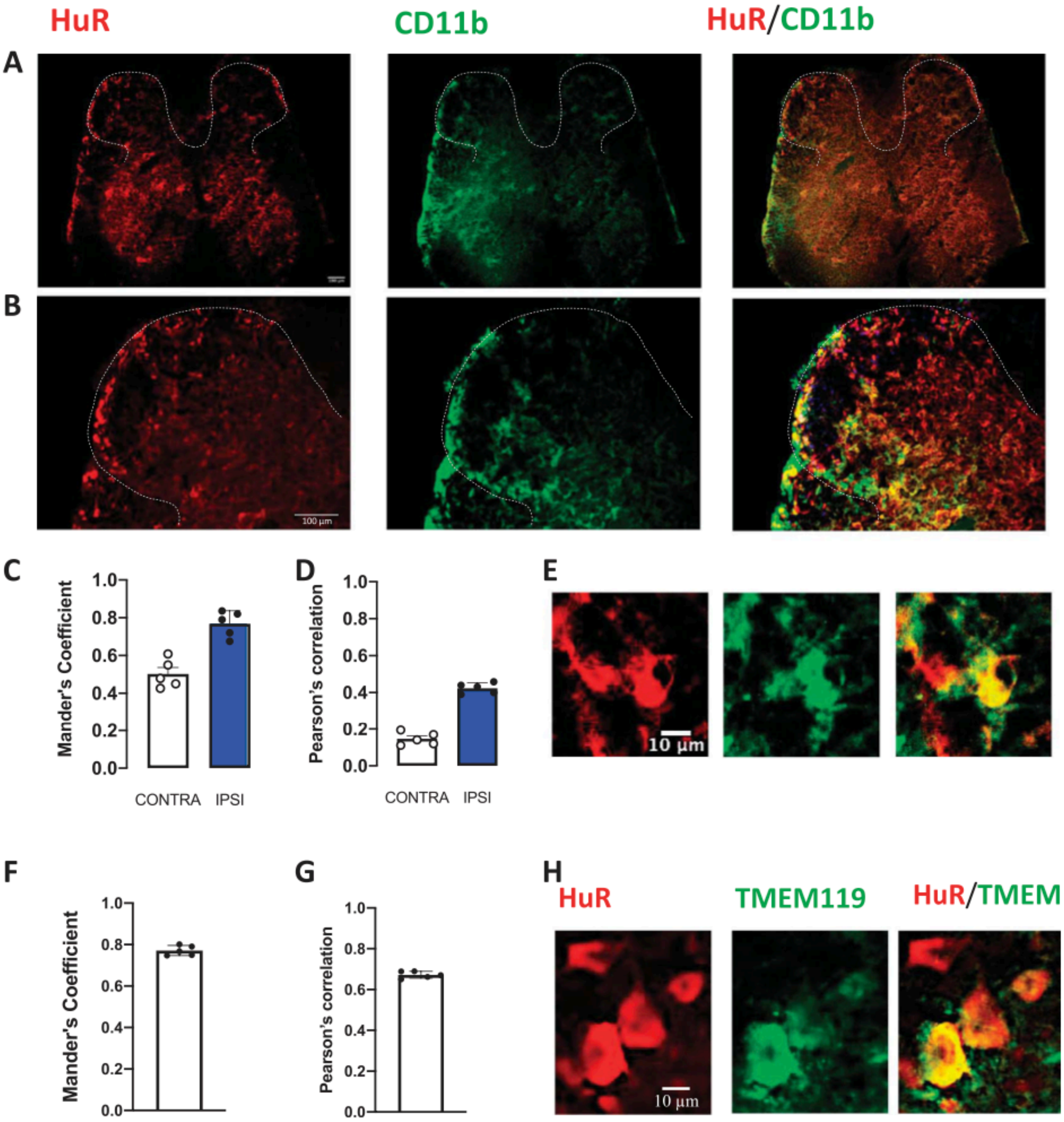

Figure 4.3. HuR microglial localization in the spinal cord dorsal horn of SNI mice. Spinal cord sections were harvested 7 days after SNI and double-immunostained for HuR and glial markers to determine colocalization (merged images). Immunostaining for the marker of microglia CD11b showed that HuR is expressed on activated microglial cells (A, spinal cord; B, ipsilateral dorsal horn low magnification; E, ipsilateral dorsal horn high magnification). Dorsal horn is delimited by dashed lines. Scale bar 5 100 mm. (C, D) Colocalization analysis. (H) HuR colocalized with TMEM119, a selective marker of microglial cells that does not detect infiltrated macrophages; Scale bar 5 100 mm. (F, G) Colocalization analysis. SNI, spared nerve injury.

4.2.1.5. Anti-HuR inhibition of spared nerve injury-induced microglia activation

Nerve injury results in remarkable microgliosis in the spinal cord, and numerous studies have demonstrated the contribution of microglia in the development of NP[129]. The expression of HuR on activated microglia encouraged us to investigate the role of this RBP on the activation of microglia induced by SNI. Our findings showed a robust upregulation of the microglia marker IBA1 in the ipsilateral side of the spinal cord of SNI mice on day 7 post-surgery that was inhibited by i.n. anti-HuR treatment. This effect was comparable to that obtained after i.t ASO administration (Figure 4.4A). Similarly, an increased immunostaining of the activated microglia marker CD11b was detected in the ipsilateral side, in comparison with the contralateral side, and this increase was reduced by anti-HuR administration, as showed by immunofluorescence photomicrographs (Figure 4.4B) and quantification analysis (Figure 4.4C). Microglia in the classic activation state (M1 phenotype) promote inflammation by the upregulation of iNOS and nuclear factor-kB (NF-kB) pathways and the release of proinflammatory cytokines such as tumor necrosis factor-a (TNF-α), interleukin-1b (IL-1β), and interleukin-6 (IL-6)[4]. The activated M2 microglia include the states of both alternative activation and acquired deactivation, which are induced by IL-13, IL-10, and transforming growth factor-b (TGF-β), and upregulate anti-inflammatory mediators, such as arginase-1 (Arg-1)[130].

Our results showed that, compared with control mice, SNI mice exhibited markedly increased expression of pNF-kB p65 (Figure 4.4D) and a decrease of the NF-kB inhibitory protein IkBa (Figure 4.4E), which were both reversed by ASO (i.n. and i.t). Fluorescence microscopy images of spinal cord slices showed the cytosolic localization of IkBa protein. Images showed the immunostaining of HuR in IkBa-expressing cells, indicating that both proteins are coexpressed in the same cellular population (Figure 4.4F). Similarly, levels of the proinflammatory cytokines IL-1 β (Figure 4.4G) and of the M1 marker iNOS (Figure 4.4H) were largely increased by SNI surgery. Antisense oligonucleotide robustly reduced IL-1β and iNOS overexpression. Comparable results were obtained after i.t. or i.n. anti-HuR administration.

Although not significant, there was a trend toward an increase in the expression of the M2 markers IL-10 in the ipsilateral side of SNI mice. The level of this anti-inflammatory cytokine was largely upregulated after anti-HuR administration (Figure 4.4I). These results suggest that anti-HuR ASO blocked microglia activation and switched these cells from an M1 to M2 phenotype.

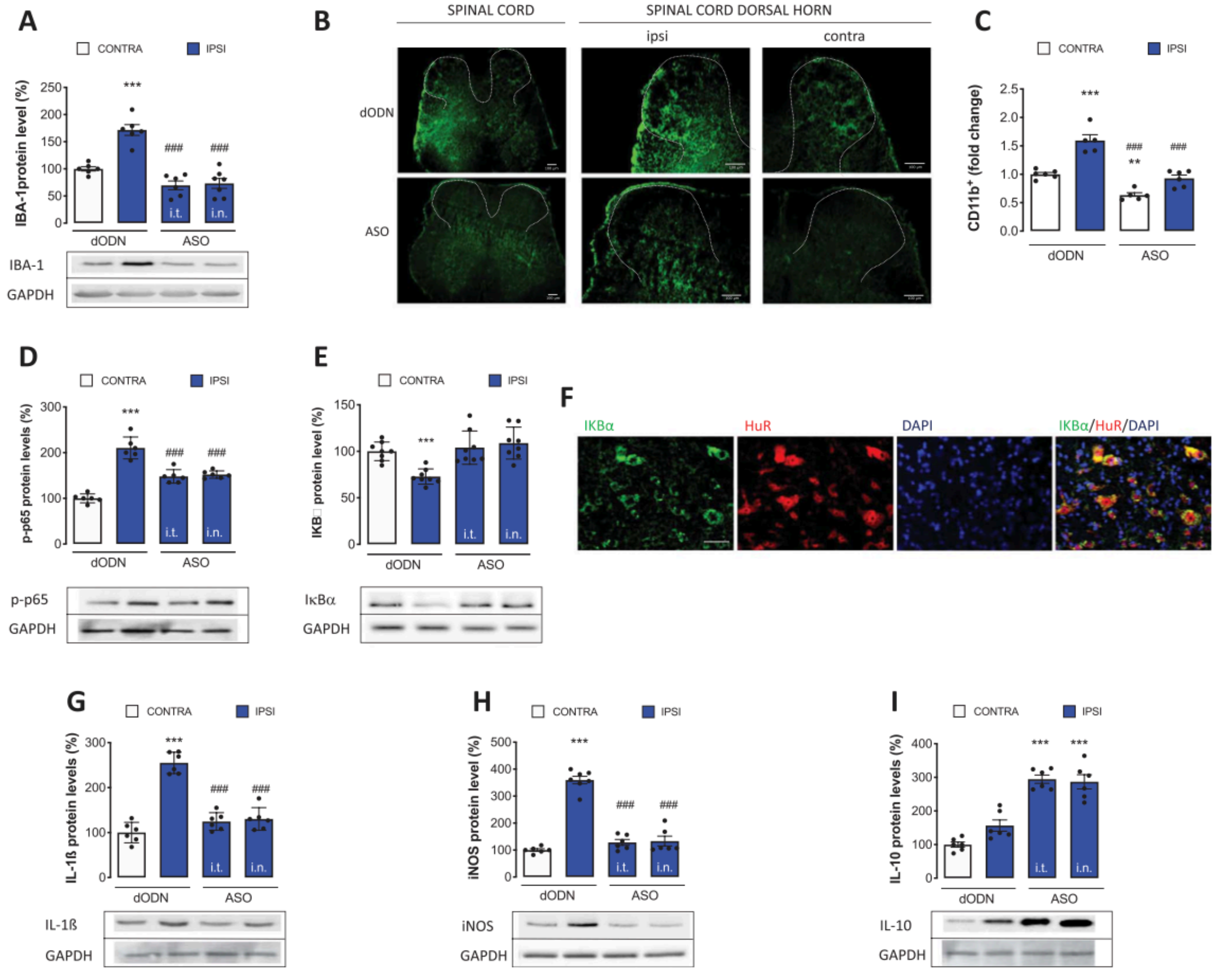

Figure 4.4 Anti-HuR ASO reduced SNI-induced microglia activation. (A) SNI mice showed increased expression of the microglia markers IBA-1 in the spinal cord that was reduced by i.t. and i.n. anti-HuR ASO with similar efficacy. (B) Representative photomicrographs illustrate the increased expression of CD11b within the ipsilateral side of spinal cord dorsal horn in SNI mice and the decrease of CD11b expression after i.n. anti-HuR ASO treatment. Higher magnification of the ipsilateral (ipsi) and contralateral (contra) sides are reported. Dorsal horn is delimited by dashed lines. Scale bars 5 100 mm. (C) Quantification of CD11b expression. Data were reported as fold change vs contra dODN group. (D) Spinal cord samples from SNI mice showed an increase of expression of p-p65 in the ipsilateral side in comparison with the contralateral side that was significantly reduced by i.t and i.n. anti-HuR ASO. (E) Reduction of the NF-kB inhibitory protein IkBa that was restored by ASO. (F) Fluorescence microscopy images showed the expression of HuR on IkBa-expressing cells (PCC 5 0.661 6 0.031; MOC 5 0.768 6 0.034). Nuclei were counterstained with DAPI. Antibodies are shown at the top. Scale bars 5 50 mm. Increase of the levels of (G) M1 cytokine IL-1β and of (H) the microglial M1 marker iNOS in the ipsilateral side of SNI spinal cord samples that was restored by i.t. and i.n. ASO. (I) I.t. and i.n. HuR silencing also increased the expression of the microglial M2 marker IL-10 in the ipsilateral side. Experiments were conducted on day 7 post-SNI. **p <0.01, ***p < 0.001 in comparison with dODN-treated SNI contralateral side. $^{###}$p <0.001 in comparison with dODN-treated SNI ipsilateral side. ASO, antisense oligonucleotide; iNOS, inducible nitric oxide synthase; MOC, Mander overlap coefficient; PCC, Pearson correlation coefficient; SNI, spared nerve injury

4.2.1.6. Prevention of the spinal increased mitogen-activated protein kinases phosphorylation by HuR silencing

Mitogen-activated protein kinases (MAPKs) are involved in the spinal mechanisms of NP. Accumulating evidence has proven that inhibiting p38 can suppress microglial activation and alleviate pain-related behaviours in animal models, thereby acting as an important analgesic target[131,132.] Consistently with these findings, we observed that the SNI procedure promoted a strong increase in the phosphorylation of spinal p38 within the ipsilateral side. Phosphorylation of extracellular signal-regulated kinases 1/2 (ERK1/2) was found in spinal microglia after nerve injury[86]. It is well known that damaged neurons activate microglia very quickly, and it has been hypothesized that activated microglia might promote and maintain astrocyte activation[133]. Consistently, JNK is activated persistently in astrocytes after nerve injury[134]. In addition, the involvement of JNK has been proposed in the regulation of both microglial iNOS and IL-1β expression[135]. To investigate into the cellular pathway modulated by HuR and to determine whether HuR could modulate the MAPK signaling pathway activation, the protein expression of phosphorylated spinal ERK, JNK, and p38 were measured in SNI neuropathic mice. The effect induced by anti-HuR at doses that produced an antinociceptive phenotype was, then, evaluated.

An increase of p-p38 contents was observed in the ipsilateral side of SNI mice spinal cord samples 7 days after surgery. I.n. anti-HuR treatment completely prevented p-p38 increase with an efficacy comparable to that obtained after i.t. administration (Figure 4.5A).

Although both JNK1 and JNK2 are heavily expressed in the spinal cord, pJNK1 (p46) is the predominant active form in the spinal cord and a selective increase of pJNK1 levels in the ipsilateral side of SNI mice spinal cord was detected after SNI (Figure 4.5B). No band corresponding to pJNK2 molecular weight was detected. I.n. or i.t. treatment with anti-HuR ASO prevented the phosphorylation of pJNK1with similar magnitude (Figure 4.5B). We also detected an increase in the phosphorylation of both spinal ERK1 (Figure 4.5C) and ERK2 (Figure 4.5D) isoforms, which was prevented by HuR silencing regardless the anti-HuR ASO delivery route, showing overlapping effects.

No significant modification in the p-p38, pJNK1, pERK1, and pERK2 was produced on the contralateral side of SNI mice, and no modification of total p38, JNK1, JNK2, ERK1, and ERK2 was detected. Representative immunoblots of changes in phosphorylated MAPK contents were illustrated in Figure 4.5.

Double staining immunofluorescence experiments showed the co-expression of HuR with p-p38 in the spinal cord (Figure 4.6A) and spinal dorsal horn (Figure 4.6B) of SNI control mice (quantification in Figure 4.6C). Similar results were observed for spinal cord (Figure 4.6D) and dorsal horn (Figure 4.6E) of anti-HuR ASO (quantification in Figure 4.6F)-treated SNI mice. HuR expression also partially overlaps with pERK immunostaining (Figures. 4.6G, I).

Colocalization experiments to identify the cell type that expresses p-p38 (Figures. 6 J, K) and pERK (Figures. 6 L, M) showed a microglial localization for p-p38, confirmed by quantification analysis (Figures. 6N and O). pERK was mainly expressed in neurons (Figure 6P), but it was also partially expressed on microglia (Figure 6Q).

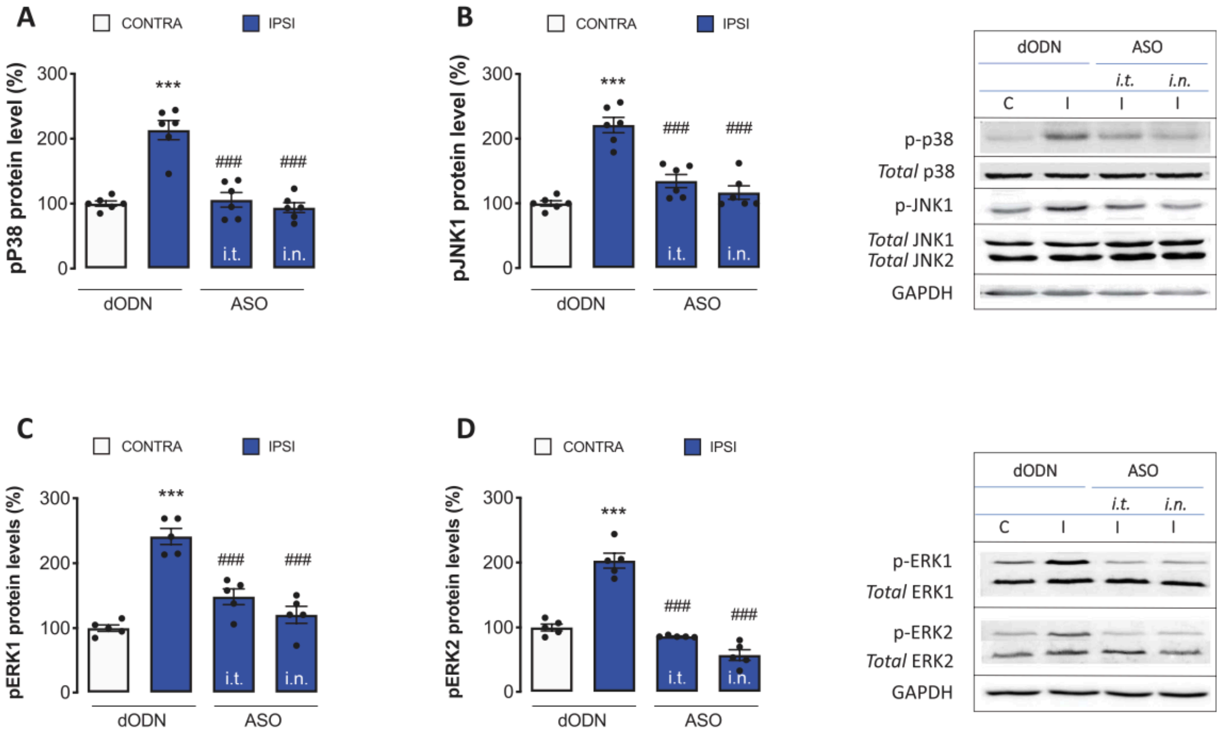

Figure 4.5. Anti-HuR ASO inhibited MAPK phosphorylation in SNI mice. Mice exposed to SNI showed an increased phosphorylation of (A) p38, (B) JNK1, (C) ERK1, and (D) ERK2 in the ipsilateral side in comparison with the contralateral side. I.t. and i.n. repeated administration of anti-HuR ASO reduced the overphosphorylation of MAPKs with similar effects. Experiments were conducted on day 7 post-SNI. $^{*}p < 0.05$ in comparison with SNI contralateral side. $^{\#}p < 0.05$ in comparison with SNI ipsilateral side. ASO, antisense oligonucleotide; MARK, mitogen-activated protein kinases; SNI, spared nerve injury.

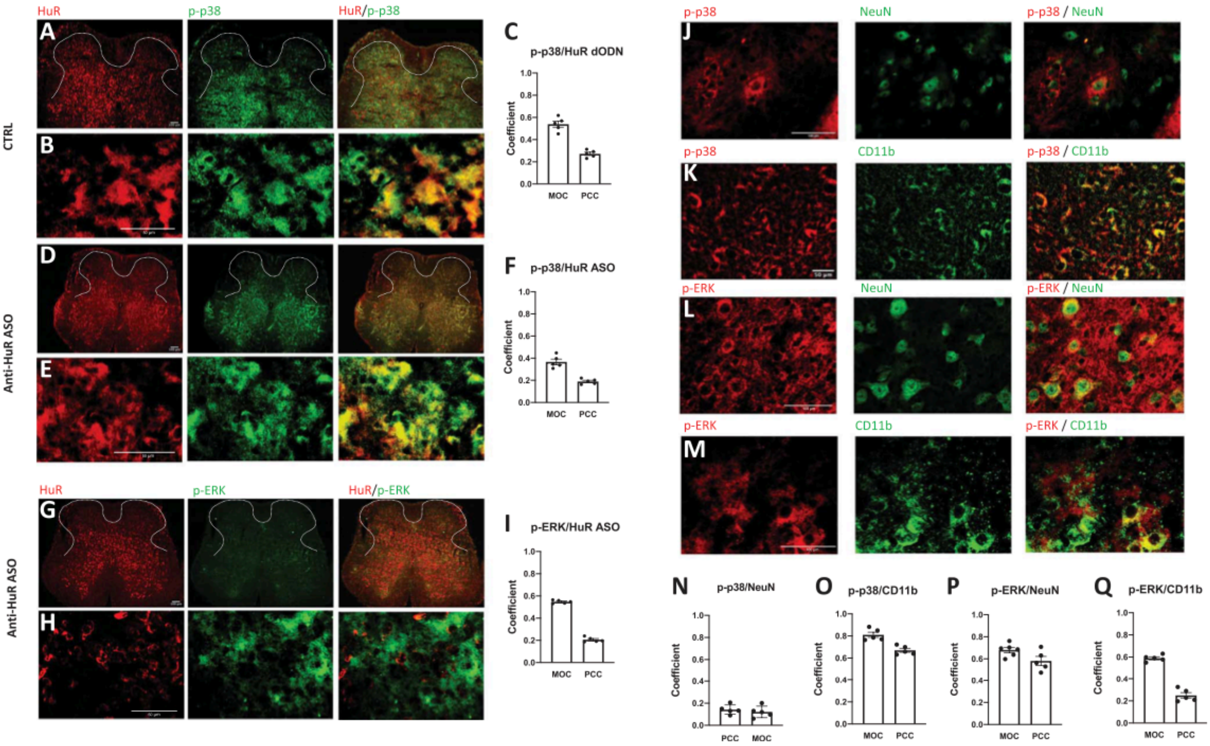

Figure 4.6. Double immunofluorescence staining to detect colocalization of HuR with MAPK. Co-expression of HuR with p-p38 was detected in (A, D) the spinal cord and (B, E) spinal dorsal horn of SNI mice. (A, B) Microphotographs from dODN-treated control mice SNI mice. (C) Colocalization analysis for dODN mice. (D, E) Microphotographs from i.n. anti-HuR ASO treated SNI mice. (F) Colocalization analysis for ASO mice. HuR immunostaining partially overlaps with pERK immunostaining in spinal cord (G) and spinal dorsal horn (H) of ASO-treated mice. (I) Colocalization analysis for ASO mice. Scale bar 5 100 mm. Colocalization experiments to identify the cell type that expresses (J, K) pP38 and (L, M) pERK showed a prominent microglial localization as confirmed by (N, O) colocalization analysis. pERK was mainly expressed in neurons as showed by (P) merged images and colocalization analysis, but it was also partially expressed on microglia (Q) merged images and colocalization analysis. Dorsal horn is delimited by dashed lines. Scale bar is reported in each photomicrograph. ASO, antisense oligonucleotide; MARK, mitogen-activated protein kinases; SNI, spared nerve injury.

4.2.2. Targeting the RNA-Binding Protein HuR Alleviates Neuroinflammation in Experimental Autoimmune Encephalomyelitis

4.2.2.1. HuR Protein Overexpression in the Spinal Cord of EAE Mice

The present study aimed to elucidate the role of post- transcriptional regulation of gene expression in the EAE-related neuroinflammation by investigating the role of the RBP HuR, a member of the ELAV family. As most MS patients manifest a relapsing–remitting form of MS (RRMS)[136], the study was conducted in a model of EAE obtained by immunization of SJL female mice with PLP$_{139-151}$, recognized as an animal model of RRMS[137].

Immunofluorescence experiments were performed on spinal cord slices collected on day 30 after immunization with $PLP_{139–151}$. Microphotographs showed the presence of a homogeneous HuR immunostaining in nonimmunized control spinal cord samples (CTRL) that was increased in PLP-EAE mice. An antisense strategy was used to investigate the role of HuR in EAE-related symptoms. HuR silencing was obtained through the repeated intrathecal administration of a specific and selective anti-HuR ASO. A dODN of the same length and chemical structure was used as control ODN. Microphotographs showed the reduction of HuR immunolabeling following treatment with an anti-HuR ASO (Figure 4.7A). Quantification analysis confirmed the increase of HuR immunostaining in EAE mice, as well as the significant decrease of HuR protein expression by HuR silencing, showing the efficacy of the antisense treatment (Figure 4.7B). No difference was observed among dODN-, vehicle-, and saline-treated mice, ruling out the presence of sequence-independent effects.

4.2.2.2. Anti-HuR ASO treatment reduced activated microglia

Reactive gliosis is a common feature in MS. Studies using EAE have revealed that microglia and astrocytes actively participate in the pathogenesis of EAE progression[138]. The role of HuR on glial cell activation was, therefore, investigated. We used immunofluorescence to detect HuR expression in glial cells from spinal cord slices of EAE mice. Immunization with PLP induced an increased immunostaining of the astrocyte marker GFAP (Figure 4.7C) and of the microglia marker IBA1 (Figure 4.7E) that were both attenuated by anti-HuR ASO administration. IBA1 staining detects both quiescent and reactive microglia and infiltrated macrophages. To evaluate the role of HuR on activated microglia, we investigated the immunostaining of CD11b. In the lumbar spinal cord of PLP-EAE mice, we observed an abundant number of cells with intense CD11b immunoreactivity, consistent with activated microglia, which was largely reduced by HuR knock- down (Figure 4.7G). Quantification analysis showed that the GFAP immunoreactivity in EAE mice exceeded that of the CTRL by 2.5-fold (Figure 4.7D), the IBA1 immunoreactivity by 3.5-fold (Figure 4.7F), and the CD11b immunoreactivity by 4.5-fold (Figure 4.7H). A significant reduction by anti-HuR ASO of GFAP (Figure 4.7D) and IBA1 (Figure 4.7F) immunostaining, and a drastic reduction of CD11b immunostaining (Figure 4.7H), were also confirmed.

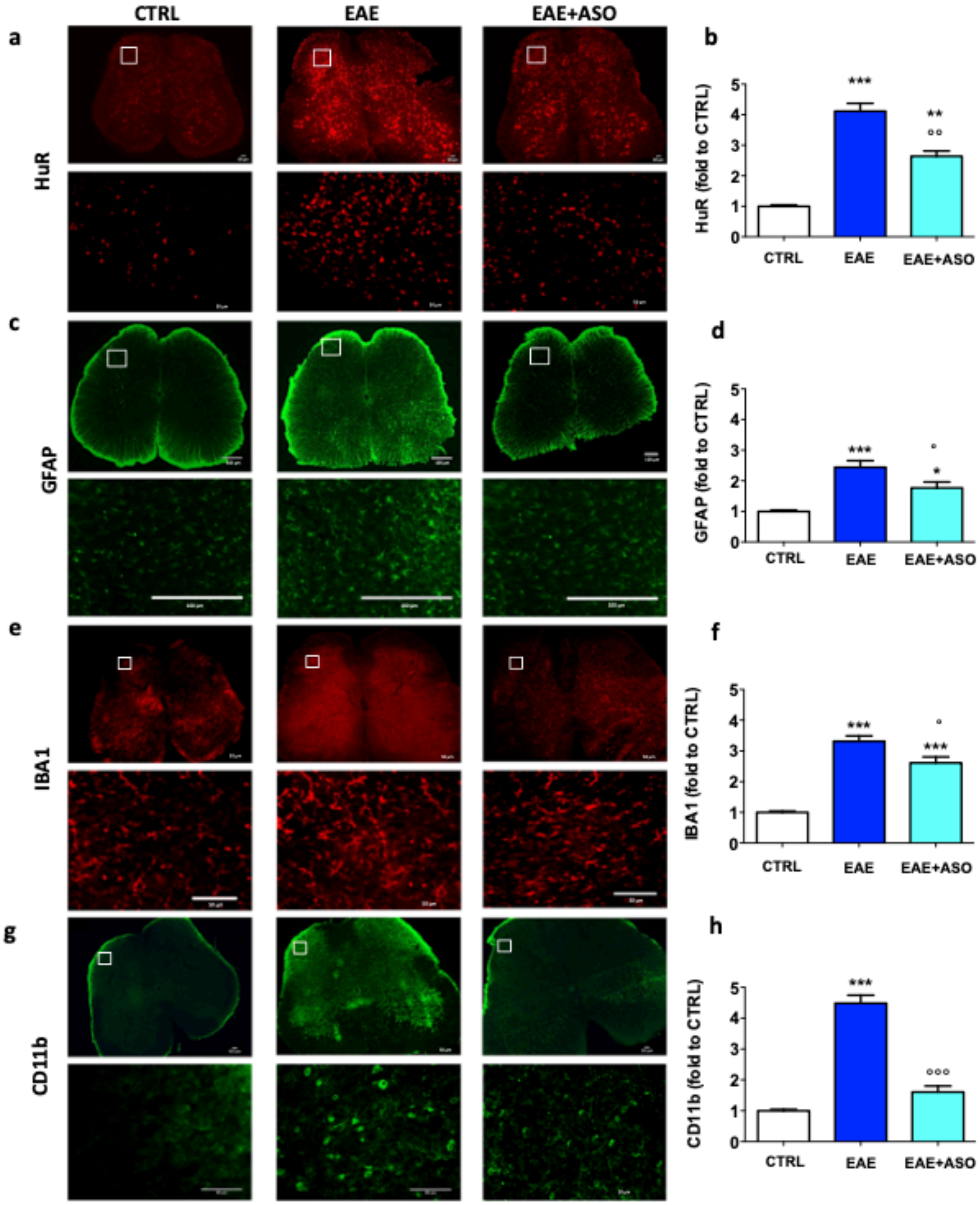

Figure 4.7 Increased expression of HuR and glial cells in spinal cords of EAE mice. (a) Representative images (low and high magnification) showing immunofluorescence staining for HuR in the spinal cords of control (CTRL), EAE, or anti-HuR ASO-treated EAE mice at 30 days postimmunization. (b) Quantification of the increased HuR immunostain- ing in spinal cords and significant reduction by anti-HuR ASO. Representative images (low and high magnification) show the immuno- staining for (c) GFAP, (e) IBA1, and (f) CD11b in the spinal cord of control (CTRL), EAE, or EAE + anti-HuR ASO mice at 30 days postimmunization. Quantification of the (e) GFAP, (f) IBA1, and (h) CD11b content showing the increased expression in the EAE section and attenuation by anti-HuR ASO. CTRL, dODN-

treated nonimmunized mice; EAE, dODN-treated EAE mice; EAE + ASO, anti-HuR ASO- treated EAE mice. **p < 0.01, ***p < 0.001 versus CTRL; °p < 0.05, °°°p < 0.001 versus EAE (ANOVA). Error bars represent the standard error of the mean. Antibodies are shown on the left. Scale bar = 50 µm (HuR, IBA1, CD11b); 100 µm (GFAP)

4.2.2.3. HuR expression on activated microglia

A diffuse activation of microglia is detected in the spinal cord of PLP-EAE mice on day 30 postimmunization (Figure 4.8A, higher magnification in Figure 4.8B) in comparison with non-immunized control (CTRL) mice. Spinal cord sections also showed a diffuse HuR immunoreactivity in CTRL mice that was homogeneously increased in EAE mice (Figure 4.8A), where localized prominently in the cytoplasm (Figure 4.8B), a pattern associated with its increased activity. In most of the EAE microglia, there was a prominent merging of HuR and CD11b signals, with a pattern of cytoplasm colocalization. A high degree of expression of HuR in CD11b-positive cells was further supported by evaluation of colocalization (Mander's coefficient, Figure 2M).

Because macrophages and microglia will both express CD11b, to distinguish microglial cells from macrophages, the TMEM119 staining was used (Figure 4.8G–L). A high degree of expression of HuR in TMEM119-expressing cells (Mander's coefficient, Figure 4.8N) confirmed the expression of HuR on microglial cells.

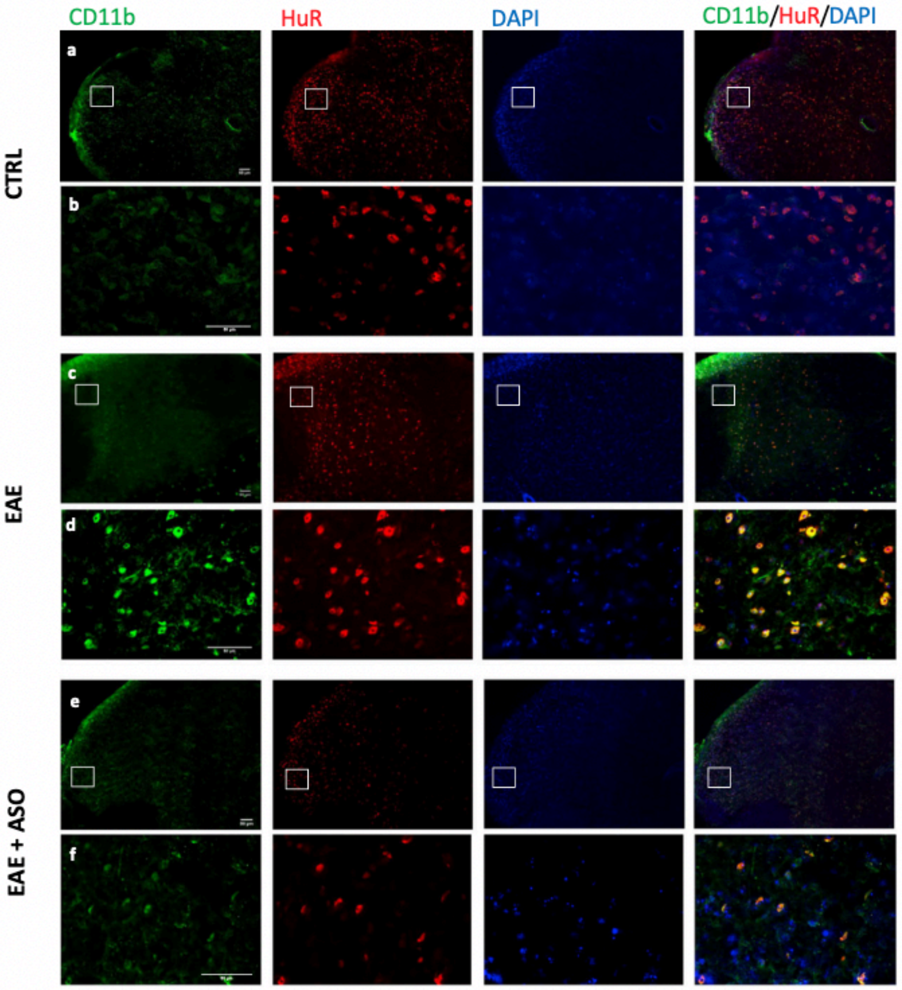
CD11b
HuR
DAPI
CD11b/HuR/DAPI
CTRL
EAE
EAE + ASO
a
b
c
d
e
f

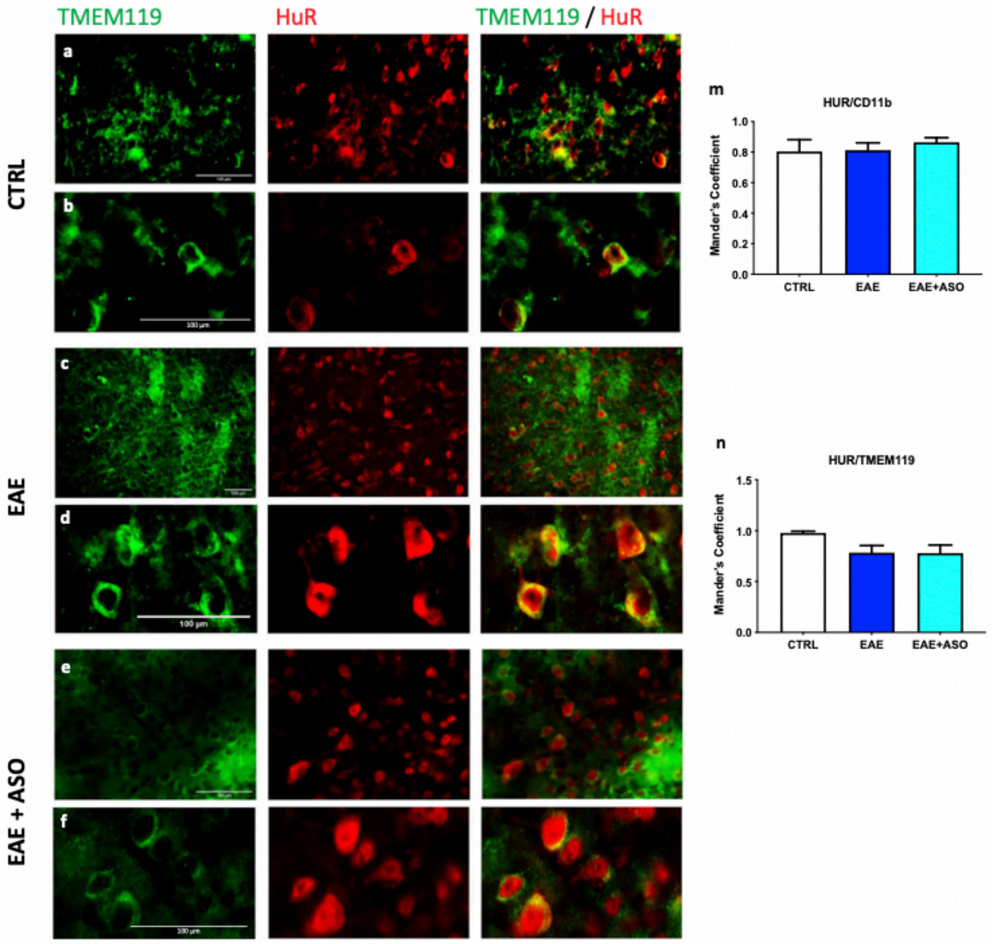
TMEM119
HuR
TMEM119 / HuR
CTRL
EAE
EAE + ASO
a
b
c
d
e
f
100 µm
m
HUR/CD11b
Mander's Coefficient
1.0
0.8
0.6
0.4
0.2
0.0
CTRL
EAE
EAE+ASO
n
HUR/TMEM119
Mander's Coefficient
1.5
1.0
0.5
0.0
CTRL
EAE
EAE+ASO

Figure 4.8 Localization of HuR protein in activated microglia from EAE spinal cord. Fluorescence microscopy images showed the microglial localization of HuR in the spinal cord of control (CTRL), EAE, or EAE + anti-HuR ASO mice. (a, c, e): Low-magnification images show a homogeneous distribution of HuR within the spinal cord. Immunostaining for the microglial marker CD11b in the same section reveals similar immunoreactivity. The merged image shows HuR localization on microglial cells. b, d, f: High-magnification images show the cytosolic localization of HuR, consistent with a pattern of activation, and merged images illustrate the high degree of colocalization of HuR and CD11b. Nuclei were counterstained with DAPI. Antibodies are shown at the top. Scale bar = 50 µm. Expression of HuR protein on TMEM119-positive microglial cells. Fluorescence microscopy images showed the microglial localization of HuR in the spinal cord of control (CTRL), EAE, or EAE + anti- HuR ASO mice. g, i, k: low-magnification images. h, j, l: high-magnification images. Antibodies are shown at the top. Evaluation of colocalization of HuR and (m) CD11 or (n) TMEM119 in spinal cord sections. Scale bars = 100 µm. CTRL, dODN-treated nonimmunized mice; EAE, dODN-treated EAE mice; EAE + ASO, anti-HuR ASO- treated EAE mice.

4.2.2.4. Effect of anti-HuR ASO on inflammatory cell infiltration

To investigate whether the reduction of activated microglia produced by HuR silencing was related to a neuroinflammation dampening, we evaluated the effect of anti-HuR ASO on inflammatory cell infiltration by hematoxylin and eosin (H&E) staining of lumbar spinal cord sections. There were scarcely any inflammatory cells in samples from CTRL mice. H&E staining identified the presence of many inflammatory cells in PLP-EAE sections, which represented the successful induction of the disease. Inflammatory infiltration in the anti-HuR ASO-treated group was reduced in comparison with that in the PLP-EAE group (Figure 4.9A, B). No significant differences in inflammatory cell infiltration were observed between non-immunized (CTRL) and anti-HuR recipients, indicating to the remarkable anti-inflammatory effects of HuR silencing (Figure 4.9B).

4.2.2.5. Anti-HuR ASO attenuates proinflammatory cytokine expression

Because the histological examination of the PLP-immunized SJL mice revealed remarkable inflammatory cell infiltration in the spinal cord, we investigated the protein expression levels of the main proinflammatory cytokines involved in EAE, TNF-α (Figure 4.9C), IL-1β (Figure 4.9D), and IL-17 (Figure 4.9E) in the spinal cord of PLP-EAE mice. Analysis of data showed increased secretion of all the 3 cytokines. Treatment with anti-HuR ASO drastically reduced the content of IL-1β, IL- 17, and TNF-α returning to basal levels. The plasma level of cytokines was also analyzed to determine whether the changes observed in the spinal cord were associated with the changes in the peripheral blood. The expression of the investigated cytokines was also increased in the plasma of EAE mice in comparison with nonimmunized control mice (Figure 4.9F–H). Anti-HuR ASO treatment reduced the expression of IL-1β (Figure 4.9G) and IL-17 (Figure 4.9H), but it did not produce any effect on TNF-α level (Figure 4.9F).

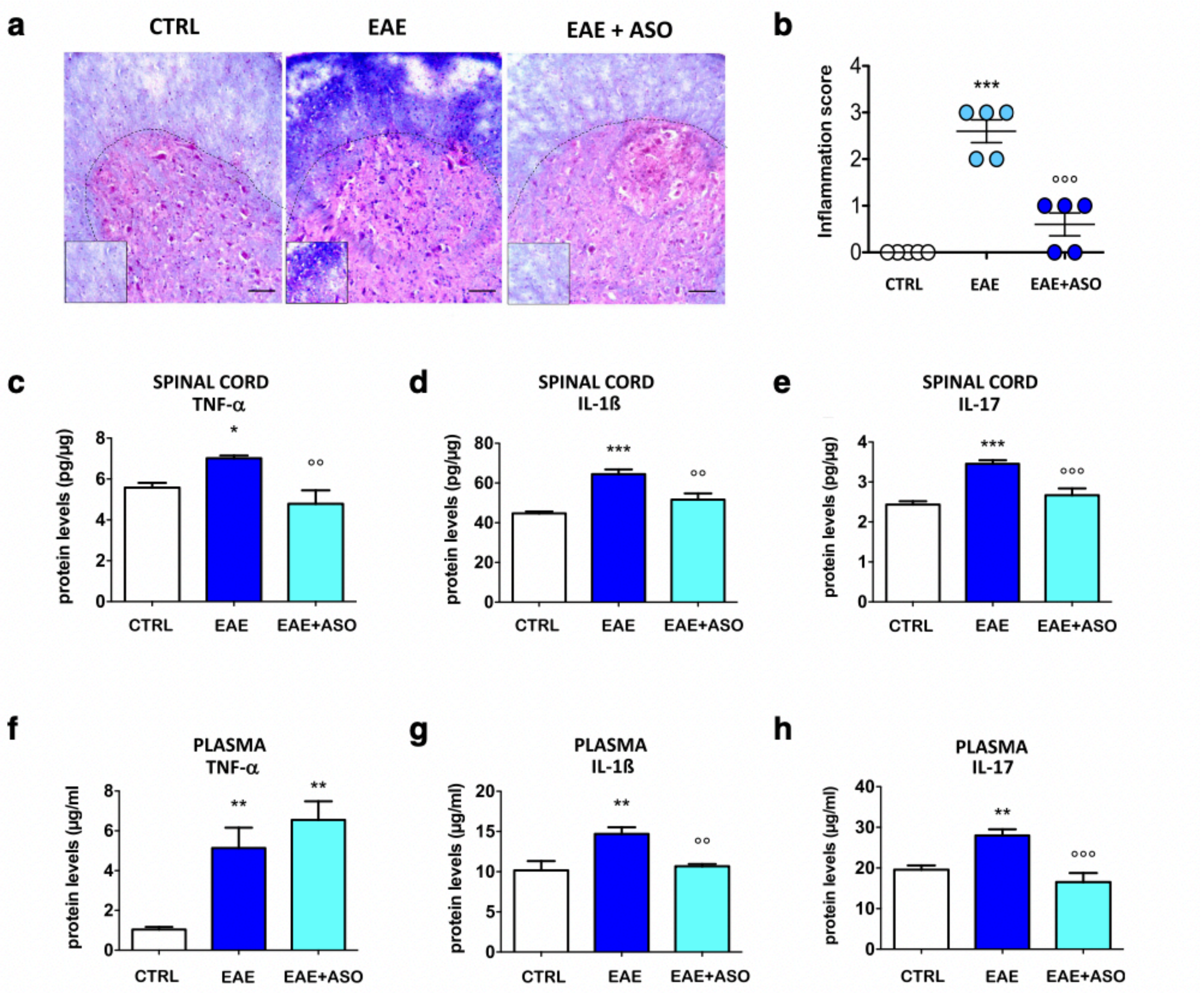

Figure 4.9 Anti-HuR ASO attenuates neuroinflammation. (a) Representative images showing spinal cord sections stained with hematoxylin and eosin (H&E) in control (CTRL), EAE, or EAE + anti-HuR ASO mice at 30 days postimmunization (high magnification on bottom images). Scale bar = 100 μm. (b) Quantification of inflammatory infiltrates indicates the large increase in their number in EAE and the reduction produced by anti-HuR treatment. Levels of (c) TNF-α, (d) IL-1β, and (e) IL-17 were increased in EAE spinal cords and reduced by anti-HuR ASO. Similarly, plasma levels of (f) TNF-α, (g) IL-1β, and (h) IL-17 were increased in EAE mice. Anti-HuR treatment reduced IL-1β and IL-17 levels and did not produce any significant modification on TNF-α levels. CTRL, dODN- treated nonimmunized mice; EAE, dODN-treated EAE mice; EAE + ASO, anti-HuR ASO-treated EAE mice. Error bars represent the standard error of the mean. $^{*}p < 0.05$, $^{**}p < 0.01$, $^{***}p < 0.001$ versus CTRL mice; $^{\circ\circ}p < 0.001$, $^{\circ\circ\circ}p < 0.01$ versus EAE mice (ANOVA)

4.2.2.6. NF-κB activation is reduced by HuR silencing

The activation of the NF-κB pathway represents the molecular driver of proinflammatory microglia, found in MS brain tissue, where it localizes in astrocytes, oligodendrocytes, microglia, and infiltrating macrophages in or near CNS lesions[139].The activation of NF-κB often results in an inflammatory environment that propagates demyelination and inhibits remyelination in the CNS[140].

TNF-α and IL-17, produced by T helper 1 cells and T helper 17 cells, respectively, can activate the NF-κB pathway, a signaling pathway involved in neuroinflammation and implicated in the pathogenesis of MS and EAE[141,142]. To investigate the role of HuR in transcriptional mechanisms that promote neuroinflammation in EAE mice, the activation of NF-κB signaling was examined by immunoblotting experiments. Under basal conditions, NF-κB is inhibited by the subunit IκBα. Following phosphorylation and degradation of IκBα, NF-κB is released and translocated to the nucleus, promoting gene transcription. PLP-EAE mice showed a progressive trend to a reduction of IκBα protein levels, indicating the degradation of the NF-κB inhibitory subunit, which became significant from day 21 post immunization. Anti-HuR ASO treatment restored IκBα levels, thus preventing the activation of the NF-κB pathway (Figure 4.10A). The activation of the NF-κB signaling is also confirmed by the staining of the phosphorylated p65 subunit of NF-κB that showed a significant increase of p-p65 expression in the spinal cord of EAE mice that was completely prevented by anti-HuR ASO treatment (Figure 4.10B). Immunofluorescence photomicrographs of spinal cord slices showed the cytosolic localization of IκBα protein. Double staining immunofluorescence images showed the expression of HuR in IκBα-expressing cells, indicating that both proteins are co-expressed in the same cellular population (Mander's coefficient, 0.832 ± 0.07; Figure 4.10C).

4.2.2.7. Lack of anti-HuR ASO effect on CD4 expression

Among CD4+ T lymphocytes, Th1, Th17, and granulocyte– macrophage colony-stimulating factor (GM-CSF)-producing CD4+ T cells have been identified as important mediators in the immunopathogenesis of EAE, and all of them can induce EAE independently. High levels of IL-17 have been detected in both plaques and CSF of patients with MS, and the high expression of IL-17 correlates with MS severity[143]. The absence of IL-23, a Th17-promoting cytokine, made IL-23−/− mice very resistant to EAE[144]. Because IL-17 is preferentially expressed by CD4+ T cells, the reduction by anti-HuR ASO of spinal IL-17 expression encouraged us to investigate the role of HuR on CD4 expression. We observed a progressive increase in the expression of CD4 in the spinal cord of EAE mice with peaks at day 11, day 21, and day 30 postimmunization (Figure 4.10D). However, HuR silencing was unable to reduce CD4 expression (Figure 4.10D). Even though HuR is involved in the maintaining of the proper function of the immune system[145], present data indicate that in PLP-EAE mice HuR has a prominent role at cytokine expression level rather than having a modulating activity of the immune response.

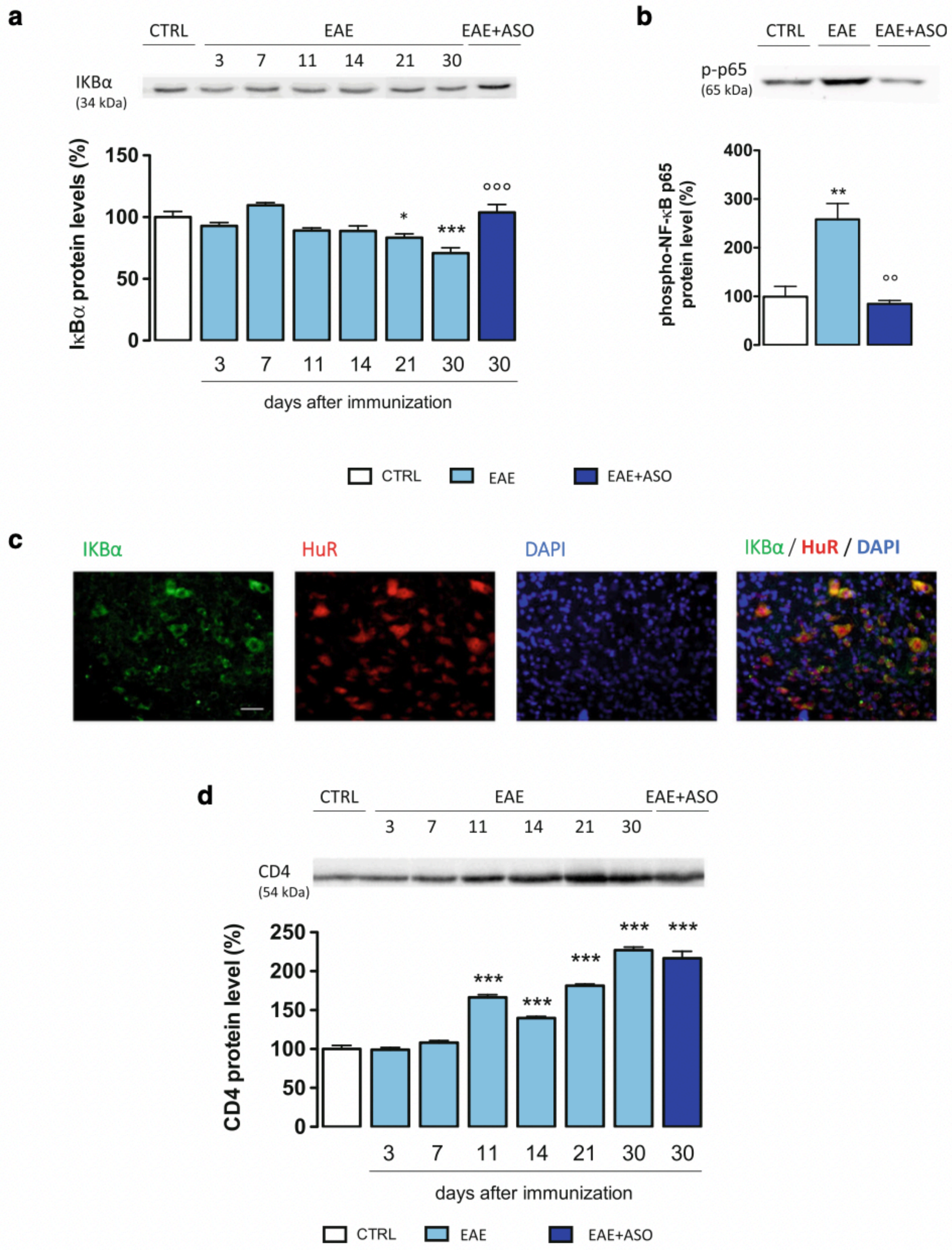

Figure 4.10 HuR silencing reduces the NF-κB signaling activation. (a) Time course evaluation showed the progressive reduction of the NF-κB inhibitory subunit IκBα. Anti-HuR ASO treatment counteracted the decrease of IκBα expression (day 30 postimmunization). (b) increased expression of the phospho NF-κB p65 subunit in the EAE spinal cord sample that is reversed by anti-HuR ASO treatment. (c) Microphotographs showed the expression of HuR on IκBα-expressing cells. Nuclei were counterstained with DAPI. Antibodies are shown at the top. Scale bars = 50 μm. (d) Time course evaluation of CD4 protein expression in spinal cord lysate of EAE mice. A significant increase in the CD4 expression was detected, and anti-HuR ASO treatment did not modify the CD4 levels on day 30 postimmunization. CTRL, dODN-treated nonimmunized mice; EAE, dODN-treated EAE mice; EAE + ASO, anti-HuR ASO-treated EAE mice. Error bars

represent the standard error of the mean. *p<0.05, **p < 0.01, ***p < 0.001 versus CTRL mice; °°p < 0.01, °°°p < 0.001 versus EAE mice (ANOVA)

4.2.2.8. Anti-HuR ASO inhibits BBB permeability during EAE

MS is characterized by a compromised BBB, infiltration of macrophages, T cells, and B cells into the CNS, and local microglia and astrocyte activation, together promoting inflammation, demyelination, and neurodegeneration[146]. The BBB disruption is an early and central event in MS pathogenesis, and we demonstrated that anti-HuR ASO largely reduced breakdown of BBB in the brain and spinal cord during EAE. Recent studies revealed this event underlies an IL-17- mediated mechanism. The structure of the BBB includes vascular endothelial cells that are strongly joined by tight junctions[147]. Endothelial cells express IL-17 receptor, and IL-17 destroys the tight junctions of the BBB to facilitate the migration of CD4+ T cells in humans and mice[148,149]. Evans Blue (EB) dye is widely used to detect a leaky BBB because it conjugates with serum albumin to form a large molecular complex which is unable to cross an intact BBB under normal circumstances. Thus, any entry of EB dye into the brain is considered an indicator of disrupted BBB permeability. Consequently, we examined the EAE-induced BBB disruption by EB leakage in mouse brain and spinal cord on day 30 to determine the effect of anti-HuR ASO on BBB integrity. The macroscopic images of peripheral tissues (spleen, liver, kidney) showed a comparable exposure to EB in all groups in comparison with naïve untreated mice. The brain and spinal cord images showed that the degree of EB leakage was increased in EAE mice. Quantification analysis showed that the EAE group had significantly higher levels of EB extravasation than the control group in both brain (Figure 4.11A) and spinal cord (Figure 4.11B). The effect produced by anti-HuR ASO was evaluated. HuR silencing largely decreased the EB content in both brain and spinal cord, returning to values comparable with the baseline level of the control mice (Figure 4.11C, D).

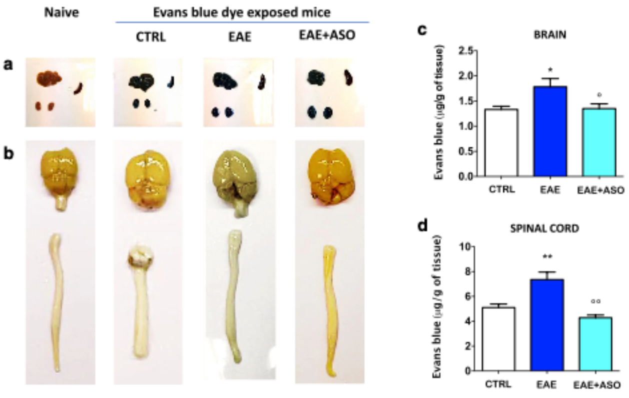

Figure 4.11 Anti-HuR ASO treatment inhibition of BBB permeability in the brain and spinal cord of EAE mice. Representative pictures of (a) liver, kidney, spleen, (b) brain, and spinal cords from naïve, CTRL, EAE, and anti-HuR

ASO-treated EAE mice are displayed. Blue color indicates extravasated Evans blue (EB) dye from blood vessels. The amount of extravasated EB dye was quantified in (c) the brain and (d) lumbar spinal cord, at 30 days after immunization (n = 7 per group). A significant increase of extravasated EB dye was detected in the brain and spinal cord of EAE that was attenuated by anti-HuR ASO. CTRL, dODN- treated nonimmunized mice; EAE, dODN-treated EAE mice; EAE + ASO, anti-HuR ASO-treated EAE mice. Error bars represent the standard error of the mean. $^{*}p < 0.05$, $^{**}p < 0.01$ versus CTRL; $^{\circ}p < 0.05$, $^{\circ\circ}p < 0.01$ versus EAE (ANOVA)

4.2.2.9. HuR silencing shifts activated microglia from proinflammatory to anti-inflammatory phenotype

Microglia display remarkable plasticity in their activation phenotypes and present different activation states with the stage of MS and EAE disease. In the early stages, microglia are expressed as the proinflammatory phenotype[150]. The proinflammatory activated microglia were deleterious in MS by releasing destructive proinflammatory mediators and were involved in the development and expansion of lesions. In the later stage, the anti-inflammatory phenotype becomes predominant in the CNS to dampen neuroinflammation and help diminish neuronal damage[151,152]. This evidence leads to the hypothesis of an important role in disease progression played by proinflammatory/anti-inflammatory phenotype balance. Different anti-inflammatory microglia subtypes with different activation and functional mechanisms have been described, including a subtype with a regenerative phenotype (CD206+) and a subtype with a wound healing phenotype (CD163+, IL-10+)[153]. Microglia phenotypes: can be detected by means of specific markers. Our results showed that anti-HuR ASO can reduce the levels of proinflammatory cytokines and reduce activated microglia. These observations prompted us to explore whether HuR might also modulate the microglial anti-inflammatory phenotype. Microphotographs from immunofluorescence experiments performed on spinal cord samples of EAE mice showed a decrease of the anti-inflammatory microglial marker CD206 that was restored by HuR silencing (Figure 4.12A). The anti-HuR positive effect was confirmed by quantification analysis (Figure 4.12B). Merged images showed a high degree of expression of HuR in CD206-positive cells (Figure 4.12A). We also quantitated the number of microglia with high intensity merged HuR and variation in the expression of the anti-inflammatory markers IL-10 was detected on spinal cord lysates from EAE mice, and the cytokine level remained unmodified following anti-HuR administration (Figure 4.12E). These results suggest that in the PLP-induced EAE model, anti-HuR ASO switched activated microglia cells from a proinflammatory to anti-inflammatory phenotype. This effect was mainly related to an increased expression of CD206-expressing cells rather than to the promotion of IL-10 anti-inflammatory cytokine release.

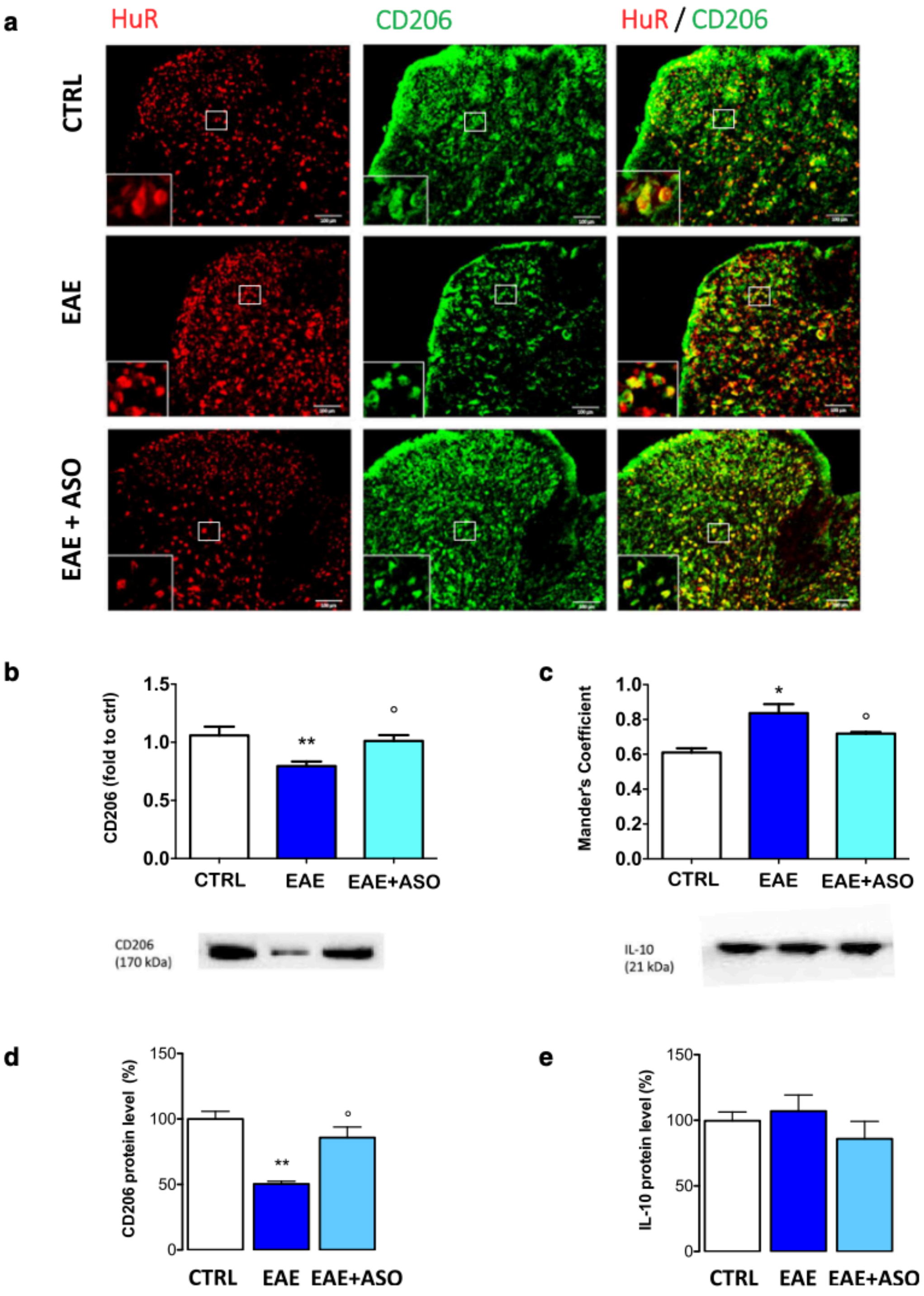

Figure 4.12 Anti-HuR ASO activated the anti-inflammatory microglial phenotype. (a) Representative microphotographs showed a decreased CD206 immunostaining in the spinal cord section of EAE mice on day 30 postimmunization. The CD206 protein expression was restored by HuR silencing. Merged images showed the expression of HuR on CD206-expressing cells. (b) Quantification analysis of immunofluorescence data showed the significant reduction of CD206 immunostaining, reversed by HuR silencing. (c) Evaluation of colocalization of HuR and CD206 in spinal cord sections. (d) Western blot results showing anti-HuR ASO reversal of EAE-induced reduction of CD206 protein expression. (e) Lack of variation of IL-10 levels in EAE mice in the absence or in the presence of HuR silencing (Western blot). (f) Representative blots of Western blotting experiments. CTRL, dODN-treated nonimmunized mice; EAE, dODN-treated

EAE mice; EAE + ASO, anti-HuR ASO- treated EAE mice. Error bars represent the standard error of the mean. Antibodies are shown at the top. Scale bar = 100 µm. $^{*}p < 0.05$, $^{**}p < 0.01$ versus CTRL; $^{\circ}p < 0.05$ versus EAE (ANOVA)

4.2.2.10. Anti-HuR ASO reduces EAE clinical disease and locomotor disability

To evaluate whether the reduction of glial cell activation induced by HuR silencing provides positive effects on EAE-related symptoms in mice, we examined the effect of anti-HuR ASO treatment on motor disability. ASO effects were compared to those produced by dODN administration, used as control ODN, and no behavioral alteration was observed in comparison with vehicle- or saline- treated mice, ruling out the presence of sequence- independent effects.

Time course experiments showed that PLP-EAE mice experienced motor disability with a relapsing–remitting disease profile. The clinical score evaluation revealed a first disease peak on day 14, followed by a remission phase. From day 20, a relapse phase appeared, and motor disability increased up to day 28 (Figure 4.13A). We additionally performed an objective measure of locomotor disability on EAE mice by using the rotarod test to avoid a potential observer bias in scoring disability in EAE scores, being a subjective evaluation. Consistent with clinical score results, the rotarod performance, tested from day 3 up to day 30 postimmunization, was characterized by a relapsing–remitting disease profile with in- creased the number of falls during relapses (Figure 4.13C). Time course experiments showed that HuR silencing drastically reduced locomotor impairment as demonstrated by the significant decrease in the clinical score values (Figure 4.13A, B) and number of falls on day 30 (Figure 4.13C, D).

4.2.2.11. HuR silencing attenuates EAE-associated pain hypersensitivity in the hind paws

In EAE mice, reactive gliosis and neuroinflammation in the spinal cord develop concurrently with robust NP behaviors[154]. Thus, we investigated whether reduction of reactive microglia was coincident with a reduction of pain hypersensitivity by evaluation of the nociceptive thresholds in response to heat and mechanical stimuli. A significant reduction of the mechanical threshold in the bilateral hind paws was observed from day 7 that fully developed on day 14. EAE mice developed a second nociceptive mechanical allodynia peak on day 21 which persisted until study completion (Figure 4.13E). Time course studies showed a relapsing–remitting nociceptive profile also for thermal hyperalgesia. The response latency towards heat stimuli dropped significantly in EAE mice on days 10–14. Mice developed a second thermal hyperalgesia peak on day 25 postimmunization which persisted until the end of the study (Figure 4.13G).

HuR silencing attenuated the EAE-induced mechanical allodynia (Figure 4.13E, F) and drastically reduced thermal hyperalgesia (Figure 4.13G, H) over time. HuR silencing did not modify the animals' pain threshold in non-immunized control mice. dODN administration did not produce any alteration of pain hypersensitivity in comparison with vehicle- or saline-treated mice.

4.2.2.12. Anti-HuR ASO improves general health and body weight loss

EAE mice showed a progressive reduction of body weight that peaked on day 14. A second peak of reduction in the body weights was detected on day 21 postimmunization which persisted up to the end of the experiment (Figure 4.13I). Time course experiments showed that treatment with the anti-HuR ASO counteracted the body weight loss observed in EAE mice (Figure 4.13I, J) and improved the general health of immunized mice. dODN did not influence body weight values in comparison with vehicle- or saline-treated mice.

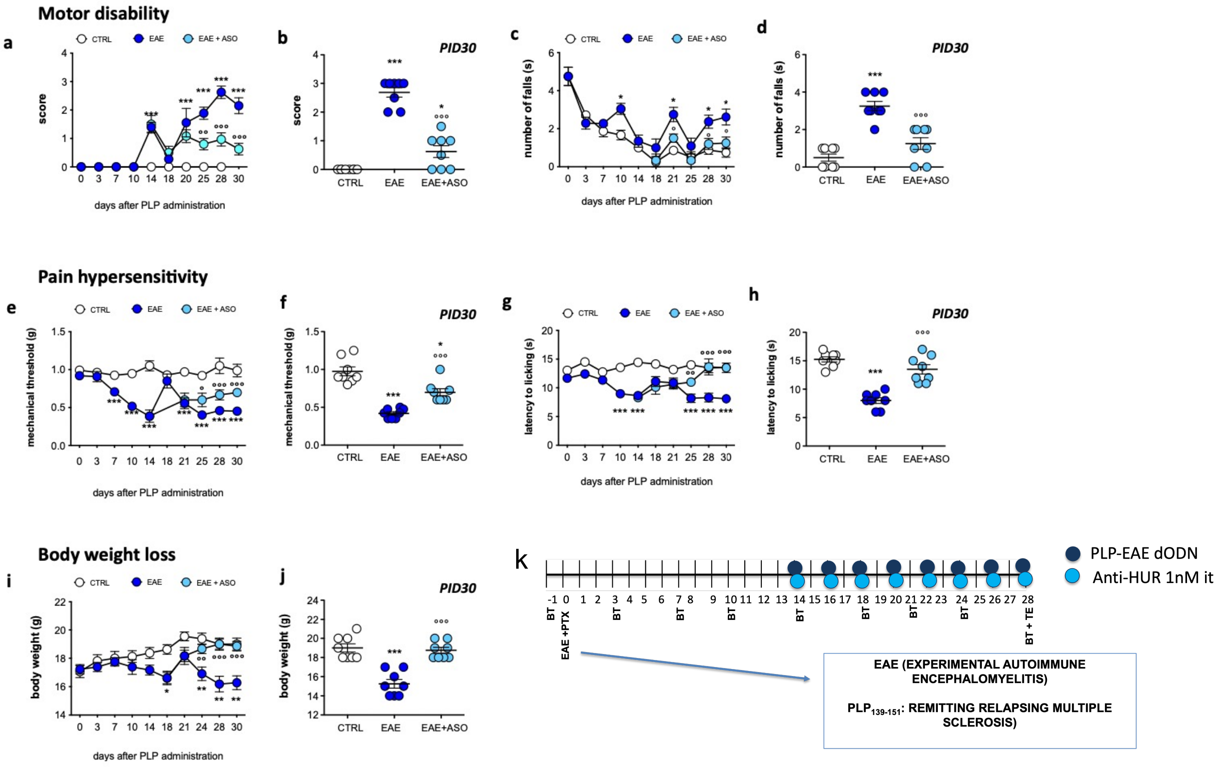

Figure 4.13 Anti-HuR ASO alleviated neurological disturbances in EAE mice. (a) Clinical disease score of PLP139–151-EAE mice compared to control mice (CTRL) showing a relapsing–remitting profile. Attenuation by HuR silencing of the increased disease clinical EAE score. (b) Scatter plot graph for anti-HuR ASO effect on day 30 postimmunization. $^{*}p < 0.05$, $^{***}p < 0.001$ versus CTRL mice (Wilcoxon test); $^{\circ\circ\circ}p < 0.01$ versus EAE mice (Kruskal–Wallis). (c) Progression of locomotor impairment in EAE mice by evaluating the rotarod performance in comparison with CTRL mice. Knockdown of HuR protein attenuated rotarod impairment over time. (d) Scatter plot graph for ASO effect on postimmunization day 30 (PID30). (e) Time course study of mechanical allodynia in EAE mice showing a relapsing–remitting profile. HuR silencing attenuated mechanical allodynia. (f) Scatter plot graph for ASO effect on postimmunization day 30 (PID30). (g) Time course evaluation of thermal hyperalgesia in EAE mice. Anti-HuR ASO alleviated thermal hypersensitivity. (h) Scatter plot graph for anti-HuR effect on postimmunization day 30 (PID30). (i) Time course evaluation of body weight loss of EAE mice in comparison with CTRL mice. Anti-HuR ASO reduced the body weight loss. (j) Scatter plot graph for anti-HuR effect on day 30 postimmunization. ASO-induced effects were

evaluated starting from postimmunization day 14 (first day of ASO treatment). CTRL, dODN- treated nonimmunized mice (n=8); EAE, dODN-treated EAE mice (n=8); EAE + anti-HuR(n=8), anti-HuR ASO-treated EAE mice. (n=8). (k) Representative figure of experimental procedure. *p < 0.05, **p < 0.01, ***p < 0.001 versus CTRL mice; °p < 0.05, °°p < 0.01, °°°p < 0.01 versus EAE mice (2-way ANOVA)

4.2.3. Silencing of the RNA-binding protein HuR promote remyelination in peripheral and central neuropathies model

4.2.3.1. HuD protein expression increases in ipsilateral side of SNI mice spinal cord and attenuates thermal and mechanical allodynia

HuR colocalized with CD11b, a well-known marker of microglia pro-inflammatory phenotype (Figure 4.14A), while HuD colocalized with neurofilament H (NF-H) (Figure 4.14B), a neuronal marker, confirming the different cellular localization of the two ELAVs described in literature38. Anti-HuR ASO reduced thermal (Figure 4.14C) and mechanical (Figure 4.14E) allodynia in SNI mice 7 and 10 days after surgery, while anti-HuD ASO was only effective10 days after surgery. The ASO did not affect mechanical allodynia on contralateral side (Figure 4.14D).

Immunofluorescence analysis showed that 10 days after nerve ligation, an increased level of HuR (Figure 4.14E, red) and HuD (Figure 4.14F, green) compared to the contralateral side can be observed in the ipsilateral side of spinal cord tissue. The administration of ASO against HuR and HuD reduced the expression after i.n. administration. These results were also confirmed by western blotting analysis (Figure 4.14G).

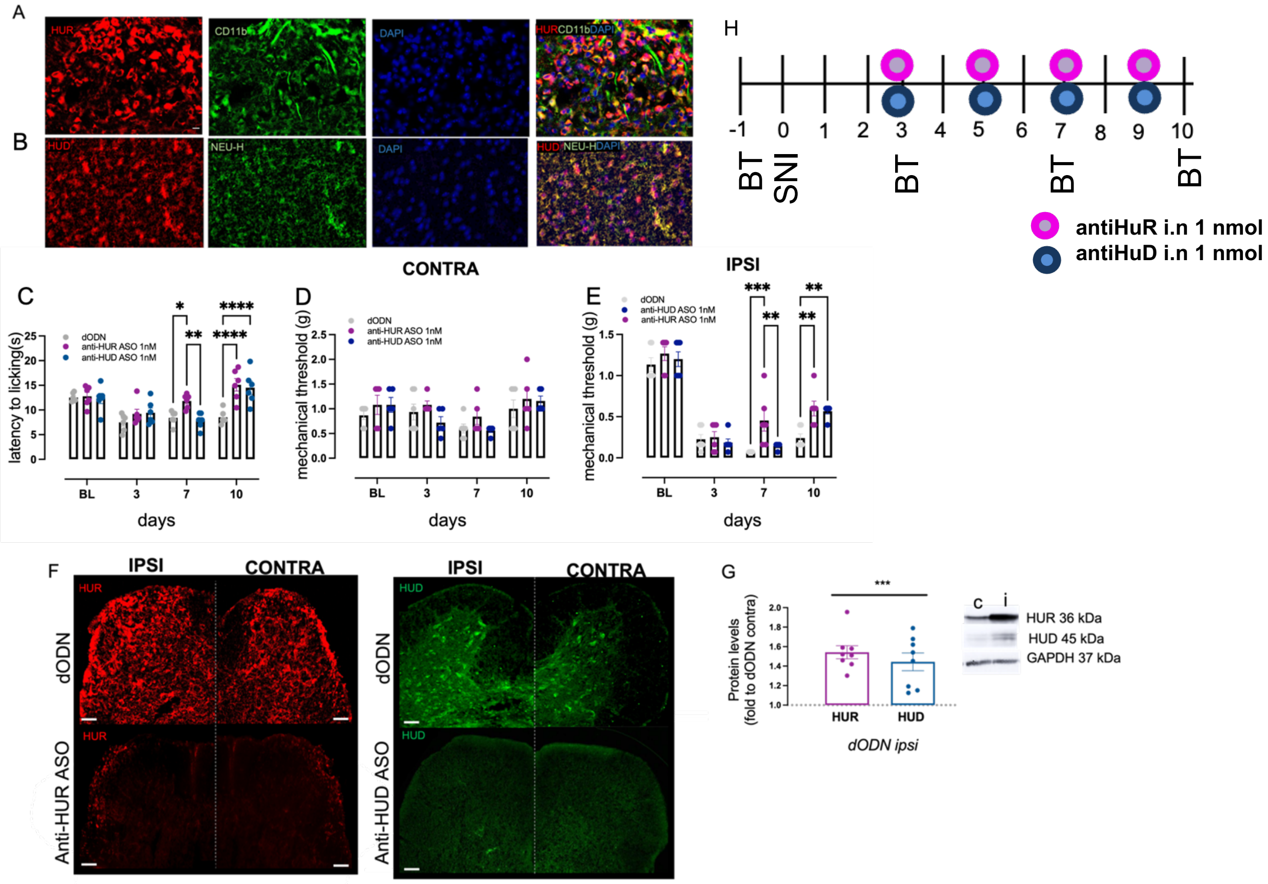

Figure 4.14 Colocalization of (A) HuR (red) with CD11b (green) and (B) HuD (red) with neurofilament H (green) (Mander's coefficient 0.89). HuR and HuD silencing attenuated (C) thermal allodynia. HuR and HuD did not alter the mechanical allodynia in contra hind paw (D) but reduced it in ipsi hind paw (E) in SNI mice, 7 and 10 days after surgery (Two-way ANOVA ***p<0.001, **p<0.01, *p<0.05). (F) HuR (red) and HuD (green) protein levels increased in the ipsi dorsal horn of SNI spinal cord mice compared to the contralateral side. Scale bar 100μm. (G) Quantitative analysis of western blotting experiments performed on spinal cord tissue of SNI mice. (H) Representative figure of experimental procedure: dODN SNI (n=8), anti HuR SNI (n=8) and anti HuD SNI (n=8). BT= behavioral test. (One-way ANOVA ***p<0.001 vs dODN contra). Representative blots are reported. BL=mice the day before starting procedure.

4.2.3.2. HuR-silencing increases central remyelination in SNI mice

A slight difference was observed in myelin basic protein (MBP) expression between ipsilateral and contralateral side in spinal cord tissue of SNI mice. At the same time, anti-HuR ASO increased the levels of MBP, while no effects were reported for anti-HuD ASO (Figure 4.15A). Quantitative immunohistochemical analysis showed a significant increase in LFB immunostaining of the spinal sections from anti-HuR ASO-SNI mice, compared to sham mice and anti-HuD ASO mice, confirming a significant remyelination effect, being the white marking much more evident than the other groups (Figure 4.15B). To identify the possible peripheral remyelination effect on Schwann cells, we quantified the levels of S100 protein levels in sciatic nerve of mice and we observed a reduction of the expression of this protein in the ipsi sciatic nerve of the SNI-mice, while anti-HuR and anti-HuD ASO groups had no effect (Figure 4.15C). Representative images of sciatic nerves show the different intensity of coloration between groups and the higher expression of S100 in the contra group (Figure 4.15D). This could be explained by the route of administration used; indeed, the intranasal administration carries the ASO oligonucleotide directly in the CNS, without affecting the peripheral system. Anti-HuD silencing did not alter the levels of MBP compared to the control group and did not promote the S100 expression.

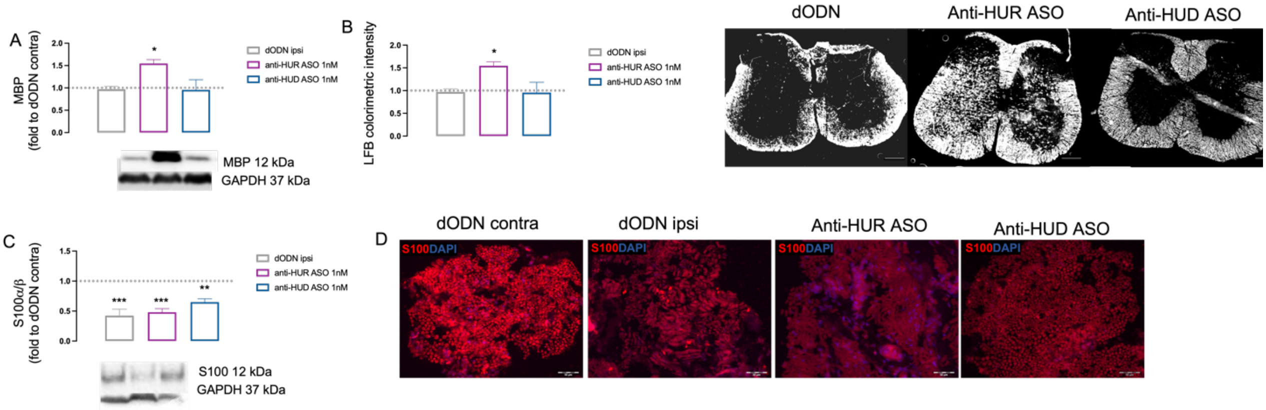

Figure 4.15 (A) Silencing of HuR leads to an increase of MBP, marker of myelin, in spinal cord of SNI mice (One-way ANOVA *p<0.05 vs dODN ipsi). Q(B) uantitative analysis of LFB colorimetric assay and representative image of spinal cord tissue of dODN, Anti-HuR ASO and Anti-HuD ASO (white color correspond to myelin, scale bar 100μm) (One-way ANOVA *p<0.05 vs dODN ipsi). (C) Silencing of HuR and HuD did not alter the expression levels of S100 in sciatic nerve (One-way ANOVA, ***p<0.001 **p<0.01 vs dODN contra). (D) Representative images of the expression of S100 (red) in the ipsilateral side of sciatic nerve in SNI mice. Scale bar 50μm.

4.2.3.3. HuR-silencing reduces mechanical allodynia and locomotor activity in MOG-induced EAE mice

To better characterize and confirm the remyelination effect obtained by the silencing of HuR, we tested the intranasal administration of the anti-HuR and anti-HuD ASO in the EAE model induced by the administration of MOG_{35-55}, resulting in an ascending flaccid paralysis caused by autoreactive immune cells in the CNS[21]. To better understand the pharmacological role of HuR, we also investigated its effects on the PLP-EAE model, which is a model that mimics the relapsing-remitting phase of the disease. MOG-EAE, on the other hand, mimics the more chronic part of the disease, due to severe demyelination.

A significant reduction of the mechanical threshold in the hind paws was observed from day 7 and persisted until day 28 (Figure 4.16A). The thermal hyperalgesia (Figure 4.16B) and a locomotor disfunction (Figure 4.16C) started from 14 days and persisted until 28 days. No significant weight loss was registered in MOG-mice (Figure 4.16D), while the clinical score (Figure 4.16E) was higher than the sham group. Silencing of HuR started from 14 days, every other day until 28 days post immunization. Anti-HuR reduced the mechanical allodynia (Figure 4.16A) and improvement the locomotor activity (Figure 4.16C) produced by MOG model at 28 days from immunization, reporting the value to the shame dODN group. No effects were observed for the other clinical signs: thermal hyperalgesia (Figure 4.16B), weight (Figure 4.16D) and clinical score (Figure 4.16E). The silencing of HuD reverted the effect on locomotor activity (Figure 4.16C) but did not alter the other symptoms starting from 24 days from immunization.

From days 14 we started the intranasal administration of anti-HuR and anti-HuD ASO. At 28-day, anti-HuR ASO completely prevented the mechanical allodynia (Figure 4.16F) and the locomotor behavior (Figure 4.16H) in both the two models. Although only in PLP model silencing of HuR reduced the thermal hyperalgesia (Figure 4.16G) and the clinical score (Figure 4.16L). No differences were observed on weight after treatments. Anti-HuD ASO promotes an improvement on locomotor activity (Figure 4.16H) but had no effects on the other clinical signs.

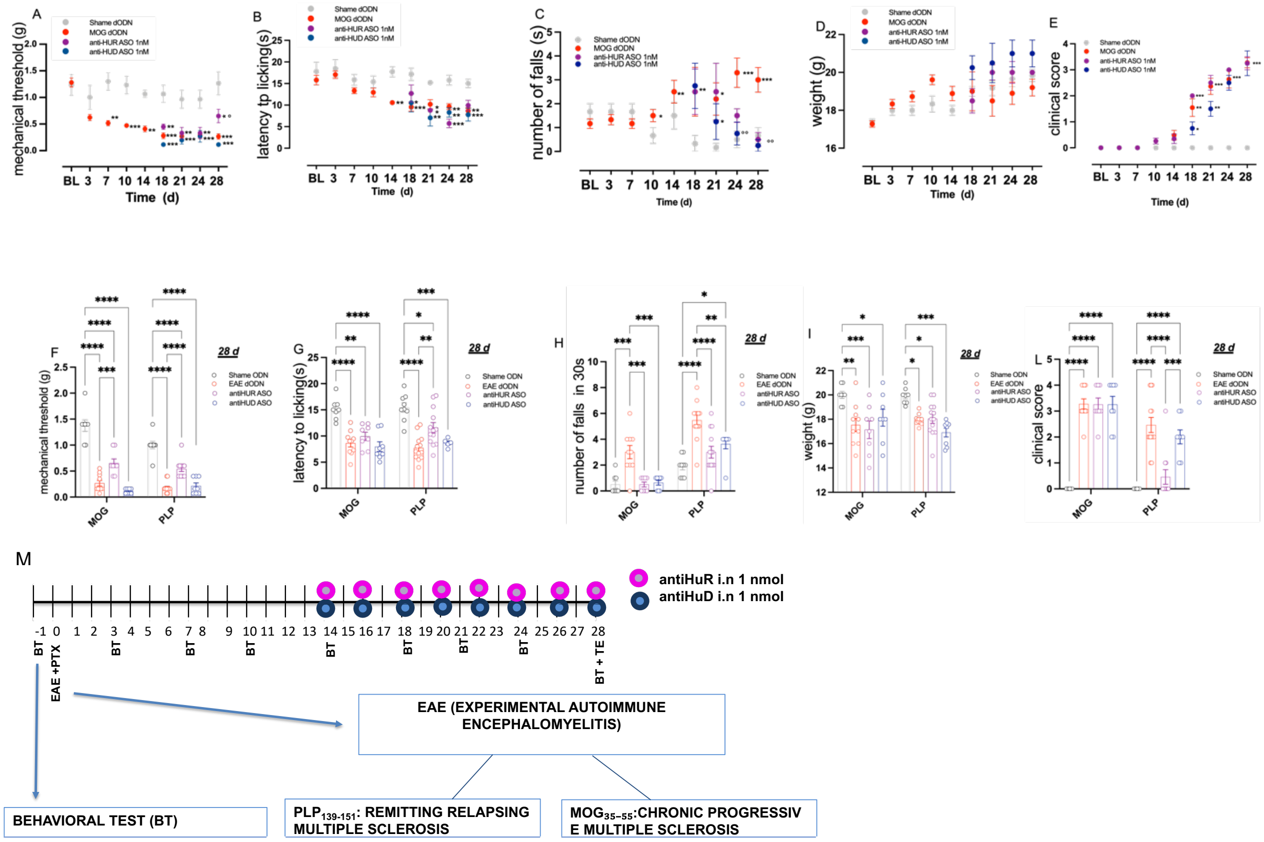

Figure 4.16 Time course of disease progression in the four experimental groups sham dODN (n=8), MOG dODN (n=9), anti-HuR ASO (n=8), anti-HuD ASO (n=8) on the clinical sign: (A) mechanical allodynia (Von Frey filaments), (B) thermal hyperalgesia (hot plate test), (C) locomotor activity (rotarod test), (D) weight variation and (E) clinical score. (Two-way ANOVA ***$p<0.001$, **$p<0.01$, * $p<0.05$ vs sham dODN, °°$p<0.01$, °$p<0.05$ vs MOG dODN). Comparison of the effect of sham dODN, MOG dODN, anti-HuR ASO, anti-HuD ASO on clinical sign observed in the PLP-EAE model (remitting relapsing multiple sclerosis:sham dODN n=9, PLP dODN n=14, anti-HuR ASO n=14 anti-HuD ASO n=8) and MOG-EAE model (chronical progressive multiple sclerosis) on (F) mechanical allodynia, (G) thermal hyperalgesia, (H) locomotor activity, (I) weight and (L) clinical score. (M) Representative image of experimental protocol.

(Two-way ANOVA ****$p<0.001$, ***$p<0.001$, **$p<0.01$, *$p<0.05$)

4.2.3.4. Anti-HuR ASO inhibits BBB permeability during EAE, but does not alter peripheral and central inflammation

One of the major features of EAE and MS is the dysfunction of the BBB. Under normal conditions EB dye conjugates with serum albumin is not able to cross the BBB, but when BBB is disrupted, EB can penetrate in the CNS, which indicates a progression of the disease[21]. An increase of dye penetration across the BBB was detected in the brain (Figure 4.17A) and spinal cord (Figure 4.17B) of MOG mice 28 days post-immunization. The brain and spinal cord images (white intensity) showed that the degree of EB leakage was increased in EAE mice. The effect produced by anti-HuR and anti-

HuD ASO was evaluated. Silencing of HuR largely decreased the EB content in both brain and spinal cord, returning to values comparable with the baseline level of the control mice. Anti-HuD reduced the dye in the brain, but not in the spinal cord tissue. The plasma level of cytokines was determined and an increase of IL17 (Figure 4.17C), TNF-α (Figure 4.17E), and IL6 (Figure 4.17F) was observed in MOG mice, while IL1β plasma levels were not affected (Figure 4.17D). Contrarily to PLP mice[22] no effects were observed on the modulation of peripheral inflammation in MOG mice treated with anti-HuR. Although there is a broad range of neurological symptoms and different disease progressions, a key hallmark of MS is neuroinflammation. In spinal cord tissue of PLP (Figure 4.17G) and MOG (Figure 4.17H) mice an increase of IBA-1 protein, a microglia marker, expression was observed, and this effect was reverted by the silencing of HuR reverted. Differently from PLP mice, silencing of HuR did not alter the effect on IBA-1 in MOG mice. This effect was also confirmed by immunofluorescence analysis, in which CD11b protein (a pro-inflammatory microglia marker) was increased in both models. However, silencing of HuR reverted this effect only in PLP mice and not in MOG mice (Figure 4.17I-L). These data suggest that the mechanism of action of anti-HuR ASO in modulating pain behavior is different in the two models.

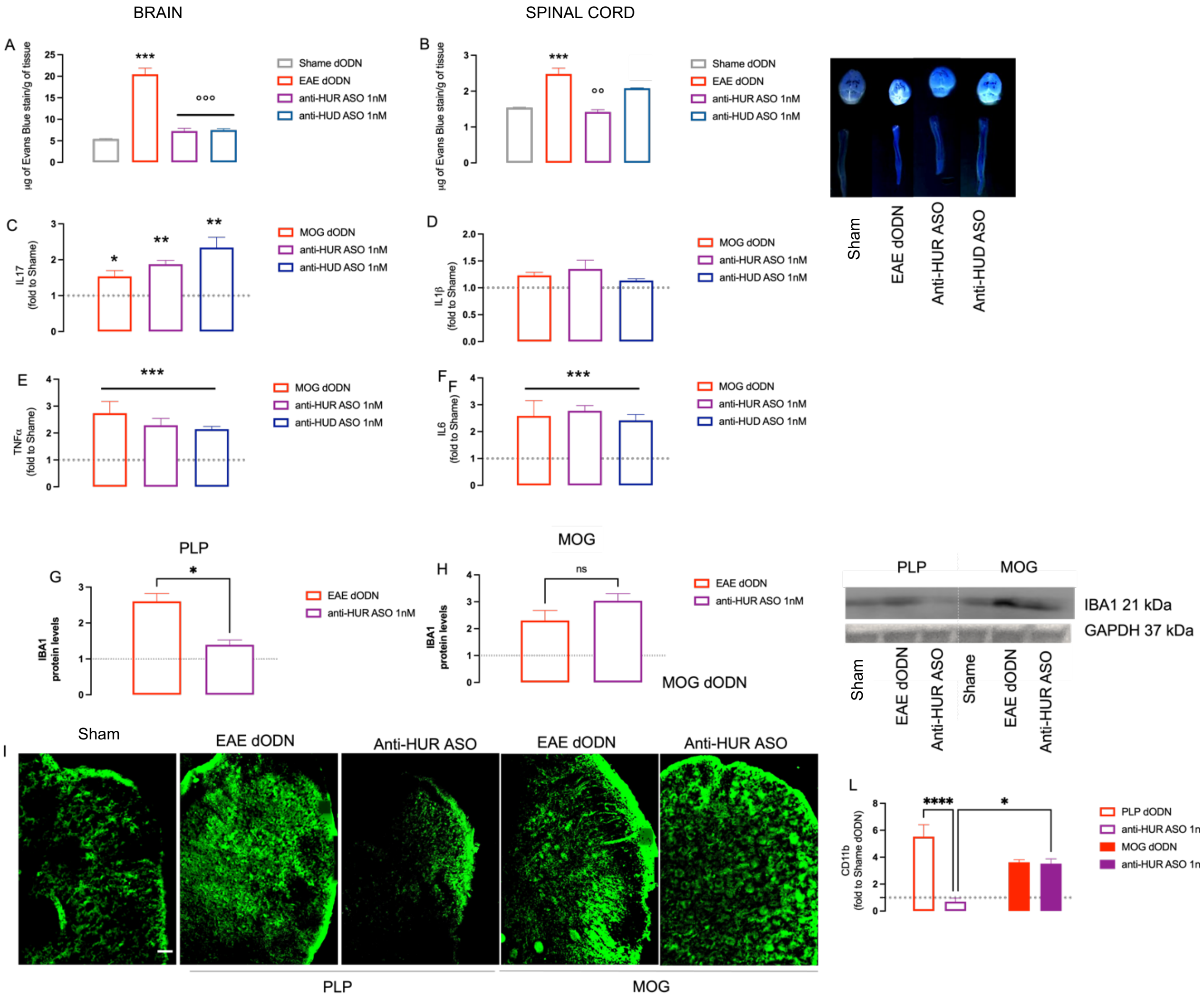

Figure 3.17 Anti-HuR ASO treatment inhibition of BBB permeability in the brain and spinal cord of EAE mice. The amount of extravasated Evans blue (EB) dye was quantified in (A) the brain and (B) lumbar spinal cord, 28 days after immunization. Representative pictures of brain, and spinal from sham, MOG-EAE dODN, anti-HuR ASO-and anti-HuD ASO treated EAE mice are displayed. White color indicates extravasated EB dye from blood vessels. (One-way ANOVA ***p<0.001 vs sham, °°°p<0.001 °°p<0.01 vs MOG dODN). Plasma levels of (C) IL-17, (D) IL-1β, (E) TNF-α, and (F) IL6 were increased in EAE mice. Anti-HuR treatment did not produce any significant modification of cytokines levels. (One-way ANOVA ***p<0.001, **p<0.01, *p<0.05). Quantification of IBA1 in (G) PLP and (H) MOG EAE dODN on spinal cord tissue of MOG-EAE and anti-HuR ASO. (One-way ANOVA *p<0.05). (I) Representative images showing immunofluorescence staining for CD11b in the spinal cords of sham, EAE dODN, and anti-HuR ASO-treated mice in PLP and MOG models, 28 days post-immunization. (L) Quantification of the immunofluorescence images (scale bar 100 µm). (Two-way ANOVA ****p<0.001 *p<0.05)

4.2.3.5. Anti-HuR ASO increases Neurofilament H, GAP43 and MBP in the spinal cord of MOG-EAE mice

In EAE mice we observed a strong reduction of proteins linked with remyelination and neuronal regeneration. Indeed, this model is widely used for generating animal model of chronical myelin loss. Neurofilament H has been demonstrated to be increased in the CSF of patients with inflammatory, degenerative, vascular, or traumatic injuries[155]. GAP43 is a presynaptic protein that induces expression of protein involved in axonal growth, and it could serve as a biomarker of axonal regeneration capacity in degenerative disease[156]. MBP is one of the most abundant components of myelin in CNS[157]. In the spinal cord tissue of PLP mice we did not observe a significant reduction of neurofilament H (Figure 4.18A), GAP43 (Figure 4.18B), and MBP (Figure 4.18C) and the silencing of HuR overexpressed the neurofilament H but did not produce any significant effect on the other two targets. Differently, we observed a loss of Neurofilament H (Figure 4.18D), GAP43 (Figure 4.18E), and MPB (Figure 4.18F) protein levels in the spinal cord tissue of MOG-mice. Silencing of HuR reversed the neuronal degeneration and the demyelination induced by MOG-EAE, increasing the levels of all these regenerative markers with a noticeable regulation of MBP (Figure 4.18F). Consistently with the results obtained in the peripheral neuropathy, anti-HuD ASO had no effects. Quantitative immunohistochemical analysis of LFB highlighted and confirmed the increase of myelinization in anti-HuR MOG-mice compared to the MOG group (Figure 4.18G).

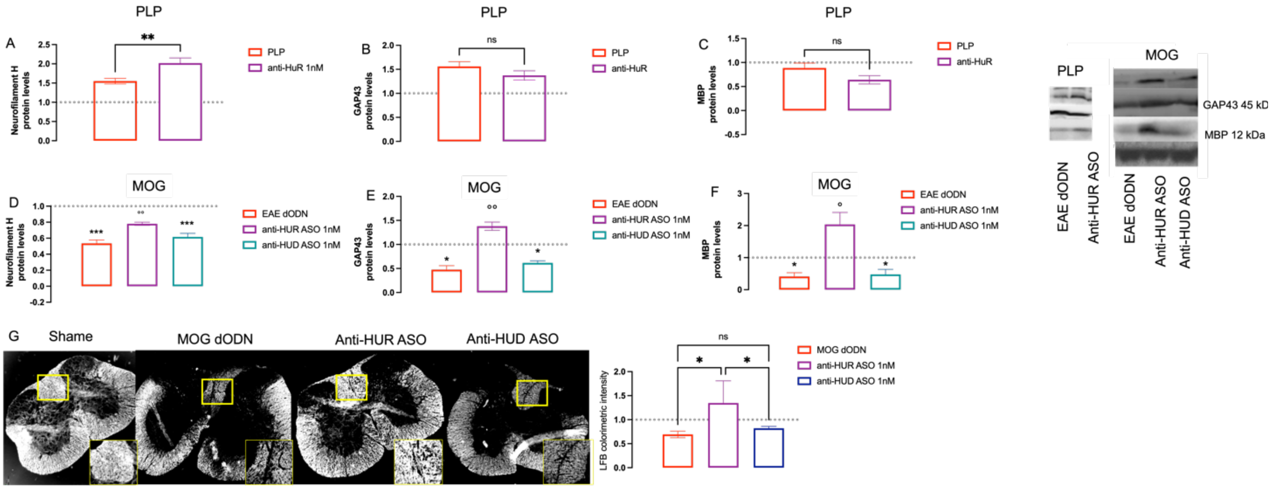

Figure 4.18 Effects of anti-HuR ASO in (A) neurofilament H, (B) GAP43, and (C) MBP in spinal cord of PLP-EAE mice (One-way ANOVA **p<0.01). Evaluation of anti-HuR ASO and anti-HuD ASO in MOG-EAE mice on (D) neurofilament H, (E) GAP43, and (F) MBP. (G) Quantitative analysis of LFB colorimetric assay and representative image of the spinal cord tissue of sham, MOG dODN, Anti-HuR ASO, and Anti-HuD ASO (white color correspond to myelin, scale bar 100µm) (One-way ANOVA, *p<0.05)

4.2.3.6. Higher levels of HuD correspond to higher levels of MBP in spinal cord of SNI and MOG mice

To find a connection between neuronal and no-neuronal ELAV/proteins, we investigated the possible modification of the levels of HuD proteins caused by HuR silencing. Interestingly, the expression of HuD and MBP showed a similar trend in the three different models, in MOG group, in which low levels of HuD correspond to a low level of MBP. Thus, the more intense the demyelination in the model, the more evident the relation between these two proteins. Anti-HuR ASO upregulated the expression of HuD in MOG mice (Figure 4.19A), reverting the effect induced by the model. At the same time, it promoted myelination, increasing the MBP protein levels (Figure 4.19B). Qualitative immunofluorescence assay showed the overexpression of GAP43 (red) and HuD (green) in Anti-HuR ASO, compared to the MOG group and anti-HuD ASO (Figure 4.19C). A colocalization quantification indicated that in Anti-HuR ASO, the levels of GAP43 completely colocalized with HuD protein, suggesting an indirect remyelination effect caused by HuR silencing (Mander's Coefficient 0.89±0.03).

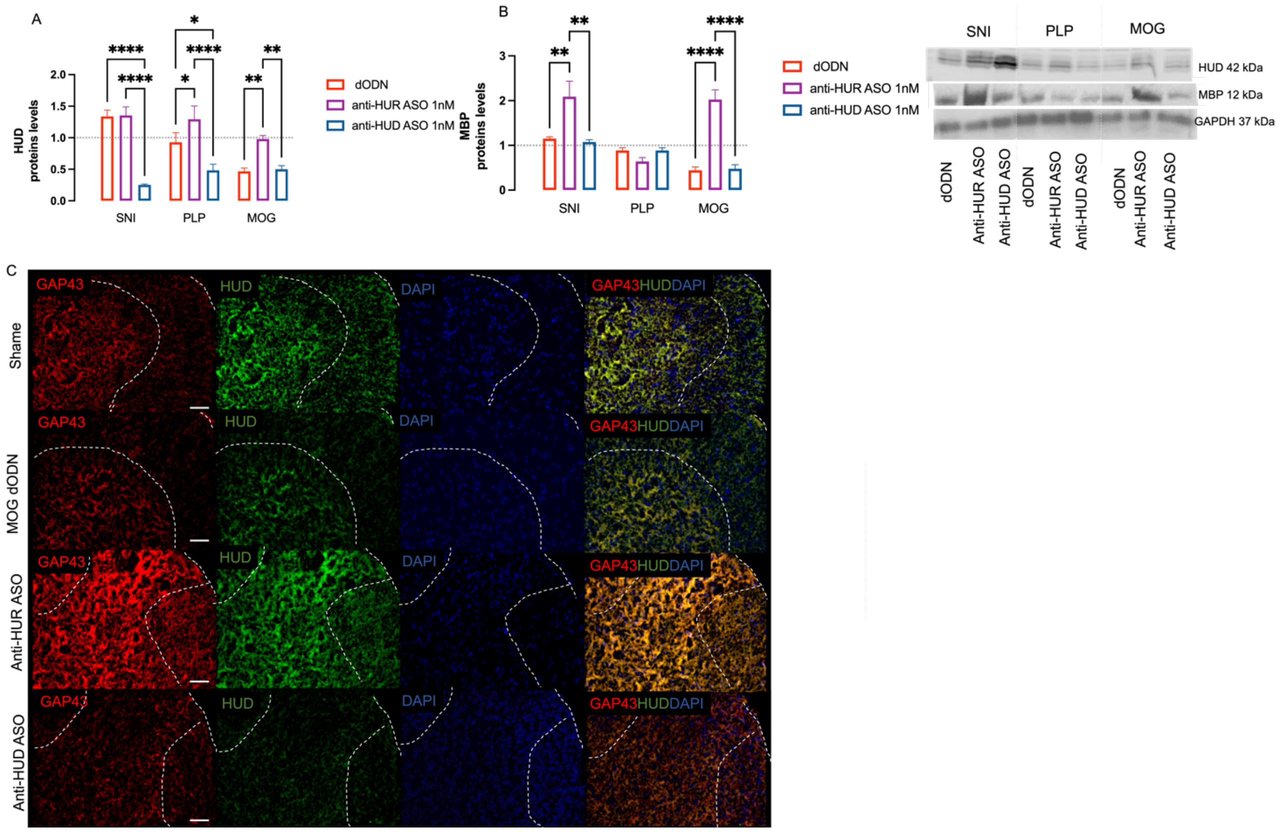

Figure 4.19 (A) Comparison of the modulation of HuD expression of dODN, anti-HuR ASO, and anti-HuD ASO in the three different models: SNI, PLP, and MOG. (B) Variation of the modulation of MBP expression of dODN, anti-HuR ASO, and anti-HuD ASO in the three different models: SNI, PLP, and MOG. (Two-way ANOVA ****p<0.001,

**$p<0.01$, *$p<0.05$). (C) Colocalization of GAP43 (red) and HuD (green) in sham, MOG dODN, anti-HuR ASO, and anti-HuD ASO (Manders coefficient 0.97).

4.3. Discussion

In the first part of this study, we showed the functional relation of HuR overexpression in the spinal cord to trauma-induced NP in SNI mice. The i.n. delivery of an anti-HuR ASO efficiently reduced spinal HuR overexpression, attenuated pain hypersensitivity, and reduced the neuropathy-induced spinal microgliosis through the modulation of MAPK phosphorylation. Antisense oligonucleotides have been widely investigated in clinical trials, and six of them have been approved for marketing by the Food and Drug Administration because clear clinical benefits have been assessed[158]. Despite these exciting prospects, the difficulty to deliver ODNs to the CNS because of their poor capability to cross the BBB limits the application of ODN-based silencing strategies in pathological conditions that require CNS penetration. Antisense oligonucleotide-based therapies require an invasive delivery, such as i.t. or intracerebroventricular (i.c.v.) administration. To avoid these unpleasant delivery methods, some chemical modifications and new formulations are under development to facilitate BBB crossing with systemic administration. However, this additional chemistry could affect efficacy and elevate toxicity. Therefore, another approach to optimizing delivery of ODNs through the BBB is i.n. administration106. Anti-HuR also shifted the M1 proinflammatory microglia to the M2 anti-inflammatory microglia by increasing the levels of the anti-inflammatory cytokine, IL-10. I.n. anti-HuR ASO, by inhibiting microglia-mediated spinal neuroinflammation and promoting an anti-inflammatory and neuroprotectant response, might represent a noninvasive promising perspective for NP therapy and it would have implications in other neuroinflammatory conditions such as MS and spinal cord injury.

For this reason, in the second part of this work we elucidated the role of post-transcriptional regulation of gene expression in the PLP-EAE-related neuroinflammation, by investigating the role of the RBP HuR, a member of the ELAV family. The results obtained showed that anti-HuR ASO intrathecal administration reduced spinal inflammatory infiltrates, proinflammatory cytokine levels, BBB disruption, and proinflammatory microglia activation; promoted the activation of CD206-expressing anti-inflammatory microglia; and alleviated the severity of EAE clinical signs. Many similarities between EAE and MS have been described, including clinical course, pathological CNS lesions, glial activation, and axonal demyelination[159]. Thus, it is plausible that targeting HuR might represent a promising perspective to control neurological disturbances in MS patients. Due to its RBP nature, HuR can simultaneously modulate mRNAs involved in inflammatory and regenerative phenomena, representing an innovative and promising target. Available MS therapies, which halt the inflammatory and immune response, do not always stop disease progression and cumulative neurological disability, and none of the current treatments halts or cures the disease[160]. Thus, evidence suggests that treatment of MS should be based on a combination of anti-inflammatory, regenerative, and neuroprotective strategies[161].

For this reason, the aim of the third part of this study was to target the RBP HuR to reduce symptoms and to promote myelination associated to NP, in the attempt to find a therapy that not only control the symptoms but also slow down the progression of the disease. To investigate the effect of ELAV proteins, we tested anti-HuR ASO and anti-HuD ASO in a peripheral model of NP (SNI). Indeed, HuD promoted neuronal regeneration following nerve injury by stimulating BDNF and GAP-43. BDNF is important for axonal and neuronal growth and regeneration, GAP-43 plays a pivotal role in neurite formation, regeneration, and neuroplasticity[29,162]. We confirmed the colocalization of HuR with microglia marker[34] and HuD with neuronal regeneration markers in mice with neuropathy[163]. HuR- and HuD-silencing reduced the mechanical and thermal allodynia in mice with neuropathy. The nociceptive behavior was consistent with previously published works[117], and was confirmed with *in vitro* spinal cord analysis, in which we observed an increase of HuR and HuD protein expression in the ipsilateral side of dorsal horn. Thus, these results suggest that an increase of protein expression is related to an aggravation of symptoms in mice. In SNI, we did not observe a reduction of central myelin content after 10 days but only a drastic reduction of Schwann cells marker, and the silencing of HuR induced the overexpression of myelin but did not affect the peripheral loss of S100. This could be explained by the route of administration used; indeed, the intranasal administration carries the ASO oligonucleotide directly in the CNS, without affecting the peripheral system. Anti-HuD silencing did not alter the levels of MBP compared to the control group and did not promote the S100 expression. Demyelination, a loss of the myelin sheath that lines the axon fibers, causing impaired neuronal transmission, is an unsolved problem among the causes of NP. Frequently, a persistent and unresolved inflammation process is at the basis of demyelination, so neuroinflammation and demyelination represent important targets for finding effective candidates for NP control[17].

To better investigate the role of HuR in myelination process, anti-HuR and anti-HuD were tested in a chronic demyelination model, the MOG-EAE. The intrathecal administration of anti-HuR ASO was already tested by us in the PLP-EAE model, in which the silencing of HuR was able to reduce all the clinical signs considered: weight loss, mechanical allodynia, thermal hyperalgesia, locomotor activity, and gross behavior[22]. Following intranasal administration, a similar behavior was observed in the remitting-relapsing model induced by the inoculation of the PLP peptide in the animal. In MOG, on the other hand, the silencing of HuR reduced mechanical allodynia and improves motor function but did not alter the other clinical signs taken in consideration. While the silencing of HuD only brings an improvement from the locomotor point of view but not in pain. A recent clinical study on PBMC of 52 MS patients showed that the level of HuR is lower than that of controls and decreases over time with the progression of the disease[117]. This is consistent with our observation in the plasma of MOG animals, in which there is no effect on plasma cytokines, unlike in that of PLP animals. Although there are no effects on plasma cytokines, HuR silencing induced a protection against the alteration of BBB permeability, reducing the presence of EB probe in brain and spinal cord tissue compared the control group. Also, no effect was observed on the expression of the typical markers used to indicate microglia pro-inflammatory phenotype in MOG animals, contrarily to what we observed in the spinal cord of PLP animals. This different effect in the two models can be related to the fact that PLP represents the initial stages of the disease, in which central inflammation is much more consistent and in an active phase, while MOG represents the final part of the disease in which inflammation is already in the chronic phase. Since HuR is predominantly expressed at the microglial level when it assumes a proinflammatory phenotype, its effect on the animal phenotype will be more evident in the early stages of the disease. At the same time, no changes in neuronal regeneration markers were observed in the PLP model, while demyelination becomes more evident in the MOG model. This effect is consistent with the available literature. Indeed, patients diagnosed with relapsing-remitting MS have less marked axonal damage with symptoms that have an intermittent trend over time, while patients with progressive MS have a higher axonal damage and loss of myelin which, when chronic, can no longer recover, and represent the most complex form of this neurologic disorder. HuR silencing overexpressed neurofilament H, GAP43, and myelin in MOG mice, contrarily to HuD silencing, which by stabilizing the corresponding mRNAs of these proteins, further reduces their expression[164]. This remyelination effect appears to be related to the neuronal modulation of HuD. In fact, in the ASO group of anti-HuR animals we observed an increase of HuD which corresponds exactly to an increase in the levels of MBP and GAP43, suggesting that a reduction of HuR in a model of chronic demyelination such as MOG, can increase the myelination process through the increase of the expression of HuD, which stabilizes and over-expresses the neuronal regeneration markers, such as GAP43 and MBP. Still, how the two ELAVs manage to communicate remains to be clarified.

4.4. Conclusion

Intranasal administration of anti-HuR ASO can simultaneously modulate mRNAs involved in inflammatory and regenerative phenomena, which makes it an innovative and promising target. Here, we showed that investigating the robust anti-inflammatory capability of HuR, together with the neuronal effects of nELAV, could represent an important step to better understand the pathophysiological role of these proteins. HuR might represent a potential target for novel drug candidates for slowing down the progression of NP-related diseases.

Chapter 5

Comorbidities of neuropathic pain and the role of senescent microglia

5.1. Introduction

Anxiety, depression, cognitive impairment, and other mood disorders are comorbidities that characterize approximately 34% of patients with NP, affecting the patient's quality of life. However, there are no effective and safe treatments able to manage these comorbidities[165]. The onset of these comorbidities can drastically worsen patients' quality of life, exacerbating the painful condition. Microglia is strongly implicated in several central pathological conditions including major depressive disorder (MDD), anxiety disorders, and post-traumatic stress disorder (PTSD)[166].The most important data come from preclinical animal studies, where hyperactivation of microglia with high levels of pro-inflammatory cytokines was detected in multiple brain regions during psychiatric pathological conditions. Indeed, microglia not only plays a key role in synaptic remodeling in the postnatal phase, but also carry out their activity in adulthood, thus it may also influence synapse stability in neuronal circuits associated with cognitive and mnemonic abilities[167]. Several studies have shown that during MDD there is a significant activation of microglia in depression-related brain regions such as the prefrontal cortex and anterior cingulate cortex[168]. In such models, where the pathological condition is induced by stimulation with bacterial lipopolysaccharide (LPS), inhibition of neuroinflammation alleviates psychological symptoms[169]. The stimulation performed induces a condition of chronic stress in animals such as to generate symptoms of depression associated with increased microglia activity and increased levels of activation markers such as IBA-1 in many sensitive brain areas. In the same areas, an increase in IL-1β levels was seen, which correlates with a pro-inflammatory M1-type microglial activation[170]. IL-1β is an inflammatory cytokine, the excessive levels of which in the hippocampus contribute importantly to memory impairment. A temporary increase in cytokine levels is functional for mnemonic processes, but if persistent, it can lead to an impairment of these processes[171]. At the same time, in animal models subjected to depression, it was found that in this area of the brain, after an initial activation of microglia, an apoptotic decline of these cells and a reduction in activity caused precisely by a reduction in numbers is established, about five weeks later. In fact, stimulation with factors that promote microglial proliferation partially or totally reverses depressive behavior, suggesting that microglia stimulators can be used as fast-acting antidepressants in pathological conditions originating from stress[172]. Constant and uncontrolled increases in microglial cell activity result in the loss of normal physiological microglial activity, with microglial senescence. Indeed, microglial aging may actively contribute to the development of neurodegenerative diseases, including Alzheimer's disorder (AD) or Parkinson's disorder (PD), due to reduced neuroprotective function, increased neurotoxicity, and altered responses to stimuli[173]. Hence, in this work we investigated the timing of the onset of the various comorbidities associated with peripheral NP and their correlation with the presence of anxiety, depression, or memory variation of cellular senescence (Table 5.1). At the same time, we optimized an *in vitro* model of microglial senescence able to reproduce the clinical condition in patients with neuropathy and associated anxiety, depression, and memory loss.

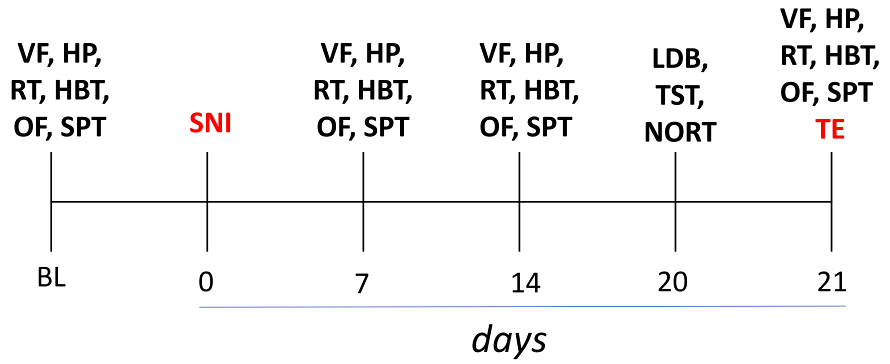

Table 5.1 Schematic representation of SNI model and tests. The experimental groups are: CTRL mice (n=21) that were not operated, and SNI mice (n=25). TE = tissue extraction, BL = baseline

5.2. Results

5.2.1. Time course of NP development and locomotor disfunction in SNI mice

To confirm that animals with neuropathy in the used cohort developed the symptoms associated with NP, we assessed mechanical allodynia, thermal hyperalgesia, and locomotor activity once a week. SNI-mice developed severe mechanical allodynia (Figure 5.1A) and thermal hyperalgesia (Figure 5.1B) as early as 7 days after surgery, that persisted until day 21 after surgery. The animals also developed motor impairment, measured by the rotarod test, as the SNI-animals fell more times in 30 seconds than the control animals, as early as 7 days after the operation. Animals appeared to have a slight recovery after 14 days but then worsen again after 21 days (Figure 5.1C). Locomotor activity was also assessed using the hole board test, in which both spontaneous activity (planes) and exploratory function (holes) are considered. SNI animals' spontaneous mobility did not change, differently from exploratory ability (Figure 5.1D).

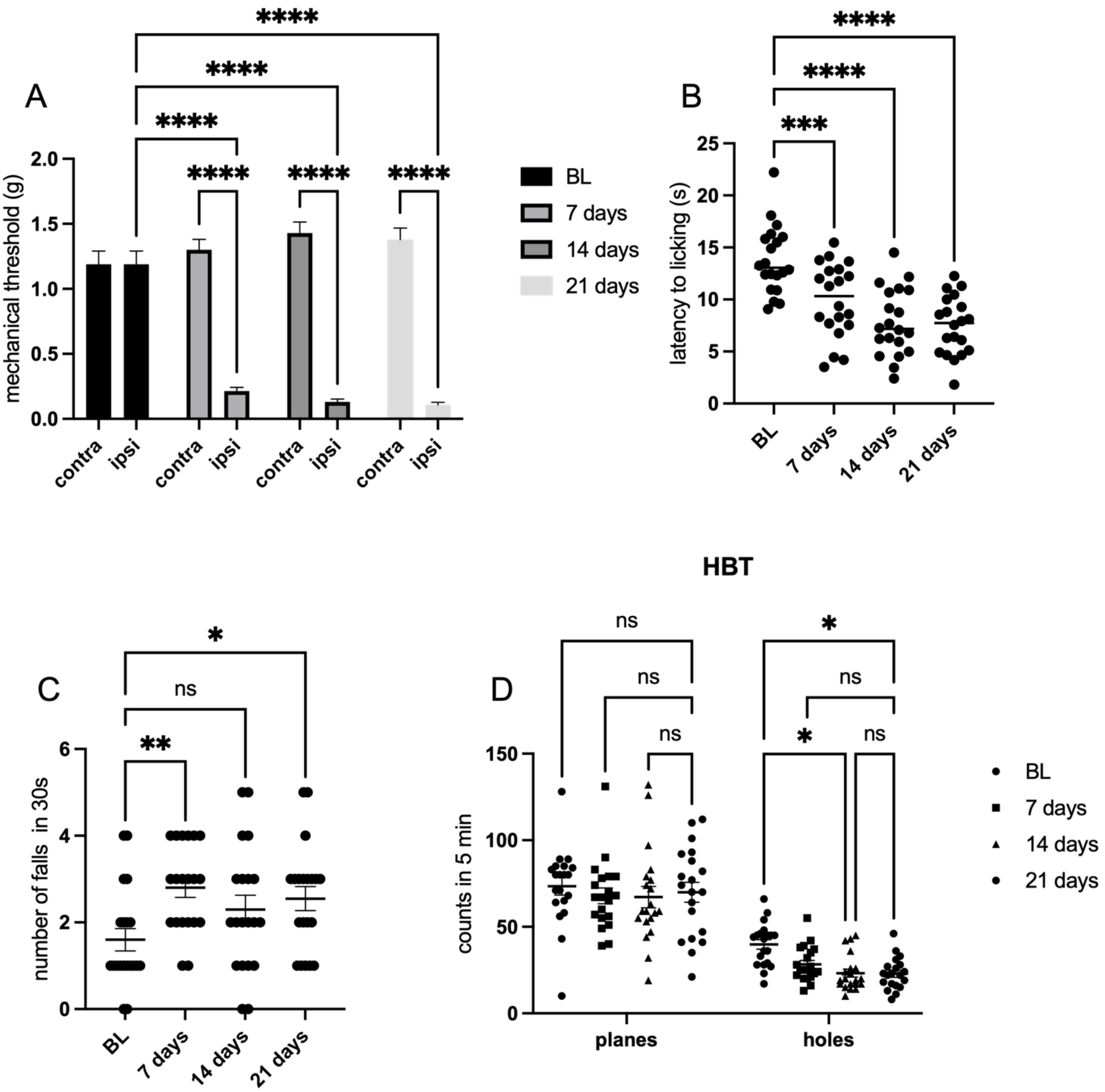

Figure 5.4 Time course of (A) mechanical allodynia (Von Frey filaments), (B) thermal hyperalgesia (Hot Plate test), (C) locomotor activity (Rotarod test) and (D) spontaneous mobility and exploratory activity (Hole board test) of SNI mice at 7, 14, and 21 days after surgery. One-way ANOVA $***p<0.001$, $**p<0.01$, $*p<0.05$.

5.2.2. Assessment of the onset of anxiety-like symptoms in animals with neuropathy

To evaluate the occurrence of anxiety in animals, the open field test (OF) was performed and repeated once a week for four weeks. The OF is one of the few tests that can be repeated on the same animal for the control of anxiety, because in this test the animal assumes a completely spontaneous behavior. In fact, in this test the animals are placed in a box with walls and the time that the animals remain in the center of the box is registered as an indication of the state of anxiety of the animals. The SNI animals developed anxiety starting from day 14 after surgery as showed by the reduction of the time spent in the center of the box, compared to time 0 (BL). This type of behavior was maintained until day 21 after surgery (Figure 5.2A). On day 21 after the operation, we confirmed the anxious symptomatology of the animals by means of the light dark box test (LDB), a test that evaluates the time spent by the animals in the light versus dark part of the box and the number of transitions the animals make to switch between compartments. SNI animals spent less time in the light than control animals, confirming an anxious state in operated versus non-operated animals (Figure 5.2B). In contrast, SNI did not appear to alter the number of transitions (Figure 5.2C).

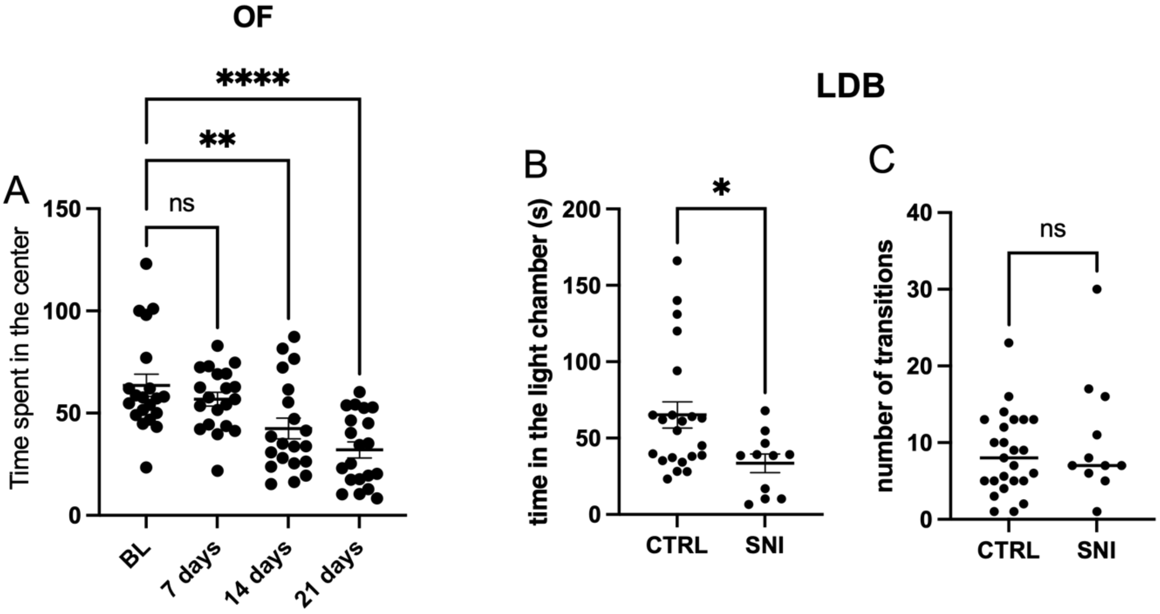

Figure 5.5 Time course of anxiety-like symptoms in SNI mice measured with (A) open field test (OF) and (B, C) light dark box (LDB). One-way ANOVA; Student's t-test ***p<0.001, **p<0.01, *p<0.05.

5.2.3. Evaluation of the onset of similar depressive symptomatology in animals with neuropathy

Aside with the evaluation of anxiety-like symptoms, we also assessed the occurrence of symptoms associated with depression. To evaluate the appearance of depression, we performed once a week the splash test (SST), a test in which the animal is placed inside a box and wet on the back with a 10% sucrose solution. The test has a total duration of 5 min, during which the time spent by the animal cleaning itself is measured, which will be inversely proportional to its depressive state. This is because, in a state of tranquility, the mouse will tend to take more care of its appearance.

SNI animals seem to develop depression-like symptomatology as early as 7 days after surgery, which persisted at 14 and 21 days (Figures 5.3A). At day 21, we performed the tail suspension test (TST). During the 6 min of the test, the first 2 min, significant of the basal depressive state of the animal, and the next 4 min, by which it is possible to evaluate the antidepressant effect of a drug, are initially measured. As showed in Figure 5.3B, SNI animals have a basal depressive-like symptomatology, while in the following 4 min there is no significant difference with the control animals (Figure 5.3C).

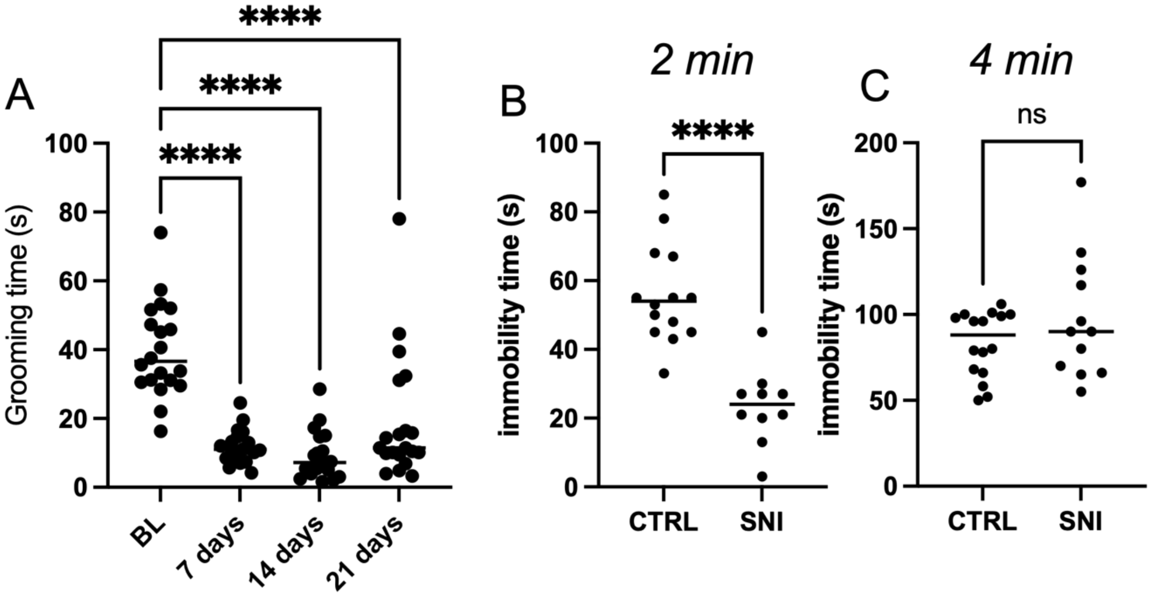

Figure 5.6 Time course of depression-like symptoms in SNI mice measured with (A) sucrose splash test (SST) and (B, C) immobility time (TST). One-way ANOVA; Student's t-test ***p<0.001, **p<0.01, *p<0.05.

5.2.4. Effect of the operation on the mnemonic state of SNI animals

The alteration of memory capacity was assessed using the novel object recognition test (NORT) test. In the training session of the NORT (internal control), the total time spent exploring both objects by SNI mice was comparable to that of the control mice group (Figure 5.4A). In the retention session (24h after the first session), the evaluation of the exploration times between the training object and the novel object illustrated that SNI treatment increased novel object (Figure 5.4B) and familiar object (Figure 5.4C) exploration time, compared to control mice, suggesting a mnemonic alteration. The discrimination index (DI) of SNI mice were comparable to those of control mice, showing that SNI did not produce any detrimental effect on recognition memory (Figure 5.4D).

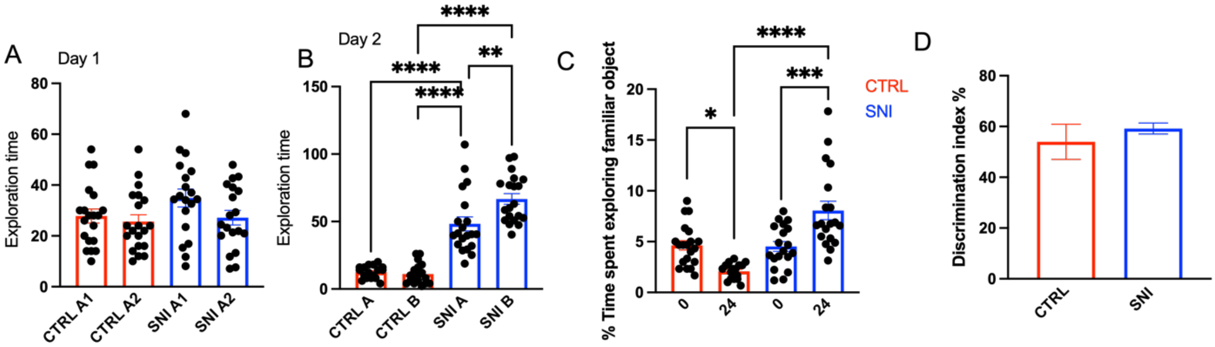

Figure 5.4 Evaluation of cognitive impairment in SNI mice measured with novel object recognition test (NORT). The parameters that we used are the exploration time at (A) day 1and (B) day 2, after 24h from the baseline condition. Comparison of (C) the time spent exploring the familiar object and of (D) the discrimination index between CTRL and SNI mice. One-way ANOVA ****p<0.0001***p<0.001, **p<0.01.

5.2.5. β-galactosidase increased in spinal cord and hippocampus tissue of SNI mice

As senescence and microglial activation seems to be involved in the physiopathology of both anxiety and pain[174], we investigated these conditions in the spinal cord and hippocampus. The main marker of senescence is the β-galactosidase, which increase in the CNS is a sign of cellular aging. In spinal cord tissue (Figure 5.5A) and hippocampus (Figure 5.5B) of animals 14 days and 28 days after surgery we observed an increase of β-galactosidase protein expression.

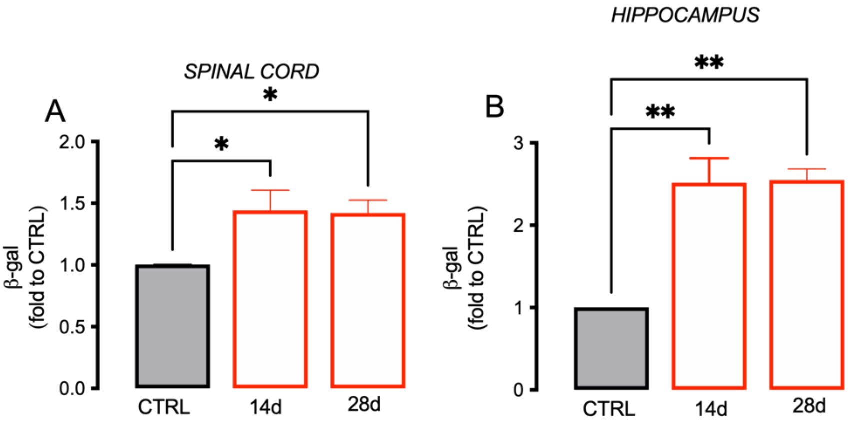

Figure 5.5 Increased expression of ß-galactosidase in (A) spinal cord and (B) hippocampus tissue of SNI mice, 14 and 28 days after surgery, compared to the CTRL group. One-way ANOVA; ***p<0.001, **p<0.01, *p<0.05.

5.2.6. Optimization of an in vitro model of microglia-senescence

As already emphasized, microglia, when subjected to continuous harmful stimuli, tends to change not only in morphology but also in activity, manifesting a hyperactivation related to increased expression of inflammatory factors that in the long term can damage the surrounding neuronal bodies, thus promoting the onset of neurodegenerative diseases[175]. A microglial senescence model was optimized by stimulating murine BV-2 cells with three different concentrations of LPS (100, 250, 500 ng mL^{-1}) for 4 h per day, at various time intervals (24, 48, 72 h, 7 days and 10 days), over a total period of 10 days. Several factors were considered to select the optimal combination:

1. Expression of β-galactosidase.
2. Expression of factors related to senescent-associated secretory phenotype (SASP).
3. Development of nuclear senescence-associated heterochromatin foci (SAHF).
4. Cell viability and morphology.

β-galactosidase is a major marker associated with cellular aging. LPS 100 ng mL^{-1} did not alter β-galactosidase levels at any time point. LPS 250 ng mL^{-1} induces a significant increase after 72 h, which became stationary after 7 and 10 days. LPS 500 ng mL^{-1} already after 48 h influenced β-galactosidase expression, which increased over time, reaching a maximum concentration after 10 days (Figure 5.6A).

Senescent cells can interact with the environment through the release of several factors with various pleiotropic effects. These are known as SASP[33,173]. NF-κB is part of these bioactive elements. By dosing the levels of this indirectly, we find that LPS 500 ng mL^{-1} leads to a gradual decrease in IKBα inhibitor over time, with the result being most pronounced after 10 days (Figure 5.6B). Cell viability is another parameter considered in the optimization of our model, as senescent cells undergo cell death more rapidly. Through the SRB test we found that LPS at concentrations of 100 and 250 ng mL^{-1} did not significantly alter the microglial survival, compared to untreated controls. The situation is different for the concentration of 500 ng mL^{-1}, which led to a significant reduction in cell viability already at 48 h, with results even more evident after 7 and 10 days (Figure 5.6C). Figure 5.6D shows the results obtained using the SAHF immunofluorescence technique, which highlights the development of senescence foci at the nuclear level. The nucleus of untreated cells is homogeneous in shape and density while the nucleus of LPS-stimulated (500 ng mL^{-1}) cells was more fragmented, with evident gaps corresponding to foci of senescence, a symptom of an ongoing process of cellular aging. Treating cells with LPS 500 ng mL^{-1} we observed a progressive increase in the percentage of foci at the level of the nucleus. Other concentrations of LPS did not give such marked results. An important increase of the foci occurs after 7 and 10 days, which is consistent with the other parameters of senescence evaluated.

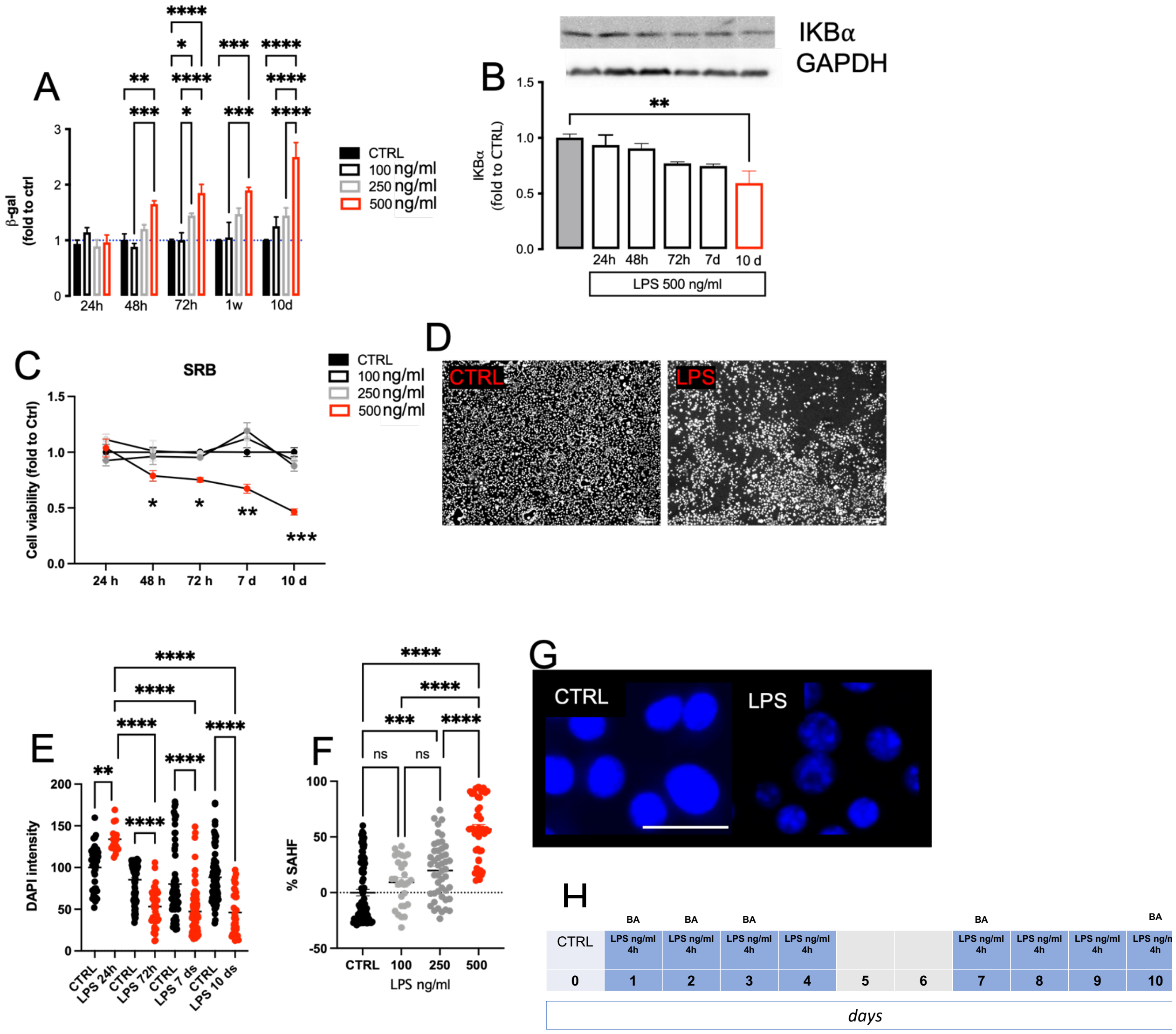

Figure 5.6 Optimization of an *in vitro* model of BV2 senescence. (A) Time course of β-galactosidase protein expression in BV2 stimulated with LPS at 100, 250, and 500 ng mL^{-1}. (B) Time course of IKBα protein expression in BV2 stimulated with LPS 500 ng mL^{-1}. (C) Cell viability test measured with SRB were observed at 24 h, 48 h, 72 h, 7 days, and 10 days in LPS-stimulated BV2 at the concentration of 100, 250, and 500 ng mL^{-1}. (D) Representative images of LPS-stimulated (500 ng mL^{-1}) BV2 at day 10 compared to the CTRL (scale bar 100 μm). (E) Time course of DAPI intensity in LPS-stimulated (500 ng mL^{-1}) BV2, and (F) the percentage of foci expressed in cells. (G) Representative images of SAHF in LPS-stimulated BV2 after 10 days (scale bar 20 μm). (H) Schematic representation of experimental protocol has been reported. BA= biological analysis. One-way and two-way ANOVA; ****$p<0.0001$ ***$p<0.001$, **$p<0.01$, *$p<0.05$. Representative blots are also showed.

5.2.7. Bioactive compounds from medicinal plants as possible strategy in the control of pain and comorbidities in neuropathies, through the reduction of senescence in vivo and in vitro

Considering the fewer side effects and greater safety associated with the use of medicinal plants[81], together with the multi-target activity of plants phytocomplex, phytotherapy could represent an important strategy for managing the main symptoms associated with NP while simultaneously counteracting the main mental comorbidities.

Formulations based on *Melissa officinalis* L. have been used for centuries as a calming or sedative agent in mood disorders such as anxiety, depression, and insomnia, which we have identified as major comorbidities of the neuropathic context[176]. This study represents a possible application of the described *in vitro* model of microglial senescence for the initial screening of new candidates for controlling neuropathy comorbidities. We used a standardized *M. officinalis* leaf extract (MD), containing high amount of rosmarinic acid (AR), which was previously found to be responsible for the activity of lemon balm in the neurodegenerative context[177]. In our model, BV2 cells are stimulated with 4 h of exposure to LPS 500 ng mL^{-1}, four times in a 10-day period. An increase in the senescent phenotype was confirmed by considering multiple parameters, such as increased levels of the enzyme β-gal (Figure 5.7A), increased release of inflammatory factors (Figure 5.7B), decreased cell viability (Figure 5.7C), and increased nuclear foci of senescence (Figure 5.7D). Pretreatment with MD 10 µgmL^{-1} reverted the senescent markers in BV2 model, indicating a reduction in the cellular aging process. To investigate whether AR was responsible for this activity, we tested it at the concentration present in the active dose of MD, i.e., 0.4 µg mL^{-1} (Figure 5.7A-D). Once we evaluated the effect of MD on neuroinflammation and microglial senescence by *in vitro* studies, we moved on to *in vivo* analyses. MD was evaluated in a model of peripheral NP (SNI). For this experiment a second cohort of animals has been used, in particular: Sham (n=8), SNI (n=10), MD (n=8) and AR (n=8). The SNI control group has been treated with CMC 1% used as vehicle.

The extract was administered at a dose of 150 mg kg^{-1}, which resulted to be the most effective dose from the dose-effect curve, and the tests were performed after 60 min, identified as the time of peak activity. The results obtained show that MD can reduce the symptoms of NP, decreasing the thermal hyperalgesia assessed by hot plate test, which is consistent with data in the literature (Figure 5.7E). Once demonstrated the activity in pain, the attention has shifted towards the main comorbidities associated to neuropathic condition. In the open field test, MD and AR possessed anxiolytic effects (Figure 5.7F). In fact, the results obtained from the administration of the AR were comparable to those obtained with MD, both in terms of pain and associated comorbidities.

The last stage of the research involved the evaluation of the development of microglial senescence in biological tissues obtained from SNI models. Our study focused on the spinal cord and hippocampus, which are mostly involved in pain and comorbidity mechanisms. Indeed, the spinal cord is the center of the pathophysiology of NP. Here we find pain pathways, with altered balance between inhibitory and excitatory synapses in neuropathy[8]. Also, the hippocampus is part of the hypothalamic-pituitary-adrenal (HPA) axis, the activation of which has been detected in anxiety and depression[178]. Microglial activation in these tissues has been detected in NP. It is thought that at the basis of the synaptic imbalance in the spinal cord, which occurs in case of neuropathy, there is a precise activation of microglia cells, as well as a quantitative increase of them, which is defined as microgliosis[4]. At the level of the hippocampus under conditions of anxiety and depression, microglial activation has been found to correlate with an increase in inflammatory factors and cytokines, as well as toxicity towards resident neurons[179]. However, to the best of our knowledge, there are no studies showing that such activation is due to the process of cellular senescence. In our study, we therefore investigated whether there could be a potential implication of cell aging at the level of these tissues in NP, and whether MD could influence this process. The results obtained show that MD reduces the levels of β-gal, suggesting that a process of cellular aging has been developed in spinal cord (Figure 5.7G) and hippocampus (Figure 5.7H), during neuropathy.

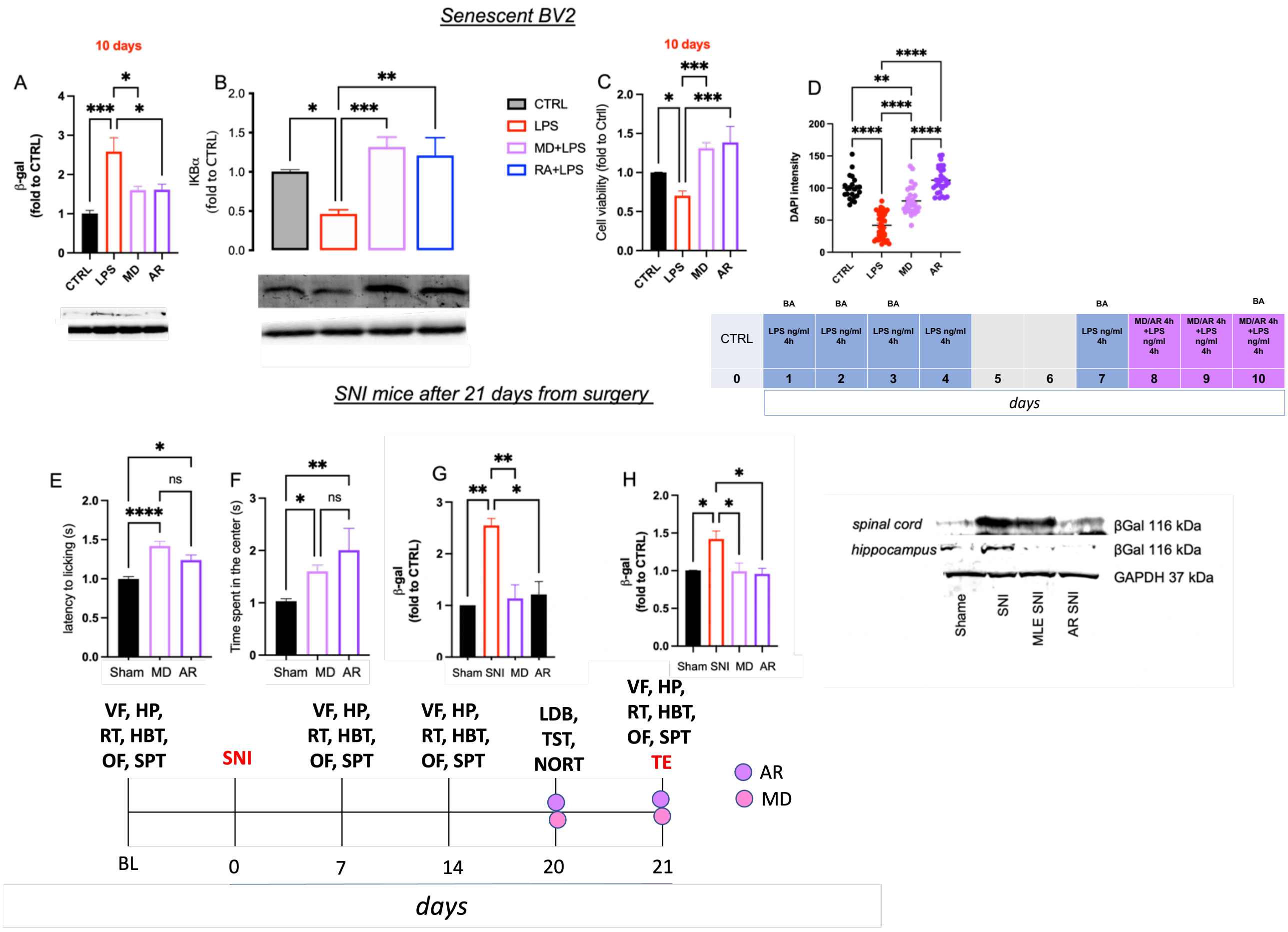

Figure 5.7 Effects of a standardized *Melissa officinalis* L. leaf extract (MD) 10 μg mL^{-1} and of its main constituent rosmarinic acid (AR) 0.4 μg mL^{-1} on (A) β-gal, (B) IKBα, (C) cell viability, and (D) SAHF, in senescent BV2. Experimental deisgn has been reported. BA= biological analysis. Evaluation of the effect on (E) thermal hyperalgesia and (F) anxiety-related symptoms produced by MD 150 mg kg^{-1} (n=8) and AR 6 mg kg^{-1} (n=8), 60 min after oral administration in SNI mice (n=10). β-gal protein expression in (G) spinal cord and (H) hippocampus in SNI mice, 21 days after surgery. One-way ANOVA; ****$p<0.0001$, **$p<0.01$, *$p<0.05$.

5.3. Discussion

In this section of the thesis, we primarily focused on identifying and characterizing the occurrence of anxiety, depression, and impaired cognitive abilities in a model of peripheral neuropathy. This is accompanied by several comorbidities such as anxiety, depression, memory impairment and sleep disorders. In a neuropathic condition, the reduction of pain of at least 30% after treatment is considered as a clinically significant result. This indicates the difficulty in finding a suitable therapy in a multifactorial disease situation such as NP. Most patients do not show sufficient relief after treatment, and it is thought that this is due to the heterogeneity of the mechanisms underlying the pathological situation and the coexisting emotional and psychological aspects[9]. Another aspect to be considered is the effectiveness of the treatment undertaken compared to comorbidities associated with pain, such as mood disorders and sleep alterations, conditions that are also debilitating. The presence of depression and anxiety may prove to be an obstacle in the treatment of pain, such that these conditions should be identified, and specific treatment strategies developed[180]. Changes in plasticity at the central level induced by SNI promote the onset and development of the negative psychological components associated with a NP condition such as anxiety, depression, and aggressive behavior[181,182]. In other models of NP, the possible occurrence of mood disorders has been observed. Studies in animals operated to develop CCI have shown that it can also be used as a model for the study of anxiety and depression behaviors related to NP, as well as mnemonic alterations[183]. The pSNL model is also used to assess the development of mood disorders associated with NP. Anxious behaviors emerge from animal tests with pSNL 28 days after surgery[184]. In the same study, the animals developed anxiety and depression already 14 days after the operation. Surely, finding a target that can simultaneously control pain and associated comorbidities is of considerable interest.

The activation of microglia toward a proinflammatory phenotype compromises neuronal integrity, due to overexpression of inflammatory cytokines and oxygen free radicals (ROS), and decreased levels of neuroprotective factor[185]. However, as occurs in many pathological contexts, the inflammatory process tends to become chronic due to excessive microglial activation, with acceleration of the aging process and loss of function[186]. Consistently, in our model we observe an increase in the expression of β-gal, a marker of cellular aging, at the level of the spinal cord and hippocampus, two distinct areas that have, however, a key role in pain and mood disorders, respectively. Interestingly, microglial aging has been reported to induce the onset of pathology in AD models[187]. Therefore, we have optimized an *in vitro* model of microglial senescence, which mimics cellular aging and thus the loss of function of these cells. In this way we could use the *in vitro* model as a screening method to evaluate the activity of new treatments. In this chapter, as an example of a study for possible treatments of comorbidities associated with NP, we started with the use of a plant such as *M. officinalis* and its main constituent, AR, as it is widely known for its sedative properties. The efficacy of bioactive compounds (such as curcumin) in modulating the occurrence of anxiety and depression in models of NP had already been reported[188]. *M. officinalis* and AR reduced neuroinflammation and microglial senescence both *in vivo* and *in vitro*, leading to an improvement in anxiety and depressive condition in animals. Further studies are in progress to investigate the role of microglia in pain comorbidities, and how its loss of function, and therefore its aging, can be considered an interesting target for new therapeutic approaches.

Chapter 6

Chronic ethanol exposure induces neuropathic pain in mice by promoting neuroinflammation

6.1. Introduction

Alcohol use disorder (AUD) is a serious problem of public health concern. Indeed, about 5.3 % of all deaths worldwide are attributed to the abuse of alcohol. The economic costs of AUD in the United States were estimated to be around 250 billion in 2010 and, nowadays, the alcohol consumption rate has increased[189]. AUD is a multifactorial condition characterized by genetic, environmental, and neurobiological components. The complexity of this disorder implies that only a few numbers of patients positively respond to the currently available therapeutic strategies[190]. Consequentially, the development of new clinically effective treatments represents an important issue[191]. The development of successful treatment requires preclinical models with high predictive validity for treatment outcome[192]. Indeed, animal models in the field of neuroscience deepened the knowledge of the principal mechanisms and neuronal substrates involved in alcohol abuse and the development of alcohol dependence[193]. The main clinical issue associated with drug seeking of AUD are under the control of specific brain regions. Neurobiological processes involved in the development of AUD are the result of complex interactions between genetic and environmental determinants[194]. It has been reported that genetic predisposition to increased alcohol drinking is associated with polymorphisms in gene expression of cytokines[195,196]. The dysregulation of cytokines release, caused by ethanol exposure, has a complex impact on brain physiology, causing a plethora of neuroadaptive changes[195] . The possibility of both a neurotoxic and a neuroprotective role mediated by the neuroimmune system represents a crucial point for the development of new therapeutic strategies. Indeed, reducing the production of pro-inflammatory cytokine by glial cells is not sufficient and it is necessary to also increase the anti-inflammatory mediators, which are also produced by glia[197]. An important aspect of chronic alcohol consumption is the damage induced in a variety of tissues including liver, central and peripheral nervous system[198]. Alcohol-related neuropathy slowly develops its clinical features with a painful sensation representing the initial and major symptom. Electrophysiological and pathologic findings mainly support a relation between axonal neuropathy and reduced nerve fiber densities[199]. The mechanism responsible for the toxicity at the peripheral nerves level has not been understood yet. However, microglia activation in the spinal cord has been hypothesized as a possible cause, leading to oxidative stress and a marked release of pro-inflammatory cytokines[200]. Alcoholic peripheral neuropathy is related to a significant decrease in quality of life as it may lead to a decrease of nociceptive threshold[201]. Conventional therapies can offer some relief, but they are generally symptomatic and characterized by several side effects, limiting their prolonged uses. However, today there is the need for more rigorous and well conducted studies, to better understand the actual therapeutic value of chemically characterized herbal products. Thus, the aims of my visit at the Department of Molecular Medicine at the Scripps Research Institute (San Diego, CA, USA) were to evaluate the possible development of neuropathy in alcohol dependence animal model. Epidemiological data indicate a strong association between chronic pain and AUD[202]. Sex differences in chronic pain are profound and not well understood yet[203] and the mechanisms responsible for the observed increased of chronic pain associated with chronic consumption of alcohol is controversial[204]. For this part of the project, I used the chronic intermittent ethanol vapor two-bottle choice (CIE-2BC) model to produce escalated ethanol intake in dependent mice[19]. Previous studies conducted in this laboratory showed that this model induce an increase of microglia activation in various regions of brain, like that observed in the human alcoholic brain[19]. Notably, neuroinflammation has been largely demonstrated to play a key role in the pathogenesis of other important diseases, such as NP.

6.2. Results

6.2.1. Chronic alcohol exposure induces mechanical allodynia in male and female mice.

The chronic intermittent ethanol two bottle choice (CIE-2BC) paradigm was used to generate ethanol dependent mice (Figure 6.1A) in C57BL/6J mice 143. Indeed, it was observed that it induces an increase of ethanol drinking, anxiety-like behavior, and rewards deficit. In this study we generated three different group of animals for both sex: 1) naïve group (n=14) that did not receive alcohol, 2) non-dependent mice (2BC; n=20) that received only two-bottle choice, and 3) dependent mice (2BC-CIE; n=19) that received two-bottle choice and chronic intermittent ethanol vapor exposure. 2BC-CIE mice achieved an average blood alcohol level (BAL) across the four rounds of CIE of 179.82 ±5.52% and 178.505 ±13.97% for male and female respectively (Figure 6.1B). A significant escalation in the group of 2BC-CIE compared to 2BC in both sex in drinking escalation was observed, with an average daily ethanol intake during the last round of 2BC in 2BC-CIE mice (3.554±0.41 g/kg for male and 3.778±0.36 g/kg for female) compared 2BC mice (0.723±0.25 g/kg for male and 0.407 g/kg for female) indicative of a dependence-like phenotype (Figure 6.1C).

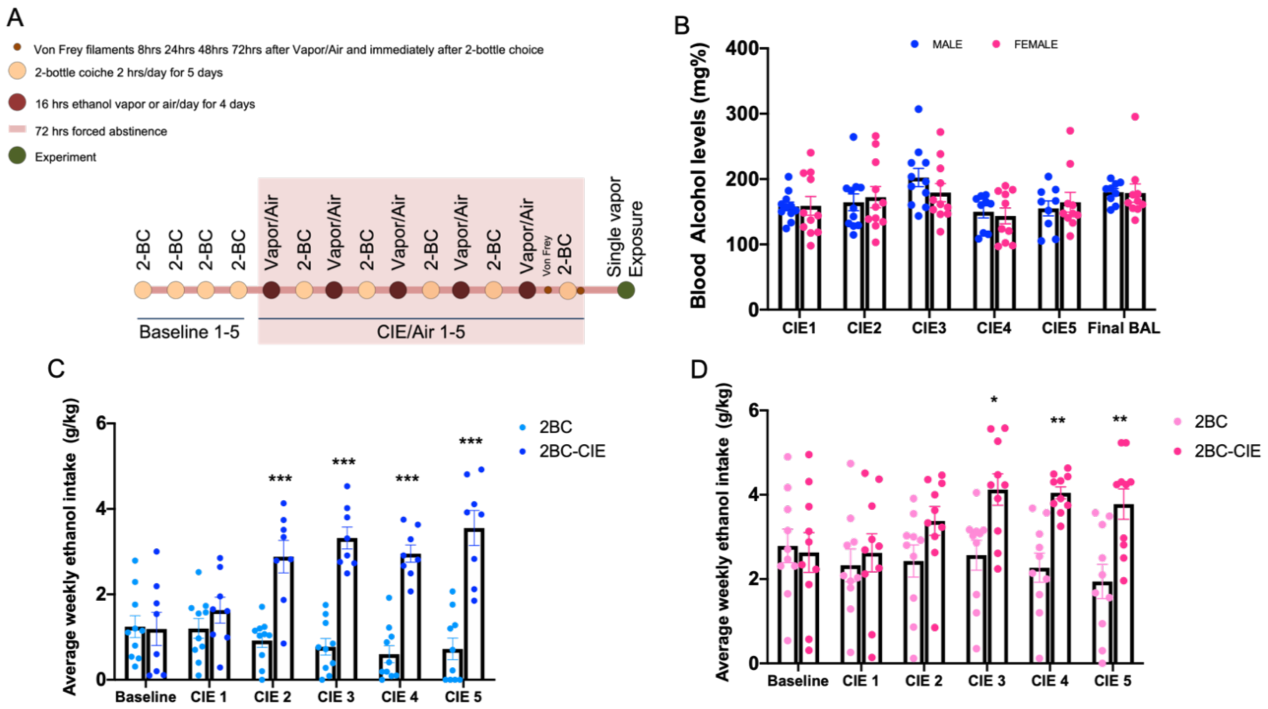

Figure 6.1 Two bottle choice - chronic intermittent ethanol (2BC-CIE) vapor exposure paradigm. (A) Schematic representation of the model. (B) Average blood alcohol levels achieved during weeks of CIE vapor exposure in Dep mice. Average ethanol intake during 2BC sessions during baseline weeks and following air or CIE vapor exposure weeks (red box) for (C) 2BC and 2BC-CIE male and (D) female mice. ***$p<0.001$ **$p<0.01$ *$p<0.05$ vs 2BC by two-way ANOVA.

Von frey filaments were used to verify the development of mechanical allodynia in this model. As reported in Figure 6.2, both male and female 2BC-CIE developed a strong mechanical allodynia 8 h after the last session of vapor, which last until the 72 h of withdrawal (Figure 6.2A, B). Immediately after the 2BC test, 2BC-CIE mice completely reverted the hypersensitivity developed during the withdrawal state, displaying a value of mechanical threshold similar to 2BC group (Figure 6.2C, D).

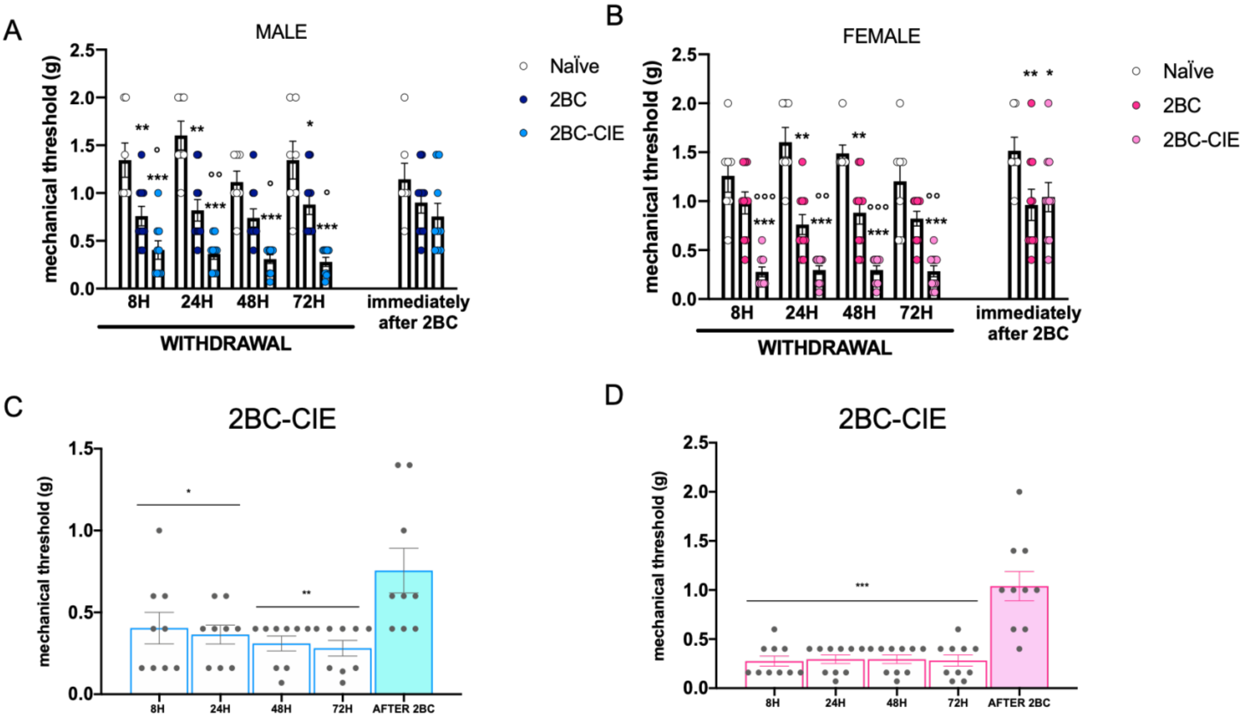

Figure 6.2 Measurement of mechanical allodynia in (A) naïve, Non-2BC and 2BC-CIE male and (B) female mice. ***p<0.001 **p<0.01 *p<0.05 vs naïve; °°°p<0.001 °°p<0.01 °p<0.05 vs 2BC. Comparison of mechanical allodynia between (C) 2BC-CIE male and (D) female mice during withdrawal and after 2-bottle choice test. ***p<0.001 **p<0.01 *p<0.05 vs AFTER 2BC by one-way ANOVA.

6.2.2. Microglia activation in spinal cord tissue of 2BC and 2BC-CIE animals

Microglia have a crucial role in the development of NP. A recent study conducted by the research group of Prof. Roberto reported the key role of microglia in the development of dependence in the 2BC-CIE model 159 in male mice. In the present study, 2BC-CIE male and female mice showed a tendency to increase the CSF-1 expression (Figure 6.3A) and a significant increase of IBA-1 (Figure 6.3B) expression in the spinal cord. Moreover, we observed an increase of p-p38 expression in male and female 2BC-CIE group (Figure 6.3C, D), and only in male group an increase of tp38 (Figure 6.3E).

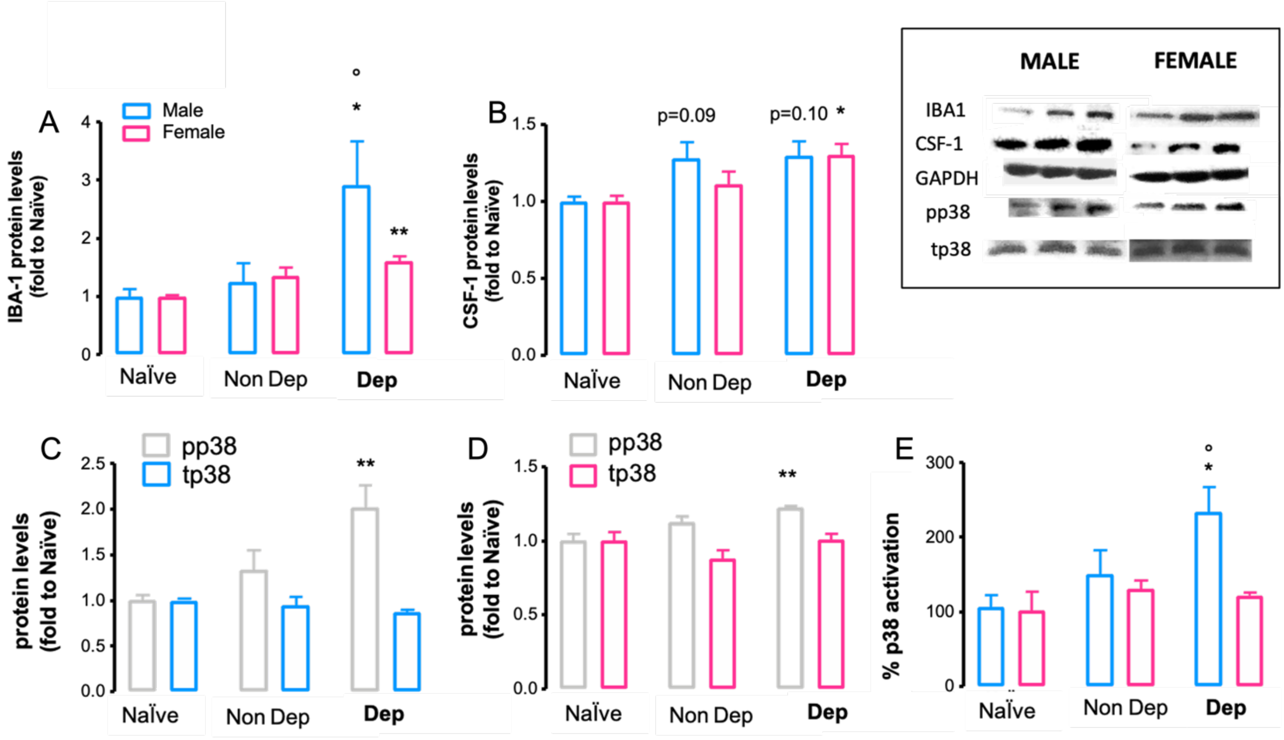

Figure 6.3 (A) IBA1, (B) CSF1, protein levels in the spinal cord of naïve, 2BC and 2BC-CIE mice. Phosphorylated and total p38 levels ratio in (C) male, (D) female and (E) %p38 activation in both sexes. All data are normalized to naïve group and represent the mean ± SEM. **p<0.01 *p<0.05 °p<0.05 vs female vs naïve by two-way ANOVA.

6.2.3. Chronic ethanol consumption induced neuropathy in 40-50% of 2BC mice

Interestingly, also the 2BC group showed a long-lasting increase of sensitivity compared to Naïve group, which was not reverted by the section of self-alcohol administration. Figure 6.4 shows the mechanical threshold of 2BC female (A), and male (B) mice and it is evident that about half of the animals for each group have a mechanical threshold lower than the minimum value registered for the naïve group. Animals reporting lower mechanical threshold value in three out of four different time were assigned to the neuropathy group (2BC-N) (Figure 6.4 C, D).

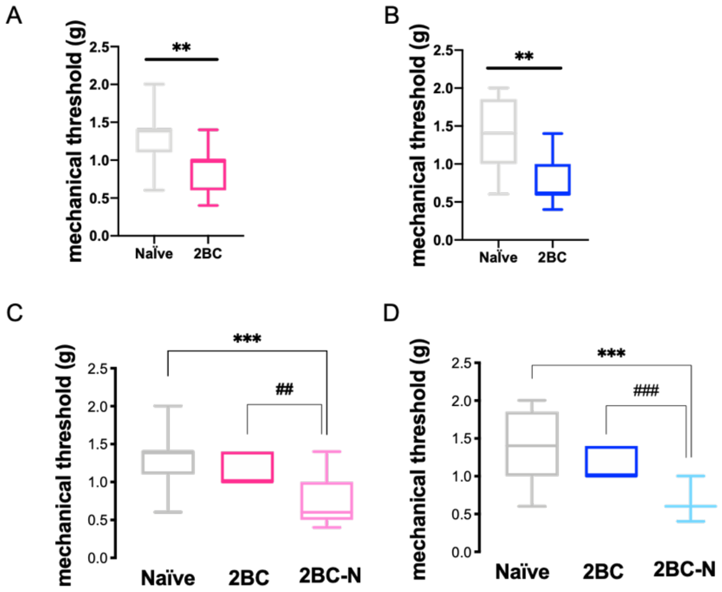

Figure 6.4 Mechanical threshold of 2BC (A) female and (B) male. Separation of 2BC in two different group (C) with (2BC-N) and (D) without (2BC) neuropathy. All data are normalized to naïve group and represent the mean ± SEM. ***p<0.001 **p<0.01 vs naïve ###p<0.01 vs 2BC by two-way ANOVA.

6.2.4. Escalation drinking in a second cohort of animals

In order to confirm the results obtained from Cohort 1, we repeated the CIE-2BC model in a second cohort of mice, and we reported the escalation drinking of Dep mice compared Non dep mice. Consistently, we observed a great significant escalation in alcohol intake in the 2BC-CIE mice (Figure 6.5A). It has been reported that in humans, the 46% of chronic alcohol abusers develop peripheral neuropathy. This data is extremely consistent with our data, where the 43% of animals developed neuropathy with 40/50% of the 2BC mice developing an increased mechanical allodynia (Figure 6.5B, C). Moreover, a clinical sign of alcohol-induced neuropathy is linked with demyelination processes in the sciatic nerve. This condition was also obtained in our model. Indeed, the 2BC-N group showed a lower expression of s100, which is a marker of myelinated Schwann cells, in the sciatic nerve (Figure 6.5D). In addition, we also observed a significant increase of microglia activation markers, IBA1 (Figure 6.5E) and %p-p38/t-p38 (Figure 6.5F) in the spinal cord of 2BC-N (mice with neuropathy).

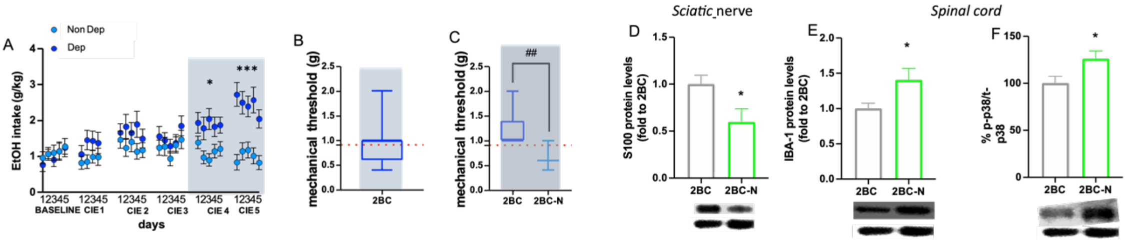

Figure 6.5 (A) Escalation drinking in a second cohort of animals (***p<0.001 **p<0.01 *p<0.05 vs 2BC by two-way ANOVA). Separation of (B) 2BC in (C) two different group with (2BC-N) and without (2BC) neuropathy. All data are normalized on naïve group and represent the mean ± SEM. ***p<0.001 **p<0.01 vs naïve ###p<0.01 vs 2BC by two-way ANOVA. (D) S100 protein expression in sciatic nerve tissue. (E) IBA1and (F) % of p-p38 protein levels in spinal cord tissue. *p<0.05 vs 2BC by student's t-test.

6.3. Discussion

AUD is defined by the emergence of negative affective symptoms during withdrawal. In particular, unrelieved chronic pain is considered a key factor contributing to the maintenance of AUD. Chronic or excessive alcohol consumption often results in a hypersensitivity state, and this is considered a negative reinforcement process that facilitates AUD progression. Notably, the results obtained in this work showed the insurgence of chronic alcohol exposure-induced hyperalgesia in 2BC-CIE, compared to the 2BC and naïve group, during withdrawal, which was completely reverted after a subsequent alcohol self-administration. This effect could be considered as abstinence-related hyperalgesia, which is a phenomenon that occurs when the chronic administration of abuse substances is abruptly stopped. This phenomenon has been reported in clinical studies using nicotine and opioids. This condition is different from the alcohol-induced neuropathy. Indeed, it has been estimated that in the United States 25% to 66% of chronic alcohol users develop some form of neuropathy, with women being more likely affected[205]. In our model we observed that increased hypersensitivity occurs also in 40% and 50% of 2BC male and female mice, respectively, compared to the naïve group. Thus, we can speculate that, in this model, the chronic consumption of alcohol also induces a direct alcohol-related neuropathy. The actual therapy for the management of alcohol-related NP is based on analgesics and opioid alternatives, that generally are ineffective and rarely cure the actual causes[206]. For this reason, the research of alternatives targets to be exploited for the management of this chronic condition is current and important issue, particularly, regarding pathways that involve both dependence and pain development. Neuroinflammation is a key contributor to alcohol reinforcement, and it is well known that it plays a key role also in the pathogenesis of NP[207]. Microglia depletion prevented escalations in voluntary alcohol intake and decreased anxiety-like behavior associated with alcohol dependence[19]. For these reasons we investigated the possible microglia activation in spinal cord samples of 2BC and 2BC-CIE mice. Our findings showed an up-regulation of the microglia marker IBA-1 in the Dep mice of both sexes. The p38 MAPK is considered a key modulator of proinflammatory process that characterize microglia activation[132,208], and its activation was found to be highly increased in 2BC and 2BC-CIE. Thus, targeting microglia activation could be considered a novel therapeutic approach for the management of AUD.

Chapter 7

Conclusion

Microglia cells constitute, depending on the region where they are located, 5% to 12% of the cells found in the CNS[184]. They are the main resident cells of the immune system in the brain, involved in the maintenance of homeostasis, protection against pathogens, and disorders of the CNS. In NP, microglia represent an important key to modulate the various processes that characterize this chronic and disabling disease, which can be summarized as:
neuroinflammation, neurodegeneration and demyelination.

During the acute phase, microglia assume a pro-inflammatory phenotype (M1) and potentially release a large amount of pro-inflammatory cytokines, which are thought to induce tissue damage, demyelination, and neuronal death in the CNS. Normally, under physiological conditions during the peak of the disease the anti-inflammatory microglia (M2) increase its activity and repair the damage produced. If the stimulus chronicize and is not resolved, due to environmental or genetic factors, the anti-inflammatory microglia lose its function and what we get is a latent and continuous damage that leads to degeneration[138]. In this thesis work we wanted to find some microglial targets that can vary the activity to restore the normal activity of these cells without going to inactivate them completely. In fact, we need to restore the microglia to function as in physiological conditions without causing any kind of change that could lead to alterations in the central homeostasis. The targets on which we have mainly focused our attention are modulators of genetic transcription: HDAC1 and HuR.

Regarding HDAC1 we have used a pharmacological treatment on two different fronts, a dual inhibitor that goes simultaneously to act on HDAC1 and its readers BRD4, and bioactive compounds extracted from medicinal plants, having identified terpenes as a possible class of phytocompounds able to interact with this epigenetic enzyme. What is most innovative in this therapeutic approach is the selective action of these molecules towards a single class of HDAC, thus reducing the side effects related to the non-specificity of pan-inhibitors. Innovative is also the type of administration, the intranasal delivery, used to have an effect at the level of the CNS in a non-invasive way compared to more complex and disabling routes such as intrathecal. In fact, the use of non-invasive routes favors an increase in compliance with the patient, which also ensures a greater possibility of effectiveness of therapy and increased quality of life. Another advantage of this route of administration is essentially that of avoiding the dispersion of the molecule in peripheral tissues, which could lead to numerous side effects.

This approach of optimizing the routes of administration was then also used for therapy with antisense oligonucleotides (ASO), molecules that do not readily cross the blood brain barrier making ASO-based therapies to require an i.c.v. or i.t. delivery. Anti-HuR ASO used intranasally, reduces the expression of this protein back to control-like levels with similar efficacy to intrathecal administration. The protein knockdown produced by ASO avoids the onset of compensation mechanisms of a knockout intervention that would make difficult the use of such molecules in the clinic, as the total silencing of a protein would disturb excessively the surrounding environment. Especially when we are talking about very fragile and difficult to adapt tissues, such as the CNS.

The multiple mechanisms of these innovative treatments in reducing microglial activation produced two main effects: reduction of neuroinflammation by promoting the phenotypic shift of microglia, and induction of a pro-myelinating effect. Our findings highlight the key role of microglia in the neuronal maintenance and open a broader vision of NP therapy through an approach that can resolve the causes rather than being a simple symptomatic intervention.

Therefore, at the basis of this research there is the need to find therapies that reduce symptoms by slowing down the progression of the disease, representing a concrete improvement of the quality of life of the patient.

Neuropathies are chronic diseases whose main symptom is associated with pain, but which involve, given their difficulty in resolving, the onset of long-term comorbidities such as anxiety, depression, insomnia, loss of cognitive ability.

All these certainly make the clinical picture even more complex; therefore, finding a pharmacological target that links these alterations is certainly of interest. As described in this thesis work, microglia are a cell that adapts to any type of disturbance of the homeostasis of the CNS and its lack of activity can lead to permanent and unresolvable damage. NP starts with an inflammatory process, which if unresolved can lead to alteration of the normal activity of the central system environment. In this condition the microglia may not withstand this continuous stimulus and lose its function, as already mentioned, until it becomes senescent. Using a marker of cellular senescence, we wanted to see if at the level of the spinal cord (central site of pain) and of the hippocampus (important site of the development of anxiety and depression) can develop microglial aging. Further studies are being conducted to better investigate this very new and poorly known aspect. Indeed, preventing microglial senescence means reducing the possibility of having an alteration in the homeostasis of the CNS, thus leading to an aging and a deterioration of the cognitive abilities of the person. So, targeting senescent microglia could be considered an interesting target to prevent neurodegeneration.

Another aspect that has emerged rather recently is that microglia seem to play a role in all addictive conditions, including those produced by alcohol. In about 50% of individuals who exhibit alcohol dependence, neuropathy develops defined precisely as alcoholic neuropathy. This condition can not only alter the normal quality of life of the patient, but it can also worsen the emotional state of the subject, triggering a loop mechanism in which pain will cause a sense of discomfort and will lead to the intake of alcohol to reduce this feeling. In fact, after acute administration, alcohol provokes a very powerful transient analgesic effect that attenuates pain, highlighting a point of contact between the pathways of the CNS that transmit pain and those that lead to the development of addiction. As extensively described in this thesis work, microglia play a role in NP, representing for this reason perhaps a common point in the development of neuropathy and addiction.

From this basis comes the interest in observing in addicted mice the development of neuropathy, in a study that was conducted at The Scripps Research Institute in the laboratory of Professor Marisa Roberto during my time abroad. In the spinal cords of dependent animals that develop neuropathy, an increase in the expression of microglial markers was observed, thus opening a new avenue in the possible involvement of microglia also in these forms of neuropathy.

As summarized in figure 7.1, a stressful correlation between neuroinflammation, demyelination, and degeneration is observed in this thesis work in central and peripheral neuropathies. Given that microglia are an important crossroads in the onset and regulation of these processes, it seems interesting to investigate their role and consider them as an important drug target. Microglia can therefore be considered a key point in the homeostatic maintenance at the level of the CNS even in those conditions such as NP, in which this balance is lost, thus promoting the advancement of the pathology. Restoring normal physiological conditions in the nervous environment through the modulation of specific microglial targets is an innovative approach to move towards more effective, safe, and personalized therapies.

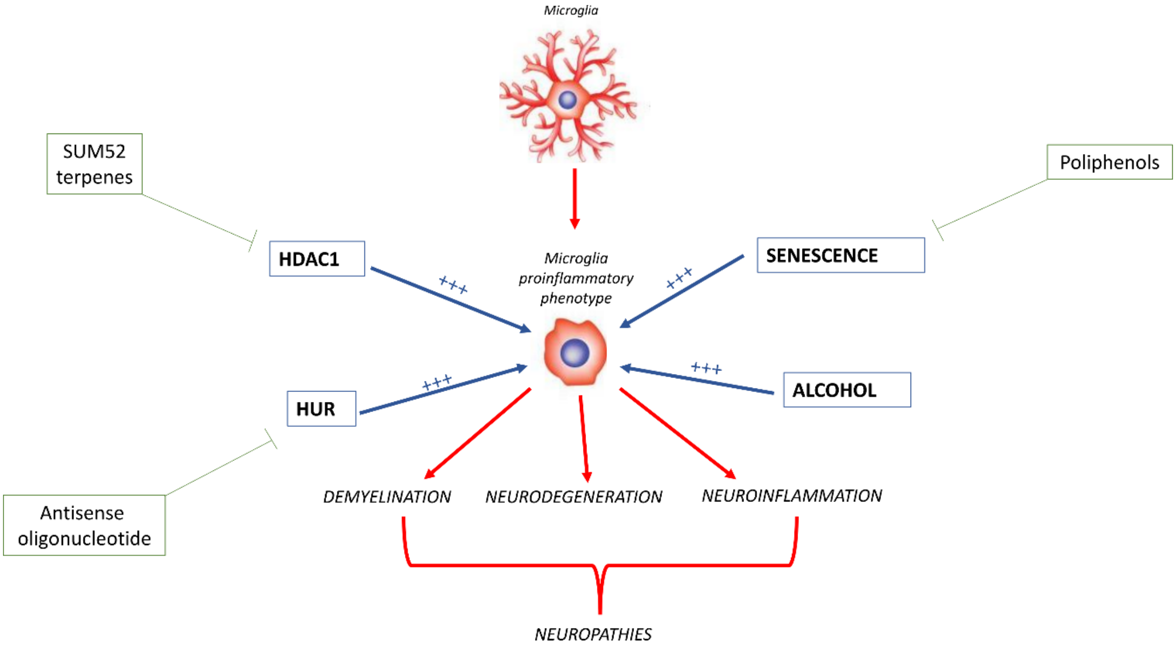

Figure 7.1 Graphical abstract

References

1. Chaplin, D. D. Overview of the immune response. *J. Allergy Clin. Immunol.* **125**, S3–S23 (2010).
2. Kwan, T., Floyd, C. L., Kim, S. & King, P. H. RNA Binding Protein Human Antigen R Is Translocated in Astrocytes following Spinal Cord Injury and Promotes the Inflammatory Response. *J. Neurotrauma* **34**, 1249–1259 (2017).
3. Kettenmann, H., Hanisch, U.-K., Noda, M. & Verkhratsky, A. Physiology of microglia. *Physiol. Rev.* **91**, 461–553 (2011).
4. Block, M. L., Zecca, L. & Hong, J.-S. Microglia-mediated neurotoxicity: uncovering the molecular mechanisms. *Nat. Rev. Neurosci.* **8**, 57–69 (2007).
5. David, S. & Kroner, A. Repertoire of microglial and macrophage responses after spinal cord injury. *Nat. Rev. Neurosci.* **12**, 388–399 (2011).
6. Donnelly, D. J. & Popovich, P. G. Inflammation and its role in neuroprotection, axonal regeneration and functional recovery after spinal cord injury. *Exp. Neurol.* **209**, 378–388 (2008).
7. Colton, C. A. & Wilcock, D. M. Assessing activation states in microglia. *CNS Neurol. Disord. Drug Targets* **9**, 174–191 (2010).
8. Kuner, R. & Flor, H. Structural plasticity and reorganisation in chronic pain. *Nat. Rev. Neurosci.* **18**, 20–30 (2017).
9. Cohen, S. P. & Mao, J. Neuropathic pain: mechanisms and their clinical implications. *BMJ* **348**, f7656 (2014).
10. Guerrero, B. L. & Sicotte, N. L. Microglia in Multiple Sclerosis: Friend or Foe? *Front. Immunol.* **11**, 374 (2020).
11. Neumann, B., Segel, M., Chalut, K. J. & Franklin, R. J. Remyelination and ageing: Reversing the ravages of time. *Mult. Scler.* **25**, 1835–1841 (2019).
12. Traiffort, E., Kassoussi, A., Zahaf, A. & Laouarem, Y. Astrocytes and Microglia as Major Players of Myelin Production in Normal and Pathological Conditions. *Front. Cell. Neurosci.* **14**, 79 (2020).
13. Salter, M. W. & Stevens, B. Microglia emerge as central players in brain disease. *Nat. Med.* **23**, 1018–1027 (2017).
14. Streit, W. J., Mrak, R. E. & Griffin, W. S. T. Microglia and neuroinflammation: A pathological perspective. *J. Neuroinflammation* **1**, 1–4 (2004).
15. Berta, T. *et al.* Extracellular caspase-6 drives murine inflammatory pain via microglial TNF-α

secretion. *J. Clin. Invest.* **124**, 1173–1186 (2014).

16. Finnerup, N. B., Kuner, R. & Jensen, T. S. Neuropathic Pain: From Mechanisms to Treatment. *Physiol. Rev.* **101**, 259–301 (2021).
17. Franklin, R. J. M. & Goldman, S. A. Glia Disease and Repair-Remyelination. *Cold Spring Harb. Perspect. Biol.* **7**, a020594 (2015).
18. Decosterd, I. & Woolf, C. J. Spared nerve injury: an animal model of persistent peripheral neuropathic pain. *Pain* **87**, 149–158 (2000).
19. Warden, A. S. *et al.* Microglia Control Escalation of Drinking in Alcohol-Dependent Mice: Genomic and Synaptic Drivers. *Biol. Psychiatry* **88**, 910–921 (2020).
20. Constantinescu, C. S., Farooqi, N., O'Brien, K. & Gran, B. Experimental autoimmune encephalomyelitis (EAE) as a model for multiple sclerosis (MS). *Br. J. Pharmacol.* **164**, 1079–1106 (2011).
21. Borgonetti, V., Sanna, M. D., Lucarini, L. & Galeotti, N. Targeting the RNA-Binding Protein HuR Alleviates Neuroinflammation in Experimental Autoimmune Encephalomyelitis: Potential Therapy for Multiple Sclerosis. *Neurother. J. Am. Soc. Exp. Neurother.* **18**, 412–429 (2021).
22. Sanna, M. D., Quattrone, A. & Galeotti, N. Silencing of the RNA-binding protein HuR attenuates hyperalgesia and motor disability in experimental autoimmune encephalomyelitis. *Neuropharmacology* **123**, 116–125 (2017).
23. Borgonetti, V., Governa, P., Biagi, M., Pellati, F. & Galeotti, N. Zingiber officinale Roscoe rhizome extract alleviates neuropathic pain by inhibiting neuroinflammation in mice. *Phytomedicine* **78**, 153307 (2020).
24. Sanna, M. D., Borgonetti, V. & Galeotti, N. μ Opioid Receptor-Triggered Notch-1 Activation Contributes to Morphine Tolerance: Role of Neuron-Glia Communication. *Mol. Neurobiol.* **57**, 331–345 (2020).
25. Borgonetti V, Governa P, Biagi M, G. N. Novel Therapeutic Approach for the Management of Mood Disorders: In Vivo and In Vitro Effect of a Combination of L-Theanine, Melissa officinalis L. and Magnolia officinalis Rehder & E.H. Wilson. *Nutrients* **12**, 1803 (2020).
26. Brachman, R. A. *et al.* Ketamine as a Prophylactic Against Stress-Induced Depressive-like Behavior. *Biol. Psychiatry* **79**, 776–786 (2016).
27. Galeotti, N., Sanna, M. D. & Ghelardini, C. Pleiotropic effect of histamine H4 receptor modulation in the central nervous system. *Neuropharmacology* **71**, 141–147 (2013).
28. Antunes, M. & Biala, G. The novel object recognition memory: neurobiology, test procedure, and its modifications. *Cogn. Process.* **13**, 93–110 (2012).

29. Sanna, M. D., Ghelardini, C. & Galeotti, N. HuD-mediated distinct BDNF regulatory pathways promote regeneration after nerve injury. *Brain Res.* **1659**, 55–63 (2017).
30. Borgonetti V, Governa P, Biagi M, Dalia P, C. L. Rhodiola rosea L. modulates inflammatory processes in a CRH-activated BV2 cell model. *Phytomedicine* **68**, 153143 (2020).
31. Borgonetti, V. *et al.* A honokiol-enriched Magnolia officinalis Rehder \\& E.H. Wilson. bark extract possesses anxiolytic-like activity with neuroprotective effect through the modulation of CB1 receptor. *J. Pharm. Pharmacol.* **73**, 1161–1168 (2021).
32. Wu, F. Y.-H., Liao, W.-C. & Chang, H.-M. Comparison of antitumor activity of vitamins K1, K2 and K3 on human tumor cells by two (MTT and SRB) cell viability assays. *Life Sci.* **52**, 1797–1804 (1993).
33. Yu, H.-M. *et al.* Repeated Lipopolysaccharide Stimulation Induces Cellular Senescence in BV2 Cells. *Neuroimmunomodulation* **19**, 131–136 (2012).
34. Borgonetti, V. & Galeotti, N. Intranasal delivery of an antisense oligonucleotide to the RNA-binding protein HuR relieves nerve injury-induced neuropathic pain. *Pain* **162**, 1500–1510 (2021).
35. Borgonetti, V. & Galeotti, N. Fluorescence Colocalization Analysis of Cellular Distribution of MOR-1. in *Opioid Receptors: Methods and Protocols* (ed. Spampinato, S. M.) 27–34 (Springer US, 2021). doi:10.1007/978-1-0716-0884-5_3.
36. Curtis, M. J. *et al.* Experimental design and analysis and their reporting II: updated and simplified guidance for authors and peer reviewers. *Br. J. Pharmacol.* **175**, 987–993 (2018).
37. Denk, F. & McMahon, S. B. Chronic Pain: Emerging Evidence for the Involvement of Epigenetics. *Neuron* **73**, 435–444 (2012).
38. Luger, K. & Hansen, J. C. Nucleosome and chromatin fiber dynamics. *Curr. Opin. Struct. Biol.* **15**, 188–196 (2005).
39. Romanelli, M. N., Borgonetti, V. & Galeotti, N. Dual BET/HDAC inhibition to relieve neuropathic pain: Recent advances, perspectives, and future opportunities. *Pharmacol. Res.* **173**, 105901 (2021).
40. Peixoto, P., Cartron, P.-F., Serandour, A. A. & Hervouet, E. From 1957 to Nowadays: A Brief History of Epigenetics. *Int. J. Mol. Sci.* **21**, (2020).
41. Gregoretti, I., Lee, Y.-M. & Goodson, H. V. Molecular Evolution of the Histone Deacetylase Family: Functional Implications of Phylogenetic Analysis. *J. Mol. Biol.* **338**, 17–31 (2004).
42. Cui, S.-S., Lu, R., Zhang, H., Wang, W. & Ke, J.-J. Suberoylanilide hydroxamic acid prevents downregulation of spinal glutamate transporter-1 and attenuates spinal nerve ligation-induced neuropathic pain behavior. *Neuroreport* **27**, (2016).

43. Cherng, C.-H. *et al.* Baicalin ameliorates neuropathic pain by suppressing HDAC1 expression in the spinal cord of spinal nerve ligation rats. *J. Formos. Med. Assoc.* **113**, 513–520 (2014).

44. Borgonetti, V. & Galeotti, N. Combined inhibition of histone deacetylases and BET family proteins as epigenetic therapy for nerve injury-induced neuropathic pain. *Pharmacol. Res.* **165**, 105431 (2021).

45. Li, Z. *et al.* HDAC2, but not HDAC1, regulates Kv1.2 expression to mediate neuropathic pain in CCI rats. *Neuroscience* **408**, 339–348 (2019).

46. Ouyang, B. *et al.* Normalizing HDAC2 Levels in the Spinal Cord Alleviates Thermal and Mechanical Hyperalgesia After Peripheral Nerve Injury and Promotes GAD65 and KCC2 Expression. *Front. Neurosci.* **13**, 346 (2019).

47. Sanna, M. D., Guandalini, L., Romanelli, M. N. & Galeotti, N. The new HDAC1 inhibitor LG325 ameliorates neuropathic pain in a mouse model. *Pharmacol. Biochem. Behav.* **160**, 70–75 (2017).

48. Maiarù, M. *et al.* Complex regulation of the regulator of synaptic plasticity histone deacetylase 2 in the rodent dorsal horn after peripheral injury. *J. Neurochem.* **138**, 222–232 (2016).

49. Torrance, N., Smith, B. H., Bennett, M. I. & Lee, A. J. The Epidemiology of Chronic Pain of Predominantly Neuropathic Origin. Results From a General Population Survey. *J. Pain* **7**, 281–289 (2006).

50. Inoue, S., Taguchi, T., Yamashita, T., Nakamura, M. & Ushida, T. The prevalence and impact of chronic neuropathic pain on daily and social life: A nationwide study in a Japanese population. *Eur. J. Pain* **21**, 727–737 (2017).

51. van Hecke, O., Austin, S. K., Khan, R. A., Smith, B. H. & Torrance, N. Neuropathic pain in the general population: A systematic review of epidemiological studies. *Pain* **155**, (2014).

52. Valente, S. & Mai, A. Small-molecule inhibitors of histone deacetylase for the treatment of cancer and non-cancer diseases: a patent review (2011 – 2013). *Expert Opin. Ther. Pat.* **24**, 401–415 (2014).

53. van de Donk, N. W. C. J. *et al.* Treatment of relapsed and refractory multiple myeloma in the era of novel agents. *Cancer Treat. Rev.* **37**, 266–283 (2011).

54. Göttlicher, M. *et al.* Valproic acid defines a novel class of HDAC inhibitors inducing differentiation of transformed cells. *EMBO J.* **20**, 6969–6978 (2001).

55. Hontecillas-Prieto, L. *et al.* Synergistic Enhancement of Cancer Therapy Using HDAC Inhibitors: Opportunity for Clinical Trials. *Front. Genet.* **11**, 1113 (2020).

56. Zhang, Q., Wang, S., Chen, J. & Yu, Z. Histone Deacetylases (HDACs) Guided Novel Therapies for T-cell lymphomas. *Int J Med Sci* **16**, 424–442 (2019).

57. Lardenoije, R. *et al.* The epigenetics of aging and neurodegeneration. *Prog. Neurobiol.* **131**, 21–64 (2015).

58. He, X.-T. *et al.* Suppression of histone deacetylases by SAHA relieves bone cancer pain in rats via inhibiting activation of glial cells in spinal dorsal horn and dorsal root ganglia. *J. Neuroinflammation* **17**, 125 (2020).

59. Pradhan, A. A., Tipton, A. F., Zhang, H., Akbari, A. & Pandey, S. C. Effect of Histone Deacetylase Inhibitor on Ethanol Withdrawal-Induced Hyperalgesia in Rats. *Int. J. Neuropsychopharmacol.* **22**, 523–527 (2019).

60. Danaher, R. J. *et al.* Histone deacetylase inhibitors prevent persistent hypersensitivity in an orofacial neuropathic pain model. *Mol. Pain* **14**, 1744806918796763 (2018).

61. Hobo, S., Eisenach, J. C. & Hayashida, K. Up-regulation of spinal glutamate transporters contributes to anti-hypersensitive effects of valproate in rats after peripheral nerve injury. *Neurosci. Lett.* **502**, 52–55 (2011).

62. Guo, A. *et al.* Valproic acid mitigates spinal nerve ligation-induced neuropathic pain in rats by modulating microglial function and inhibiting neuroinflammatory response. *Int. Immunopharmacol.* **92**, 107332 (2021).

63. Chen, S. *et al.* Valproic acid attenuates traumatic spinal cord injury-induced inflammation via STAT1 and NF-κB pathway dependent of HDAC3. *J. Neuroinflammation* **15**, 150 (2018).

64. Elsherbiny, N. M. *et al.* Inhibitory effect of valproate sodium on pain behavior in diabetic mice involves suppression of spinal histone deacetylase 1 and inflammatory mediators. *Int. Immunopharmacol.* **70**, 16–27 (2019).

65. Russo, R. *et al.* Sodium butyrate and its synthetic amide derivative modulate nociceptive behaviors in mice. *Pharmacol. Res.* **103**, 279–291 (2016).

66. Kukkar, A., Singh, N. & Jaggi, A. S. Attenuation of neuropathic pain by sodium butyrate in an experimental model of chronic constriction injury in rats. *J. Formos. Med. Assoc.* **113**, 921–928 (2014).

67. Brilli, L. L., Swanhart, L. M., de Caestecker, M. P. & Hukriede, N. A. HDAC inhibitors in kidney development and disease. *Pediatr. Nephrol.* **28**, 1909–1921 (2013).

68. Fraczek, J., Vanhaecke, T. & Rogiers, V. Toxicological and metabolic considerations for histone deacetylase inhibitors. *Expert Opin. Drug Metab. \& Toxicol.* **9**, 441–457 (2013).

69. Garden, G. A. Epigenetics and the Modulation of Neuroinflammation. *Neurotherapeutics* **10**, 782–788 (2013).

70. Lee, C. *et al.* Sodium butyrate inhibits the NF-kappa B signaling pathway and histone deacetylation, and attenuates experimental colitis in an IL-10 independent manner. *Int.*

Immunopharmacol. **51**, 47–56 (2017).

71. Kannan, V. *et al.* Histone deacetylase inhibitors suppress immune activation in primary mouse microglia. *J. Neurosci. Res.* **91**, 1133–1142 (2013).
72. Durham, B. S., Grigg, R. & Wood, I. C. Inhibition of histone deacetylase 1 or 2 reduces induced cytokine expression in microglia through a protein synthesis independent mechanism. *J. Neurochem.* **143**, 214–224 (2017).
73. Lin, F.-L. *et al.* HDAC8 Inhibitor WK2-16 Therapeutically Targets Lipopolysaccharide-Induced Mouse Model of Neuroinflammation and Microglial Activation. *Int. J. Mol. Sci.* **20**, (2019).
74. Bolognesi, M. L. & Cavalli, A. Multitarget Drug Discovery and Polypharmacology. *ChemMedChem* **11**, 1190–1192 (2016).
75. DeMars, K. M., Yang, C., Castro-Rivera, C. I. & Candelario-Jalil, E. Selective degradation of BET proteins with dBET1, a proteolysis-targeting chimera, potently reduces pro-inflammatory responses in lipopolysaccharide-activated microglia. *Biochem. Biophys. Res. Commun.* **497**, 410–415 (2018).
76. Kami, K., Taguchi, S., Tajima, F. & Senba, E. Histone Acetylation in Microglia Contributes to Exercise-Induced Hypoalgesia in Neuropathic Pain Model Mice. *J. Pain* **17**, 588–599 (2016).
77. Singh, H. *et al.* Alternative treatment strategies for neuropathic pain: Role of Indian medicinal plants and compounds of plant origin-A review. *Biomed. Pharmacother.* **92**, 634–650 (2017).
78. Sun, J. *et al.* Role of curcumin in the management of pathological pain. *Phytomedicine* **48**, 129–140 (2018).
79. Zhao, S., Pi, C., Ye, Y., Zhao, L. & Wei, Y. Recent advances of analogues of curcumin for treatment of cancer. *Eur. J. Med. Chem.* **180**, 524–535 (2019).
80. Semwal, R. B., Semwal, D. K., Combrinck, S. & Viljoen, A. M. Gingerols and shogaols: Important nutraceutical principles from ginger. *Phytochemistry* **117**, 554–568 (2015).
81. Quintans, J. S. S., Antoniolli, Â. R., Almeida, J. R. G. S., Santana-Filho, V. J. & Quintans-Júnior, L. J. Natural Products Evaluated in Neuropathic Pain Models - A Systematic Review. *Basic \& Clin. Pharmacol. \& Toxicol.* **114**, 442–450 (2014).
82. Choi, J. G., Kim, S. Y., Jeong, M. & Oh, M. S. Pharmacotherapeutic potential of ginger and its compounds in age-related neurological disorders. *Pharmacol. Ther.* **182**, 56–69 (2018).
83. European Medicine Agency. *EMA Assessment Report on Zingiber officinale Roscoe rhizome*. (2021).
84. Edelmayer, R. M., Brederson, J.-D., Jarvis, M. F. & Bitner, R. S. Biochemical and

pharmacological assessment of MAP-kinase signaling along pain pathways in experimental rodent models: a potential tool for the discovery of novel antinociceptive therapeutics. *Biochem. Pharmacol.* **87**, 390–398 (2014).

85. Subedi, L., Lee, J. H., Yumnam, S., Ji, E. & Kim, S. Y. Anti-Inflammatory Effect of Sulforaphane on LPS-Activated Microglia Potentially through JNK/AP-1/NF-κB Inhibition and Nrf2/HO-1 Activation. *Cells* **8**, (2019).

86. Zhuang, Z.-Y., Gerner, P., Woolf, C. J. & Ji, R.-R. ERK is sequentially activated in neurons, microglia, and astrocytes by spinal nerve ligation and contributes to mechanical allodynia in this neuropathic pain model. *Pain* **114**, (2005).

87. Shih, R. H., Wang, C. Y. & Yang, C. M. NF-kappaB signaling pathways in neurological inflammation: A mini review. *Front. Mol. Neurosci.* **8**, 1–8 (2015).

88. Yu, W. *et al.* Discovery of ethyl ketone-based HDACs 1, 2, and 3 selective inhibitors for HIV latency reactivation. *Bioorg. Med. Chem. Lett.* **30**, 127197 (2020).

89. Pellati, F. *et al.* Cannabis sativa L. and Nonpsychoactive Cannabinoids: Their Chemistry and Role against Oxidative Stress, Inflammation, and Cancer. *Biomed Res. Int.* **2018**, 1691428 (2018).

90. Brunt, T. M. & Bossong, M. G. The neuropharmacology of cannabinoid receptor ligands in central signaling pathways. *Eur. J. Neurosci.* **n/a**,.

91. Borgonetti V, Governa P, Montopoli M, Biagi M. Cannabis sativa L. Constituents and Their Role in Neuroinflammation. *Curr. Bioact. Compd.* **15**, 147–158 (2019).

92. Fernández-Ruiz, J. *et al.* Cannabidiol for neurodegenerative disorders: important new clinical applications for this phytocannabinoid? *Br. J. Clin. Pharmacol.* **75**, 323–333 (2013).

93. Ruiz-Valdepeñas, L. *et al.* Cannabidiol reduces lipopolysaccharide-induced vascular changes and inflammation in the mouse brain: an intravital microscopy study. *J. Neuroinflammation* **8**, 5 (2011).

94. Chiurchiù, V., Lanuti, M., De Bardi, M., Battistini, L. & Maccarrone, M. The differential characterization of GPR55 receptor in human peripheral blood reveals a distinctive expression in monocytes and NK cells and a proinflammatory role in these innate cells. *Int. Immunol.* **27**, 153–160 (2015).

95. Gertsch, J. *et al.* Beta-caryophyllene is a dietary cannabinoid. *Proc. Natl. Acad. Sci. U. S. A.* **105**, 9099–9104 (2008).

96. Guo, K., Mou, X., Huang, J., Xiong, N. & Li, H. Trans-Caryophyllene Suppresses Hypoxia-Induced Neuroinflammatory Responses by Inhibiting NF-κB Activation in Microglia. *J. Mol. Neurosci.* **54**, 41–48 (2014).

97. Ojha, S., Javed, H., Azimullah, S. & Haque, M. E. β-Caryophyllene, a phytocannabinoid attenuates oxidative stress, neuroinflammation, glial activation, and salvages dopaminergic neurons in a rat model of Parkinson disease. *Mol. Cell. Biochem.* **418**, 59–70 (2016).
98. Faraco, G. *et al.* Histone deacetylase (HDAC) inhibitors reduce the glial inflammatory response in vitro and in vivo. *Neurobiol. Dis.* **36**, 269–279 (2009).
99. Sun, T. *et al.* Alleviation of neuropathic pain by intrathecal injection of antisense oligonucleotides to p65 subunit of NF-κB. *Br. J. Anaesth.* **97**, 553–558 (2006).
100. Guo, S. *et al.* Intranasal Delivery of Mesenchymal Stem Cell Derived Exosomes Loaded with Phosphatase and Tensin Homolog siRNA Repairs Complete Spinal Cord Injury. *ACS Nano* **13**, 10015–10028 (2019).
101. Meredith, M. E., Salameh, T. S. & Banks, W. A. Intranasal Delivery of Proteins and Peptides in the Treatment of Neurodegenerative Diseases. *AAPS J.* **17**, 780–787 (2015).
102. Gershenzon, J. & Dudareva, N. The function of terpene natural products in the natural world. *Nat. Chem. Biol.* **3**, 408–414 (2007).
103. Nave, K.-A. & Werner, H. B. Myelination of the Nervous System: Mechanisms and Functions. *Annu. Rev. Cell Dev. Biol.* **30**, 503–533 (2014).
104. Schuschel, K. *et al.* RNA-binding proteins in acute leukemias. *Int. J. Mol. Sci.* **21**, 1–29 (2020).
105. Hentze, M. W., Castello, A., Schwarzl, T. & Preiss, T. A brave new world of RNA-binding proteins. *Nat. Rev. Mol. Cell Biol.* **19**, 327–341 (2018).
106. Glisovic, T., Bachorik, J. L., Yong, J. & Dreyfuss, G. RNA-binding proteins and post-transcriptional gene regulation. *FEBS Lett.* **582**, 1977–1986 (2008).
107. Gerstberger, S., Hafner, M. & Tuschl, T. A census of human RNA-binding proteins. *Nat. Rev. Genet.* **15**, 829–845 (2014).
108. Díaz-Muñoz, M. D. & Turner, M. Uncovering the role of RNA-binding proteins in gene expression in the immune system. *Front. Immunol.* **9**, (2018).
109. Darnell, R. B. RNA Protein Interaction in Neurons. *Annu. Rev. Neurosci.* **36**, 243–270 (2013).
110. Re, A., Joshi, T., Kulberkyte, E., Morris, Q. & Workman, C. T. *RNA – Protein Interactions : An Overview. RNA sequence, Structure and Function: Computational and Bioinfromatic Methods* vol. 1097 (2014).
111. Cookson, M. R. RNA-binding proteins implicated in neurodegenerative diseases. *Wiley Interdiscip. Rev. RNA* **8**, 1–18 (2017).
112. De Bruin, R. G., Rabelink, T. J., Van Zonneveld, A. J. & Van Der Veer, E. P. Emerging roles for RNA-binding proteins as effectors and regulators of cardiovascular disease. *Eur. Heart J.* **38**, 1380–1388 (2017).

113. Wurth, L. Versatility of RNA-Binding Proteins in Cancer. *Comp. Funct. Genomics* **2012**, 178525 (2012).

114. Newman, R., McHugh, J. & Turner, M. RNA binding proteins as regulators of immune cell biology. *Clin. Exp. Immunol.* **183**, 37–49 (2016).

115. Pascale, A. & Govoni, S. The complex world of post-transcriptional mechanisms: is their deregulation a common link for diseases? Focus on ELAV-like RNA-binding proteins. *Cell. Mol. Life Sci.* **69**, 501–517 (2012).

116. Ince-Dunn, G. *et al.* Neuronal Elav-like (Hu) Proteins Regulate RNA Splicing and Abundance to Control Glutamate Levels and Neuronal Excitability. *Neuron* **75**, 1067–1080 (2012).

117. Pistono, C. *et al.* Unraveling a new player in multiple sclerosis pathogenesis: The RNA-binding protein HuR. *Mult. Scler. Relat. Disord.* **41**, 102048 (2020).

118. Bakheet, T., Williams, B. R. G. & Khabar, K. S. A. ARED 3.0: the large and diverse AU-rich transcriptome. *Nucleic Acids Res.* **34**, 111–114 (2006).

119. Bolognani, F. & Perrone-Bizzozero, N. I. RNA–Protein Interactions and Control of mRNA Stability in Neurons. *J. Neurosci. Res.* **86**, 481–489 (2008).

120. Srikantan, S. & Gorospe, M. HuR function in disease. *Front. Biosci.* **17**, 189–205 (2012).

121. Matsye, P. *et al.* HuR promotes the molecular signature and phenotype of activated microglia: Implications for amyotrophic lateral sclerosis and other neurodegenerative diseases. *Glia* **65**, 945–963 (2017).

122. Gwak, Y. S., Hulsebosch, C. E. & Leem, J. W. Neuronal-Glial Interactions Maintain Chronic Neuropathic Pain after Spinal Cord Injury. *Neural Plast.* **2017**, 2480689 (2017).

123. Gao, Z. & Tsirka, S. E. Animal Models of MS Reveal Multiple Roles of Microglia in Disease Pathogenesis. *Neurol. Res. Int.* **2011**, 383087 (2011).

124. Davalos, D. *et al.* Fibrinogen-induced perivascular microglial clustering is required for the development of axonal damage in neuroinflammation. *Nat. Commun.* **3**, 1227 (2012).

125. Lucchinetti, C. F. *et al.* Inflammatory cortical demyelination in early multiple sclerosis. *N. Engl. J. Med.* **365**, 2188–2197 (2011).

126. Brennan, C. M. & Steitz*, J. A. HuR and mRNA stability. *Cell. Mol. Life Sci. C.* **58**, 266–277 (2001).

127. Lu, L. *et al.* Hu Antigen R (HuR) Is a Positive Regulator of the RNA-binding Proteins TDP-43 and FUS/TLS: Implications for Amyotrophic Lateral Sclerosis*. *J. Biol. Chem.* **289**, 31792–31804 (2014).

128. O'Loughlin, E., Madore, C., Lassmann, H. & Butovsky, O. Microglial Phenotypes and Functions in Multiple Sclerosis. *Cold Spring Harb. Perspect. Med.* **8**, (2018).

129. Tsuda, M., Inoue, K. & Salter, M. W. Neuropathic pain and spinal microglia: a big problem from molecules in ‘small’ glia. *Trends Neurosci.* **28**, 101–107 (2005).

130. Saijo, K. & Glass, C. K. Microglial cell origin and phenotypes in health and disease. *Nat. Rev. Immunol.* **11**, 775–787 (2011).

131. Luo, X. *et al.* Intrathecal administration of antisense oligonucleotide against p38α but not p38β MAP kinase isoform reduces neuropathic and postoperative pain and TLR4-induced pain in male mice. *Brain. Behav. Immun.* **72**, 34–44 (2018).

132. Taves, S. *et al.* Spinal inhibition of p38 MAP kinase reduces inflammatory and neuropathic pain in male but not female mice: Sex-dependent microglial signaling in the spinal cord. *Brain. Behav. Immun.* **55**, 70–81 (2016).

133. Alisi, A., Spaziani, A., Anticoli, S., Ghidinelli, M. & Balsano, C. PKR is a novel functional direct player that coordinates skeletal muscle differentiation via p38MAPK/AKT pathways. *Cell. Signal.* **20**, 534–542 (2008).

134. Zhuang, Z.-Y. *et al.* A peptide c-Jun N-terminal kinase (JNK) inhibitor blocks mechanical allodynia after spinal nerve ligation: respective roles of JNK activation in primary sensory neurons and spinal astrocytes for neuropathic pain development and maintenance. *J. Neurosci.* **26**, 3551–3560 (2006).

135. Zhang, D., Hu, X., Qian, L., O’Callaghan, J. P. & Hong, J.-S. Astrogliosis in CNS Pathologies: Is There A Role for Microglia? *Mol. Neurobiol.* **41**, 232–241 (2010).

136. Trapp, B. D. & Nave, K.-A. Multiple Sclerosis: An Immune or Neurodegenerative Disorder? *Annu. Rev. Neurosci.* **31**, 247–269 (2008).

137. Batoulis, H., Recks, M. S., Addiks, K. & Kuerten, S. Experimental autoimmune encephalomyelitis – achievements and prospective advances. *APMIS* **119**, 819–830 (2011).

138. Brosnan, C. F. & Raine, C. S. The astrocyte in multiple sclerosis revisited. *Glia* **61**, 453–465 (2013).

139. Jiang, Z., Jiang, J. X. & Zhang, G.-X. Macrophages: A double-edged sword in experimental autoimmune encephalomyelitis. *Immunol. Lett.* **160**, 17–22 (2014).

140. Bonetti, B. *et al.* Activation of NF-κB and c-jun Transcription Factors in Multiple Sclerosis Lesions: Implications for Oligodendrocyte Pathology. *Am. J. Pathol.* **155**, 1433–1438 (1999).

141. Mc Guire, C., Prinz, M., Beyaert, R. & van Loo, G. Nuclear factor kappa B (NF-κB) in multiple sclerosis pathology. *Trends Mol. Med.* **19**, 604–613 (2013).

142. Lock, C. *et al.* Gene-microarray analysis of multiple sclerosis lesions yields new targets validated in autoimmune encephalomyelitis. *Nat. Med.* **8**, 500–508 (2002).

143. Bulek, K. *et al.* The inducible kinase IKKi is required for IL-17-dependent signaling associated

with neutrophilia and pulmonary inflammation. *Nat. Immunol.* **12**, 844–852 (2011).

144. Becher, B. & Segal, B. M. TH17 cytokines in autoimmune neuro-inflammation. *Curr. Opin. Immunol.* **23**, 707–712 (2011).

145. Papadaki, O. *et al.* Control of Thymic T Cell Maturation, Deletion and Egress by the RNA-Binding Protein HuR. *J. Immunol.* **182**, 6779 LP – 6788 (2009).

146. Dendrou, C. A., Fugger, L. & Friese, M. A. Immunopathology of multiple sclerosis. *Nat. Rev. Immunol.* **15**, 545–558 (2015).

147. Abbott, N. J., Rönnbäck, L. & Hansson, E. Astrocyte–endothelial interactions at the blood–brain barrier. *Nat. Rev. Neurosci.* **7**, 41–53 (2006).

148. Kebir, H. *et al.* Human TH17 lymphocytes promote blood-brain barrier disruption and central nervous system inflammation. *Nat. Med.* **13**, 1173–1175 (2007).

149. Huppert, J. *et al.* Cellular mechanisms of IL-17-induced blood-brain barrier disruption. *FASEB J.* **24**, 1023–1034 (2010).

150. Beatriz Almolda Berta Gonzalez, B. C. Antigen presentation in EAE: role of microglia, macrophages and dendritic cells. *Front. Biosci.* **16**, 1157–1171 (2011).

151. Jiang, H.-R. *et al.* IL-33 attenuates EAE by suppressing IL-17 and IFN-γ production and inducing alternatively activated macrophages. *Eur. J. Immunol.* **42**, 1804–1814 (2012).

152. Mayo, L., Quintana, F. J. & Weiner, H. L. The innate immune system in demyelinating disease. *Immunol. Rev.* **248**, 170–187 (2012).

153. Murray, P. J. *et al.* Macrophage Activation and Polarization: Nomenclature and Experimental Guidelines. *Immunity* **41**, 14–20 (2014).

154. Olechowski, C. J., Truong, J. J. & Kerr, B. J. Neuropathic pain behaviours in a chronic-relapsing model of experimental autoimmune encephalomyelitis (EAE). *Pain* **141**, (2009).

155. Varhaug, K. N., Torkildsen, Ø., Myhr, K.-M. & Vedeler, C. A. Neurofilament Light Chain as a Biomarker in Multiple Sclerosis. *Front. Neurol.* **10**, 338 (2019).

156. Rot, U., Sandelius, Å., Emeršič, A., Zetterberg, H. & Blennow, K. Cerebrospinal fluid GAP-43 in early multiple sclerosis. *Mult. Scler. J. - Exp. Transl. Clin.* **4**, 2055217318792931 (2018).

157. Boggs, J. M. Myelin basic protein: a multifunctional protein. *Cell. Mol. Life Sci. C.* **63**, 1945–1961 (2006).

158. Bennett, C. F., Krainer, A. R. & Cleveland, D. W. Antisense Oligonucleotide Therapies for Neurodegenerative Diseases. *Annu. Rev. Neurosci.* **42**, 385–406 (2019).

159. Kipp, M. *et al.* Experimental in vivo and in vitro models of multiple sclerosis: EAE and beyond. *Mult. Scler. Relat. Disord.* **1**, 15–28 (2012).

160. Ziemssen, T. *et al.* Optimizing treatment success in multiple sclerosis. *J. Neurol.* **263**, 1053–

1065 (2016).

161. Feinstein, A., Freeman, J. & Lo, A. C. Treatment of progressive multiple sclerosis: what works, what does not, and what is needed. *Lancet Neurol.* **14**, 194–207 (2015).

162. Pascale, A. *et al.* ELAV–GAP43 pathway activation following combined exposure to cocaine and stress. *Psychopharmacology (Berl).* **218**, 249–256 (2011).

163. Sanna, M. D., Peroni, D., Quattrone, A., Ghelardini, C. & Galeotti, N. Spinal RyR2 pathway regulated by the RNA-binding protein HuD induces pain hypersensitivity in antiretroviral neuropathy. *Exp. Neurol.* **267**, 53–63 (2015).

164. Sanna, M. D., Quattrone, A., Ghelardini, C. & Galeotti, N. PKC-mediated HuD-GAP43 pathway activation in a mouse model of antiretroviral painful neuropathy. *Pharmacol. Res.* **81**, 44–53 (2014).

165. Nicholson, B. & Verma, S. Comorbidities in Chronic Neuropathic Pain. *Pain Med.* **5**, S9–S27 (2004).

166. Wolf, S. A., Boddeke, H. W. G. M. & Kettenmann, H. Microglia in Physiology and Disease. *Annu. Rev. Physiol.* **79**, 619–643 (2017).

167. Wu, Y., Dissing-Olesen, L., MacVicar, B. A. & Stevens, B. Microglia: Dynamic Mediators of Synapse Development and Plasticity. *Trends Immunol.* **36**, 605–613 (2015).

168. Setiawan, E. *et al.* Role of Translocator Protein Density, a Marker of Neuroinflammation, in the Brain During Major Depressive Episodes. *JAMA Psychiatry* **72**, 268–275 (2015).

169. Wohleb, E. S. *et al.* Peripheral innate immune challenge exaggerated microglia activation, increased the number of inflammatory CNS macrophages, and prolonged social withdrawal in socially defeated mice. *Psychoneuroendocrinology* **37**, 1491–1505 (2012).

170. Hinwood, M. *et al.* Chronic Stress Induced Remodeling of the Prefrontal Cortex: Structural Re-Organization of Microglia and the Inhibitory Effect of Minocycline. *Cereb. Cortex* **23**, 1784–1797 (2013).

171. Goshen, I. *et al.* A dual role for interleukin-1 in hippocampal-dependent memory processes. *Psychoneuroendocrinology* **32**, 1106–1115 (2007).

172. Kreisel, T. *et al.* Dynamic microglial alterations underlie stress-induced depressive-like behavior and suppressed neurogenesis. *Mol. Psychiatry* **19**, 699–709 (2014).

173. Martínez-Cué, C. & Rueda, N. Cellular Senescence in Neurodegenerative Diseases. *Front. Cell. Neurosci.* **14**, 16 (2020).

174. Vainchtein, I. D. & Molofsky, A. V. Astrocytes and Microglia: In Sickness and in Health. *Trends Neurosci.* **43**, 144–154 (2020).

175. Abraham, J. & Johnson, R. W. Central inhibition of interleukin-1β ameliorates sickness

behavior in aged mice. *Brain. Behav. Immun.* **23**, 396–401 (2009).

176. Kennedy, D. O. *et al.* Modulation of Mood and Cognitive Performance Following Acute Administration of Single Doses of Melissa Officinalis (Lemon Balm) with Human CNS Nicotinic and Muscarinic Receptor-Binding Properties. *Neuropsychopharmacology* **28**, 1871–1881 (2003).
177. Noguchi-Shinohara, M. *et al.* Safety and efficacy of Melissa officinalis extract containing rosmarinic acid in the prevention of Alzheimer's disease progression. *Sci. Rep.* **10**, 18627 (2020).
178. Juruena, M. F., Eror, F., Cleare, A. J. & Young, A. H. The Role of Early Life Stress in HPA Axis and Anxiety. in *Anxiety Disorders: Rethinking and Understanding Recent Discoveries* (ed. Kim, Y.-K.) 141–153 (Springer Singapore, 2020). doi:10.1007/978-981-32-9705-0_9.
179. Ekdahl, C. T., Claasen, J.-H., Bonde, S., Kokaia, Z. & Lindvall, O. Inflammation is detrimental for neurogenesis in adult brain. *Proc. Natl. Acad. Sci.* **100**, 13632 LP – 13637 (2003).
180. Moulin, D. E. *et al.* Pharmacological Management of Chronic Neuropathic Pain: Revised Consensus Statement from the Canadian Pain Society. *Pain Res. Manag.* **19**, 754693 (2014).
181. Kremer, M., Becker, L. J., Barrot, M. & Yalcin, I. How to study anxiety and depression in rodent models of chronic pain? *Eur. J. Neurosci.* **53**, 236–270 (2021).
182. Guida, F. *et al.* Behavioral, Biochemical and Electrophysiological Changes in Spared Nerve Injury Model of Neuropathic Pain. *Int. J. Mol. Sci.* **21**, (2020).
183. Fonseca-Rodrigues, D. *et al.* Nociceptive, emotional, electrophysiological, and histological characterization of the chronic constriction injury model in female Wistar Han rats. *Brain Res. Bull.* **167**, 56–70 (2021).
184. Wang, X.-Q. *et al.* Differential roles of hippocampal glutamatergic receptors in neuropathic anxiety-like behavior after partial sciatic nerve ligation in rats. *BMC Neurosci.* **16**, 14 (2015).
185. Cunningham, C. Microglia and neurodegeneration: The role of systemic inflammation. *Glia* **61**, 71–90 (2013).
186. Streit, W. J. & Xue, Q.-S. Life and Death of Microglia. *J. Neuroimmune Pharmacol.* **4**, 371 (2009).
187. Hemonnot, A.-L., Hua, J., Ulmann, L. & Hirbec, H. Microglia in Alzheimer Disease: Well-Known Targets and New Opportunities. *Front. Aging Neurosci.* **11**, 233 (2019).
188. Saffarpour, S., Janzadeh, A., Rahimi, B., Ramezani, F. & Nasirinezhad, F. Chronic nanocurcumin treatment ameliorates pain-related behavior, improves spatial memory, and reduces hippocampal levels of IL-1β and TNFα in the chronic constriction injury model of neuropathic pain. *Psychopharmacology (Berl).* **238**, 877–886 (2021).

189. www.who.int.

190. Ubaldi, M., Cannella, N. & Ciccocioppo, R. Emerging targets for addiction neuropharmacology: From mechanisms to therapeutics. in *Neuroscience for Addiction Medicine: From Prevention to Rehabilitation - Methods and Interventions* (eds. Ekhtiari, H. & Paulus, M. P.) vol. 224 251–284 (Elsevier, 2016).

191. Cannella, N. *et al.* Building better strategies to develop new medications in Alcohol Use Disorder: Learning from past success and failure to shape a brighter future. *Neurosci. Biobehav. Rev.* **103**, 384–398 (2019).

192. Vengeliene, V., Bilbao, A. & Spanagel, R. The alcohol deprivation effect model for studying relapse behavior: a comparison between rats and mice. *Alcohol* **48**, 313–320 (2014).

193. Spanagel, R. Recent animal models of alcoholism. *Alcohol Res. Heal. J. Natl. Inst. Alcohol Abus. Alcohol.* **24**, 124–131 (2000).

194. Guerrini, I., Quadri, G. & Thomson, A. D. Genetic and environmental interplay in risky drinking in adolescents: a literature review. *Alcohol Alcohol* **49**, 138–142 (2014).

195. Patel, R. R. *et al.* IL-1β expression is increased and regulates GABA transmission following chronic ethanol in mouse central amygdala. *Brain. Behav. Immun.* **75**, 208–219 (2019).

196. Marshall, S. A., McKnight, K. H., Blose, A. K., Lysle, D. T. & Thiele, T. E. Modulation of Binge-like Ethanol Consumption by IL-10 Signaling in the Basolateral Amygdala. *J. neuroimmune Pharmacol. Off. J. Soc. NeuroImmune Pharmacol.* **12**, 249–259 (2017).

197. Crews, F. T., Lawrimore, C. J., Walter, T. J. & Coleman, L. G. J. The role of neuroimmune signaling in alcoholism. *Neuropharmacology* **122**, 56–73 (2017).

198. Koike, H. *et al.* Alcoholic neuropathy is clinicopathologically distinct from thiamine-deficiency neuropathy. *Ann. Neurol.* **54**, 19–29 (2003).

199. Walsh, J. C. & McLeod, J. G. Alcoholic neuropathy. An electrophysiological and histological study. *J. Neurol. Sci.* **10**, 457–469 (1970).

200. Dina, O. A. *et al.* Key role for the epsilon isoform of protein kinase C in painful alcoholic neuropathy in the rat. *J. Neurosci.* **20**, 8614–8619 (2000).

201. Dina, O. A., Gear, R. W., Messing, R. O. & Levine, J. D. Severity of alcohol-induced painful peripheral neuropathy in female rats: role of estrogen and protein kinase (A and Cepsilon). *Neuroscience* **145**, 350–356 (2007).

202. Beasley, M. J., Macfarlane, T. V & Macfarlane, G. J. Is alcohol consumption related to likelihood of reporting chronic widespread pain in people with stable consumption? Results from UK biobank. *Pain* **157**, (2016).

203. Mogil, J. S. Sex differences in pain and pain inhibition: multiple explanations of a controversial

phenomenon. *Nat. Rev. Neurosci.* **13**, 859–866 (2012).

204. Edwards, S., Vendruscolo, L. F., Gilpin, N. W., Wojnar, M. & Witkiewitz, K. Alcohol and Pain: A Translational Review of Preclinical and Clinical Findings to Inform Future Treatment Strategies. *Alcohol. Clin. Exp. Res.* **44**, 368–383 (2020).
205. Sadowski, A. & Houck, R. C. Alcoholic Neuropathy. in *StatPearls [Internet]* (2021).
206. Delery, E. C. & Edwards, S. Neuropeptide and cytokine regulation of pain in the context of substance use disorders. *Neuropharmacology* **174**, 108153 (2020).
207. He, J. & Crews, F. T. Increased MCP-1 and microglia in various regions of the human alcoholic brain. *Exp. Neurol.* **210**, 349–358 (2008).
208. Rajasingh, J. *et al.* IL-10-induced TNF-alpha mRNA destabilization is mediated via IL-10 suppression of p38 MAP kinase activation and inhibition of HuR expression. *FASEB J.* **20**, 2112–2114 (2006).

Appendix I

List of publications

1. **Borgonetti V.**, Coppi E., Galeotti N. "Targeting the RNA-binding protein HUR as potential therapeutic approach for neurological disorders: Focus on amyotrophic lateral sclerosis (ALS), spinal muscle atrophy (SMA) and multiple sclerosis" Int. J. Mol. Sci. 2021, 22(19), 10394.
2. Romanelli, M.N., **Borgonetti, V.**, Galeotti, N. "Dual BET/HDAC inhibition to relieve neuropathic pain: Recent advances, perspectives, and future opportunities" Pharmacol. Res. 2021, 173:105901.
3. **Borgonetti V.**, Governa P., Manetti F., Miraldi E., Biagi M., Galeotti N. "A honokiol-enriched *Magnolia officinalis* Rehder & E.H. Wilson. bark extract possesses anxiolytic-like activity with neuroprotective effect through the modulation of CB1 receptor". J. Pharm. Pharmacol. 2021, 73(9):1161-1168.
4. Cocetta V., Governa P., **Borgonetti V.**, Tinazzi M., Catanzaro D., Peron G., Berretta M., Biagi M., Manetti F., Dall'Acqua S., Montopoli M. "Cannabidiol isolated from *Cannabis sativa* L. protects intestinal barrier from *in vitro* inflammation and oxidative stress". Front. Pharmacol. 2021, 12:641210.
5. Mazzotta S., Governa P., **Borgonetti V.**, Marcolongo P., Gamberucci A., Manetti F., Pessina F., Carullo G., Brizzi A., Aiello F. "Pinocembrin and its linolenoyl ester derivative induce wound healing activity in HaCaT cell line potentially involving a GPR120/FFA4 mediated pathway". Bioorg. Chem. 2021, 108:104657.
6. **Borgonetti V.**, Galeotti N. "Combined inhibition of histone deacetylases and BET family proteins as epigenetic therapy for nerve injury-induced neuropathic pain". Pharmacol. Res. 2021, 165:105431.
7. **Borgonetti V.**, Galeotti N. "Quantitative Analysis of MOR-1 Internalization in Spinal Cord of Morphine-Tolerant Mice". Methods Mol. Biol. 2021, 99-108.
8. **Borgonetti V.**, Galeotti N. "Fluorescence Colocalization Analysis of Cellular Distribution of MOR- 1". Methods Mol. Biol. 2021, 27-34.
9. **Borgonetti V.**, Galeotti N. "Intranasal delivery of an antisense oligonucleotide to the RNA-binding protein HuR relieves nerve injury-induced neuropathic pain". Pain. 2021, 162(5):1500-1510.

10. **Borgonetti V.**, Sanna M.D., Lucarini L., Galeotti N. “Targeting the RNA-Binding Protein Alleviates Neuroinflammation in Experimental Autoimmune Encephalomyelitis: Potential Therapy for Multiple Sclerosis”. Neurotherapeutics. 2021, 18(1):412-429.
11. Patel RR, Wolfe SA, Bajo M, Abeynaike S, Pahng A, **Borgonetti V.**, D'Ambrosio S, Nikzad R, Edwards S, Paust S, Roberts AJ, Roberto M. “IL-10 normalizes aberrant amygdala GABA transmission and reverses anxiety-like behavior and dependence-induced escalation of alcohol intake”. Prog. Neurobiol. 2021, 199:101952.
12. **Borgonetti V.**, Les F., Lopez V., Galeotti N. “Attenuation of Anxiety-Like Behavior by *Helichrysum stoechas* (L.) Moench Methanolic Extract through Up-Regulation of ERK Signaling Pathways in Noradrenergic Neurons”. Pharmaceuticals. 2020, 13(12):472.
13. **Borgonetti V.**, Governa P, Biagi M, Pellati F, Galeotti N. “*Zingiber officinale* Roscoe rhizome extract alleviates neuropathic pain by inhibiting neuroinflammation in mice”. Phytomedicine. 2020, 78:153307.
14. **Borgonetti V.**, Governa P, Biagi M, Galeotti N. “Novel Therapeutic Approach for the Management of Mood Disorders: *In Vivo* and *In Vitro* Effect of a Combination of L-Theanine, *Melissa officinalis* L. and *Magnolia officinalis* Rehder & E.H. Wilson. Nutrients. 2020, 12(6):1803.
15. **Borgonetti V.**, Cocetta V, Biagi M, Carnevali I, Governa P, Montopoli M. “Anti-inflammatory activity of a fixed combination of probiotics and herbal extract in an *in vitro* model of intestinal inflammation by stimulating Caco-2 cells with LPS- conditioned THP-1 cells medium”. Minerva Pediatrica. 2020, doi: 10.23736/S0026-4946.20.05765-5.
16. **Borgonetti** V., Governa P., Biagi M., Dalia P., Corsi L. “*Rhodiola rosea* L. modulates inflammatory processes in a CRH-activated BV2 cell model. Phytomedicine, 2020, 68:153143.
17. Sanna MD., **Borgonetti V.**, Masini, E., Galeotti N. “Histamine H4 receptor stimulation in the locus coeruleus attenuates neuropathic pain by promoting the coeruleospinal noradrenergic inhibitory pathway”. Eur. J. Pharmacol. 2020, 5;868:172859.
18. Sanna MD., **Borgonetti V.**, Galeotti N. “μ opioid receptor-triggered Notch-1 activation contributes to morphine tolerance: role of neuron-glia communication”. Mol. Neurobiol. 2020, 57(1), 331-345.
19. Cocetta V., Catanzaro D., **Borgonetti V.**, Ragazzi E., Giron MC., Governa P., Carnevali I., Biagi M., Montopoli M. “A fixed combination of probiotics and herbal extracts attenuates intestinal barrier dysfunction from inflammatory stress in an *in vitro* model using Caco-2 cells. Rec. Pat. Food Nut. Agr. 2019, 10(1):62-69.

20. **Borgonetti V.,** Governa P., Montopoli M., Biagi M. "*Cannabis sativa* L. constituents and their role in neuroinflammation". Curr. Bioact. Compds. 2019, 15(2):147-158.
21. Pellati F., **Borgonetti V.**, Brighenti V., Biagi M., Benvenuti S., Corsi L. "*Cannabis sativa* L. and nonpsychoactive cannabinoids: their chemistry and role against oxidative stress, inflammation, and cancer". BioMed Res. Int. 2018, 1691428.
22. Governa P., Baini G., **Borgonetti V.,** Cettolin G., Giachetti D., Magnano A.R., Miraldi E., Biagi M. "Phytotherapy in the management of diabetes: a review". Molecules, 2018, 23(1): E105.

Appendix II

Conferences participation

1. Borgonetti V., Galeotti N. “Anti-nociceptive effects of a standardized extract of *Zingiber officinale* Roscoe in a mice model of neuropathic pain” Oral presentation S.I.Fit. Young Researchers Project-Imola, 14 January 2019-
2. Borgonetti, V., Galeotti N. “Evaluation of anti-nociceptive effects of a standardized *Zingiber officinale* roscoe extract in spared nerve injury mice model” PhD Day X edizione- Firenze 23 Maggio- Poster session
3. Borgonetti, V., Galeotti N. “Attività neuroprotettiva *in vitro* di L-teanina e *Magnolia officinalis* Rehder & E.H. Wilson “. Oral presentation XXVII Congresso Nazionale di Fitoterapia - Reggio Emilia, 25 maggio 2019 -
4. Borgonetti V., Sanna M.D., Galeotti N. “Targeting neuropathic pain and axonal damage in multiple sclerosis through genetic modulation of ELAV RNA binding proteins”. – Poster session: Congresso Scientifico Annuale AISM- FISM - Roma 29-31 maggio 2019
5. Borgonetti V., Governa P., Biagi M., Galeotti N. “A standardized extract of *Zingiber officinale* roscoe is more effective than its main constituents in reducing neurotoxicity *in vitro* and shows anti- nociceptive activity in a mice model of neuropathic pain” Poster session 1st International conference on neuroprotection by drugs, nutraceuticals, and physical activity - Bologna 6-7 giugno 2019 – Poster session
6. Borgonetti V., Galeotti N. “The Intranasal administration of HuR ELAV-like RNA-binding proteins inhibitors is effective in reducing the symptoms of neuropathic pain in spared nerve injury mice model” Poster session 39° Congresso Nazionale SIF, Palazzo dei congressi, Firenze 19-23 Novembre 2019
7. Borgonetti V., Galeotti N. A standardized *Helichrysum stoechas* (L.) Moench extract showed anxiolytic effect in mice models. Oral presentation X SYRP: S.I.Fit. Young Researchers Project – Siena, 23 Ottobre 2020
8. Borgonetti V., Galeotti N. "Combined inhibition of histone deacetylases and BET family proteins as epigenetic therapy for nerve injury-induced neuropathic pain" Poster session 3rd Brainstorming research assembly for young neuroscientists, web conference, November 25th-26th 2020
9. Borgonetti V., Governa P., Biagi M., Pellati F., Galeotti N. “*Zingiber officinale* Roscoe rhizome extract alleviates neuropathic pain in mice by reducing neuroinflammation through the

inhibition of class I HDAC isoforms" Oral presentation XXIII SIF Seminar on Pharmacology for PhD Students, Fellows, Post Doc and Specialist Trainees March 8th, 2021.

10. Borgonetti V., Roberts A., Galeotti N., Roberto M. "Chronic ethanol exposure induces neuropathic pain in mice by promoting neuroinflammation" Poster session 40° Congresso Nazionale SIF – il valore scientifico e l'uso appropriato del farmaco 9-13 marzo 2021

11. Borgonetti V. Galeotti N. "Nuovi approcci terapeutici per il trattamento di ansia e depressione con piante medicinali: valutazione dell'effetto ansiolitico di un estratto standardizzato di *Magnolia officinalis* Rehder & E.H. Wilson in vivo ed in vitro" Oral session XXVIII Congressso Nazionaledi Fitoterapia 21-23 maggio 2021

12. Borgonetti V., Galeotti N. "A honokiol-enriched *Magnolia officinalis* Rehder & E.H. Wilson. bark extract alleviates neuropathic pain by inhibiting neuroinflammation" Poster session GA – 69th Annual Meeting 2021, Virtual conference, 5 – 8 Sept. 2021